



Croissance par MBE et caractérisation de structures GaInAsP pour la réalisation de circuits intégrés photoniques à base d'amplificateurs optiques à très large bande spectrale

Quentin Hochart

► To cite this version:

Quentin Hochart. Croissance par MBE et caractérisation de structures GaInAsP pour la réalisation de circuits intégrés photoniques à base d'amplificateurs optiques à très large bande spectrale. Optique / photonique. INSA de Toulouse, 2023. Français. NNT : 2023ISAT0022 . tel-04327747

HAL Id: tel-04327747

<https://theses.hal.science/tel-04327747>

Submitted on 6 Dec 2023

HAL is a multi-disciplinary open access archive for the deposit and dissemination of scientific research documents, whether they are published or not. The documents may come from teaching and research institutions in France or abroad, or from public or private research centers.

L'archive ouverte pluridisciplinaire **HAL**, est destinée au dépôt et à la diffusion de documents scientifiques de niveau recherche, publiés ou non, émanant des établissements d'enseignement et de recherche français ou étrangers, des laboratoires publics ou privés.



THÈSE

En vue de l'obtention du

DOCTORAT DE L'UNIVERSITÉ DE TOULOUSE

Délivré par :

Institut National des Sciences Appliquées de Toulouse (INSA de Toulouse)

Présentée et soutenue par :
Quentin HOCHART

le jeudi 28 septembre 2023

Titre :

Croissance par MBE et caractérisation de structures GaInAsP/InP pour la réalisation de circuits intégrés photoniques à base d'amplificateurs optiques à très large bande spectrale

École doctorale et discipline ou spécialité :
ED GEET : Photonique et Systèmes Optoélectroniques

Unité de recherche :

Laboratoire de Physique Chimie des Nano-Objets (LPCNO) & Nokia (III-V Lab)

Directeur/trice(s) de Thèse :

Hélène CARRERE

Jury :

Nicolas BERTRU - Professeur - Institut FOTON INSA Rennes (Rapporteur)
Éric TOURNIÉ - Professeur - IES Montpellier (Rapporteur)
Guilhem ALMUNEAU - Directeur de recherche - LAAS-CNRS Toulouse
Noëlle GOGNEAU - Chargée de recherche - C2N Université Paris-Saclay
Hélène CARRERE - Professeure - LPCNO INSA Toulouse
Arnaud WILK - Ingénieur de recherche - III-V Lab Nokia (Encadrant industriel)

A ma famille,

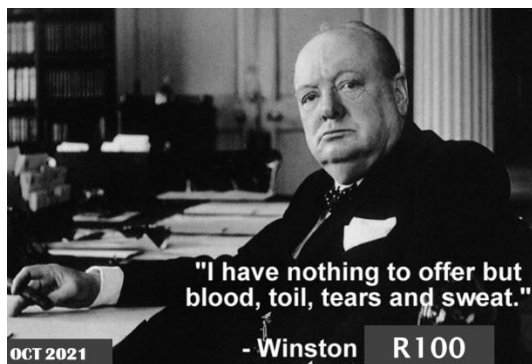
A mi suegra,

A ma Choupette.

Remerciements

Quatre ans au III-V Lab qui s'achèvent avec l'écriture de ce manuscrit. Quatre ans d'apprentissage, de rire, de joie, mais aussi de doutes, de remises en question et de migraines. Il y a tant de personnes que j'ai pu rencontrer et avec qui j'ai pu discuter au cours de ces années, j'espère n'en oublier aucune.

Je remercie en premier lieu l'équipe MBE412 du III-V Lab, Arnaud Wilk, bon encadrant, mais surtout un humain incroyable. Un jour, tu l'auras ton nouveau vélo avec cadre titane ! Merci aussi à Olivier Delorme, et bon courage pour la nouvelle aventure que tu vas démarrer. Merci pour votre patience, votre capacité d'écoute et pour votre gentillesse. Ça va me manquer de vous attendre pour partir du laboratoire pour lancer ces fameux batchs de nuits et surtout du week-end. Une pensée aussi pour le R100, et ce magnifique montage d'Arnaud qui le résume si bien :



Je vous souhaite bon courage avec son successeur, Quasar. En espérant qu'il vous procure moins de larmes, de frayeurs et de douleurs et beaucoup plus de plaques !

Merci aux « Robers du 49 », Gabin Grégoire et Théo Sabardeil, vos blagues et votre franche camaraderie sont d'une importance capitale pour le groupe, et aussi pour l'esprit « Ministère de l'homme ».

Merci aussi à l'équipe du « PMU chez Michmich », pour leur bonne humeur, Michel Garcia, Alexandre Larrue, Claire Théveneau, Bouzid Simozrag, Eva Izquierdo et Guillaume Daccord. Merci pour la bonne humeur et l'ambiance que vous apportez pendant les repas et les pauses café. 5 étoiles sur MonpetitPMU.com, une superbe adresse.

Merci aux collègues du bureau, le poto Risab Gnanamani, Gustavo Alfonso de Castro et Shirley Prado de la Cruz. On a quand même bien rigolé malgré le travail, et non, je ne viendrais pas au karaoké ! Pour les stagiaires, Pierre Gadras, Anaël Sedilot et Amin Souleiman (oui, aucun respect Amin), avec qui j'ai pu échanger et qui ont réussi à ramener un peu de potins et toujours plus de rires dans ce bureau, je vous remercie aussi. Bon courage à Célia Cruz et Emmanuel Bourgon pour vos thèses et à Sara Bassil et Mayssa Dammak pour vos futures thèses !

Je remercie également l'équipe du V5, composée de Jean Decobert, Claire Besançon, Nicolas Vaissière, Florence Martin et Gusgus. Merci pour votre saine concurrence qui nous pousse à aller de l'avant sur les projets et s'améliorer.

Une pensée également aux personnes avec qui j'ai discuté au quotidien en épitaxie, Charles « Charo » Pitaval, Cédric Lacam, Nadia El Bondry, Antoine Elias, Olivier Parillaux, Axel Evirgen, Jean Pierre Le Goec et Bruno Gérard. Nos discussions m'ont toujours beaucoup appris aussi bien dans vos domaines techniques qu'humainement. Une pensée particulière à Agnès Chateigner dont la gentillesse n'avait d'égale que sa franchise.

Côté Techno maintenant, un grand merci à Cosimo Calò, Catherine Fortin et Antoine Bobin pour l'aide et la formation que vous m'avez apporté pour réaliser mes composants. J'aurais vraiment été dans la panade sans votre aide et vos conseils. Merci aussi à Alexandre Garreau et Jean François Paret, avec qui j'ai eu la chance de soumettre un brevet, dont les réunions étaient quand même bien animées.

Merci à Vladyslav Vakarin, Hervé Bertin, Frédéric Pommereau, Dalila Make, Estelle Derouin, Delphine Néel, Colin Mismer et Virginie Nodjiadjim avec qui j'ai pu discuter plus ou moins longtemps, mais toujours avec plaisir. Mention spéciale pour Jorge Pereira qui m'a beaucoup appris sur l'aspect humain et qui a toujours été là pour me remonter le moral au cours d'une longue discussion ou d'une blague.

Merci aux personnes du GaN, Nicolas Michel, Sébastien Aroulanda, Nicolas Delpuech et même à l'alternante, Audrey Romain. Bon courage à toi si tu fais une thèse par la suite, c'est sympa, mais qu'est-ce que c'est dur à rédiger. Merci aussi à ceux que j'ai rencontré durant mon stage et qui sont parti vers d'autres horizons, Olivier Patard, Philippe Altuntas et Yohann Corniellere.

Au back-end, merci énormément à Karim Mekhzni pour tous les montages qu'il a réalisé pour moi, mais aussi pour l'ensemble du laboratoire. Tu as de l'or dans les doigts et beaucoup trop de boulot. Merci aussi à l'équipe de caractérisations, avec en tête de ligne, Delphine Lanteri, le « cerbère du banc SOA ». Je te remercie beaucoup pour le gain de confiance que tu m'as donné pour caractériser mes composants et pour les explications sur les bancs de mesure que tu m'as répétées bien trop de fois. Merci aussi à Mokhtar Korti, Harry Gariah, François Duport, Bernadette Duval, Fabrice Blache et David Bitauld avec qui j'ai aussi pu échanger. Merci aussi aux concepteurs pour leurs connaissances théoriques et leur sympathie, Giancarlo Cerulo, François Van Dijk, Christophe Caillaud.

C'est incroyable de se retourner pour se souvenir du nombre, impressionnant, de personnes avec lesquelles on interagit au quotidien.

Je remercie aussi l'ensemble des membres du jury, en commençant par Guilhem Almuneau qui a accepté d'en être président, ainsi que l'examinatrice, Noëlle Gogneau. Je remercie tout particulièrement les rapporteurs Eric Tournié et Nicolas Bertru pour l'attention portée à mon travail.

Pour terminer sur l'aspect professionnel, merci beaucoup à ma directrice de thèse, Hélène Carrère, pour ses connaissances théoriques mais surtout pour son côté humain. Avec Arnaud, vous avez réussi à me faire garder le cap malgré les coups durs. Vous avez vraiment été très compréhensifs et je vous en remercie énormément !

Au-delà du professionnel, merci à l'ensemble des amis que j'ai pu me faire pendant cette aventure. Merci aussi à ceux qui étaient là dès le départ, Jojo, Clem, Ana. Nos parties de play me manquent, c'est dur de grandir et devenir adultes.

Merci à mes parents, à Céline et Nico, Ephram et Esmée, pour m'avoir redonné le moral et le courage de continuer jusqu'au bout tout ce travail et de toujours m'accueillir à bras ouverts dans le Nord. Ne vous inquiétez pas, je remonte bientôt.

Muchísimas gracias también a mi suegra, Licenciada María Elena Zander, y sus padres, por su apoyo, sus conversaciones y los chimi-chimis que tanto me hacían reír durante estos tres años.

Oui, trois ans, parce que cela fait trois ans que tu me soutiens, toi qui est sûrement la seule à avoir lu tous les remerciements. Merci pour tout Choupette.

Une thèse c'est long. Une thèse c'est dur. Mais qu'est-ce qu'on a bien rigolé quand même. Merci à tous.

Table des matières

Résumé de la thèse en français.....	1
1. Introduction	1
1.1. Applications nécessitant des amplificateurs large bande.....	1
1.2. Les amplificateurs optiques.....	2
1.3. Amplification large bande	4
2. Conception des amplificateurs optiques à semiconducteur	5
2.1. Conception de la zone active	5
2.2. Simulation du confinement optique.....	6
2.3. Structures proposées	8
3. Fabrication.....	9
3.1. Croissances par épitaxie par jets moléculaires à sources gazeuses	9
3.2. Procédés de fabrication.....	11
3.3. Etapes de back-end	13
4. Caractérisations des composants	15
4.1. Composants produits par SIBH 2-étapes.....	15
4.2. Composants produits par SIBH 1-étape et comparaisons des performances.....	19
5. Conclusions	23
Bibliographie	i
Figures	iv
Tableaux	iv

Résumé de la thèse en français

1. Introduction

Dans ce chapitre, nous présentons une revue des applications nécessitant une amplification large bande et pourquoi les Amplificateurs Optiques à Semiconducteur (SOA) et SOA Reflectifs (RSOA) sont des solutions d'intérêt. Ensuite, nous décrivons brièvement les autres solutions d'amplification existantes ainsi que les paramètres caractéristiques d'un amplificateur optique (Gain, Bande passante optique, Facteur de bruit (NF), Puissance de saturation (P_{sat}) et Dépendance à la polarisation). Enfin, nous détaillons les solutions d'amplification large bande existantes, pour mettre en avant les arguments en faveur de l'utilisation de SOA.

1.1. Applications nécessitant des amplificateurs large bande

Le trafic internet est en croissance continue depuis les années 2000 et l'arrivée d'internet dans nos foyers. Beaucoup de systèmes sont développés pour améliorer le transfert, tels que le Multiplexage en longueur d'onde (WDM) [1] et le Multiplexage spatial (SDM) [2]. Les améliorations des composants optiques pour les rendre compatibles avec des flux de données plus importants permettent aussi d'améliorer les performances de nos réseaux. Parmi les axes d'amélioration en cours de développement, l'élargissement de la bande passante disponible est une solution particulièrement intéressante pour plusieurs raisons.

Les réseaux optiques de communication sont basés sur les fibres optiques. Plusieurs développements permettent à ces dernières de réduire les phénomènes d'absorption [3] ou de Dispersion Chromatique (CD) [4]. Cela permet d'augmenter la largeur des bandes passantes utilisées pour les télécommunications, montrées en Figure 1.

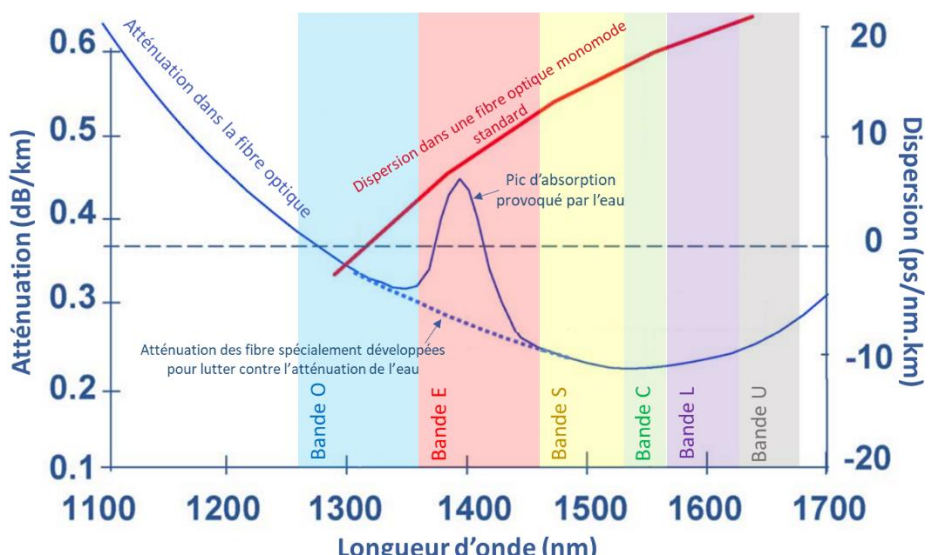


Figure 1. Graphique d'absorption et de dispersion chromatiques dans les fibres optiques standards avec la représentation des différentes bandes optiques [5].

Pour les communications longues distances, les bandes optiques utilisées sont celles présentant le minimum d'absorption dans la fibre optique. Les amplificateurs sont ici nécessaires pour permettre aux signaux de recouvrir la puissance perdue par l'absorption dans la fibre, pour atteindre le récepteur. Les premiers développements ont concerné la bande C, puis la bande L, suivies, plus récemment, par la bande S.

Pour les communications courtes distances, la bande privilégiée est la O, car à ces longueurs d'onde, les fibres optiques standards ne subissent que très peu la CD. Les réseaux d'accès, basés sur des technologies de Réseaux Optiques Passifs (PON) [6] opèrent en bande O. Dans ce cadre, les amplificateurs utilisés sont intégrés aux transmetteurs dits « transparents » qui permettent d'utiliser différentes longueurs d'onde de travail, sans interaction humaine [7]. Le principal facteur de ces réseaux étant le prix, devant être bas, l'utilisation de SOA et RSOA larges bandes permettrait d'augmenter les capacités de ces réseaux, en limitant le coût des composants.

Les bandes C+L (allant de 1530 à 1625 nm) et O (de 1260 à 1360 nm) sont les bandes optiques d'intérêt pour lesquels nous travaillons au développement de SOA et RSOA large bande. D'autres domaines d'application sont la fabrication d'analyseurs de spectres optiques, ou encore, la Tomographie en Cohérence Optique (OCT) [8]. Le premier domaine permet la mesure de la puissance optique sur une plage de longueur d'onde choisie par l'utilisation. Ces systèmes sont utilisés dans la recherche et le développement, mais aussi dans l'industrie. Cette technologie est utilisée dans les télécommunications, mais aussi dans les domaines de la sécurité, de la surveillance environnementale, ou encore de la santé. Le second domaine, la tomographie en cohérence optique est une technique d'imagerie médicale non invasive qui utilise les ondes lumineuses pour générer des images 2D ou 3D du milieu observé. Les longueurs utilisées sont partiellement communes à celles des télécommunications [9].

Pour ces applications, le développement de SOA et RSOA, larges bandes, opérant en bandes C+L et O, est bénéfique. Cependant, d'autres types d'amplificateurs optiques ont vu le jour et se sont développés.

1.2. Les amplificateurs optiques

1.2.1. *Les amplificateurs optiques à fibre dopée*

Les transmissions longues distance et l'utilisation de plusieurs longueurs d'onde dans une unique fibre optique ont été permis avec l'invention, dans les années 1990, des Amplificateurs à Fibre Dopée Erbium (EDFA). Ce type d'amplificateur optique a simplifié le procédé d'amplification en utilisant uniquement un signal optique. Auparavant, à chaque répéteur, le signal optique devait être converti en signal électrique, puis reconvertis en signal optique pour être amplifier. Les EDFA permettent aussi l'amplification simultanée de plusieurs longueurs d'onde avec un unique composant. La bande passante optique de ces composants est généralement inférieure à 50 nm.

Dans ces dispositifs, le milieu à gain est une fibre optique dopée avec des ions Er^{3+} . Cette fibre est couplée avec un laser de pompe, opérant à 980 nm ou 1480 nm. Ce laser génère une inversion de population vers des états excités métastables. Cela permet au signal d'entrée d'être amplifié par des recombinaisons stimulées, à des longueurs d'onde définies par la différence d'énergie entre les états métastables et l'état fondamental [10].

L'Erbium n'est pas l'unique dopant utilisé dans les fibres, bien que le plus commun, car il permet l'amplification des signaux en bande C et en bande L. Pour permettre l'amplification en bande O, différents dopants sont étudiés comme le Praséodyme (Pr^{3+}), le Néodyme (Nd^{3+}), le Thulium (Tm^{3+}) ou encore le Bismuth (Bi) [11].

1.2.2. *Les amplificateurs Raman*

L'autre type d'amplificateur optique se base sur la diffusion Raman stimulée, produit par l'interaction entre les photons incidents et les molécules d'un milieu solide [12]. Ainsi, les amplificateurs Raman sont aussi équipés de lasers de pompe qui permettent l'amplification de signaux optiques dont la longueur d'onde est plus courte, de quelques dizaines de nanomètres, que celle de pompe. Les principaux problèmes de ce type d'amplificateur sont son coût et sa taille, qui empêchent son intégration sur les lignes de transmissions ou dans des systèmes compacts. Aussi, sa bande passante ne dépasse pas les 40 nm avec un unique laser de pompe.

1.2.3. Les amplificateurs optiques à semiconducteur

Les SOA ont vu leur développement débuter dans les années 1960. Cependant, il faudra attendre les années 1980 et l'amélioration de la qualité des traitements antireflets (AR) pour obtenir de hautes valeurs de gain. Les SOA et RSOA bénéficient de ce type de traitement pour permettre l'amplification du signal suite à un et deux passages, respectivement, du signal dans le composant, comme montré par la Figure 2. Le RSOA nécessite un traitement haute réflectivité (HR) pour que le signal entre et sorte la même facette.

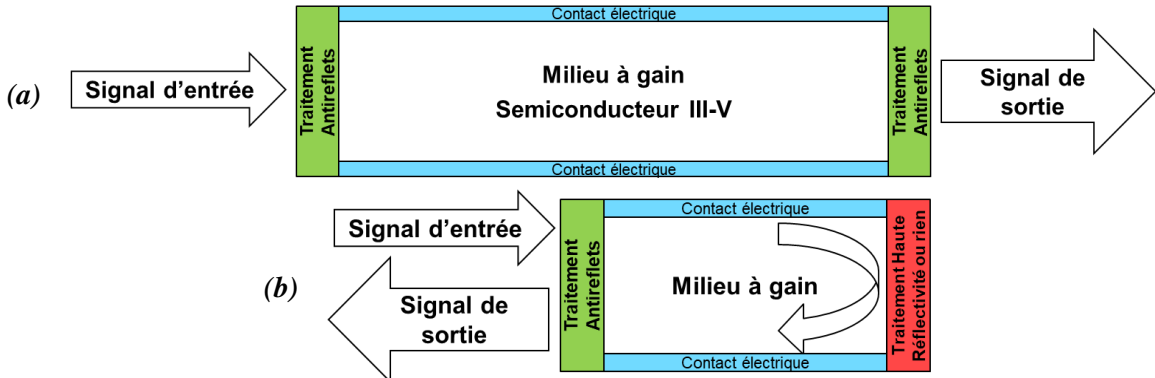


Figure 2. Schémas (a) d'un SOA et (b) d'un RSOA.

Les SOA sont réalisés à partir de matériaux semiconducteurs issus des systèmes GaInAsP ou AlGaInAs. Dans notre cas, le matériau de base utilisé est le GaInAsP, à bande interdite directe, déposé sur des substrats en InP. Les extrema des bandes de valence et de conduction ont le même vecteur d'onde et sont séparés par une bande d'énergie interdite, notée E_g . Ils permettent aux porteurs électriques de recombiner en émettant un photon d'énergie proche de E_g . Dans notre contexte, les énergies couvertes par les compositions du quaternaire GaInAsP permettent l'émission de photon, dont la longueur d'onde est en bande C+L ou O.

Il existe deux types de recombinaisons radiatives : (i) l'émission spontanée et (ii) l'émission stimulée. Dans le premier cas, il s'agit d'un événement aléatoire produisant un photon d'énergie E_g , dont la direction et la phase sont aléatoires. Elle est à l'origine de l'Emission Spontanée Amplifiée (ASE) en profitant du second type d'émission. Ce second cas survient quand un photon incident d'une énergie proche de E_g provoque une recombinaison résultant en un deuxième photon, identique au premier. Il s'agit de l'émission utilisée pour permettre l'amplification des signaux optiques.

La structure des SOA est étudiée pour faciliter ces recombinaisons. Tout d'abord, la zone active du matériau est placée entre deux couches de matériaux dopés p et n pour obtenir une diode PiN. La zone active est faite d'un alliage GaInAsP, de manière à émettre sur la plage de longueur d'onde souhaitée. Cela permet aussi à cette zone d'avoir l'indice de réfraction le plus élevé et donc, de créer un effet de guidage optique favorisant l'émission stimulée. La concentration de photons dans cette zone est quantifiable, grâce au recouvrement de la zone active par le signal optique, par le confinement optique, noté Γ , donnée en pourcentage. Ce paramètre évolue avec le type de structure utilisé dans la zone active, pouvant être un matériau uniforme massif, des Puits Quantiques (QW), des fils quantiques ou des Boîtes Quantiques (QD). Chacune correspond à un degré de confinement supplémentaire (1D pour les QW à 3D pour les QD) des porteurs dans l'espace et possède des caractéristiques propres. Les Multiples Puits Quantiques (MQW) proposent un équilibre entre confinement optique et courant d'injection nécessaire pour générer l'amplification. Il s'agit donc du type de structure réalisé pour ce travail.

1.2.4. Paramètres caractéristiques d'un amplificateur optique

Cinq paramètres sont importants pour l'amplification optique large bande : (i) le gain (G), (ii) la bande passante optique, déduite du gain, (iii) le NF, (iv) la P_{sat} et (v) la sensibilité à la polarisation, qui sera

abordée pendant la conception des composants. Les trois grandeurs restantes sont définies par les équations 1 à 3 [13]:

$$\text{Équation 1. } G_{chip} = \exp^{[(\Gamma g_m(n) - \alpha(n)) * L]}$$

$$\text{Équation 2. } NF = \frac{1}{G_{chip}} + \frac{2 * P_{ASE}}{G_{chip} * h\nu * B_0} = 2 * \left(\frac{n_{sp}}{C_1} \right)$$

$$\text{Équation 3. } P_{sat} = \ln(2) * \frac{A}{\Gamma} * \frac{h\nu}{a_1 \tau} * \frac{G_0}{G_0 - 2}$$

Où, G_{chip} est le gain puce ne prenant pas en compte les pertes de couplage, Γ le confinement optique, g_m le gain matériau, n la densité de porteurs électriques, α les pertes, L la longueur de la zone active, P_{ASE}/B_0 la densité spectrale d'ASE, $h\nu$ l'énergie d'un photon, n_{sp} le facteur d'inversion quantifiant le remplissage des niveaux d'énergie, C_1 le coefficient de couplage en entrée du SOA compris entre 0 et 1, A la section de la zone active correspondant à sa largeur par son épaisseur, a_1 le gain différentiel, τ le temps de vie des porteurs et G_0 le gain nominal à la densité de porteur considérée.

Le gain doit être le plus élevé possible avec un NF faible et une P_{sat} importante. De manière générale, un bon couplage optique et de faibles pertes de la zone active permettent l'obtention de bonnes performances pour un SOA. Pour minimiser le NF, il faut un bon rapport signal à bruit. Nous pouvons utiliser un faible confinement qui permettrait parallèlement d'augmenter la valeur de P_{sat} , mais au détriment du gain. Ce dernier peut être amélioré par une grande longueur de composant.

Pour la bande passante, il s'agit de l'ensemble des longueurs d'onde pour lesquelles le gain est compris entre sa valeur maximale et cette même valeur divisée par deux, ou réduite de 3 dB, dans le cas d'une échelle logarithmique. Les valeurs habituellement citées pour les différents types d'amplificateur sont listées dans le Tableau 1.

	<i>Gain</i>	<i>NF</i>	<i>P_{sat}</i>	<i>Bande passante optique</i>	<i>Sensibilité à la polarisation</i>
EDFA	> 40 dB	< 7 dB	Entre 15 et 20 dBm	< 50 nm	Non
Raman	< 30 dB	< 7 dB	Dépendant du nombre de lasers de pompe	< 40 nm	Non
SOA	> 30 dB	< 10 dB	< 18 dBm	< 110 nm	Oui

Tableau 1. Paramètres caractéristiques des différents types d'amplificateurs optiques.

1.3. Amplification large bande

L'élargissement de la bande passante est le moteur de notre recherche sur les SOA et RSOA. Différentes techniques sont déjà utilisées pour proposer une amplification large bande. L'utilisation de filtres permettant une réduction de la valeur du gain maximal est une, mais est parfois sujet à des difficultés de réalisation [14]. Il est également possible d'utiliser plusieurs amplificateurs en série ou en parallèle. Ainsi, les amplificateurs dits « hybrides » ont vu le jour en combinant EDFA et Raman [15], EDFA et SOA [16] ou encore, Raman et SOA [17].

En bande C+L, des travaux précédemment réalisés au III-V Lab ont permis le développement de SOA basés sur des MQW en GaInAsP offrant une bande passante de plus de 100 nm. L'un de nos buts est donc de proposer un élargissement encore plus important de cette bande passante. En bande O, il existe des solutions telles qu'un amplificateur hybride entre un SOA et un amplificateur à fibre dopée praséodyme (PDFA), un amplificateur à fibre dopée bismuth (BDFA), ou des SOA utilisant le système de matériaux AlGaInAs. Il n'existe pas de solution basée sur des MQW en GaInAsP. Notre travail consiste donc aussi à développer une telle solution.

2. Conception des amplificateurs optiques à semiconducteur

A présent, nous commençons la conception de nos structures SOA. Dans un premier temps, nous examinons les paramètres de la zone active afin d'obtenir un comportement large bande pour nos composants. Ensuite, nous réalisons des simulations optiques afin de générer des variantes de structures pour étudier l'influence du confinement optique sur les performances finales des composants. Enfin, nous présentons les structures proposées pour répondre aux objectifs de ce travail, à savoir élargir l'amplification en bande C+L et proposer une première structure SOA large bande opérante en bande O, basée sur des MQW en GaInAsP. Les RSOA et SOA fabriqués possédant la même structure, nous nous référerons uniquement aux SOA, durant cette section, pour ne pas nuire à sa compréhension.

2.1. Conception de la zone active

La conception de la zone active est une étape cruciale de la fabrication des SOA car elle va paramétriser la bande passante optique des composants mais aussi d'autres aspects tels que le gain matériau ou la sensibilité à la polarisation. L'ingénierie de structure de bande permise par les semiconducteurs rend possible l'ajustement de ces propriétés.

2.1.1. Longueurs d'onde et polarisation

A travers l'ingénierie de bande passante, la notion de contrainte dans le matériau a une grande importance. Cette contrainte peut être en tension, quand le matériau épitaxié possède un paramètre de maille inférieur à celle du substrat, ou inversement, en compression. Ce paramètre est directement lié aux compositions du substrat et de la couche réalisée. Il en résulte un impact non négligeable sur l'énergie de bande interdite et donc, sur la longueur d'émission des composants.

La contrainte induit aussi une modification importante de la bande de valence. Une valeur de contrainte négative, donc en tension, permet d'obtenir des niveaux fondamentaux de type léger. Inversement, une valeur de contrainte positive, en compression, place les trous lourds en haut de la bande de valence [18]. La présence d'une contrainte dans le matériau influe sur la sensibilité à la polarisation des composants. Un signal lumineux est une combinaison aléatoire de deux modes de polarisation, le mode Transverse Electrique (TE) et le mode Transverse Magnétique (TM). Pour les matériaux contraints en compression, l'amplification du mode TE est la seule rendue possible par les fonctions d'onde [19].

Cependant, à cause de la complexité de mettre en place une zone active contrainte en tension, des solutions ont vu le jour pour qu'à partir de composants sensibles à la polarisation, nous obtenions des modules, intégrables aux systèmes, qui y soient insensibles. Grâce à ces modules, nous pouvons utiliser la contrainte en compression, plus permissive pendant l'épitaxie, afin de fabriquer nos matériaux.

2.1.2. Les transitions optiques pour une amplification large bande

La composition permet aussi de contrôler les énergies, et donc, les longueurs d'onde des transitions optiques. Cependant, d'autres paramètres impactent ces transitions, comme l'épaisseur des QW. Avec une épaisseur réduite, les niveaux électroniques sur lesquels sont basés l'amplification large bande ont des énergies très différentes. Il faut donc de hautes valeurs de densité de courant pour permettre une amplification large bande [20]. Néanmoins, en utilisant des puits suffisamment épais, il devient possible de confiner deux niveaux d'électron, ce qui réduit drastiquement la densité de courant à injecter. Pour cette raison, nous basons nos structures sur des QW « épais ».

Dans cette configuration, le gain est généré par les transitions en les niveaux d'électrons et les niveaux de trous lourds (e_i-hh_i). Comme illustré par la Figure 3, à faible courant d'injection, le gain est permis par la transition de basse énergie, donc de haute longueur d'onde, e_1-hh_1 . En augmentant le courant, la transition e_2-hh_2 participe aussi au spectre de gain et permet d'atteindre un gain dit « plat » couvrant une

bande passante maximale. Une fois le courant de gain plat dépassé, la transition e_2-hh_2 devient prépondérante, ce qui réduit la bande passante au niveau des faibles longueurs d'onde.

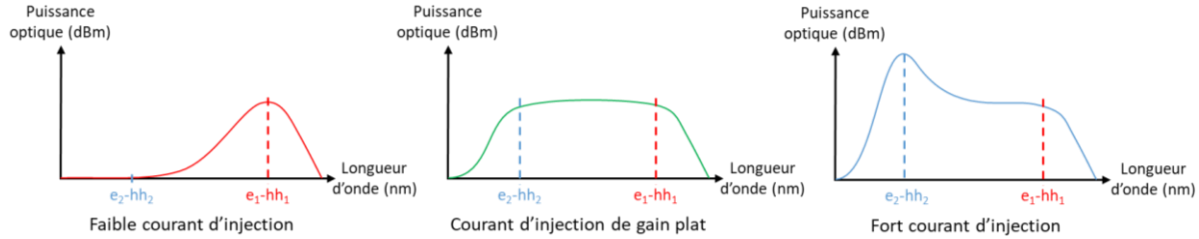


Figure 3. Comportement du gain en fonction du courant injecté, dans un SOA dont l'amplification est basée sur 2 transitions énergétiques.

Les notions de composition, de contrainte, d'épaisseur de puits permettent, une fois combinées de simuler le gain matériau des potentielles structures. A celles-ci s'ajoute l'offset de bande entre les QW et les barrières qui composent la zone active pour confiner correctement les deux niveaux d'électron e_1 et e_2 . L'étude de ces quatre paramètres a permis de proposer 2 structures de zone active pour une amplification en bande C+L et 1 pour la bande O.

2.1.3. Structures de zone active proposées

L'utilisation de l'Epitaxie par Jets Moléculaires à Sources Gaz (GSMBE) et les optimisations précédemment réalisées au III-V Lab permettent d'obtenir des interfaces abruptes entre puits et barrière si leur différence de composition est uniquement régie par les éléments V (Arsenic (As) et Phosphore (P)). Pour la bande C+L, le matériau utilisé pour les barrières est l'alliage quaternaire GaInAsP émettant à 1,17 μm , noté $Q_{1,17}$. Pour la bande O, le matériau utilisé, noté $Q_{1,03}$, devra émettre à une longueur d'onde de 1,03 μm . Avec ces bases, nous avons fait le choix des matériaux des QW, ainsi que de leurs épaisseurs pour proposer 2 zones actives en bande C+L, notées designs A et B, et 1 en bande O, notée design O, toutes présentées dans le Tableau 2.

<i>Caractéristiques</i>	<i>Design A</i>	<i>Design B</i>	<i>Design O</i>
<i>Epaisseur des QW</i>	140 Å	110 Å	110 Å
<i>Epaisseur des barrières</i>	100 Å	90 Å	100 Å
<i>Contrainte des QW</i>	+1,23 %	+1,27 %	1,20 %
<i>Contrainte des barrières</i>	A l'accord de maille	A l'accord de maille	A l'accord de maille
<i>Longueur d'onde e_1-hh_1</i>	1624 nm	1626 nm	1361 nm
<i>Longueur d'onde e_1-hh_3</i>	1559 nm	1527 nm	1296 nm
<i>Longueur d'onde e_2-hh_2</i>	1478 nm	1425 nm	1230 nm
<i>Bande passante théorique</i>	146 nm	201 nm	131 nm

Tableau 2. Caractéristiques des zones actives conçues.

Afin de compléter la conception des composants, nous devons à présent simuler le reste de la structure. Celle-ci est une Hétérostructure Enterrée dans du Semi-Isolant (SIBH). Cette structure a été sélectionnée car elle permet d'obtenir une faible résistance série, une bonne dispersion thermique et un faible confinement optique dans le matériau dopé p, connu pour être fortement absorbant. La fabrication de cette structure est détaillée dans la section 3.

2.2. Simulation du confinement optique

Pour les simulations optiques, nous avons utilisé le logiciel Fimmwave, développé par Photon Design. Ces simulations nous ont permis de concevoir 2 variantes de structures par zone active proposées précédemment. Pour cela, nous avons établi différentes valeurs de confinement optiques à l'aide des couches entourant la zone active. Les couches sont définies par leurs dimensions (largeurs et épaisseurs)

mais aussi par leurs indices de réfraction. Afin d'obtenir ces derniers, nous avons réalisé un important exercice de bibliographie afin de savoir sur quel modèle de calcul les baser.

2.2.1.Les indices de réfraction

Pour les couches de matériau InP, le modèle présenté par Pettit et Turner est utilisé [21]. Ce modèle se base sur l'équation de Sellmeier, mais a surtout servi de base pour obtenir une multitude de modèles utilisés pour calculer les indices de réfraction des alliages GaInAsP. Parmi ceux-ci, nous pouvons citer : (i) le modèle basé sur l'interpolation de l'équation de Sellmeier [22], qui se base sur des coefficients attribués aux quatre alliages binaires composant le quaternaire GaInAsP (GaAs, GaP, InAs et InP), (ii) le modèle de l'oscillateur simple [23], qui introduit les notions d'énergie de dispersion (E_d) et d'oscillation (E_0), (iii) le modèle de Tanguy [24], qui permet le calcul des indices de réfraction aux abords de la zone d'absorption des matériaux, tout comme (iv), le modèle basé sur la proportion d'As dans le quaternaire [25], (v) le modèle de l'oscillateur simple modifié [26], qui est une amélioration du premier modèle pour s'approcher de valeurs expérimentales, et enfin, (vi) le modèle basé sur le calcul de fonction diélectrique [27].

Des mesures antérieures à ce travail ont été réalisées au sein du laboratoire sur une série d'alliages quaternaires GaInAsP. Pour les mesures réalisées en bande C+L, les deux derniers modèles donnent des approximations satisfaisantes mais qui semblent inférieures aux valeurs mesurées. Nous avons donc choisi de nous baser sur une régression linéaire pour l'indice du Q_{1,17}, car il s'agissait du comportement des modèles sur cette plage de composition. En bande O, les valeurs mesurées sont en accord avec le modèle de l'oscillateur simple modifié. Nous avons donc suivi ce modèle pour l'indice du Q_{1,03}.

Nous avons aussi étudié l'impact du dopage sur l'indice de réfraction des matériaux, pour les couches InP qui servent à la création de la structure PiN. Ainsi, nous avons utilisé le modèle proposé par Bennett, Soref, et Del Alamo, qui est une amélioration de celui de Henry, Logan et Bertness, en prenant en compte la masse des trous lourds et trous légers [28]. Avec l'obtention des indices de réfractions, nous avons la possibilité de simuler nos structures. Afin de limiter l'impact dû à l'absorption des couches de matériau dopé p, notre structure possède un cladding asymétrique.

2.2.2.Le cladding asymétrique

Ce cladding asymétrique permet d'attirer le mode vers les couches dopées n et donc le confinement optique dans les couches dopées p. Ce phénomène est rendu possible par la présence d'une épaisse couche de matériau sous la zone active [29]. Les couches de séparation du confinement d'héterostructure (SCH) peuvent aussi attirer le mode vers le bas si l'épaisseur du SCH sous les puits quantiques est plus importante que celle au-dessus. Pour nos structures, ces couches sont de même épaisseur. Dans de précédents travaux, en bande C+L, cette couche, nommée « semelle », était faite d'un matériau massif, de 4 µm d'épaisseur, en Q_{1,03}. Ici, nous remplaçons ce matériau massif par un super-réseau (SL) fait de Q_{1,17} et InP. En utilisant les bonnes périodes, la semelle en SL est vue par le signal optique comme une couche de matériau massif de Q_{1,03}.

L'ajout du SL a deux avantages majeurs sur l'utilisation d'un matériau massif. Du point de vue de l'épitaxie, la croissance d'une semelle massive de 4 µm est un exercice complexe, car le moindre écart de composition pendant la croissance peut engendrer de lourdes conséquence à cause de l'épaisseur. Il y a aussi un avantage du point de vue de la fabrication. Au cours du procédé technologique, il faut graver la semelle pour obtenir le confinement optique souhaité et permettre la reprise d'épitaxie des couches semi-isolantes. Lors de cette gravure, suivie par réflectométrie, il est plus facile d'observer une profondeur dans un SL que dans un matériau uniforme.

La profondeur de gravure dans la semelle est déterminée grâce à la simulation optique de la structure complète. Elle est le dernier paramètre permettant d'obtenir un composant monomode et de jouer sur les valeurs de confinement optique dans les QW. L'aspect monomode est important pour nos

composants car l'amplification de plusieurs modes dégraderait de manière substantielle leurs performances.

Suite à l'obtention et l'étude des différents paramètres, nous sommes en mesure de proposer des structures SOA opérantes en bandes C+L et O.

2.3. Structures proposées

Deux variantes de structures ont été réalisées à partir de chaque zone active précédemment conçues. Ces variantes présentent à chaque fois une structure dont le confinement optique peut être qualifier de « fort » et l'autre de « faible ». Ainsi, nous proposons quatre structures en bande C+L, présentées dans le Tableau 3 et deux en bande O, détaillées dans le Tableau 4.

Dans chaque tableau, les confinements optiques sont donnés pour des largeurs de rubans de 4,5 µm qui sont ceux principalement étudiés, bien que, suite à la fabrication, des rubans de 5 et 4 µm sont aussi disponibles.

Les indices 1 et 2 dans les tableaux représentent les structures à « fort » et « faible » confinements optiques, respectivement. Ainsi, par exemple, le design A1, correspond à la structure fort confinement, avec des SCH de 80 nm, basée sur des QW de 140 Å d'épaisseur.

<i>Couches</i>	<i>Matériaux</i>	<i>Design A</i>		<i>Design B</i>	
		<i>Epaisseurs</i>	<i>Répétitions</i>	<i>Epaisseurs</i>	<i>Répétitions</i>
<i>Top cladding</i>	InP:p	200 nm	-	200 nm	-
<i>SCH</i>	GaInAsP ($\lambda=1,17 \mu\text{m}$)	80 nm ¹ / 60 nm ²	-	80 nm ¹ / 63 nm ²	-
<i>QW</i>	GaInAsP	140 Å	4	110 Å	4
<i>Barrières</i>	GaInAsP ($\lambda=1,17 \mu\text{m}$)	100 Å	3	90 Å	3
<i>SCH</i>	GaInAsP ($\lambda=1,17 \mu\text{m}$)	80 nm ¹ / 60 nm ²	-	80 nm ¹ / 63 nm ²	-
<i>Semelle</i>	GaInAsP:n ($\lambda=1,17 \mu\text{m}$)	29 nm	73	23 nm	73
<i>Semelle</i>	InP:n	26 nm	73	32 nm	73
<i>Buffer</i>	InP:n	500 nm	-	500 nm	-
<i>Confinement optique (%)</i>		5,33 ¹ / 3,38 ²		5,97 ¹ / 4,34 ²	

Tableau 3. Structures proposées pour les SOA en bande C+L.

<i>Couches</i>	<i>Matériaux</i>	<i>Design O</i>	
		<i>Epaisseurs</i>	<i>Répétitions</i>
<i>Top cladding</i>	InP:p	200 nm	-
<i>SCH</i>	GaInAsP ($\lambda=1,03 \mu\text{m}$)	75 nm ¹ / 55 nm ²	-
<i>QW</i>	GaInAsP	110 Å	4
<i>Barrières</i>	GaInAsP ($\lambda=1,03 \mu\text{m}$)	100 Å	3
<i>SCH</i>	GaInAsP ($\lambda=1,03 \mu\text{m}$)	75 nm ¹ / 55 nm ²	-
<i>Semelle</i>	GaInAsP:n ($\lambda=1,03 \mu\text{m}$)	29 nm	73
<i>Semelle</i>	InP:n	26 nm	73
<i>Buffer</i>	InP:n	500 nm	-
<i>Confinement optique (%)</i>		4,79 ¹ / 3,13 ²	

Tableau 4. Structures proposées pour les SOA en bande O.

Ces structures ont pour objectif d'étudier l'impact du confinement optique sur les performances des composants, tout en observant les effets provoqués par la réduction de l'épaisseur des puits quantiques. En bande O, afin d'amplifier le signal sur un maximum de longueurs d'onde, les deux structures proposées sont basées sur des puits plus fins que la structure de référence (A1) en bande C+L.

3. Fabrication

Intéressons-nous, à présent, à la fabrication des composants. Deux techniques d'épitaxie ont été mises à profit pour réaliser les différentes étapes de croissance, l'Epitaxie par Jets Moléculaire (MBE) et le Dépôt Chimique en phase Vapeur des Métallo-Organiques (MOCVD). Durant ce travail, nous avons aussi réalisé le transfert de technologie entre le réacteur MBE utilisé pour nos échantillons, un réacteur V100, produit par Thermo VG Scientific et modifié par RIBER, vers un nouvel équipement, le MBE412, produit par RIBER, équipé d'une large gamme d'outils de caractérisation *in situ* à l'état de l'art. Un total de 21 plaques a été épitaxié afin d'étudier deux procédés de fabrications, le « SIBH 2-étapes », classiquement utilisé au laboratoire pour la fabrication des SOA et RSOA, et le « SIBH 1-étape », nouvellement développé. De ces plaques, 15 ont été finalisées et permettent de comparer les différents designs de zone active, les différents confinements optiques et les procédés de fabrication. Ils pourront aussi définir les prémisses d'une ligne de production pilote au III-V Lab.

3.1. Croissances par épitaxie par jets moléculaires à sources gazeuses

Dans la réalisation des étapes d'épitaxie, la GSMBE a été employée pour la croissance des structures de base comprenant la semelle en super réseau, la zone active, les couches SCH et un fin top cladding. La MOCVD a servi aux étapes de reprise d'épitaxie des matériaux semi-isolant. Pour le SIBH 2-étapes, habituellement utilisé au III-V Lab, pour les SOA et RSOA, la reprise est opérée avec un réacteur horizontal AIX200/4, permettant une croissance homogène sur le substrat. Pour le développement du SIBH 1-étape, la reprise est assurée par un réacteur équipé d'un showerhead (CCS), qui permet une régulation plus fine de la température de croissance.

La croissance de base est réalisée grâce à un réacteur V100 modifié pour accueillir des sources gazeuses. Cette technique d'épitaxie permet le suivi de la croissance grâce à divers outils de caractérisation *in situ* tels qu'un pyromètre, un spectromètre de masse, une jauge de flux et la diffraction des électrons de haute énergie en incidence rasante (RHEED). L'utilisation de sources gazeuses permet d'utiliser une unique source pour les éléments V, ce qui rend le contrôle des compositions des couches précis et reproductible. De plus, le Dihydrogène (H_2) produit par le craquage des molécules d'Arsine (AsH_3) et de Phosphine (PH_3) améliore la diffusion des espèces à la surface du substrat et donc améliore le procédé de reprise d'épitaxie, en évitant le phénomène de Croissance Sélective (SAG), observé en MOCVD.

La croissance de l'alliage GaInAsP peut être complexe à cause des différences d'incorporation entre l'Arsenic et le Phosphore et de la dépendance de cette incorporation face aux conditions de croissance. De plus, l'existence d'une lacune de miscibilité dans le diagramme de phase du quaternaire GaInAsP demande une grande précision dans l'optimisation de la croissance de ce matériau. Pour nos alliages, l'utilisation de contraintes en compression dans les zones actives permet de contrer l'effet de cette lacune, bien que les conditions de croissance doivent toujours être étudiées avec soin.

Des calibrations de base sont nécessaires pour toute croissance, ainsi, nous utilisons le RHEED, ainsi que la Diffraction des Rayons X (XRD) pour obtenir les courbes d'Arrhenius des différentes sources, comme illustré en Figure 4, pour les sources Indium. Les valeurs obtenues par mesures RHEED dépendent de la position du faisceau d'électrons à la surface du substrat. Pour vérifier ces mesures, la XRD est nécessaire. Pour cela, il faut faire croître plusieurs super réseaux d'InAsP/InP, pour la mesure de la vitesse de croissance de l'InP. Sur la Figure 4, chaque point « XRD » représente une structure. Pour déterminer la vitesse de croissance du GaAs, via la XRD, nous extrapolons cette valeur de celle obtenue pour l'InP en réalisant la croissance de 200 nm de GaInAs en accord de maille sur InP. Une technique plus fiable serait de faire des doubles super réseaux de GaInAs/AlInAs, avec différentes épaisseurs. Cependant, pendant notre étude, la charge de la source Aluminium n'était pas encore fondu.

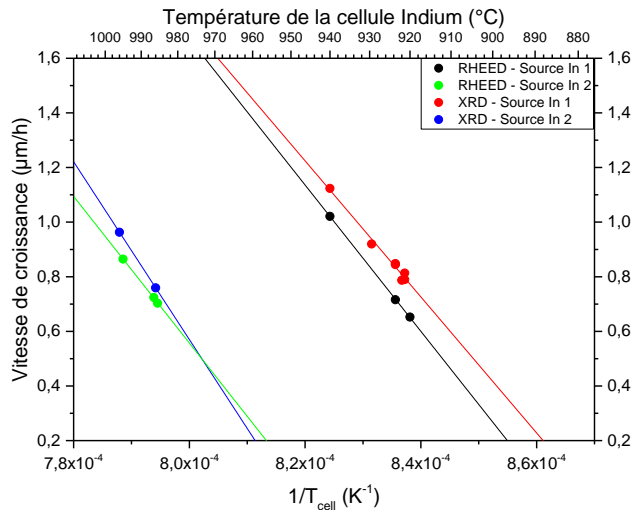


Figure 4. Courbes Arrhenius des vitesses de croissances de deux sources In en fonction de leurs températures.

Pour les éléments V, les oscillations induites observables au RHEED permettent de déterminer la limite, en terme de flux, entre une croissance pauvre en éléments V, ne permettant pas l'obtention d'un matériau de qualité, et une croissance riche en éléments V. Les mesures de Photoluminescence (PL) des alliages quaternaires de nos structures ($Q_{1,17}$ et $Q_{1,03}$) permettent, grâce à l'uniformité de l'intensité et de la longueur d'onde sur l'ensemble du substrat, de déterminer précisément le ratio V/III nécessaire à l'obtention de matériaux de haute qualité cristalline. Cette détermination fait partie de l'optimisation des conditions de croissances de ces alliages, avec celle de la température de croissance.

Les conditions de croissance des zones actives doivent aussi être optimisées. Pour cela, en bande C+L, un détecteur GaInAs étendu est requis pour mesurer leurs longueurs d'onde d'émission. En effet, un détecteur standard permet de mesurer précisément les longueurs d'ondes jusqu'à 1,62 μm , or, nos structures doivent émettre de 1530 à 1625 nm en bande C+L et nécessitent un détecteur avec une plage de longueur d'onde étendue. Nous avons donc validé les calibrations de PL au LPCNO pour ajuster la longueur d'onde grâce au rapport entre As et P. Nous avons ensuite ajusté la température de croissance pour améliorer l'intensité de PL. Nous avons également réalisé des mesures de photocourant pour observer les différentes transitions obtenues avec nos structures. La dernière étape d'optimisation des structures en bande C+L concerne la semelle en super réseau. Pour celle-ci, la période a été étudiée avec des mesures de XRD et le dopage avec des mesures Electrochimique de Capacité-Tension (ECV).

En bande O, les premières croissances sont réalisées avec les mêmes conditions de croissance que pour les structures en bande C+L. Cependant, on observe la présence de Cross-hatch, visible au microscope, mais surtout lors des mesures de cartographie de PL. Ce phénomène pourrait être causé par un excès de contrainte dans la zone active, mais la mesure XRD indique que celle-ci est inférieure à celles mesurées dans les structures en bande C+L. Ce cross-hatch peut être le résultat de la présence de la lacune de miscibilité dans le diagramme de phase de l'alliage GaInAsP, discutée précédemment. En réduisant la température de croissance de la zone active, ce phénomène n'apparaît plus sur les échantillons, et l'optimisation du ratio As/P permet d'obtenir une transition $e_1\text{-}hh_1$ à 1363 nm.

Suite aux optimisations des conditions de croissance, nous avons fabriqué l'ensemble des structures conçues et nous les avons caractérisées. L'ensemble des résultats de caractérisation est visible dans le Tableau 5. Les plaques sont nommées d'après leurs designs (A1, A2, B1, B2, O1, O2). Les lettres A et B représentent, respectivement, les designs à puits quantiques épais et fin, en bande C+L et la lettre O, représente les structures en bande O. Le chiffre correspond au confinement optique de la zone active (1 pour les « hauts » confinements et 2 pour les « faibles »).

	<i>Structure</i>	<i>A1</i>	<i>A2</i>	<i>B1</i>	<i>B2</i>	<i>O1</i>	<i>O2</i>
<i>XRD</i>	<i>Période des MQW (Å)</i>	239,0	235,7	198,4	193,1	201	201
	<i>Période de la semelle (Å)</i>	534,1	518,9	515,9	517,3	499,4	502,2
	<i>Désaccord de maille des MQW (%)</i>	+1,083	+1,087	+1,090	+1,072	+0,990	+1,007
<i>PL</i>	<i>Longueur d'onde $e_1\text{-}hh_1$ (nm)</i>	1629	1619	1611	1623	1359	1359
	<i>Longueur d'onde $e_2\text{-}hh_2$ (nm)</i>	1505	1490	1461	1461	1253	1253
	<i>Largeur de bande optique (nm)</i>	124	129	150	162	106	106

Tableau 5. Résultats des caractérisations matériau des différents designs.

Pour l'ensemble des structures, les MQW sont plus fins que prévus (240 Å pour les designs A et 200 Å pour les designs B et 210 Å pour les designs O), ce qui devrait élargir encore la bande optique. La contrainte moyenne mesurée dans les puits est aussi inférieure à ce qui était visé, ce qui montre que la composition de ces couches est différente de celle voulue et décale les longueurs d'onde des transitions $e_1\text{-}hh_1$ et $e_2\text{-}hh_2$, en comparaison avec les simulations réalisées préalablement. L'ensemble des structures ont été réalisées dans une configuration multi plaques (3x2’’), pour suivre les procédés de fabrications SIBH 1-étapes et 2-étapes avec des plaques jumelles.

Après plusieurs années de service et une dégradation de son temps de fonctionnement, le V100 a été remplacé par un réacteur MBE412 fabriqué par RIBER, présentant beaucoup d'avantages face à son prédécesseur. Parmi ceux-ci, nous pouvons citer la possibilité d'ajouter des modules supplémentaires, comme une seconde chambre de croissance ou une chambre de préparation, pour répondre aux futurs besoins de développement, ou encore les multiples outils de caractérisations dont ce nouveau réacteur est équipé (un RHEED, un outil de mesure de la contrainte et de la courbure du substrat (EZ-Curve), un thermomètre basé sur la mesure de la longueur d'onde émise par le substrat (BandiT)). La présence de ces outils a permis de rapidement transférer les procédés de croissance, développés pour les SOA et RSOA, du V100 au MBE412. Ce dernier poursuit déjà le développement de ces structures en bandes C+L et O, mais aussi en bande S+C, comme illustré par les mesures de PL, en Figure 5.

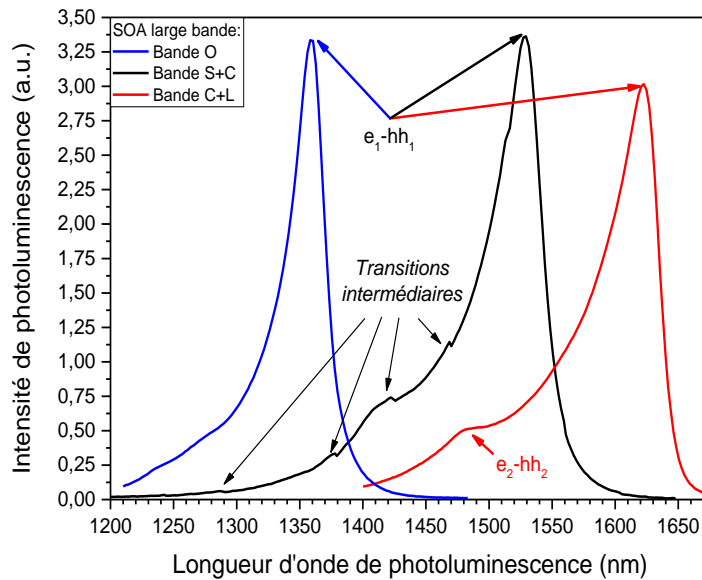


Figure 5. Mesures de photoluminescence de structures en bande O, S+C et C+L, réalisées avec le MBE412.

3.2. Procédés de fabrication

Une fois la première épitaxie réalisée sur les substrats, et les caractérisations matériau réalisées, les procédés de fabrication diffèrent. Nos structures sont prêtes pour le SIBH 2-étapes. Pour le SIBH 1-étape, une reprise de croissance comprenant une épaisse couche de top cladding et une couche de contact en alliage GaInAs est nécessaire. Les deux procédés sont résumés dans la Figure 6.

Le procédé SIBH 1-étape est développé pour réduire le nombre d'étapes requises pour obtenir les composants. Il nécessite une reprise d'épitaxie d'une épaisseur importante et dont les conditions doivent être parfaitement réglée pour obtenir un matériau de qualité avec les propriétés recherchées.

Une fois les structures de bases obtenues, un diélectrique est déposé par Dépôt Chimique en phase Vapeur Assisté par Plasma (PECVD) sur toute la plaque pour protéger les rubans lors de leur gravure. Une lithographie de contact définit les dimensions des rubans, et le diélectrique entourant les rubans, protégés par la résine, est gravé par Gravure Ionique Réactive (RIE). Une fois cette étape menée à son terme, la résine aux sommets des rubans est nettoyée et le processus de gravure des rubans dans le matériau III-V commence. Il s'agit d'une gravure au Plasma à Couplage Inductif (ICP), contrôlée par reflectométrie. Durant cette phase du procédé, la présence de matériaux d'indices de réfraction différents dans la semelle en SL permet un suivi de gravure plus simple. Un dernier nettoyage des échantillons est effectué à l'acide fluorhydrique (HF) avant d'envoyer les plaques pour reprise SIBH.

La reprise SIBH est réalisée par MOCVD, à des épaisseurs différentes selon le procédé de fabrication. Nous avons profité de ce travail pour étudier l'impact des températures utilisées pendant cette reprise sur la structure déjà présente. Nous en concluons que la reprise génère un décalage en longueur d'onde, vers les hautes énergies, du pic d'émission en PL, sans modification des courbes issues des mesures XRD. Il y a donc une inter-diffusion entre les atomes d'In et de Ga dans la zone active. Cette reprise impacte aussi les dopants, qui peuvent être passivés et même diffuser en fonction de la structure observée.

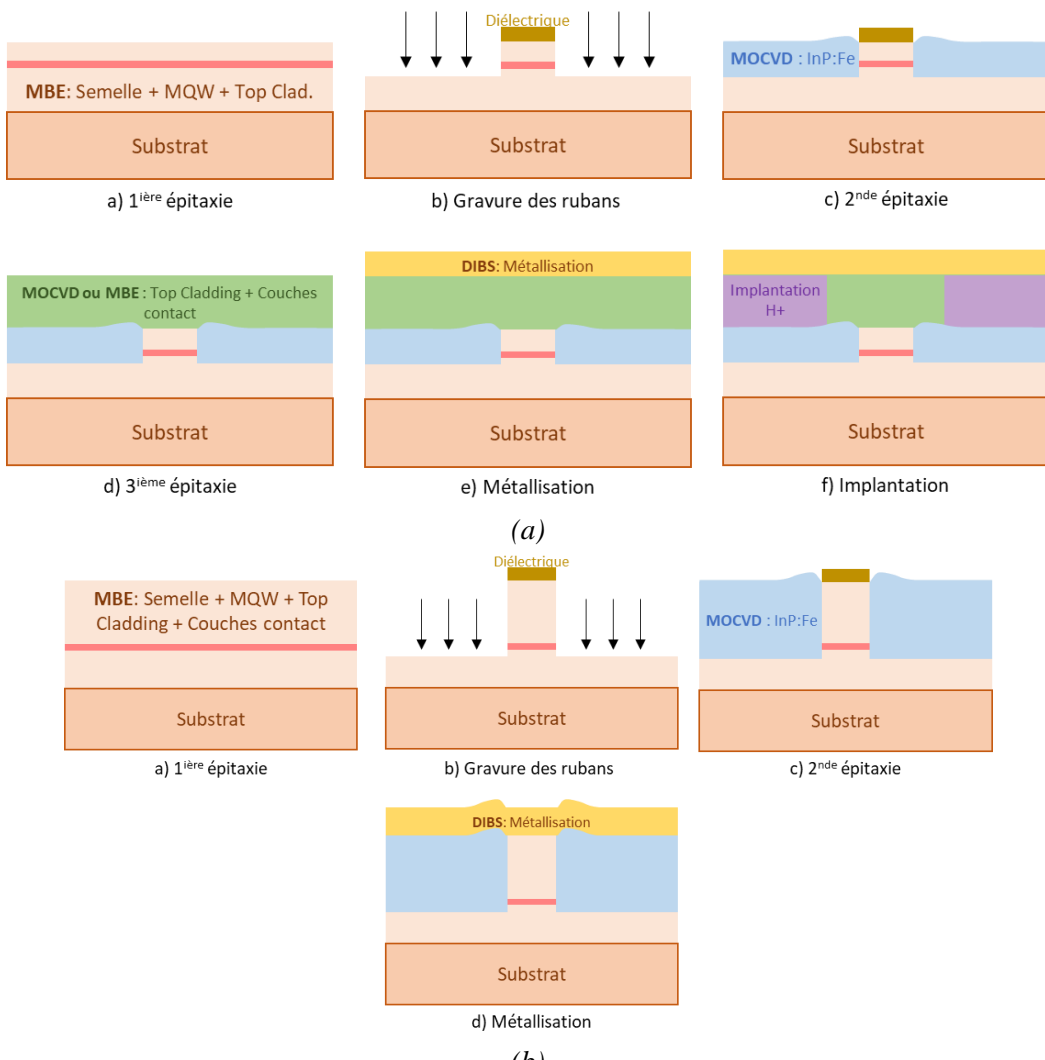


Figure 6. Résumé des procédés de fabrication (a) SIBH 2-étapes et (b) SIBH 1-étape.

Une fois la reprise SIBH réalisée, les plaques SIBH 2-étapes doivent subir une seconde reprise d'épitaxie comprenant les couches top cladding et de contact. Ensuite, pour assurer l'isolation entre les rubans, une étape d'implantation de protons est nécessaire. Pour cela, les rubans sont protégés par une résine épaisse et les échantillons sont envoyés au CNRS pour cette étape. Une fois de retour, ils peuvent rejoindre les plaques SIBH 1-étape pour les dernières étapes de fabrication.

Deux résines sont déposées et développées pour effectuer le dépôt métallique des contacts p avec des couches de Platine (Pt) et d'Or (Au), au-dessus des rubans, par Pulvérisation à Double Faisceau Ionique (DIBS). Ce dépôt étant fait sur l'entièreté de la surface, les métaux déposés sur la résine sont retirés par lift-off. Une fois les plaques nettoyées, elles sont amincies et nous procédons à un dépôt DIBS de Titane (Ti), Pt et Au à la surface arrière des plaques. Une fois cette étape achevée, les plaques, dont les structures finales sont présentées en Figure 7, par images de Microscopie Electronique à Balayage (SEM), subissent les étapes de back-end pour sélectionner les composants à monter sur embase, décrites dans la section suivante.

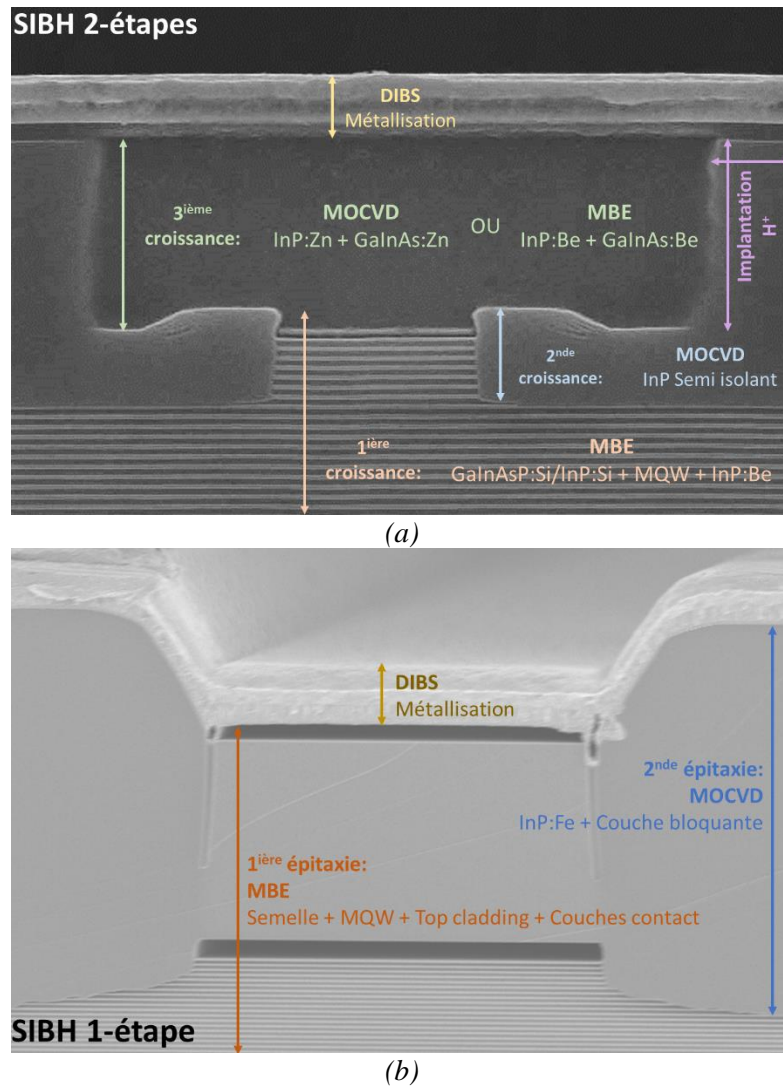


Figure 7. Images SEM des structures SOA et RSOA observées après (a) SIBH 2-étapes et (b) SIBH 1-étape.

3.3. Etapes de back-end

Les étapes de back-end permettent d'obtenir, à partir des plaques fabriquées, dont l'une est présentée en Figure 8 (a), les composants unitaires, afin de les monter sur des embases, comme illustré en Figure 8 (b) et (c), pour enfin, les caractériser et les intégrer aux systèmes.

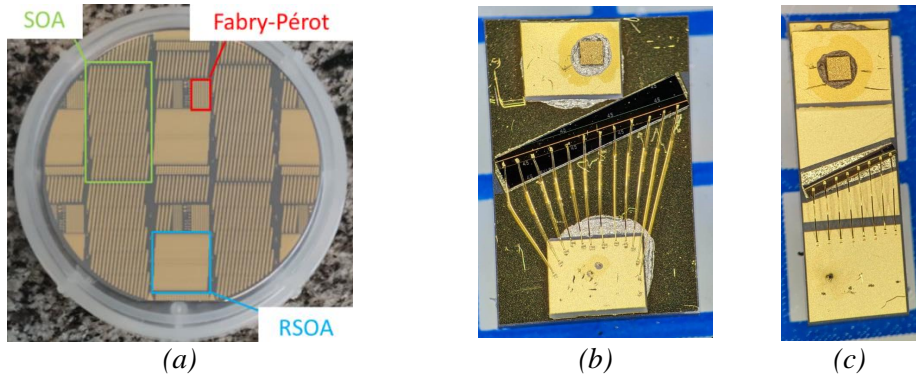


Figure 8. Photos (a) d'une plaque finalisée, (b) d'un SOA et (c) d'un RSOA, montés sur embases.

Sur chaque plaque, les composants sont répartis en cellules, pour être clivés en barrettes et sélectionner les meilleurs composants à monter sur embase. Cette sélection a pour but de limiter le nombre de montages à réaliser par plaque. Les barrettes de cavités Fabry-Pérot (FP), longues de 2 mm et parallèles au grand méplat des plaques, sont les plus rapide à caractériser et permettent d'évaluer si le procédé de fabrication s'est bien déroulé. Pour cela nous réalisons des mesures de puissance optique et de tension en fonction de l'intensité de courant, notés respectivement $P(I)$ et $V(I)$. Nos composants SOA, comme RSOA, nécessitent des traitements aux facettes qui augmentent le nombre d'étapes de back-end.

Les SOA sont clivés en barrettes de 4 mm de long pour compenser les faibles valeurs de confinement optique. Ces composants sont assez espacés sur la Figure 8 (a) pour pouvoir récupérer chaque composant sans sacrifier ses voisins. Ils possèdent aussi un angle de 7° par rapport au méplat afin de réduire les réflexions aux facettes dès la fabrication. Cette réduction est amplifiée par l'application d'un traitement AR à chaque facette.

Les RSOA sont clivés en barrettes de 2 mm afin d'obtenir la même distance parcourue par le signal dans le semiconducteur que celle des SOA. Leur architecture est particulière, une partie de leurs rubans sont perpendiculaires au grand méplat, puis un virage permet à la seconde facette d'avoir un angle de 7° par rapport à ce même méplat. Nous avons donc une facette réfléchissante comme pour un FP, et une facette à faible réflectivité, comme pour un SOA. Sur la première facette, un traitement HR peut être appliqué pour limiter les pertes. Cependant, suite à une disponibilité machine réduite, nous n'avons pas réalisé ce traitement. Pour l'autre facette, qui servira d'entrée et de sortie au signal, un traitement AR est appliqué.

Chaque composant des barrettes est caractérisé en $P(I)$, $V(I)$, mais aussi en champs lointain et en spectre ASE pour s'assurer des propriétés : (i) monomode et (ii) large bande. La comparaison des performances des composants permet la sélection des meilleurs qui sont brasés sur des embases pour améliorer la gestion thermique et donc leurs performances. Dans ce but, une résistance thermique est placée au plus près des composants pour les réguler en température. Les embases permettent aussi de faciliter l'injection de courant avec le « wire bonding », visible sur la Figure 8 (b) ou (c). Enfin, les composants sont brasés avec un angle de 23° , permettant au signal d'entrer et de sortir de la puce perpendiculairement à l'embase, ce qui facilite le couplage avec des fibres optiques.

Au total, 21 plaques ont été épitaxiées par GSMBE et 15 d'entre elles ont vu leurs procédés de fabrication finalisées. Cela nous permet de mesurer des composants provenant de toutes les structures proposées, mais aussi issues des deux procédés de fabrications. Une fois des montages réalisés, nous pouvons entamer les caractérisations des composants de manière unitaire.

4. Caractérisations des composants

Les différentes caractérisations des SOA et RSOA sont toutes réalisées avec un contrôle en température à 20°C. Dans un premier temps, nous nous sommes intéressés aux performances des composants réalisés en suivant le procédé de fabrication classique du III-V Lab, le SIBH 2-étapes. Ensuite, nous évaluons les performances des composants obtenus par SIBH 1-étape, dans le but de comparer les performances obtenues avec les deux procédés de fabrications.

Les performances analysées sont le profil de champs lointain, afin de s'assurer du comportement monomode des composants ainsi que de leur facilité de couplage avec une fibre. Nous analysons également leurs spectres ASE afin de définir une première bande passante. Enfin, les mesures de gain, NF et P_{sat} sont réalisées sur un unique banc de mesure dont la source limite les caractérisations en terme de puissance d'entrée dans les composants, ainsi qu'en longueur d'onde pour les composants opérant en bande C+L.

Les résultats présentés proviennent des mesures réalisées sur des SOA de 4 mm et des RSOA de 2 mm de long, ayant tous des rubans de 4,5 μm de large. Les composants sont nommés d'après leurs types (SOA, RSOA), leurs procédés de fabrication (SIBH 1-étape, SIBH 2-étape) et leurs designs (A1, A2, B1, B2, O1, O2).

4.1. Composants produits par SIBH 2-étapes

4.1.1. Imagerie de champs lointains

Une fois montés sur embase, la caractérisation des composants commence par une mesure d'imagerie de champs lointain. Celle-ci permet de vérifier l'aspect monomode des composants et si les facettes n'ont pas été endommagées pendant les étapes de back-end. De cette mesure, nous obtenons une image 2D du profil du signal optique émis par le composant, ainsi que des courbes représentant les coupes de ce profil suivant les axes horizontal et vertical, comme montré par la Figure 9.

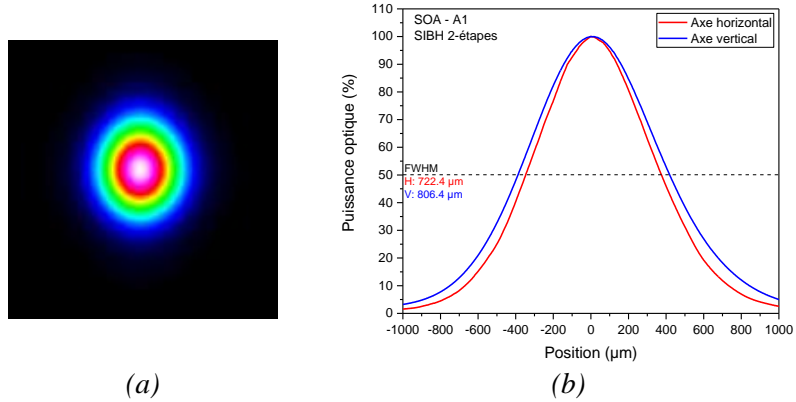


Figure 9. Résultats obtenus par la mesure du champ lointain du SOA SIBH 2-étapes A1 avec (a) le profil 2D du champ lointain, (b) les courbes représentatives des sections selon les axes horizontal et vertical.

Pour le SOA SIBH 2-étape A1, nous observons un mode légèrement elliptique pour lequel des largeurs à mi-hauteur (FWHM) de 722,4 μm horizontalement et de 806,4 μm ont été mesurées. La comparaison de deux mesures effectuées à des distances composant-détecteur différentes est nécessaire au calcul des angles de divergence (2). Les résultats, obtenus à partir des FWHM des courbes observées à un courant d'injection de 500 mA, sont listés dans le Tableau 6.

Nous avons aussi étudié l'évolution du champ lointain en fonction de l'injection de courant dans les composants. Cela a mis en lumière qu'un mode parfaitement elliptique nécessite d'être à proximité, ou au-delà du courant de seuil. Avant cela, le profil du signal optique est fortement déformé sur l'axe

horizontal, comme montré par la Figure 10. Les faibles valeurs obtenues avec le RSOA A2 sont dues à la faible puissance optique recueillie par le détecteur, qui fausse la mesure de la FWHM.

Design	SOA		RSOA	
	Axe horizontal	Axe vertical	Axe horizontal	Axe vertical
A1	10.94°	12.83°	10.32°	12.62°
A2	15.29°	14.51°	9.22°	7.78°
A2R	13.82°	13.97°	11.36°	15.18°
B1	10.53°	12.63°	10.66°	13.18°
B2	10.92°	12.83°	-	-
O1	12.48°	12.18°	10.28°	16.02°
O2	11.04°	14.24°	-	-

Tableau 6. Angles de divergences calculés pour chaque composant SIBH 2-étapes, à partir des largeurs à mi-hauteur mesurées à 500 mA.

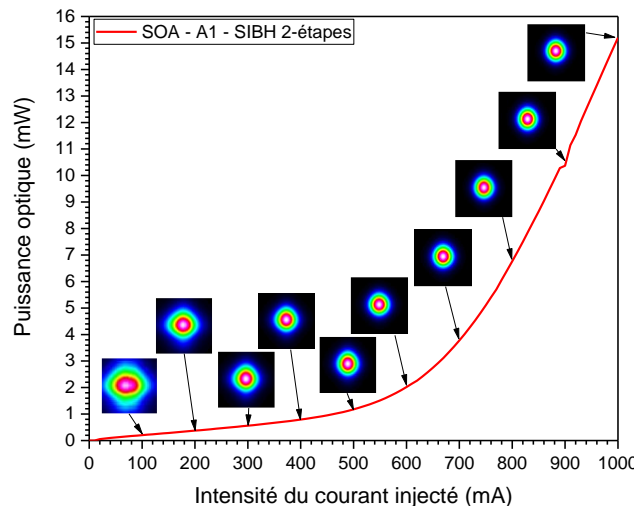


Figure 10. Evolution du profil de champ lointain du SOA SIBH 1-étape A1 en fonction de sa puissance optique de sortie.

Une fois l'aspect des profils de champs lointain vérifiés pour chaque composant et de chaque côté des SOA, nous pouvons entamer le reste des caractérisations, dont la première est la mesure des spectres ASE.

4.1.2. Spectres ASE

Les spectres ASE sont ensuite mesurés pour évaluer le caractère large bande de nos composants. L'émission spontanée, comme le gain, résulte des transitions entre les états liés dans les trous quantiques et permet donc une première estimation des largeurs de bandes passantes. Pour cette mesure, le composant est injecté électriquement, puis couplé à une fibre optique à l'une de ses facettes. Cette fibre est connectée à un OSA pour mesurer la puissance optique en fonction de la longueur d'onde, comme illustré par la Figure 11.

A faible courant, seule la transition e_1-hh_1 , à faible énergie participe à l'émission. En augmentant le courant, le comportement du spectre diffère en fonction du design de la zone active. Les designs A (Figure 11 (a)) montrent une apparition progressive de la transition e_2-hh_2 jusqu'à ce qu'elle prenne le dessus sur la première transition, réduisant la bande passante optique. Avec les designs B (Figure 11 (b)), la seconde transition participe de plus en plus dans la formation du spectre, sans pour autant afficher un pic nettement défini et réduire la longueur d'onde. Ce phénomène est dû au confinement plus faible du second niveau d'électron (e_2) dans les trous. Les RSOA et SOA ont le même comportement, dépendant de leur zone active, et les performances extraites de ces mesures sont présentées dans le Tableau 7, pour les SOA et dans le Tableau 8, pour les RSOA. Ces performances concernent : (i) les

densités de courant d'ASE plat, qui correspondent aux courants pour lesquels la bande passante d'ASE est la plus large, (ii) la bande passante maximale d'ASE et (iii) les limites de cette bande passante.

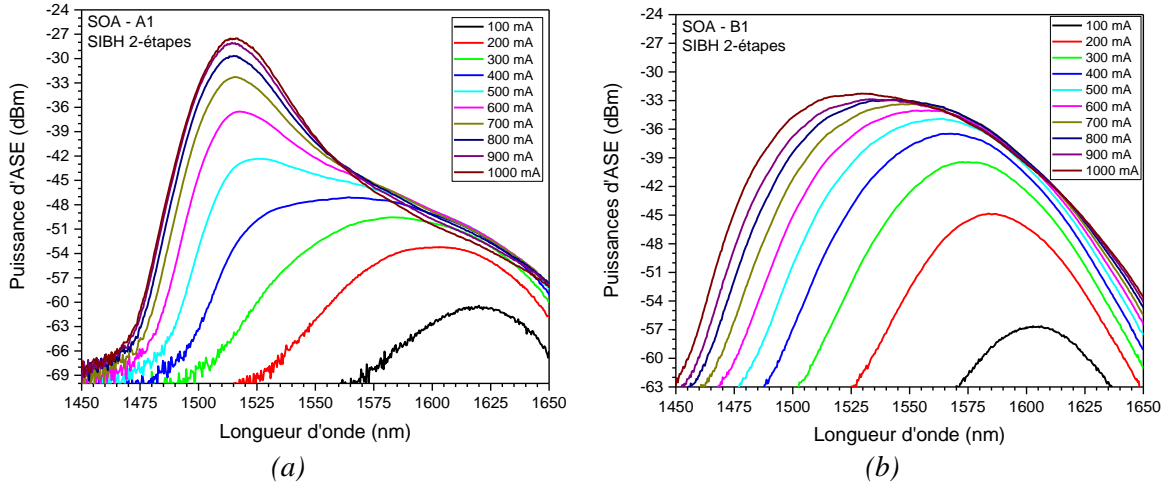


Figure 11. Spectres ASE mesurés à différents courants pour les composants (a) SOA SIBH 2-étapes A1 et (b) SOA SIBH 2-étapes B1.

Design	SOA						
	A1	A2	A2R	B1	B2	O1	O2
Densité de courant d'ASE plat (kA/cm^2)	1.11	0.83	0.83	2.78	2.78	1.94	2.78
Bandé passante d'ASE maximale (nm)	85	101	109	77	99	79	91
Longueur d'onde limite minimale (nm)	1524	1512	1508	1497	1493	1277	1270
Longueur d'onde limite maximale (nm)	1609	1613	1617	1574	1592	1356	1361

Tableau 7. Performances d'ASE obtenues avec les différents SOA SIBH 2-étapes.

Design	RSOA				
	A1	A2	A2R	B1	O1
Densité de courant d'ASE plat (kA/cm^2)	1.11	1.39	1.67	3.89	1.67
Bandé passante d'ASE maximale (nm)	94	126	123	88	95
Longueur d'onde limite minimale (nm)	1523	1500	1504	1477	1260
Longueur d'onde limite maximale (nm)	1617	1626	1627	1565	1355

Tableau 8. Performances d'ASE obtenues avec les différents RSOA SIBH 2-étapes.

Nous remarquons que les bandes passantes obtenues avec les designs à faibles confinements optiques (designs X2) sont les plus larges, et que, les designs basés sur des puits de 11 nm (designs B) nécessitent des densités de courant plus élevées pour atteindre leurs bandes passantes d'ASE maximales. Cependant, tous les composants mesurés montrent bien un comportement large bande, qui doit être confirmé par les mesures de gain.

4.1.3. Spectres de gain

Pour la mesure de gain, il faut injecter un signal optique d'entrée dans le composant. Ce signal est donné par une source laser accordable, et sa puissance est contrôlée par un atténuateur. L'OSA permet de connaître la puissance de sortie, à laquelle on soustrait la puissance d'ASE, également visible sur l'OSA. Avec la puissance d'entrée connue, nous pouvons établir le rapport P_{in}/P_{out} , qui donne le gain. Malheureusement, la source accordable utilisée en bande C+L est limitée en terme de longueur d'onde et ne permet des mesures que de 1520 à 1610 nm, ce qui donne des mesures de bande passante limitées à 90 nm.

Les spectres de gain ont le même comportement que les spectres ASE, comme le montre la Figure 12 (a). Cette figure montre les spectres de gains des SOA en bande C+L à leurs différents courants de gain

plat pour une puissance injectée de -25 dB pour s'assurer d'être dans le régime linéaire des composants. Les Figure 12 (b) et Figure 12 (c) montrent, respectivement ces mêmes courbes pour les RSOA en bande C+L et les SOA en bande O.

Nous observons rapidement que les spectres de gain des designs à fort confinement (designs X1) montrent des valeurs de gain supérieures. Pour les SOA de la bande C+L, les bandes passantes observées couvrent toute l'entièreté des plages de longueur d'onde mesurées, sauf pour le design B1, dont la bande passante est de 71 nm, mais dont le gain est le plus important. Les densités de courants de gain plats sont supérieures à celles d'ASE plat car l'émission stimulée consomme plus de porteur que l'émission spontanée. Pour les RSOA, les mêmes commentaires sont applicables, en ajoutant que leurs valeurs de gain sont réduites en comparaison avec les SOA.

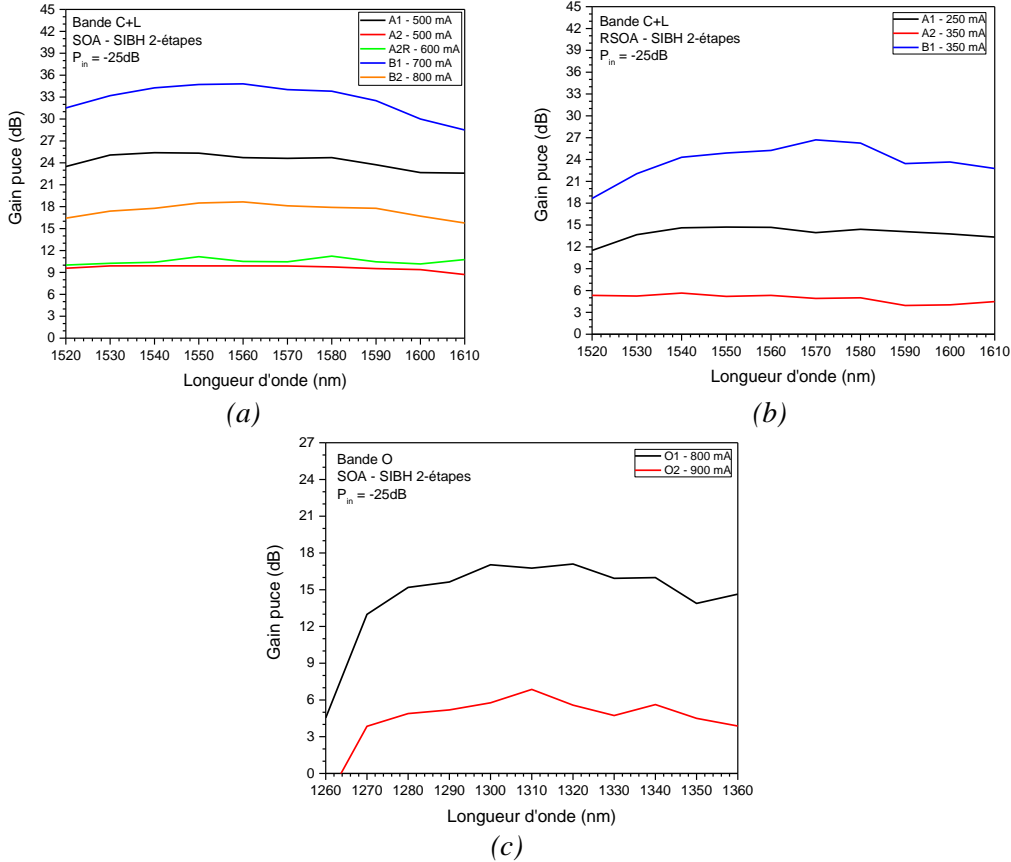


Figure 12. Spectres de gain, aux courants de gain plat, (a) des SOA en bande C+L, (b) des RSOA en bande C+L et (c) des SOA en bande O, fabriqués avec le procédé SIBH 2-étapes.

En bande O, les deux composants montrent un comportement large bande, cependant, le faible gain produit par le design O2, ne permet pas son incorporation dans les systèmes. Le composant basé sur le design O1 représente donc la première démonstration de SOA large bande opérant en bande O, basé sur des MQW en GaInAsP.

4.1.4. Facteurs de bruit et puissance de saturation

La mesure du NF correspond à la mesure du rapport signal sur bruit du composant, en prenant en compte la résolution de l'OSA et l'énergie des photons. L'ensemble des courbes obtenues aux courants de gain plats sont tracées en Figure 13 (a), (b) et (c), pour les SOA en bande C+L, les RSOA en bande C+L et les SOA en bande O, respectivement. La valeur du NF décroît aux faibles énergies suite à la diminution du facteur d'inversion de population. Les valeurs obtenues avec les RSOA sont supérieures à celles des SOA pour les composants en bande C+L et le NF minimal atteint par le composant O1 est de 4,8 dB, à 1360 nm, ce qui est un excellent résultat pour une première démonstration.

La puissance de saturation est obtenue à partir des courbes de gain tracées en fonction de la puissance de sortie des composants, pour un courant d'injection constant (ici, 500 mA). Pour obtenir la valeur de P_{sat} , pour une longueur d'onde, il faut injecter le signal en augmentant progressivement la puissance optique à l'entrée du composant, jusqu'à observer une diminution du gain de 3 dB. Une fois cette mesure réalisée pour l'ensemble des longueurs, nous traçons les courbes de P_{sat} en fonction de la longueur d'onde, comme illustré en Figure 13 (d). La chute de gain a pu être observée pour seulement 2 SOA en bande C+L. Pour les autres, la puissance en entrée et le gain, tous deux limités n'ont pas permis l'observation ou la prédition de la chute du gain.

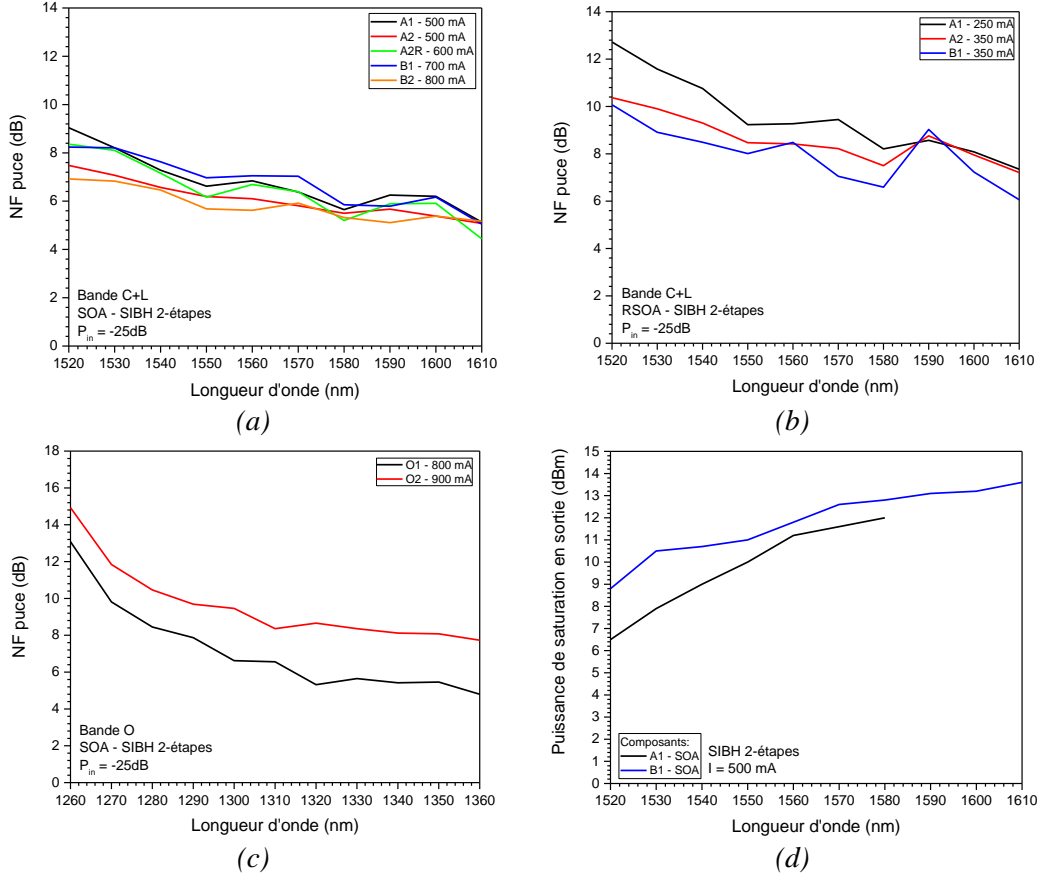


Figure 13. Résultats des mesures de NF des composants (a) SOA en bande C+L, (b) RSOA en bande C+L et (c) SOA en bande O, ainsi que (d) les résultats des mesures de P_{sat} à 500 mA, pour les composants SIBH 2-étapes.

Nous observons que le design B1 permet l'obtention d'une meilleure P_{sat} , malgré un plus important confinement optique, grâce à une section de zone active réduite.

Nous pouvons dès à présent conclure sur l'utilisation de la MBE ou de la MOCVD pour la croissance des couches top cladding et de contact en disant que l'impact observé sur les performances de nos composants, basés sur le design A2, est minime. A présent, nous devons caractériser les composants fabriqués avec le procédé SIBH 1-étape afin de comparer leurs performances entre eux et avec les composants SIBH 2-étapes.

4.2. Composants produits par SIBH 1-étape et comparaisons des performances

Pour les composants SIBH 1-étape, les caractérisations entreprises sont les mêmes. Nous sommes donc plus concis et présentons nos résultats ainsi que les observations afin de conclure sur les comparaisons entre les designs et les procédés de fabrication.

4.2.1. Imagerie de champs lointains

Les angles de divergence, mesurés avec les FWHM des courbes de sections horizontale et verticale des profils de modes, sont listés dans le Tableau 9, pour l'ensemble des composants réalisés.

Design	SOA		RSOA	
	Axe horizontal	Axe vertical	Axe horizontal	Axe vertical
A1	11.94°	14.00°	10.02°	12.38°
A2	14.33°	16.46°	12.94°	15.70°
B1	12.43°	13.31°	-	-
B2	12.24°	13.53°	11.12°	13.90°
O2 (1)	10.76°	14.32°	-	-
O2 (2)	14.84°	15.35°	-	-

Tableau 9. Angles de divergences calculés pour chaque composant SIBH 1-étapes, à partir des largeurs à mi-hauteur mesurées à 500 mA.

L'ensemble des angles de divergences obtenus avec les composants fabriqués par SIBH 1-étapes sont plus grands que ceux calculés pour les composants SIBH 2-étapes. Cela peut s'expliquer par une baisse de puissance optique que nous pourrons observer au niveau des puissances d'ASE ou, plus précisément, lors des mesures de gain.

4.2.2. Spectres ASE

Pour les spectres ASE, les comportements observés avec les composants SIBH 2-étapes sont toujours visibles car provoqués par la zone active qui est commune aux composants basés sur les mêmes designs. Les valeurs extraites des mesures sont présentées, dans le Tableau 10 pour les SOA et dans le Tableau 11 pour les RSOA.

Design	SOA					
	A1	A2	B1	B2	O2(1)	O2(2)
Densité de courant d'ASE plat (kA/cm ²)	1.67	1.39	2.78	2.78	2.78	2.78
Bandé passante d'ASE maximale (nm)	103	89	72	103	105	99
Longueur d'onde limite minimale (nm)	1519	1507	1541	1509	1274	1246
Longueur d'onde limite maximale (nm)	1622	1596	1613	1612	1379	1345

Tableau 10. Performances d'ASE obtenues avec les différents SOA SIBH 1-étape.

Design	RSOA		
	A1	A2	B2
Densité de courant d'ASE plat (kA/cm ²)	1.39	1.39	2.78
Bandé passante d'ASE maximale (nm)	90	126	108
Longueur d'onde limite minimale (nm)	1513	1507	1508
Longueur d'onde limite maximale (nm)	1603	1633	1616

Tableau 11. Performances d'ASE obtenues avec les différents RSOA SIBH 1-étape.

De manière générale, les densités de courant d'ASE plat sont supérieures pour les composants fabriqués par SIBH 1-étape, pour des bandes passantes globalement plus larges. Cela est dû aux puissances de sortie observées qui, réduites, donnent des bandes passantes plus larges, comme ce que nous avons vu avec les comparaisons entre les structures à faible et à fort confinement optique. Nous pouvons à présent comparer les composants en terme de gain, sachant que les spectres de gain sont toujours limités en longueur d'onde par la source laser accordable utilisée.

4.2.3. Spectres de gain

Les graphiques présents dans la Figure 14 présentent les spectres de gain plats mesurées pour les composants SIBH 1-étapes. Tous les composants précédemment mesurés n'ont pas pu être mesuré en

terme de gain, NF et P_{sat} . Ainsi, nous n'avons pu analyser que 3 SOA et 2 RSOA en bande C+L, et 1 SOA en bande O.

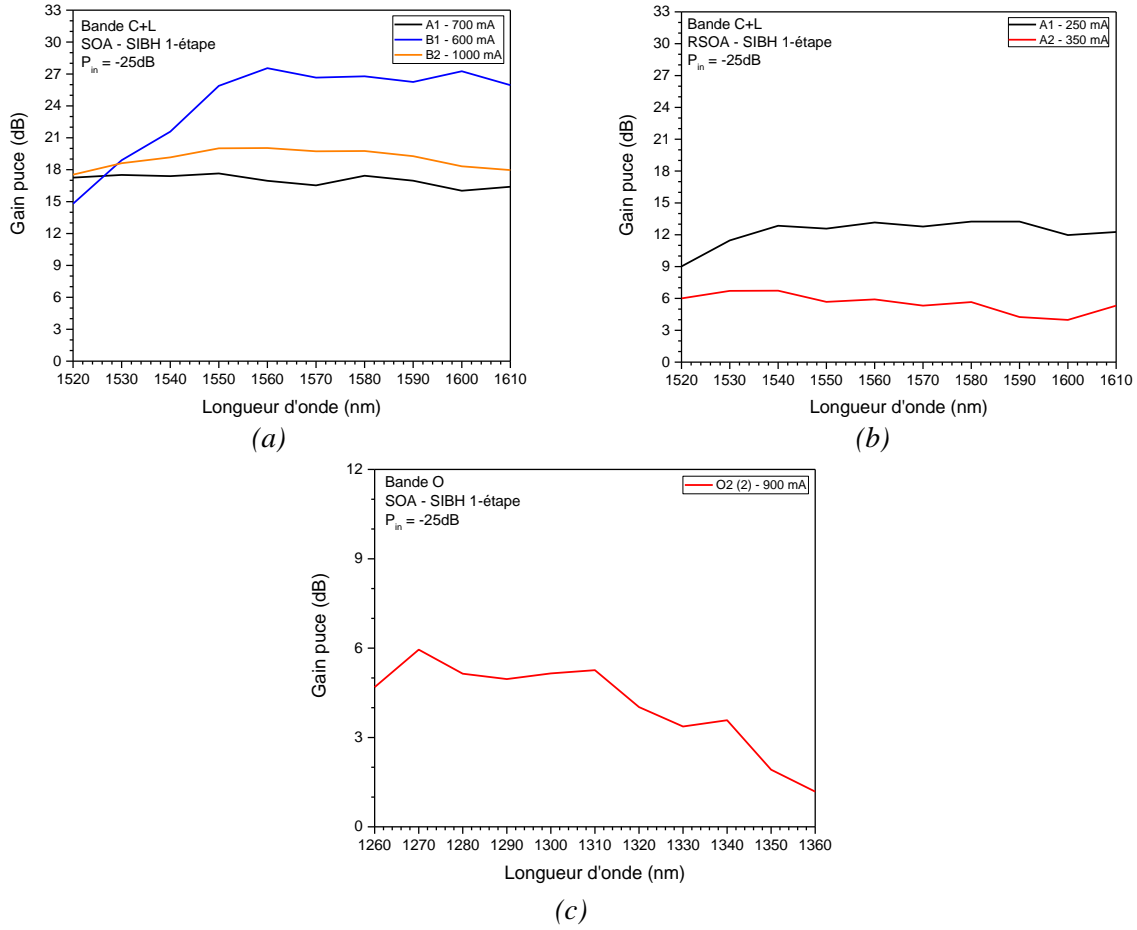


Figure 14. Spectres de gain, aux courants de gain plat, (a) des SOA en bande C+L, (b) des RSOA en bande C+L et (c) un SOA en bande O, fabriqués avec le procédé SIBH 1-étape.

Le comportement du SOA basé sur le design B1, visible en Figure 14 (a), est causé par la faible participation de la transition e_2-hh_2 . L'augmentation du courant n'a pas permis l'obtention d'une plage de longueur d'onde plus importante, contrairement à ce qui était attendu. Pour le SOA basé sur le design B2, la limite de 1 A est imposée par la source de courant/tension utilisée. Nous pouvons attendre une plus large bande passante avec un plus au gain maximal sur cette plage, à des courants supérieurs. Pour la bande O, visible en Figure 14 (c), le procédé SIBH 1-étape montre des performances réduites en comparaison avec la plaque jumelle ayant suivi le procédé SIBH 2-étapes. De manière générale, les composants montrent des gains maximaux aux densités de courant de gain plat inférieures aux composants SIBH 2-étapes. Cela montre que le procédé 1-étape doit encore subir des améliorations afin d'améliorer le gain des composants.

4.2.4. Facteurs de bruit et puissances de saturation

Pour les mesures de NF, présentées en Figure 15 (a), (b) et (c), dans les plages de longueurs d'onde correspondant aux bandes passantes optiques des composants, nous atteignons des valeurs plus importantes avec le SIBH 1-étape. Nous observons aussi que les valeurs de NF sont supérieures à celles de gain pour les designs à faible confinement optique. Cela est préjudiciable pour leur utilisation dans les systèmes.

Du point de vue de la P_{sat} , visible en Figure 15 (d), la même limitation sur la puissance d'entrée n'a permis de mesurer que le composant SOA B1. Les valeurs obtenues sont inférieures à celles mesurées pour les composants B1 et A1 réalisés en SIBH 2-étapes.

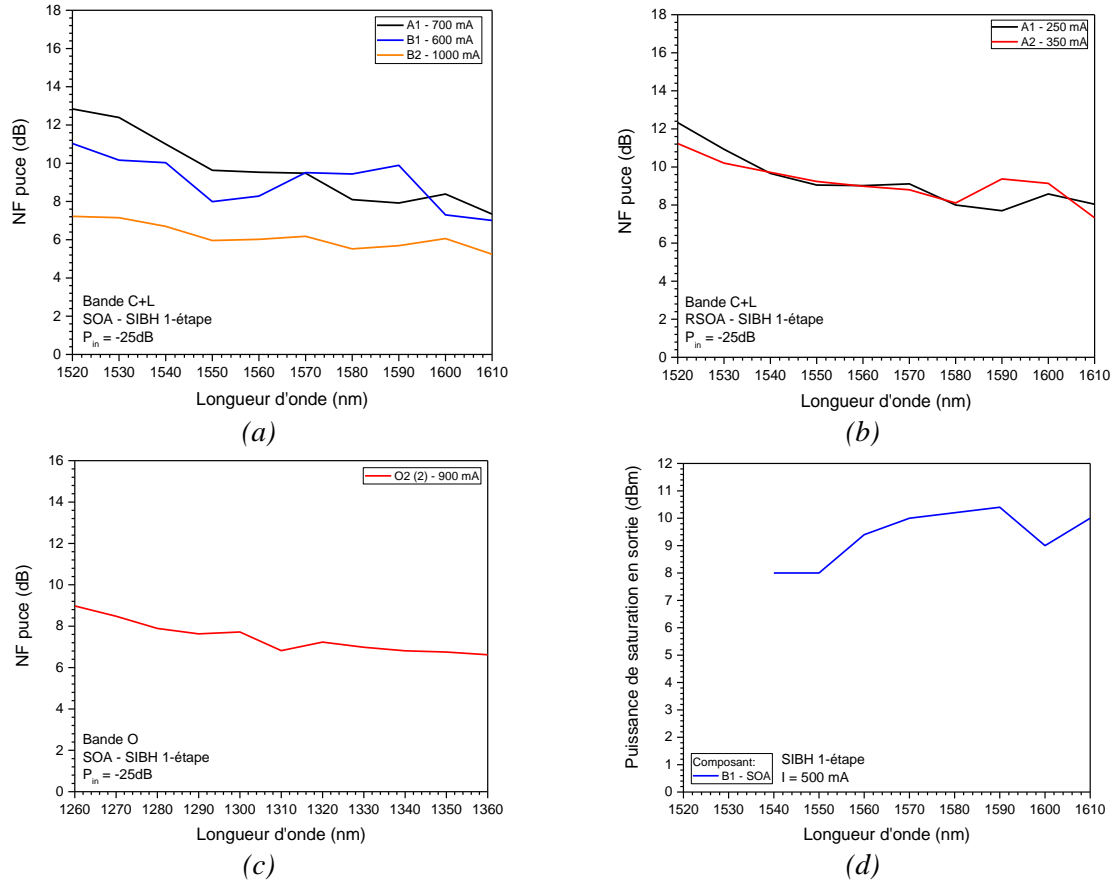


Figure 15. Résultats des mesures de NF des composants (a) SOA en bande C+L, (b) RSOA en bande C+L et (c) SOA en bande O, ainsi que (d) les résultats des mesures de P_{sat} à 500 mA, pour les composants SIBH 1-étape.

En conclusion, sur chacun des paramètres de performance, les composants fabriqués en suivant le procédé SIBH 1-étape se sont montrés moins bons que ceux fabriqués avec le SIBH 2-étapes. Il faut donc poursuivre le développement du procédé SIBH 1-étape pour obtenir les mêmes performances que le SIBH 2-étapes classiquement utilisé, tout en bénéficiant du nombre d'étapes réduites du nouveau procédé.

5. Conclusions

La croissance et la fabrication de composants tels que les SOA ou RSOA représente un challenge à cause des objectifs de hautes performances et de la difficulté d'obtenir un compromis satisfaisant entre toutes ces performances. Durant ce travail, nous avons conçu plusieurs designs de composants suivant différents paramètres (confinement optique, épaisseur des MQW et procédé de fabrication utilisé pour la reprise d'épitaxie des couches de contact). Cela nous a fourni beaucoup de données approfondissant notre compréhension des SOA et RSOA. Ce travail nous a aussi permis de mettre au point, pour la première fois, un SOA en bande O basé sur une structure MQW en quaternaire GaInAsP.

Dans une première partie, nous avons mis en place le contexte dans lequel évolue le développement des SOA et RSOA. Nous avons présenté les domaines d'applications mais aussi les technologies avec lesquelles nos composants sont en concurrence (xDFA et amplificateurs Raman). Nous avons également détaillé les paramètres clés que sont le gain, le NF, la P_{sat} et la bande optique d'amplification.

Dans un second temps, nous avons discuté de la conception des différents designs de composants, avec un premier point sur la zone active et un deuxième sur les transitions optiques dans ces zones actives. Cela nous a permis de mettre au point 3 designs (2 en bande C+L et 1 en bande O). Nous avons simulé optiquement nos composants afin de réaliser deux variantes de chaque design, possédant un « fort » et un « faible » confinement optique dans les MQW. Ces variations ont permis l'étude de deux facteurs, l'épaisseur des puits quantiques et le confinement optique dans ceux-ci.

La troisième partie était dédiée à la fabrication de nos structures avec la combinaison de la GSMBE et de la MOCVD pour obtenir nos structures. Nous avons montré que la croissance du quaternaire GaInAsP n'est pas triviale, surtout dans la zone active. L'optimisation des conditions de croissance a été l'une des clés dans la réussite de ce travail, suite à leur impact sur les performances finales des composants. Les caractérisations matériau (PL, XRD, ECV, Photocourant) ont permis de valider les croissances pour la suite des procédés de fabrication des SOA et RSOA (SIBH 1-étape et 2-étapes). Nous avons aussi eu l'opportunité de parler du transfert de technologie entre deux réacteurs MBE. Un total de 21 plaques a été réalisé par MBE et 15 d'entre elles ont permis l'obtention de composants pour ce travail.

Dans la dernière partie, nous avons caractérisé les composants en tant que tels, avec : (i) l'imagerie de champs lointain, pour vérifier le mode optique des composants, (ii) les spectres ASE, pour une première détermination de la largeur de bande optique, (iii) les mesures de gain, de NF et de P_{sat} . Ces caractérisations nous ont permis de comparer les performances des puces fabriquées avec le procédé SIBH 2-étapes. Ces dernières ont montré, en bande C+L, que, malgré l'utilisation de puits plus fins, la bande passante présente un pic de gain important, limitant la largeur de bande optique d'amplification. La comparaison avec les RSOA a permis de mettre en avant les performances réduites de ce composant, dues au virage du ruban, ainsi que de la nécessité de trouver des conditions de croissance pour les reprises d'épitaxie satisfaisantes pour la partie droite et la partie courbée du composant. En bande O, le design O1 présente des résultats prometteurs pour le développement de SOA hautes performances en bande O. Ces composants représentent d'ailleurs la première démonstration de SOA basé sur une structure MQW en GaInAsP, opérant en bande O. Nous avons aussi caractérisé les composants issus du procédé SIBH 1-étape. Les résultats obtenus sont inférieurs aux performances des composants SIBH 2-étapes. Ce procédé nécessite encore des améliorations afin d'être complètement développé et permettre l'obtention de performances similaires au SIBH 2-étapes avec des temps de cycle réduits.

Afin d'améliorer les performances des SOA et RSOA, plusieurs pistes sont étudiées, dont la plus prometteuse est celle du confinement variable. Ce principe consiste à faire varier le confinement optique de la zone active le long du composant afin de minimiser le NF tout en ayant de hautes performances en termes de gain et de P_{sat} . Pour cela, nous pouvons faire croître et mettre en forme un matériau d'indice optique élevé, au-dessus de la zone active, ou encore, faire varier la profondeur de gravure dans la semelle pour faire varier le confinement optique.

En se concentrant sur nos résultats, les performances de gain et de P_{sat} sont à améliorer pour notre structure référence. Cela peut facilement être fait pour le gain en augmentant le confinement, cependant, cela serait au détriment de la P_{sat} . Pour ce paramètre, l'utilisation de puits quantiques « fins » reste la meilleure option. Hélas, nous avons observé avec ce type de design que la largeur de bande optique est réduite. Pour parer cette réduction, nous pourrions modifier le couple de matériau présent dans la zone active pour augmenter la contribution des transitions de hautes énergies au spectre de gain. Une autre solution est d'ajouter un filtre qui réduirait le gain maximal du signal mais permettrait d'étendre la plage d'amplification. Nos structures à puits « fins » ont aussi montré les prémisses pour la réalisation de composants opérant en bande S+C. Cela est important à noter car, dans la conjoncture actuelle, la bande S sera amenée à être utilisée au même titre que les bandes C et L pour les transmissions longues distances. En bande O, nos composants posent les bases du développement d'un composant permettant l'amplification sur l'entièreté des 100 nm de la bande optique, avec des valeurs de gain et de NF satisfaisantes pour améliorer les performances de nos systèmes actuels. Pour cela, le gain doit être amélioré avec un plus fort confinement optique, et la bande passante doit encore être élargie pour couvrir les plus petites longueurs d'onde. Suite aux résultats obtenus en bande C+L, nous pourrions envisager une augmentation de l'épaisseur des puits quantiques pour obtenir une bande passante plus large, ou une modification du matériau des barrières afin d'obtenir un meilleur confinement du second niveau électronique. Enfin, pour le SIBH 1-étapes, d'importants travaux sont menés au III-V Lab pour améliorer les conditions de croissance et réduire leur impact sur les performances finales des composants pour, à terme, obtenir des composants de hautes performances avec un procédé simplifié et plus rapide que le SIBH 2-étapes, faisant actuellement office de référence pour la fabrication de SOA et RSOA.

Bibliographie

- [1] N. S. Bergano and C. R. Davidson, "Wavelength division multiplexing in long-haul transmission systems," *Journal of lightwave technology*, vol. 14, no. 6, pp. 1299-1308, 1996.
- [2] D. J. Richardson, J. M. Fini and L. E. Nelson, "Space division multiplexing in optical fibres," *Nature photonics*, vol. 7, pp. 354-362, 2013.
- [3] Y. Tamura, H. Sakuma, K. Morita, M. Suzuki, Y. Yamamoto, K. Shimada, Y. Honma, K. Sohma, T. Fujii and T. Hasegawa, "The first 0.14-dB/km loss optical fiber and its impact on submarine transmission," *Journal of lightwave technology*, vol. 36, no. 1, pp. 44-49, 2018.
- [4] R. Udayakumar, V. Khanaa and T. Saravanan, "Chromatic dispersion compensation in optical fiber communication system and its simulation," *Indian journal of science and technology*, vol. 6, no. 6, pp. 4762-4766, 2013.
- [5] M.-J. Li and D. A. Nolan, "Optical transmission fiber design evolution," *Journal of lightwave technology*, vol. 26, no. 9, pp. 1079-1092, 2008.
- [6] M. Kumari, R. Sharma and A. Sheetal, "Passive optical network evolution to next generation passive optical network: a review," in *2018 6th edition of international conference on wireless networks & embedded systems (WECON)*, Rajpura, INDIA, 2018.
- [7] N. N. Cikan and M. Aksoy, "A review of self-seeded RSOA based on WDM PON," *Canadian journal of electrical and computer engineering*, vol. 42, no. 1, 2019.
- [8] A. G. Podoleanu, "Optical coherence tomography," *Journal of microscopy*, vol. 247, no. 3, pp. 209-219, 2012.
- [9] R. A. Leitgeb and B. Baumann, "Multimodal optical medical imaging concepts based on optical coherence tomography," *Frontiers in physics*, vol. 6, no. 114, 2018.
- [10] B. Pendersen, A. Bjarklev, J. H. Povlsen, K. Dybdal and C. C. Larsen, "The design of erbium-doped fiber amplifiers," *Journal of lightwave technology*, vol. 9, no. 9, pp. 1105-1112, 1991.
- [11] V. Mikhailov, J. Luo, D. Inniss, M. F. Yan, Y. Sun, G. S. Puc, R. S. Windeler, P. S. Westbrook, Y. Dulashko and D. J. DiGiovanni, "Amplified transmission beyond C- and L- bands: Bismuth doped fiber amplifier for O-band transmission," *Journal of lightwave technology*, vol. 40, no. 10, pp. 3255-3262, 2022.
- [12] M. N. Islam, "Raman amplifiers for telecommunications," *IEEE journal of selected topics in quantum electronics*, vol. 8, no. 3, pp. 548-559, 2002.
- [13] A. Verdier, "Modélisation, conception, fabrication, caractérisation et valorisation d'amplificateurs optiques à semiconducteur de très large bande spectrale. (Ph.D Thesis)," Université de Toulouse, Toulouse, FRANCE, 2018.
- [14] M. Tachibana, R. I. Laming, P. R. Morkel and D. N. Payne, "Erbium-doped fiber amplifier with flattened gain spectrum," *IEEE photonics technology letters*, vol. 3, no. 2, pp. 118-120, 1991.

- [15] H. Masuda, "Review of wideband hybrid amplifiers," in *Optical Fiber Communication conference (OFC)*, Baltimore, USA, 2000.
- [16] C. H. Yeh and S. Chi, "Utilizations of EDFA and SOA in series for broadband gain amplification," *Laser physics letters*, vol. 4, no. 6, pp. 433 - 436, 2007.
- [17] A. Arnould, A. Ghazisaeidi, D. Le Gac, P. Brindel, M. Makhsyian, K. Mekhazni, F. Blache, N. Fontaine, D. Neilson, R. Ryf, H. Chen, M. Achouche and J. Renaudier, "103 nm ultra-wideband hybrid Raman/SOA transmission over 3 x 100 km SSMF," *Journal of lightwave technology*, vol. 38, no. 2, pp. 504-508, 2020.
- [18] H. Carrère, S. R. Joshya, Q. Hochart, C. Calò, X. Marie, O. Delorme, A. Balocchi and A. Wilk, "Materials for wide-band amplification," in *13th International Symposium on Communication Systems, Networks and Digital Signal Processing (CSNDSP)*, Porto, PORTUGAL, 2022.
- [19] G. Bastard, *Wave mechanics applied to semiconductor heterostructures*, 1990.
- [20] K. Morito, S. Tanaka, S. Tomabechi and A. Kuramata, "A broad-band MQW semiconductor optical amplifier with high saturation output power and low noise figure," *IEEE photonics technology letters*, vol. 17, no. 5, pp. 974-976, 2005.
- [21] G. D. Pettit and W. J. Turner, "Refractive index of InP," *Journal of applied physics*, vol. 36, p. 2081, 1965.
- [22] J. Buus and M. J. Adams, "Phase and group indices for double heterostructure lasers," *Solid-state and electron devices*, vol. 3, no. 6, pp. 189-195, 1979.
- [23] S. H. Wemple and M. DiDomenico Jr., "Behavior of the electronic dielectric constant in covalent and ionic materials," *Physical review B*, vol. 3, no. 4, pp. 1338-1351, 1971.
- [24] C. Tanguy, "Refractive index of direct bandgap semiconductors near the absorption threshold: Influence of excitonic effects," *IEEE journal of quantum electronics*, vol. 32, no. 10, pp. 1746-1751, 1996.
- [25] H. Burkhard, H. W. Dinges and E. Kuphal, "Optical properties of In_{1-x}GaxP_{1-y}Asy, InP, GaAs, and GaP determined by ellipsometry," *Journal of applied physics*, vol. 53, no. 1, pp. 655-662, 1982.
- [26] B. Broberg and S. Lindgren, "Refractive index of In_{1-x}GaxAsyP_{1-y} layers and InP in the transparent wavelength region," *Journal of applied physics*, vol. 55, no. 9, pp. 3376-3381, 1984.
- [27] S. Adachi, "Refractive indices of III-V compounds: key properties of InGaAsP relevant to device design," *Journal of applied physics*, vol. 53, no. 8, pp. 5863-5869, 1982.
- [28] B. R. Bennett, R. A. Soref and J. A. Del Alamo, "Carrier-induced change in refractive index of InP, GaAs, and InGaAsP," *IEEE journal of quantum electronics*, vol. 26, no. 1, pp. 113-122, 1990.
- [29] P. W. Juodawlkis, J. J. Plant, W. Loh, L. J. Missaggia, F. J. O'Donnell, D. C. Oakley, A. Napoleone, J. Klamkin, J. T. Gopinath, D. J. Ripin, S. Gee, P. J. Delfyett and J. P. Donnelly, "High-Power, Low-Noise 1.5-μm Slab-Coupled Optical Waveguide (SCOW) Emitters: Physics, Devices, and Applications," *IEEE Journal of Selected Topics in Quantum Electronics*, vol. 17, no. 6, pp. 1698-1714, Nov-Dec 2011.

[30] R. Paschotta, "Optical Spectrum analyzers," RP photonics, [Online]. Available: https://www.rp-photonics.com/optical_spectrum_analyzers.html. [Accessed 04 January 2023].

Figures

Figure 1. Graphique d'absorption et de dispersion chromatiques dans les fibres optiques monomodes standards avec la représentation des différentes bandes optiques [5].....	1
Figure 2. Schémas (a) d'un SOA et (b) d'un RSOA.	3
Figure 3. Comportement du gain en fonction du courant injecté, dans un SOA dont l'amplification est basée sur 2 transitions énergétiques.	6
Figure 4. Courbes Arrhenius des vitesses de croissances de deux sources In en fonction de leurs températures.	10
Figure 5. Mesures de photoluminescence de structures en bande O, S+C et C+L, réalisées avec le MBE412.	11
Figure 6. Résumé des procédés de fabrication (a) SIBH 2-étapes et (b) SIBH 1-étape.	12
Figure 7. Images SEM des structures SOA et RSOA observées après (a) SIBH 2-étapes et (b) SIBH 1-étape.	13
Figure 8. Photos (a) d'une plaque finalisée, (b) d'un SOA et (c) d'un RSOA, montés sur embases.	14
Figure 9. Résultats obtenus par la mesure du champ lointain du SOA SIBH 2-étapes A1 avec (a) le profil 2D du champ lointain, (b) les courbes représentatives des sections selon les axes horizontal et vertical.	15
Figure 10. Evolution du profil de champ lointain du SOA SIBH 1-étape A1 en fonction de sa puissance optique de sortie.	16
Figure 11. Spectres ASE mesurés à différents courants pour les composants (a) SOA SIBH 2-étapes A1 et (b) SOA SIBH 2-étapes B1.	17
Figure 12. Spectres de gain, aux courants de gain plat, (a) des SOA en bande C+L, (b) des RSOA en bande C+L et (c) des SOA en bande O, fabriqués avec le procédé SIBH 2-étapes.	18
Figure 13. Résultats des mesures de NF des composants (a) SOA en bande C+L, (b) RSOA en bande C+L et (c) SOA en bande O, ainsi que (d) les résultats des mesures de P_{sat} à 500 mA, pour les composants SIBH 2-étapes.....	19
Figure 14. Spectres de gain, aux courants de gain plat, (a) des SOA en bande C+L, (b) des RSOA en bande C+L et (c) un SOA en bande O, fabriqués avec le procédé SIBH 1-étape.	21
Figure 15. Résultats des mesures de NF des composants (a) SOA en bande C+L, (b) RSOA en bande C+L et (c) SOA en bande O, ainsi que (d) les résultats des mesures de P_{sat} à 500 mA, pour les composants SIBH 1-étape.	22

Tableaux

Tableau 1. Paramètres caractéristiques des différents types d'amplificateurs optiques.....	4
Tableau 2. Caractéristiques des zones actives conçues.	6
Tableau 3. Structures proposées pour les SOA en bande C+L.....	8
Tableau 4. Structures proposées pour les SOA en bande O.	8
Tableau 5. Résultats des caractérisations matériau des différents designs.	11
Tableau 6. Angles de divergences calculés pour chaque composant SIBH 2-étapes, à partir des largeurs à mi-hauteur mesurées à 500 mA.	16
Tableau 7. Performances d'ASE obtenues avec les différents SOA SIBH 2-étapes.	17
Tableau 8. Performances d'ASE obtenues avec les différents RSOA SIBH 2-étapes.....	17
Tableau 9. Angles de divergences calculés pour chaque composant SIBH 1-étapes, à partir des largeurs à mi-hauteur mesurées à 500 mA.	20
Tableau 10. Performances d'ASE obtenues avec les différents SOA SIBH 1-étape.	20
Tableau 11. Performances d'ASE obtenues avec les différents RSOA SIBH 1-étape.	20

Contents

Introduction	1
Chapter 1 - Wideband amplification, concept and state of the art.....	3
1. Applications requiring wideband amplification	3
1.1. Optical telecommunications	3
1.2. Optical spectrum analyzer	12
1.3. Optical Coherence Tomography, a medical application.....	14
2. Optical Amplifiers	16
2.1. Rare earth doped fiber amplifiers	16
2.2. Raman amplifiers.....	18
2.3. Semiconductor Optical Amplifiers and Reflective SOA Structures.....	19
3. Wide bandwidth amplification solutions.....	27
3.1. Passive elements.....	27
3.2. Multiple amplifiers	28
3.3. Optical amplifiers state of the art	31
3.4. Previous projects	33
4. Conclusion.....	34
Bibliography	i
Figures	ix
Tables	ix
Chapter 2 – Conception of Semiconductor Optical Amplifiers	35
1. Active region simulation	35
1.1. Band structure engineering.....	35
1.2. Optical transitions in wideband amplification.....	40
1.3. Designed active regions.....	46
1.4. SOA structure	51
2. Optical confinement simulation	52
2.1. Refraction indices in C+L- and O-Bands	52
2.2. Our refractive indices	59
2.3. Asymmetric cladding.....	61
3. Complete designs of C+L and O-Bands devices	64
3.1. C+L-Band structures	64
3.2. O-Band structures.....	65
4. Conclusion.....	66
Bibliography	i
Figures	v
Tables	v

Chapter 3 – Molecular Beam Epitaxy of wideband SOA and technological process fabrication	67
1. Epitaxy techniques	68
1.1. Metal-Organic Chemical Vapor Deposition for SIBH process	68
1.2. Molecular Beam Epitaxy of InP and related materials.....	70
1.3. Gas-Source Molecular Beam Epitaxy	75
2. MBE growth of GaInAsP quaternary alloys.....	79
2.1. The issue of miscibility gap in the GaInAsP/InP system	79
2.2. MBE reactor initial calibrations	81
2.3. GaInAsP quaternary alloys' growths, from bulk material to MQW based active zone ...	87
3.1. C+L-Band full structure	92
3.2. O-Band material growth	96
3.3. O-Band SOA growth process transfer to the MBE412 reactor	100
4. Fabrication processes	104
4.1. SIBH processes descriptions	104
4.2. Wafers preparation for 1-step SIBH process	106
4.3. Ridge etching.....	107
4.4. SIBH regrowth steps.....	109
4.5. Fabrication process finalization.....	113
5. Back-end.....	115
5.1. Preparation for the first measurements.....	115
5.2. Selection process of the individual devices	117
6. Conclusion.....	120
Bibliography	i
Figures	iii
Tables	v
Chapter 4 – Devices' characterizations	121
1. 2-step SIBH devices' performances	121
1.1. Far field imaging	121
1.2. ASE Spectra	127
1.3. Gain Spectra - G	132
1.4. Noise Figure - NF.....	138
1.5. Saturation output power - P_{sat}	142
2. 1-step SIBH processes.....	144
2.1. Far field imaging	144
2.2. ASE Spectra	146
2.3. Gain Spectra – G	149
2.4. Noise Figure - NF.....	152

2.5. Saturation output power - P_{sat}	154
3. Comparison between the fabrication processes.....	155
4. Conclusion.....	161
Bibliography.....	i
Figures.....	i
Conclusions & Perspectives	121

Introduction

The strong communication data traffic growth associated with the limits encountered by the spectral efficiency of the systems leads to an ever increasing demand to expand the bandwidths available for the telecommunications networks. In this optic, Semiconductor Optical Amplifiers (SOAs) and Reflective Semiconductor Optical Amplifiers (RSOAs) are ideal candidates, due to their broadband amplification capabilities, as well as their low dimensions and manufacturing costs. The wavelengths used for long distance transmissions correspond to the minimum absorption in optical fibers, between 1530 and 1625 nm. In this interval, called "C+L band", another type of amplifier is already well established, the Erbium Doped Fiber Amplifier (EDFA). It provides high gain values (> 30 dB) and low Noise Figure (NF) (< 5 dB) which are better performances than the current SOAs' one. However, its bandwidth is limited to 50 nm, its costs is high and its dimensions do not enable its implementation in every type of systems. Consequently, SOAs and RSOAs, could become competitive with EDFA if improvement of their gain value and reduction of their NF were provided, as they already allow broadband amplification combined with low manufacturing cost and small dimensions.

This dimension problematic is particularly true for short distance transmissions, intended for interconnections between routers, data centers and customer interfaces, where the wavelengths used for these applications are the ones minimizing the chromatic dispersion, between 1260 and 1360 nm. These transmission lines require compact and inexpensive devices. In this wavelength range, labelled "O-Band", broadband SOAs or RSOAs based on GaInAsP Multi-Quantum Wells (MQW) do not exist.

The objective of this work is the conception, the fabrication and the characterization of wideband SOAs operating in C+L and O-Band. We begin with the optimization of the structures through the conception of different designs simulated in the C+L-Band. Then, we develop two GaInAsP quantum wells based designs to explore the possibilities for wideband SOAs operation in the O-Band. This report is structured around four chapters corresponding to the different steps in the manufacturing process of optical amplifiers: (i) the presentation of systems requiring broadband amplification, (ii) the conception of the different SOA designs, (iii) the manufacture of the devices and finally (iv) their characterizations.

The first chapter of this thesis is dedicated to the presentation of applications requiring broadband amplification. These applications include telecommunications, but also the fields of security, environmental monitoring and healthcare. We present the various amplification solutions already available, as well as a specific state-of-the-art on broadband amplification. We show the advantages and disadvantages of SOAs and RSOAs over their competitors. We also introduce the key parameters for optical amplifiers, such as gain, bandwidth, noise figure and saturation output power. Finally, we set targets for each of these parameters that will enable our devices to be implemented in systems.

In the second chapter, we detail the design steps of our devices. We begin with a presentation of the band-structure engineering and its impact on the devices' amplification. We model the material gain and active zones enabling broadband amplification in C+L band, then in O band. We also present the carried out optical simulations, with the refractive index calculation models and asymmetrical cladding used. Finally, we propose six different designs, four in C+L-band and 2 in O-band, to study devices' behavior as a function of, the optical confinement in the active zone and the quantum well size.

The third chapter deals with the epitaxy and processing of the previously designed structures. We present the epitaxy techniques involved in the fabrication process. The basic structures are fabricated by Molecular Beam Epitaxy (MBE), while MetalOrganic Chemical Vapor Deposition (MOCVD) is used for the regrowth steps. The MBE steps are described in depth, through the calibrations, the growth conditions' optimizations and material characterizations of the manufactured wafers. 21 epiwafers, based on the proposed designs, were grown. We also present the technology transfer between two Gas

Source Molecular Beam Epitaxy (GSMBE) reactors, due to the replacement of the RIBER modified V100 from Thermo VG Scientific reactor, used for our base structures, by a RIBER MBE412 system. We also detail the two fabrication processes used in the laboratory for SOAs and RSOAs, the 2-step Semi Insulating Buried Heterostructure (SIBH) and the newly developed 1-step SIBH. A final section is dedicated to the back-end steps involved in the transition from wafer to base-mounted unitary device. In total, 15 wafers have been fully processed. With them, we are able to analyze the devices' performance as a function of the followed fabrication process.

The fourth chapter covers the characterizations carried out on the produced SOAs and RSOAs. We compare the performances obtained between the designs, as well as between the devices fabricated following the 2-step SIBH and the 1-step SIBH. The results presented concern: (i) the far field imaging, (ii) the amplified spontaneous emission spectra, (iii) the chip gain, (iv) the optical bandwidth, (v) the noise figure and (vi) the output saturation power. After describing these characterizations thoroughly, we analyze the results to propose possible improvements for our SOAs and RSOAs.

Chapter 1 - Wideband amplification, concept and state of the art

In this first chapter, we identify applications requiring wideband amplification and show how SOA can be a valid option. Details about the currently used optical amplification technologies are provided to illustrate the necessity of the more compact and cost efficient solution that SOAs are. We discuss the material gain used for the devices. The characteristic parameters (gain, optical bandwidth, noise figure, saturation output power and polarization dependency) are also presented. The developed wideband solutions are exposed and a state of the art of optical amplification devices is realized to set the targeted performances of our devices which contain, the amplification on wider bandwidths, centered on the C+L-Band, and the first time realization of MQW based O-Band SOAs.

1. Applications requiring wideband amplification

1.1. Optical telecommunications

1.1.1. Optical fiber telecommunication networks

Internet traffic is still increasing after an acceleration since the 2000's and the diffusion of internet from professional to domestic uses. Figure 16 illustrates the monthly data traffic exponential growth.

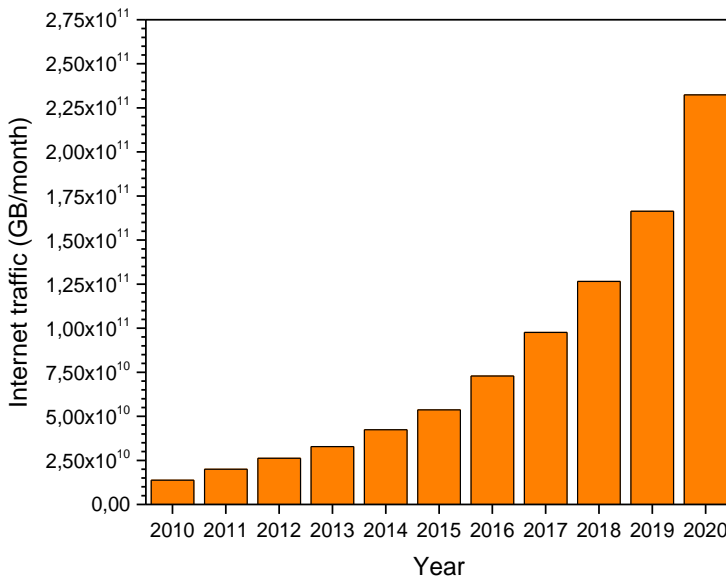


Figure 16. Growth of monthly internet data traffic from 2010 to 2020. Sources: IEA & Cisco blog.

Transfer data, which was of $1,3 \times 10^{10}$ GB/month in 2010, was multiplied by almost 17 in ten years, to reach $2,3 \times 10^{11}$ GB/month in 2020. In the same period, the number of internet users went from 2.0 billion to 4.9 billion [1, 2]. These observations show the importance of a well-performing telecommunication network. To keep up with the growth pace, the optical transmission must be in constant evolution.

Systems developments have changed the way to transfer data. Wavelength Division Multiplexing (WDM) and Spatial Division Multiplexing (SDM) are examples of these developments and will be described further.

The design of optical devices compatible with high data flow rates also improves the telecommunication network performances. However, this type of improvement requires more complex and expensive

optoelectronic devices. Consequently, the solutions are based on the balance between cost and performances. We can distinguish three different network-levels that have different requirements: Long-haul, Metro and Access represented in Figure 17.

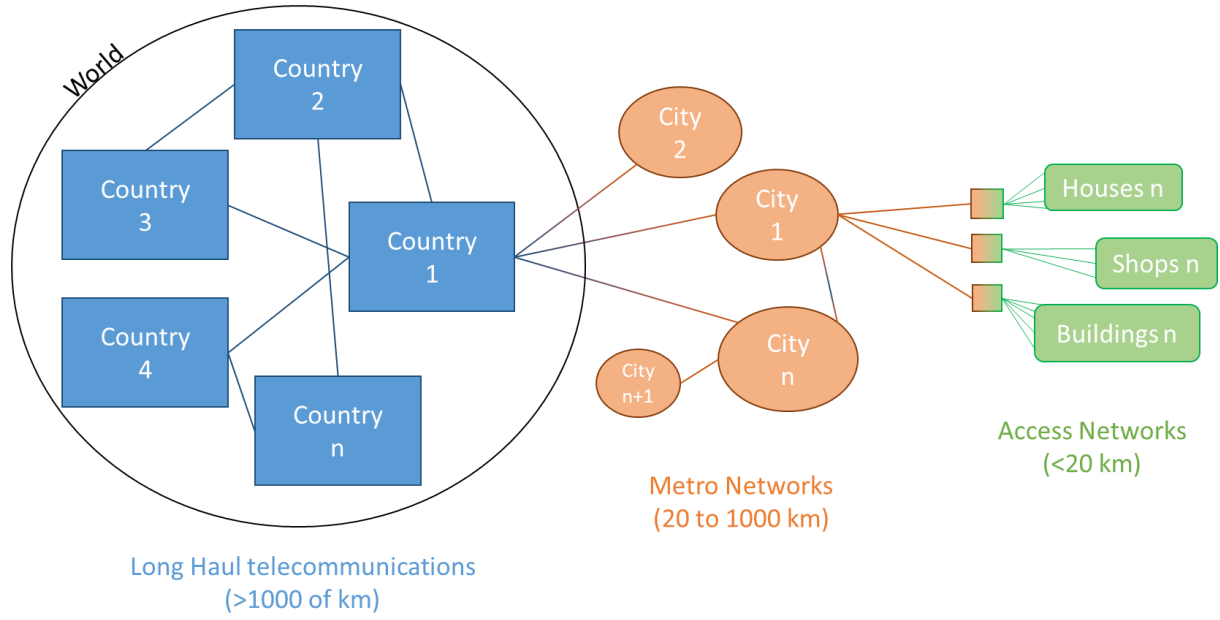


Figure 17. Long Haul, Metro and Access network illustration.

Long haul network corresponds to the high-capacity links for intercontinental or interstate connections. The long distances require optical amplifiers as in-line repeaters. Metro and Access networks correspond to smaller distances, between 1000 km and 20 km for Metro and less than 20 km for Access. These levels do not use repeaters but passive elements as optical splitters. RSOAs are developed as gain medium of the laser sources used in these levels.

The expected performances in each optical network level are fixed by the International Telecommunication Union (ITU) standards, to ensure the optical networks compatibility around the world [3]. The ITU also sets the roadmap for future device performance by taking into account the technology developments.

1.1.2. Optical fibers transmissions

Optical communication networks are based on optical fibers. Works are led to improve the fibers' performances by reducing the propagation losses and the chromatic dispersion, displayed in Figure 18 and in Figure 19, respectively.

1.1.2.1. Optical fibers' attenuation

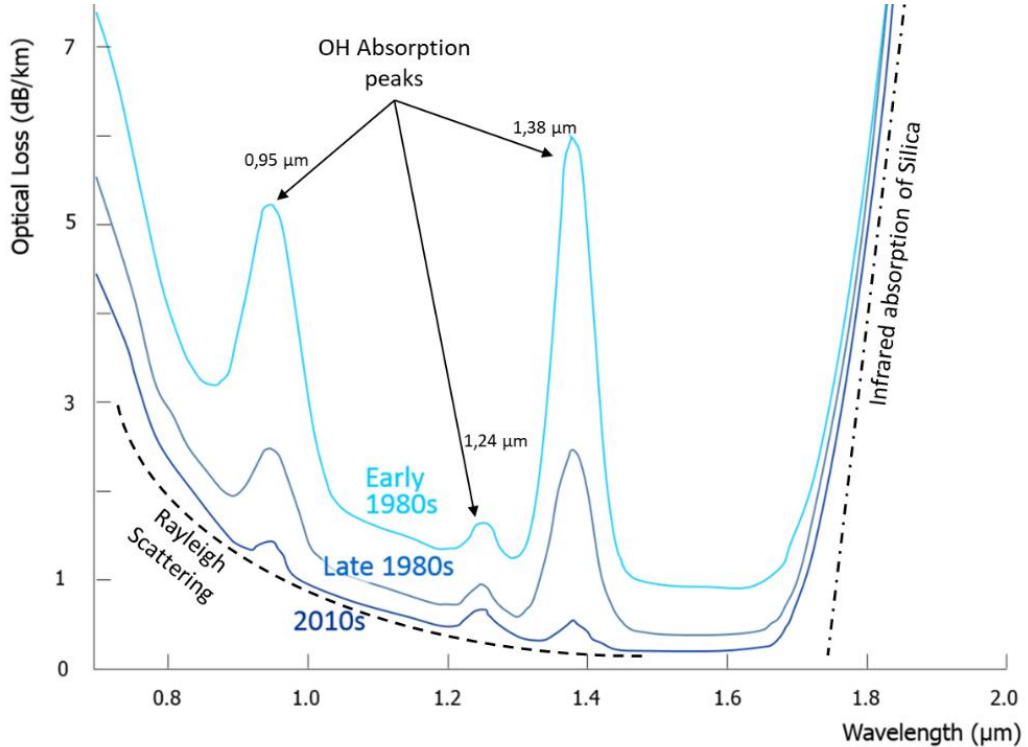


Figure 18. Evolution of the propagation losses in optical fiber [4].

The signal attenuation in fibers is caused by scattering effects and absorption. Considering this parameter in dB and the optical power of the signal in dBm, the impact of the attenuation on the signal power increases linearly with distance. Consequently, the optical losses are expressed in dB/km.

Figure 18 shows the three main mechanisms involved in the fibers' attenuation:

- *The intrinsic material absorption:* The fibers, made of SiO₂, absorb the wavelengths higher than 1.6 μm. It sets the fundamental minimum losses in the silica fibers. To overcome this mechanism, the material used in fiber fabrication must be different.
- *The Rayleigh scattering:* Under 1.6 μm, the small-scale inhomogeneities, incorporated in the fiber during the manufacturing process, are absorbents. The improvements of the optical fibers fabrication tend to reduce the scattering [5]. Every type of fiber is concerned like the Single Mode Fibers (SMF), or the Few-Mode Fibers (FMF) [6].
- *The OH ions' absorption:* The attenuation peaks at 0.95 μm, 1.24 μm and 1.38 μm correspond to this absorption. The most impacting ions come from the water dissolved in the fiber. The reduction of their concentration in the core of the fiber almost eliminates the peaks [7].

Other losses can be introduced by bending the fiber. Macro bending happens when the fiber is bent with a small enough radius, typically less than 30 mm, to reflect the light of the signal out of the fiber. Micro bending generally happens at the core/cladding interface of the fiber. It is generated by a locally placed mechanic stress that induces bends with radii of less than 1 mm.

Works are led to reduce the impact of the attenuation mechanisms and reach the lowest possible losses, especially for long haul telecommunications [8].

1.1.2.2. Optical fibers' chromatic dispersion

The fiber index depends on the signal wavelength, thus, the channels transmitted in a single fiber propagate at different velocities. It generates a broadening of the transmitted pulses in time. This phenomenon is the Chromatic Dispersion (CD), shown in Figure 19, in function of wavelength, for commercially available fibers.

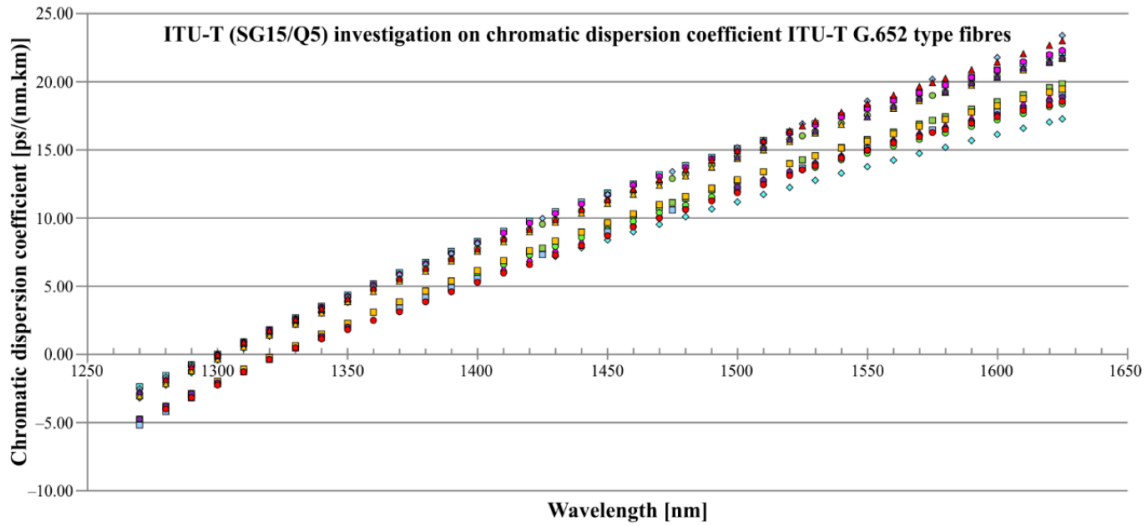


Figure 19. CD in commercially available optical fibers. Data from various vendors available in [9].

CD is near to zero around 1310 nm and varies between 12 and 22 ps/(nm.km) for long haul transmissions. Figure 20 illustrates the CD phenomenon for positive and negative values. The pulse spreading only depends on the CD value, not on its sign. Therefore, alternating positive and negative CD fibers can be a solution to obtain a total CD as near-to-zero as possible [10].

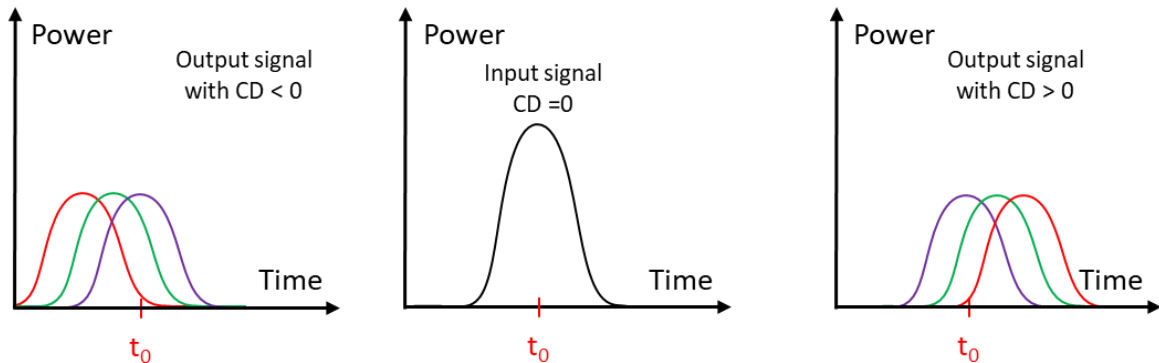


Figure 20. Illustration of chromatic dispersion in function of its sign.

The 1260 nm and 1360 nm wavelengths range has a near-to-zero CD value and moderated optical losses in standard SMF. The zero dispersion allows the use of low cost transmitters with low performances in terms of spectral efficiency. Consequently, these wavelengths were the first to be developed for the telecommunications. They are still used in Access networks, where the cost is a critical parameter, because of the great number of devices required to distribute signals to every user.

Figure 21 summarizes the attenuation and the dispersion of standard SMF for the telecommunication wavelengths.

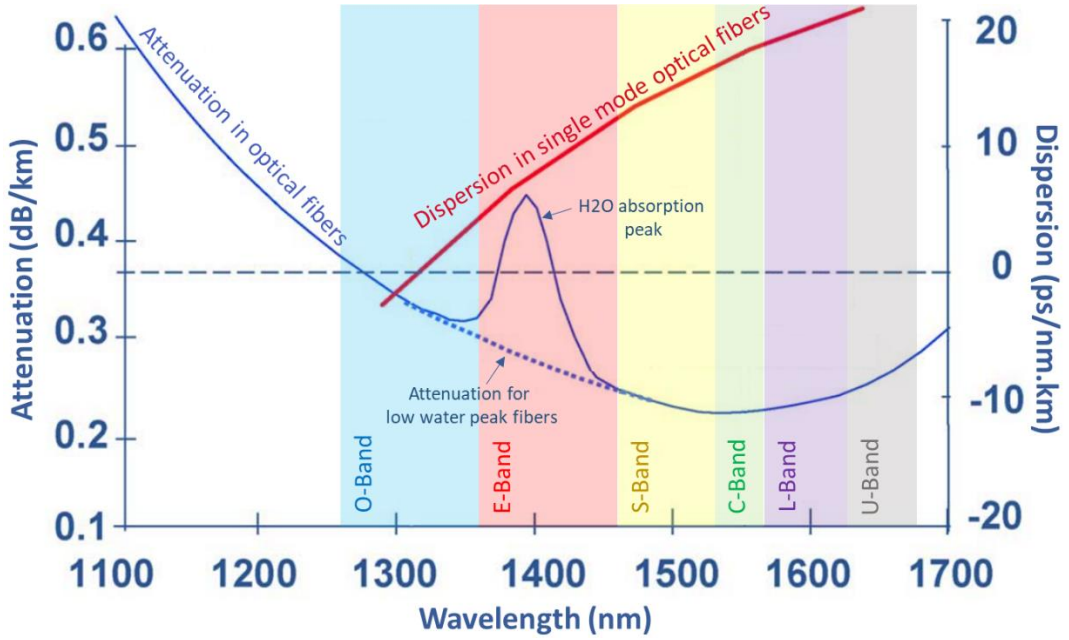


Figure 21. Optical fiber absorption and dispersion in standard single mode fiber [11].

The upper and lower limits of the standard optical bands used for telecommunications are listed in Table 12.

<i>Optical band</i>	<i>Wavelength range (nm)</i>
O-Band (Original-band)	1260 → 1360
E-Band (Extended-band)	1360 → 1460
S-Band (Short-band)	1460 → 1530
C-Band (Conventional-band)	1530 → 1565
L-Band (Long-band)	1565 → 1625
U-Band (Ultralong-band)	1625 → 1675

Table 12. The optical bands' wavelength ranges.

The wavelengths of interest for our devices are those commonly used for telecom applications: (i) C+L-band for its low attenuation in the optical fiber and (ii) O-band for its near-to-zero CD. Our objective is to develop a dedicated device for each of these wavelength ranges.

1.1.3. Passive optical network

Access networks are based on Passive Optical Networks (PON) which operate in O-Band. Figure 22 presents the PON's architecture which implements a point-to-multipoint topology. A single fiber, connected to the Optical Line Terminal (OLT), serves several endpoints, by using only passive elements. The Passive Optical Splitters (POS) divide the bandwidth among the endpoints. When these splitters are replaced by active signal repeaters, the network becomes an Active Optical Network (AON).

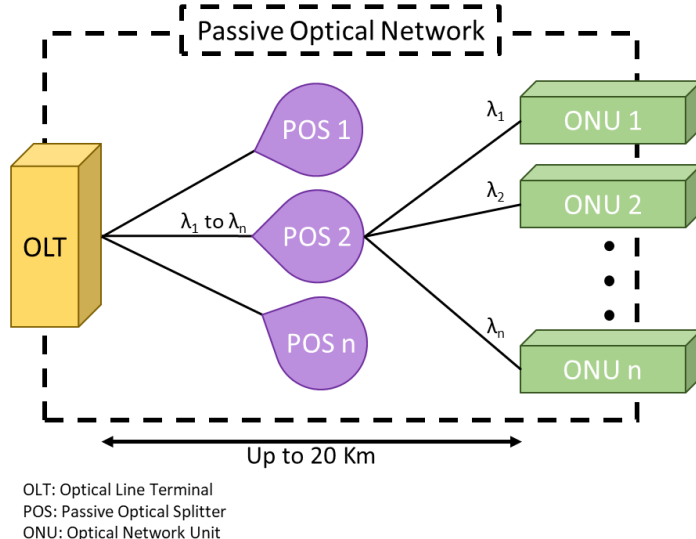


Figure 22. Illustration of a passive optical network.

At Access level, the O-Band limitations are set by the devices' cavity losses and their Relative Intensity Noise (RIN). RIN describes the fluctuations in the optical power of a laser. RSOA devices have the capability to reduce these fluctuations [12]. Consequently, O-Band RSOAs are massively used in PON, as colorless transmitters' sources for the Optical Network Units (ONU). The colorless property of a transmitter is its ability to modify its working wavelength without having to adjust it for each ONU [13]. This individual adjustment would be prohibitively expensive. Large bandwidth RSOAs' development is justified by its capability to increase the number of ONU connected to a single POS.

RSOA is not the only solution for colorless transmitters. Other sources are based on Fabry-Pérot (FP), or Reflective Electro-Absorption Modulator SOA (REAM SOA). However, one of the most promising solutions is the RSOA used in a self-seeded cavity architecture [14].

To distribute the wavelengths between the ONUs, the PON architecture uses the WDM technology. It is also the case for the long haul telecommunications.

1.1.4. Long haul telecommunications

Figure 23 illustrates a long-haul transmission line, divided in multiples spans of about 100 km. Between each span, the signal has to be amplified to keep running in the fiber.

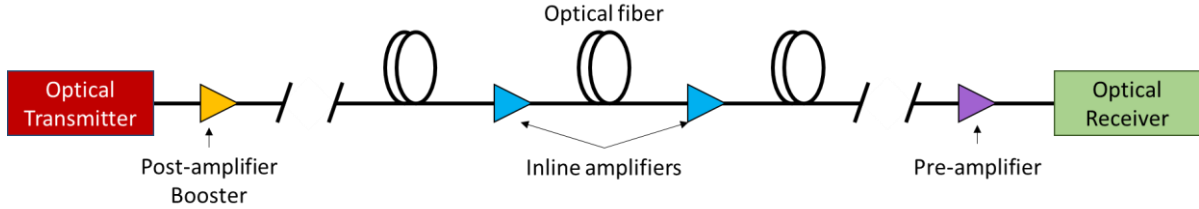


Figure 23. Amplification in a transmission line in the optical network.

The in-line amplification must have a high gain to compensate the optical losses that are proportional to the length of the fiber. They also need high Saturation Output Power (P_{sat}) to amplify the great channels' number transmitted in a unique fiber. The NF that is added at every amplification step must be as low as possible. Table 13 provides the required characteristics for each type of amplifier in the transmission line. The parameters will be detailed in Section 2.3.2

	<i>Post-amplification</i>	<i>In-line amplification</i>	<i>Pre-amplification</i>
High gain	Yes	Yes	Yes
High saturation power	Yes	Yes	No
Low noise figure	No	Yes	Yes
Low polarization sensitivity	No*	Yes	Yes
Wide bandwidth	Yes	Yes	Yes

* if the polarization mode behavior is handled by the optical transmitter

Table 13. Required performance for optical amplifier depending on its role in the transmission line [15].

The long distances covered by the signal transmissions justify the development of C+L-Band devices for this network level. This level also connects several transmitters to several receivers, consequently it benefits the WDM technology, described in the next section.

1.1.5. Wavelength division multiplexing

WDM is one of the most important technologies to improve data rates. It allows the transfer of multiple data fluxes in parallel, using different wavelengths for each flux in a single optical fiber. It uses the smallest possible wavelengths range, called “channel”, to transmit one signal without crosstalk with the others. The improvement of the spectral density and the available optical bandwidth increase the number of usable channels.

Large bandwidth SOA are developed to integrate this technology as they can amplify a large range of wavelengths with a single device. Every ONU of the WDM system, illustrated in Figure 24, will be equipped with the same device. It enables the mass production of the same device to reduce its cost.

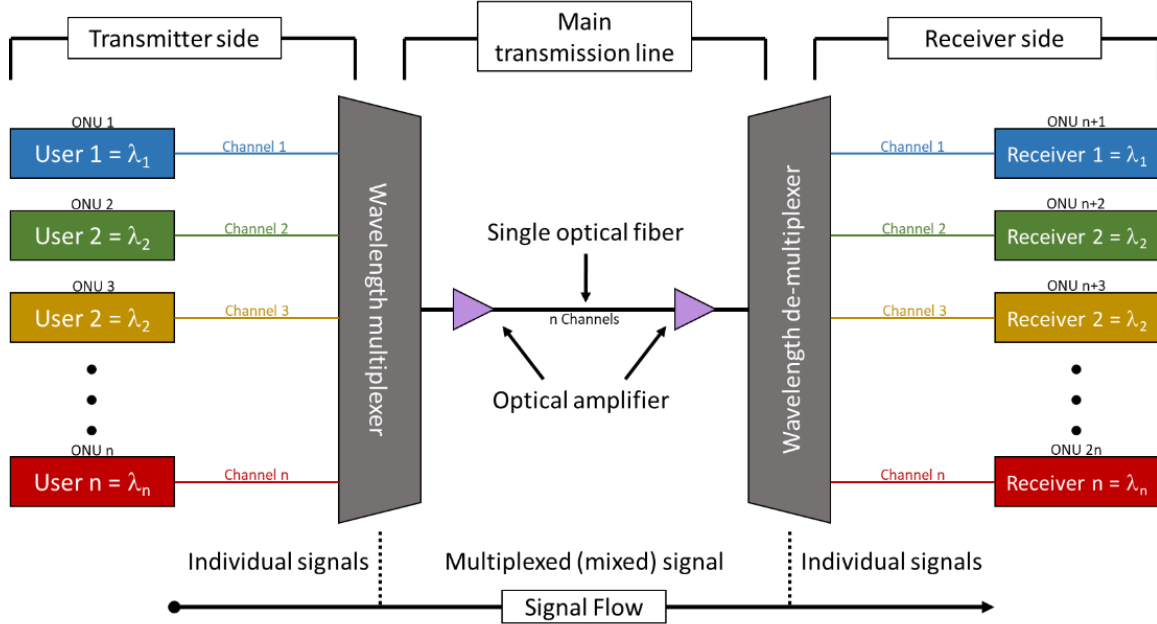


Figure 24. Illustration of a wavelength division multiplexer system.

In the C+L-Band, the use of dense WDM is helped by the CD. It prevents the cross-talk between the different channels which propagate at different speeds. This property increases the interest of C+L-Band for the long haul telecommunications.

The enlargement of the C+L-Band SOA bandwidth is required to improve the WDM performances and reduce its cost. Large bandwidth O-Band SOA design would also increase the number of available channels for the Access and Metro networks.

1.1.6. Spatial division multiplexing

Since 2010, SDM is under development [16]. This technology was made possible by the improvements of fiber fabrication and coupling techniques. SDM requires the use of fibers in which several modes can be transferred. It allows the use of a same wavelength for several signals that are spatially separated. Figure 25 shows the classes of SDM fibers commonly used in optical data transmissions.

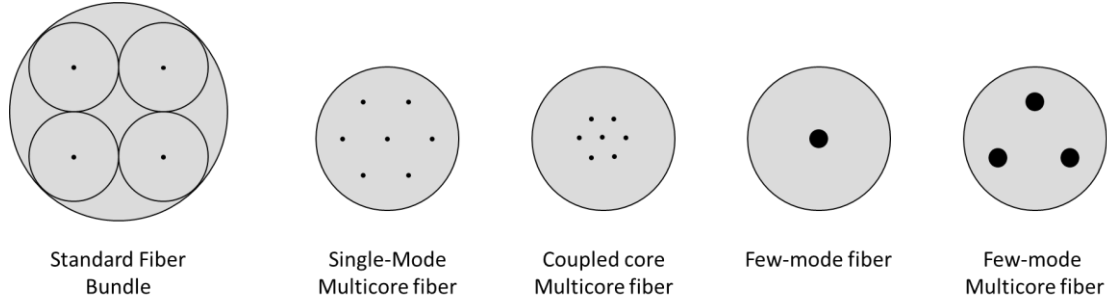


Figure 25. SDM fibers commonly used in optical data transmissions.

The multicore fibers can be subject to intercore crosstalk which is detrimental for long haul transmissions. Solutions have to be found to overpass this limitation [17]. Hence, SDM is mainly used for short-reach transmissions.

To enable the transmission of the multiple signals in these fibers, SDM systems require spatial multiplexers at each part of the fiber. They have to direct the optical signal in and out of the various spatial channels. Combinations between WDM and SDM systems, as shown in Figure 26, are studied and already allowed to reach data rates exceeding 10 Pb/s [18, 19].

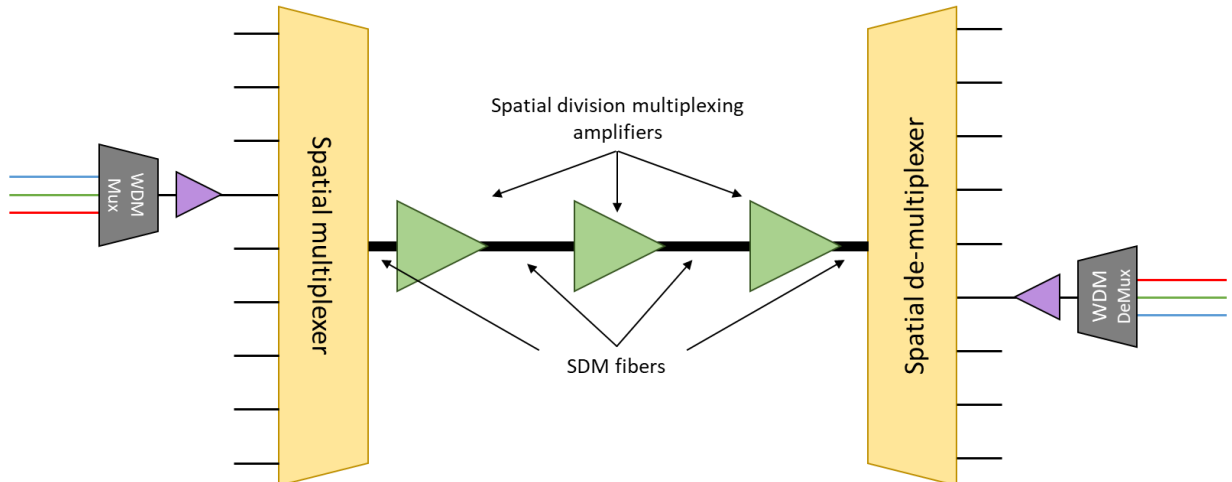


Figure 26. SDM and MDW merged systems scheme.

SOAs can also be used in other applications than fiber telecommunications. The two next sections provide examples of such applications.

1.2. Optical spectrum analyzer

The Optical Spectrum Analyzers (OSA) measure and display the optical signal's power as a function of a user-selectable wavelength range, as shown in Figure 27.

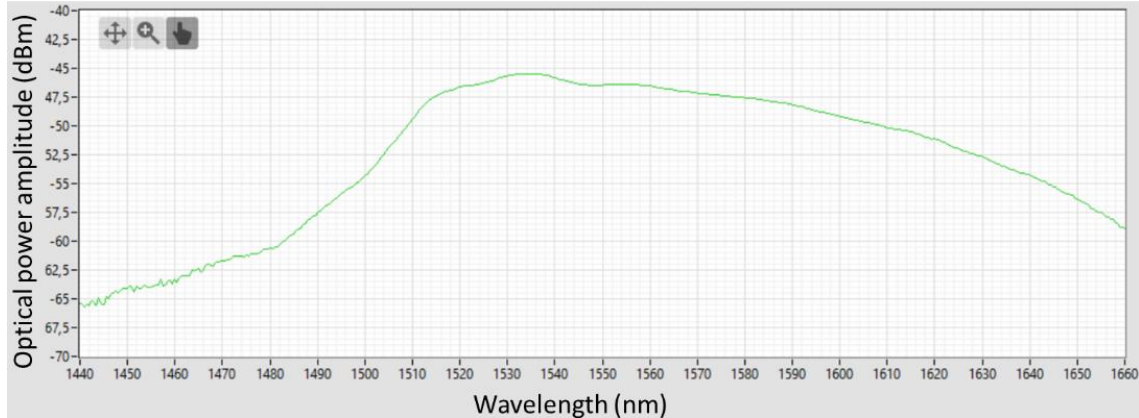


Figure 27. Optical spectrum analyzer's display.

Advanced optical spectral measurement is required in research and development and manufacturing industries. This technology is used in telecommunications, security, environmental monitoring, healthcare, ...

There are three types of OSA based on different operation principles:

- *Diffraction gratings*: The OSA based on this principle can be divided in two categories, the spectrographs, and the scanning instruments. The high-performance spectrum analyzers are mostly designed as scanning instruments, schematized in Figure 28. In this configuration, the input signal is sent through a tunable bandpass filter. The user can set the wavelengths range to analyze as well as the resolution. This last parameter is limited by the tunable bandpass filter that has the role of monochromator. A single high-dynamic-range photodiode analyses the magnitude of the optical power. During the measurement, the input light must remain constant to scan the wavelengths range.

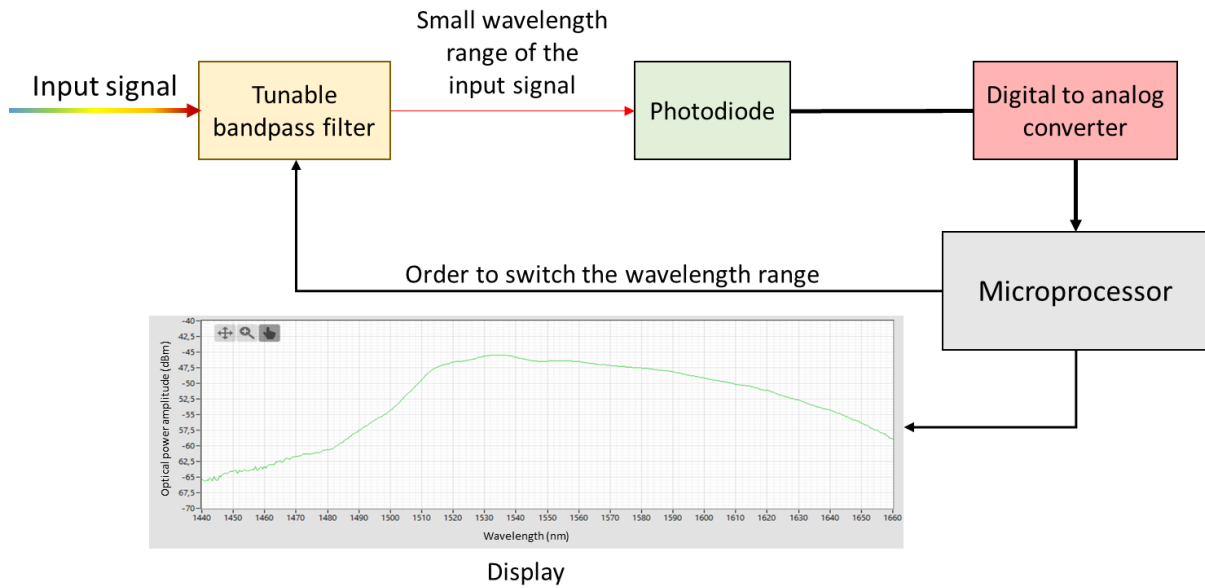


Figure 28. Scheme of a scanning optical spectrum analyzer.

- *Michelson interferometers*: This principle does not involve tunable bandpass filter and is based on Fourier transform spectroscopy. It allows to cover large bandwidths with quite high resolution. It is limited in term of dynamic range and sensitivity because of its noise properties [20].
- *Fabry-Pérot interferometers*: This principle uses the high transmittance at resonances, which can be tuned through the resonator length with a piezo transducer. This method provides the best wavelength resolution. Its fundamental limitation is its free space range, which makes this type of analyzer only suitable for high-precision applications, where a high resolution in a narrow wavelength range is required.

The performances of the OSA are based on several parameters. Its wavelength range has to be as large as possible. It must have high wavelength resolution and accuracy, as well as a high acquisition speed.

Fabry-Pérot interferometer-based OSAs can use widely external cavity tunable lasers as wavelength-tunable bandpass filters. This tunable laser source can have a RSOA as gain medium. Consequently, increasing the bandwidth of the RSOAs is a solution to overcome this OSA's fundamental limitation.

1.3. Optical Coherence Tomography, a medical application

SOAs are also useful in medical applications, like Optical Coherence Tomography (OCT). It is a non-invasive medical imaging technique that uses light waves to generate two- or three-dimensional pictures of a material. This material must be subject to optical scattering, which is the case of biological tissues. OCT is based on low-coherence interferometry and employs Near-Infrared (NIR) wavelengths, between 0.75 μm and 1.8 μm . Figure 29 details the useful wavelengths for OCT and their applications. Some of these wavelengths are the same we use in telecommunications. In this technology, SOAs are used as wide bandwidth infrared light sources.

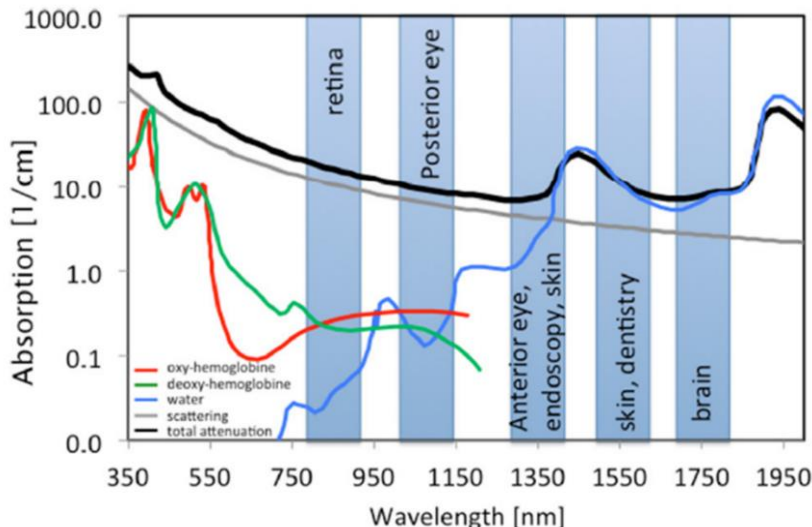


Figure 29. Spectral absorption of water and tissues chromophores together with scattering [21].

The use of the highest wavelengths of the NIR light allows a more important penetration into the scattering medium. At these wavelengths, OCT enables to capture images with micrometer-resolution. Other techniques can reach higher resolution or higher penetration but OCT combines low resolution with relatively high penetration, as detailed in Table 14.

Technic	Confocal microscopy	Optical Coherence Tomography	Ultrasound Scanning
Resolution	$\leq 1 \mu\text{m}$	1-10 μm	150 μm
Penetration	$\approx 0,2 \text{ mm}$	$\leq 2 \text{ mm}$	100 mm

Table 14. Optical medical imaging comparison in terms of resolution and penetration.

An improvement axis for OCT is the axial resolution [22, 23]. With better resolution in medical imaging, it becomes easier to identify pathologies or subtle changes in tissue structure. This characteristic depends on the spectrum width of the light source. It was exposed by Fercher, Drexler, Hitzenberger and Lasser with the Equation 1 in [24].

$$\text{Equation 1. } \delta z = \frac{2 \ln(2)}{\pi} * \frac{\lambda_m^2}{\Delta\lambda}$$

In Equation 1:

- δz , the axial resolution.
- λ_m , the mean wavelength of the light source spectrum.
- $\Delta\lambda$, the spectral bandwidth of the light source (assuming a Gaussian spectrum).

Figure 30 illustrates the bandwidth dependency on the axial resolution. To perform observations with a resolution under 10 μm , this bandwidth has to be higher than 110 nm, in the C+L-Band, and higher than 76 nm, in the O-Band. With larger bandwidth provided by SOAs, we can increase the OCT's resolution.

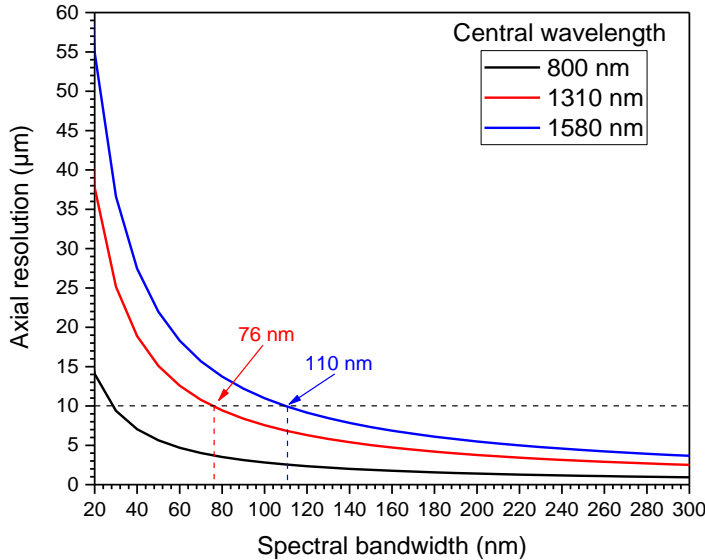


Figure 30. Relation between axial resolution and spectral bandwidth in OCT following Equation 1.

The light sources must be similar to laser diodes to have a high spatial coherence but must not exploit the lasing process to have a large and continuous optical spectrum. There are two types of OCT:

- *Time domain OCT*: It is based on the white light interferometry [25]. The typical sources for this type of OCT are Super-Luminescent Diodes (SLED), which correspond to SOAs or RSOAs without input signal [26].
- *Fourier domain OCT*: It records the frequency-dependent reflectance of the sample. This technique enables to perform higher resolution and a faster process to capture pictures [27, 28]. The light source used in Fourier domain is the wavelength-swept laser, that can be an external-cavity diode laser. In this type of laser, different gain medium can be used, as displayed in Table 15.

Gain medium	Bandwidth	Upper state lifetime	Wavelength
SOA	≈ 100 nm	380 ps to 700 ps	Depends on the energy bandgap of the gain material
Rare earth Doped Fiber Amplifier	≈ 50 nm	Erbium \rightarrow 10 ms Ytterbium \rightarrow 0,8 ms	Erbium \rightarrow 1550 nm Ytterbium \rightarrow 1060 nm [29]
Raman Amplifier	≈ 30 nm (can be easily multiplexed)	In the order of femtosecond	Depends on the pump laser wavelength

Table 15. Gain media in swept lasers and some of their characteristics.

The gain media typically used in the Fourier domain OCT swept lasers are SOAs because of their advantages on the others. They have small upper state lifetime, of only a few hundreds of picoseconds. Consequently, the laser intensity fluctuations are usually invisible for the OCT detection [30]. They offer large bandwidths of around 100 nm with a gain around 15 dB. SOA is also the most compact way to obtain a large bandwidth.

2. Optical Amplifiers

In the previous section, we understood the necessity to develop the wideband aspect of SOAs and RSOAs, in both O- and C+L-Bands. We also introduced the current technologies used for amplification. In this section, we detail and compare the operating principles of Rare-Earth Doped Fiber Amplifier (xDFA), Raman amplifiers and SOAs. We present the SOA's structure and define the notions of gain, optical bandwidth, NF, P_{sat} and polarization independency.

2.1. Rare earth doped fiber amplifiers

The transmission over long distances and multi-wavelengths operation in a single fiber was permitted in the 1990's with the invention of the EDFA. Before their development, each signal had to be converted from an optical state into an electronic one to be amplified by repeaters. Thus, EDFA simplified the amplification process by dealing only with optical signal and by enabling the simultaneous amplification of different wavelengths with a single device.

EDFA is made of an Erbium doped fiber coupled to a high power pumping laser and optical passive elements, as shown in Figure 31.

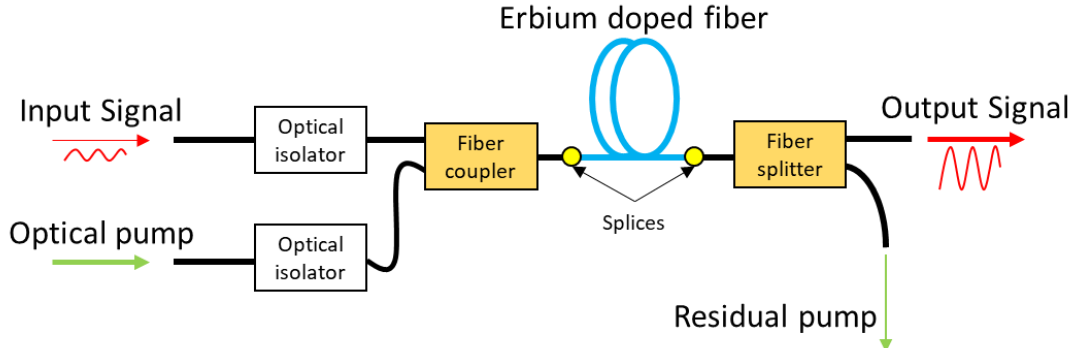


Figure 31. Erbium doped fiber amplifier [31].

The amplification medium is a fiber, made of silica and doped with Er^{3+} ions. It is coupled with optical pumps usually operating at 980 nm or 1480 nm. The amplification mechanism is displayed in Figure 32.

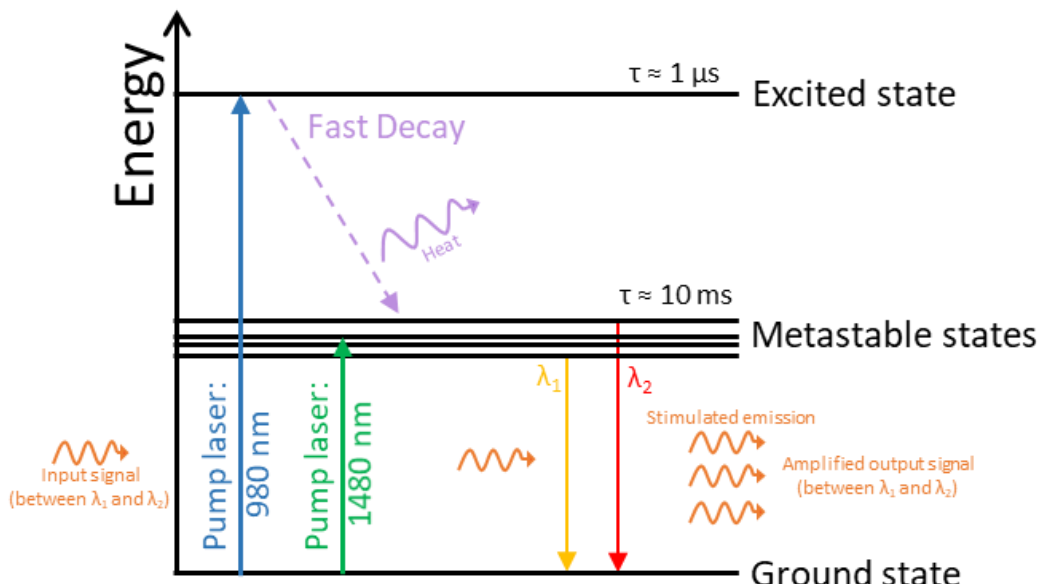


Figure 32. Amplification mechanism in EDFA.

The pump laser generates a population inversion in the doped fiber. With the 980 nm lasers, the carriers reach unstable energy levels and quickly relax by non-radiative emission (heat) to reach metastable states. The input signal generates stimulated recombination and gets amplified at the energies corresponding to the gaps between the metastable and the ground states.

EDFA can reach high gain values (> 30 dB) with low NF (< 7 dB) and a saturation power between 15 dBm and 20 dBm. The fiber's dopants enable to amplify wavelengths between 1530 nm and 1600 nm, but with a narrow optical bandwidth (< 40 nm).

To overcome this limit, different techniques are developed. (i) The silica glass of the fibers can be replaced by tellurite glass to reach bandwidths of 50 nm [32]. This material enables a larger stimulated emission cross-section to reach bandwidths of 50 nm or more [33, 34]. (ii) Multiple EDFA can be merged to reach wider bandwidths (80 to 120 nm) at the cost of bigger and more consuming devices [35, 36]. However, these features are not sufficient and optimal to be integrated in the telecommunication systems.

To reach amplification in a large wavelength range, developments led to the use of other rare earth dopants in the fibers, as displayed in Table 16.

Ions / Dopants	Main Emission wavelengths	Optical Band	References
Ytterbium (Yb^{3+})	1,0 – 1,1 μm	OCT application	[29]
Praseodymium (Pr^{3+})	1,29 – 1,32 μm	O-Band	[37, 38]
Neodymium (Nd^{3+})	1,08 μm / 1,32 – 1,35 μm	O-Band	[39, 40]
Bismuth (Bi)	1,32 – 1,36 μm	O-Band	[41, 42, 43]
Thulium (Tm^{3+})	1,45 – 1,53 μm	S-Band	[44, 45]
Erbium (Er^{3+})	1,53 – 1,60 μm	C+L-Band	[46, 47]

Table 16. Dopants used for optical fiber doped amplifiers [48].

In the C+L-Band, the EDFA are already widely deployed. In O-Band, interest is emerging to develop wide bandwidth solutions involving Bismuth Doped Fiber Amplifier (BDFA) [42].

2.2. Raman amplifiers

Raman amplification is another way to amplify an optical signal, demonstrated by Stolen and Ippen in the early 1970s [49]. It is based on stimulated Raman scattering coming from the energy exchange between the incident photon and the molecules of a solid medium. Three phenomena can occur during Raman scattering, as illustrated in Figure 33:

- *Stokes scattering*: The incident light loses energy with the creation of a phonon. The energy loss results in a red shift of the light's wavelength.
- *Anti-Stokes scattering*: The incident light absorbs the preexisting phonon and has its wavelength blue shifted.
- *Rayleigh scattering*: There is no energy exchange between the light and the medium, both the incident and diffused photons have the same energy.

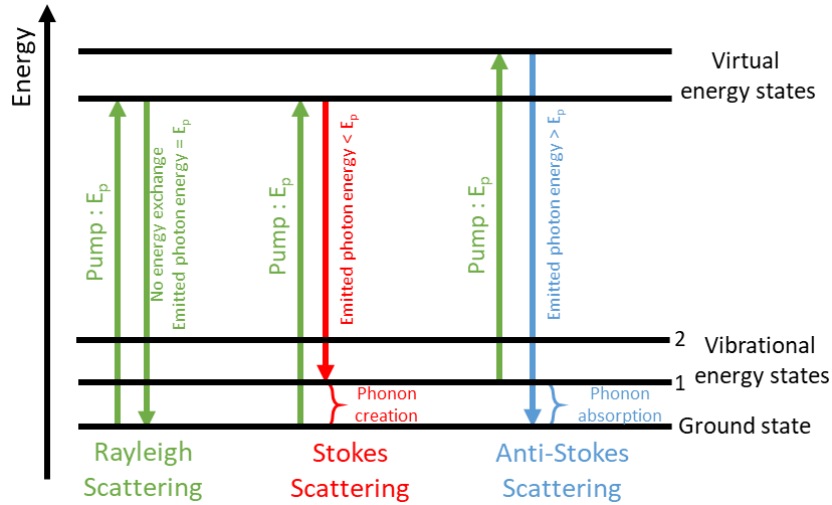


Figure 33. The different light scatterings.

The wavelength's shift depends on the medium used in the Raman amplifier, schematized in Figure 34.

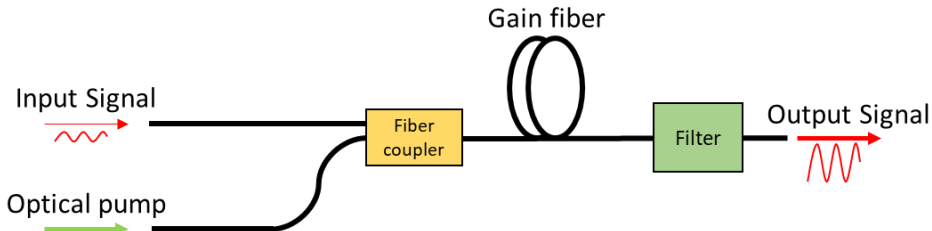


Figure 34. Raman amplifier scheme.

In Raman amplifiers, there are two signals, the one needed to be amplified and the pump's signal [50]. The wavelength used by the pump is typically few tens of nanometers shorter than the one to amplify. The pump beam is scattered by the molecules of the gain medium and its photons are lifted to virtual levels. By relaxing to vibrational states, the beam generates photons that amplify the input signal. The remaining energy that corresponds to the difference between vibrational and ground states generates a phonon. Consequently, Raman amplifiers use Stokes scattering to transfer the pump laser's power to the input signal.

Raman amplifiers can reach gains of 30 dB and NF of less than 7 dB. They are polarization independent. The use of a single pump gives bandwidth of around 40 nm. However, this value can be increased with the number of wavelengths used by pumps [51, 52, 53]. Fiber Raman Amplifiers systems have a very high energy consumption due to the high number of optical pumps and the high power required which is of the order of 1 W. Their dimensions as well as their cost are also disadvantages.

2.3. Semiconductor Optical Amplifiers and Reflective SOA Structures

At the beginning of their development, in the 1960's, the similarity between SOA and FP structures led them to be called "laser amplifiers". Their active regions were made of a GaAs homojunction [54]. Until the 1980's, gain provided by SOAs was limited by the quality of the anti-reflection coating. Developments in this field enabled to reach high gain thanks to very low reflectivity at SOAs facets [55, 56, 57]. Later, the active region was replaced with heterostructures and nowadays, InP/GaInAsP SOAs are commercially available.

Both SOA and RSOA are schematized in Figure 35 and Figure 36, respectively. SOAs have their gain medium delimited by two anti-reflection coated facets, while RSOAs have a high reflection coating at one facet.

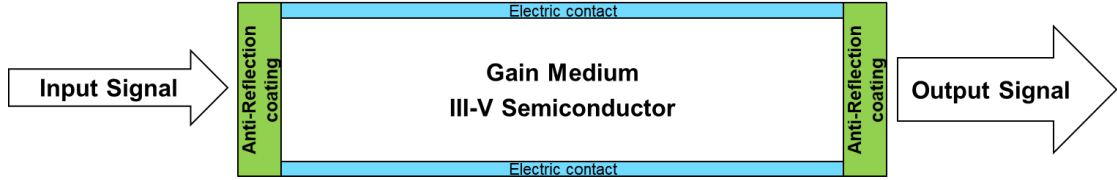


Figure 35. Semiconductor optical amplifier scheme.

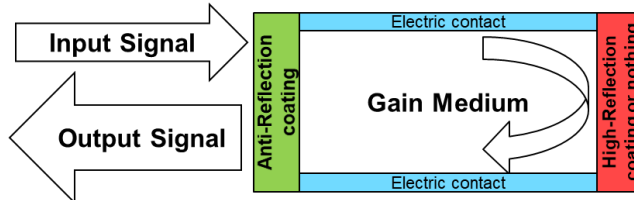


Figure 36. Reflective semiconductor optical amplifier scheme.

The antireflection coatings, at one facet or both, reduce the impact of the resonating cavity, allowing the wideband property provided by the gain medium.

2.3.1. SOA's gain medium

The SOAs' gain medium must be made of a semiconductor enabling light emission at the desired wavelengths. Figure 37 shows the energy bandgap as a function of lattice parameters, for binary compounds and their alloys.

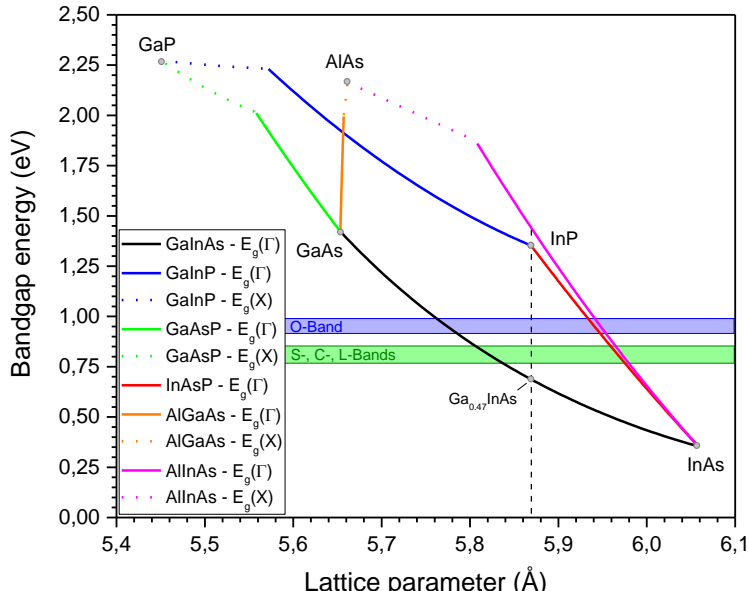


Figure 37. GaInAsP system with interest areas [58, 59].

In the telecom wavelength range, SOAs are based on Indium Phosphide (InP) alloy. In order to reach the expected wavelength, two quaternary compounds can be used, AlGaInAs and GaInAsP. A material comparison between these two alloys shows that they have different physical properties [60]. On one hand, AlGaInAs has a large conduction band offset that leads to improved electron confinement and hole density uniformity in Quantum Wells (QWs). Hence, it provides reduced current leakage and higher characteristic temperatures. On the other hand, the Al containing system is more sensitive to contamination and oxidation during the fabrication process than GaInAsP. Moreover, the refractive indices of the AlGaInAs compounds varies more with the material composition than the GaInAsP compounds. Consequently, we achieve a better control of the optical mode behavior in the GaInAsP system. For these reasons and the unavailability of Al cells during the growth campaign of our devices, the GaInAsP systems is preferred.

GaInAsP alloys grown on InP can cover the energy gaps from 0.73 eV to 1.35 eV. These energies correspond to wavelengths going from 918 to 1699 nm, covering the whole range of telecommunication networks' wavelength. Different techniques have been developed for the fabrication of these alloys: (i) MBE and (ii) MOCVD being the main epitaxy techniques that will be described in Chapter III.

GaInAsP lattice matched on InP is a direct bandgap material. The extrema of both conduction and valence bands possess the same wave vector in the Brillouin zone. The energy difference between these extrema gives the material Energy Bandgap (E_g). From this energy, we know which optical wavelength can be exhibited by the material using Equation 2.

$$\text{Equation 2. } E[\text{eV}] = \frac{h[m^2.\text{kg}.\text{s}^{-1}] * c[\text{m.s}^{-1}]}{\lambda[\mu\text{m}] * e[\text{A.s}]} \approx \frac{6,63*10^{-34}*3*10^8}{\lambda[\mu\text{m}]*10^{-6}*1,6*10^{-19}} \approx \frac{1,24}{\lambda[\mu\text{m}]} \rightarrow E_g [\text{eV}] \approx \frac{1,24}{\lambda_{\text{emitted}}[\mu\text{m}]}$$

where:

- h is Planck constant.
- c, the speed of light.
- λ , the wavelength exhibited by the material.
- e, the elementary charge.

The electric carriers injected in the material can recombine and emit photons whose energy is close to E_g . These recombinations follow two mechanisms as displayed in Figure 38:

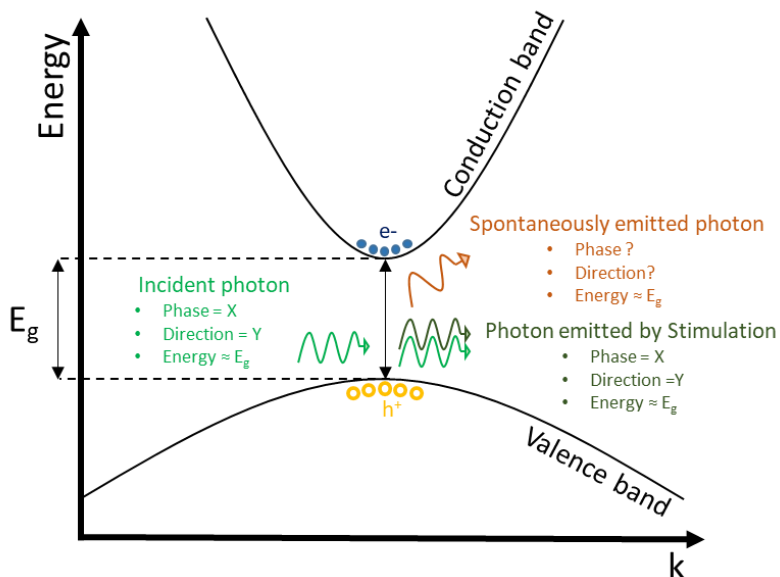


Figure 38. Spontaneous and Stimulated emissions.

- *Spontaneous emission*: This randomly appearing mechanism generates a photon with an energy close to E_g , because of the recombination of electric carriers. We cannot control its phase nor its direction.
- *Stimulated emission*: This emission happens when an incident photon with an energy close to E_g triggers the electric carrier recombination. The phase and the direction of the new photon is the same as the incident one. The stimulated emission of a spontaneously generated photon leads to Amplified Spontaneous Emission (ASE) at the device scale. The repetition of stimulated emission also leads to laser effect at the device scale.

The gain medium is sandwiched between two confinement layers that are p- and n-doped to facilitate electrons and holes free carrier injection. The gain medium, called “active” material, is remained non-intentionally doped (nid) to increase the number of recombinations. With these binary and quaternary compounds, we obtain a PiN heterostructure, as represented in Figure 39.

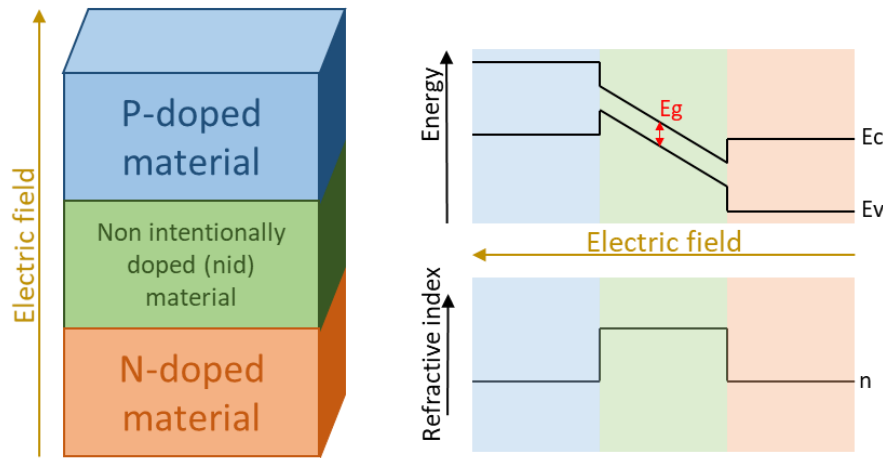


Figure 39. PiN structure, bandgaps and refractive indexes.

Heterostructures also provide optical benefits, because the confinement layers are high bandgap materials with lower refractive indices [61]. As a consequence, the active region plays the role of optical waveguide.

With the waveguide, we can introduce the optical confinement, noted Γ . This property is quantified by the ratio between the energy of the optical mode in the active region and its total energy. A visual representation of optical confinement is given in Figure 40.

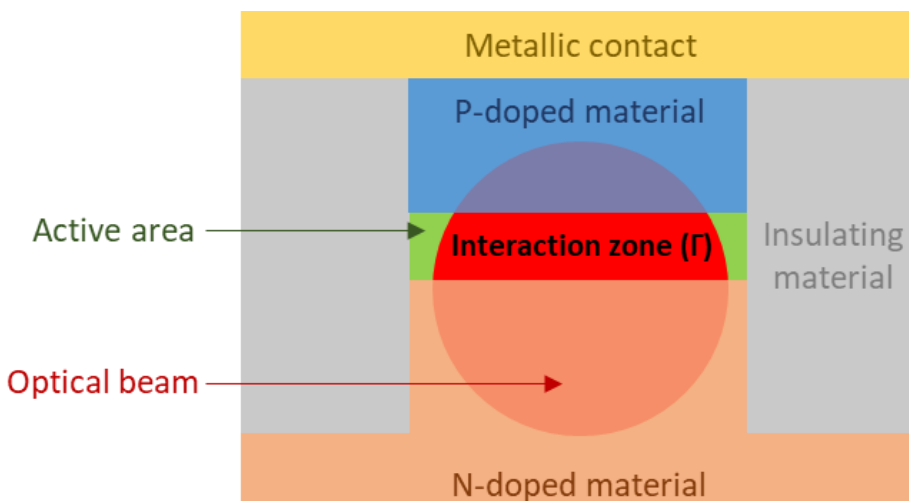


Figure 40. Overlap between optical mode and active region in the case of a buried structure.

Gain, NF and P_{sat} are depending on the optical confinement of SOA's design. These relations will be exposed in Section 2.3.2.

The active area architecture also influences the optical confinement value. The different forms of active region are displayed in Figure 41:

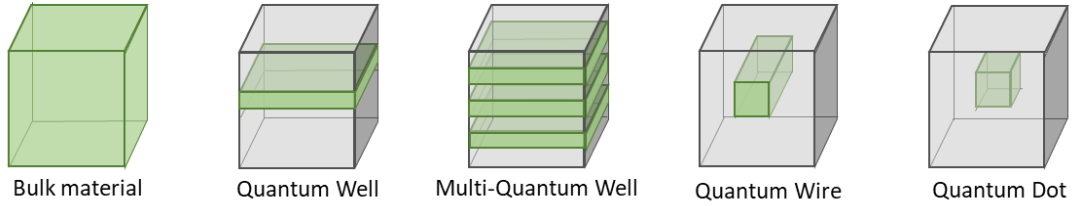


Figure 41. Bulk, Quantum Well, Multiple Quantum Wells, Quantum Wire, Quantum Dot schemes.

- *Bulk material* is thick and uniform material, made of a single alloy. It enables an important overlap between the optical mode and the active region. However, it requires high current injection to reach sufficient carrier density for amplification.
- *Quantum well* is a thin layer, a few Mono Layers (ML) thick, sandwiched between barriers of higher energy bandgap material. Active regions are usually made of MQW. In this configuration, carriers occupy discrete energy levels. It results in a better carriers' confinement, which increases the radiative recombination efficiency [62].
- *Quantum wires* deprive the carriers of one degree of freedom, enhancing the recombination efficiency.
- *Quantum Dots (QD)* deprive the carriers of their three degrees of freedom and are reduced to “0D” elements surrounded by higher energy bandgap material. All the carriers are in the same energy state, maximizing the recombination efficiency. This is the configuration requiring the lowest current injection but the overlap between the optical mode and the active region is hard to increase.

The QD-based active regions are deeply studied to improve the amplifiers performance. They exhibit discrete bound states, from the ground states to the excited states [63]. The QD can provide a wide optical emission that can reach up to 120 nm, but narrow optical bandwidths, when we consider the -3 dB bandwidth, as described in section 2.3.2.6 [64, 65]. This architecture reaches shorter gain recovery than the other SOA active region configurations [66, 67]. However, the growth of homogeneous QDs with the same size, strain, shape and composition is difficult.

We prefer the growth of MQW structures as gain medium of our devices which provides a good compromise between optical confinement and current injection. With a sufficient carrier density, the MQW can generate optical transitions at different wavelengths, resulting in a large gain bandwidth. To get the flattest gain spectrum at the output of the SOA, for high carrier densities, the energy difference between the fundamental state and the excited states has to be well-adjusted. Current injection is an important parameter for the gain flatness [68]. Its impact on the gain behavior will be detailed in Chapter II. The optical spectrum we get by combining optical transitions can be seen as cascaded amplifiers with spectra staggered from one another that are presented in section 3.2. The combination of different electron-hole transitions is the method we use in our work to obtain wide gain spectra in O- and C+L-Bands.

2.3.2. Device characteristics

Wideband SOAs have five main parameters, gain, NF, P_{sat} , polarization dependency and optical bandwidth. In this section, we define these notions as well as their relation with the optical confinement in the active region of the structure.

2.3.2.1. Gain - G

The most important parameter for SOAs is the gain, noted G, which is a quantification of the amplification provided by the device. G is defined as the ratio between the signal output power, P_{out} , and the signal input power, P_{in} , given in dB.

The gain measured from the coupling between the device and the optical fibers is the fiber to fiber gain (G_{ff}). To obtain the intrinsic gain of the device (G_{chip}), we must withdraw the coupling losses. With the hypothesis of a homogeneous carrier density, the intrinsic and fiber to fiber gains can be expressed as follows, in Equation 3 and Equation 4 [69].

$$\text{Equation 3. } G_{Chip} = \exp^{[(\Gamma g_m(n) - \alpha(n)) * L]}$$

$$\text{Equation 4. } G_{ff} = C_1 * C_2 * G_{Chip}(n)$$

These equations show the importance of the following parameters:

- Γ , the optical confinement that will be discussed in Chapter II.
- $g_m(n)$, the material gain that will be further detailed in Chapter II.
- L, the waveguide length.
- C_1 and C_2 , the input and output coupling ratio between the SOA and the optical fiber (their values are between 0 and 1). For RSOA fiber to fiber gain, C_1 and C_2 have the same value.
- $\alpha(n)$, the loss coefficient which is mainly related to Intervalence Band Absorption (IVBA) and Auger recombinations in both active region and p-doped materials [70, 71, 72].

2.3.2.2. ASE power - P_{ASE}

ASE is light, produced from the amplification provided by the device to its own spontaneous emissions. It is generated with the current injection, thus, when there is no input signal in the device, we can measure the ASE power (P_{ASE}). When generated in the SOA, it is expressed in Equation 5.

$$\text{Equation 5. } P_{ASE} = h\nu * (G_{chip} - 1) * n_{sp} * B_0$$

Where:

- $h\nu$ is the energy of amplified photon.
- B_0 is the optical bandwidth.
- $n_{sp}(n)$ is the population inversion factor.

As the ASE interacts with the input signal, it is also involved in the NF of the device.

2.3.2.3. Noise Figure - NF

The NF quantifies the noise brought to the signal by the amplifier. The nonlinear interactions between the injected signal and the ASE generate three different types of noises, the shot noise, the signal-spontaneous beat noise and the spontaneous-spontaneous beat noise [73].

The shot noise (N_{shot}) arises from the detection of the input signal and the noise from the ASE. It is given by the Equation 6.

$$\text{Equation 6. } N_{shot} = 2 * e^2 * B_e * \left(\frac{G_{chip} * P_{in}}{h\nu} + n_{sp} * B_0 * (G_{chip} - 1) \right)$$

Where:

- B_e is the electrical bandwidth of the photo-detector.

Both of the signal-spontaneous beat noise (N_{s-sp}) and the spontaneous-spontaneous beat noise (N_{sp-sp}) are produced at the same time while the ASE and the input signal coexist in the SOA. It is given by the Equation 7.

$$\text{Equation 7. } N_{s-sp} = 4 * \frac{e^2}{hv} * B_e * P_{in} * n_{sp}^2 * (G_{chip} - 1)$$

The spontaneous-spontaneous beat noise can be expressed like in Equation 8.

$$\text{Equation 8. } N_{sp-sp} = e^2 * (2 * B_0 - B_e) * B_e * n_{sp}^2 * (G_{chip} - 1)^2$$

The NF representing the amount of degradation in the signal to noise ratio caused by the amplification process, it is defined as the ratio between the optical signal to noise ratio (OSNR) of the signal at each side of the SOA. This is illustrated by Equation 9 [74] [75].

$$\text{Equation 9. } NF = \frac{SNR_{in}}{SNR_{out}}$$

In Equation 9:

- SNR_{in} and SNR_{out} correspond to the signal-to-noise ratios at each side of the SOA. It is important to note that, for RSOAs, these two values remain different, even if the input and output facets are the same.

The OSNR of the input signal is given by Equation 10. It is proportional to the power of the input signal, or more precisely, to the input number of photons per unit of time.

$$\text{Equation 10. } SNR_{in} = \frac{P_{in}}{2 * h\nu * B_e}$$

The OSNR of the output signal is defined in Equation 11.

$$\text{Equation 11. } SNR_{out} = \left(\frac{e * P_{in} * G_{chip}}{h\nu} \right)^2 * \frac{1}{N_{shot} + N_{s-sp} + N_{sp-sp}}$$

With these definitions, Equation 9 can be rewritten like in the Equation 12.

$$\text{Equation 12. } NF = \frac{1}{G_{chip}} + 2 * n_{sp} * \left(\frac{G_{chip}-1}{G_{chip}} \right) + \frac{h\nu * B_0 * n_{sp} * P_{in} * (G_{chip}-1)}{P_{out}^2} + \frac{h\nu * (2 * B_0 - B_e) * n_{sp}^2 * P_{in} * (G_{chip}-1)^2}{2 * P_{out}^2}$$

In practical case, ASE power is weak compared to the signal power, consequently, the last two terms can be neglected. Thus, the principal contribution to the NF is the signal-spontaneous emission beat noise [76]. Also, the spontaneous-spontaneous beat noise can be easily minimized with the incorporation of an optical filter at the output of the amplifier. Thus, Equation 12 can be simplified as follows in Equation 13.

$$\text{Equation 13. } NF = \frac{1}{G_{chip}} + 2 * n_{sp} * \left(\frac{G_{chip}-1}{G_{chip}} \right)$$

In this equation, $n_{sp}(n)$ decreases when absorption becomes negligible compared to stimulated emission. This means that with high carrier density, population inversion gets close to 1. Moreover, for high gain values, NF can be expressed even more simply like in Equation 14 were only population inversion have impact on it [77, 78].

$$\text{Equation 14. } NF(n) = 2 * n_{sp}$$

It allows us to set a theoretical minimum that can be reached when $n_{sp}=1$, $NF = 2$ (3 dB). In practice, this value is never reached and SOAs often have NF values between 5 and 10 dB.

2.3.2.4. Saturation output power - P_{sat}

The saturation output power, noted P_{sat} , refers to the output power for which the amplification gain is half its nominal value, G_0 , as illustrated in Figure 42.

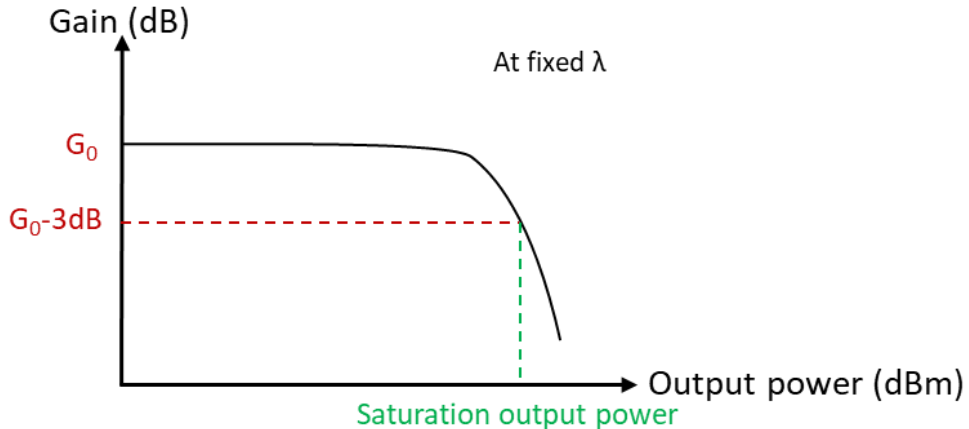


Figure 42. Saturation output power illustration.

This power saturation will vary with the temperature of the device and the carrier density. P_{sat} can be expressed as in Equation 15 [79].

$$\text{Equation 15. } P_{sat} = \ln(2) * \frac{A}{\Gamma} * \frac{hv}{a_1 \tau} * \frac{G_0}{G_0 - 2}$$

Where:

- A is the cross-section of the active area, which means the QWs' thickness multiplied by the ridge's width.
- a_1 is the differential of g_m with respect to the carrier density.
- τ corresponds to the carrier lifetime.
- G_0 is the nominal gain value at the considered carrier density.

A high P_{sat} value is desirable to extend the linear regime of SOA. This value, like gain and NF, can be tuned by varying Γ or the cross-section of active area (A).

2.3.2.5. Polarization dependency

Another parameter is the polarization dependency of the amplifier. The input signal is statistically not polarized and can be divided in two polarizations, Transverse Electric (TE) and Transverse Magnetic (TM). To be efficient, the amplifiers have to amplify both of them equally. xDFAs and Raman amplifiers are naturally polarization independent, which is not the case of SOAs. This parameter will be discussed in detail in Chapter II, with the solutions used to provide polarization independent amplification with SOAs.

2.3.2.6. Optical bandwidth

Finally, the optical bandwidth is extracted from the measurement of the device's gain as a function of the wavelength. It defines the range of wavelengths that will benefit of more than half of the maximal measured gain. Using decibel scales, it corresponds to all the wavelengths for which the gain is between its maximum and its maximum minus 3 dB, as reported in Figure 43.

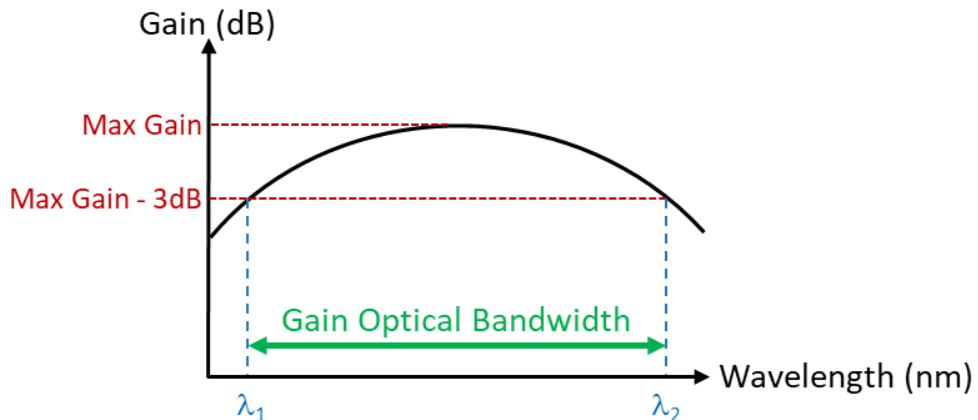


Figure 43. Gain optical bandwidth representation.

2.3.2.7. Objectives

Our objective is to develop large bandwidth SOAs, covering the C+L- for one device and the O-Band for the other device. Our devices must also exhibit high gain values to reduce the number of device in the same long distance transmission line, low NF to avoid signal distortion, and high P_{sat} to extend the linear regime of our devices. The targeted values for each parameter are given at the end of the next section. In Chapter II, we will address the polarization characteristics.

3. Wide bandwidth amplification solutions

In this section, we present current system-level solutions to provide wideband amplification with xDFA, Raman amplifiers and SOAs. These solutions can be the implementation of spectrally selective passive elements like filters or attenuators. It can also consist in systems with multiple paralleled or cascaded optical amplifiers with staggered emission spectra. We give a state of the art to compare the existing solutions and set the performances to target with our devices. Finally, we expose the previous projects led at III-V Lab on which our developments are based.

3.1. Passive elements

A first way to enlarge the devices' optical bandwidth consists in adding a filter with an adjusted optical profile to truncate the upper part of the gain spectrum, as illustrated in Figure 44. In this configuration, the attenuation spectrum of the filter must be minimal at low gain wavelengths and maximal where there is the gain peak of the amplifier.

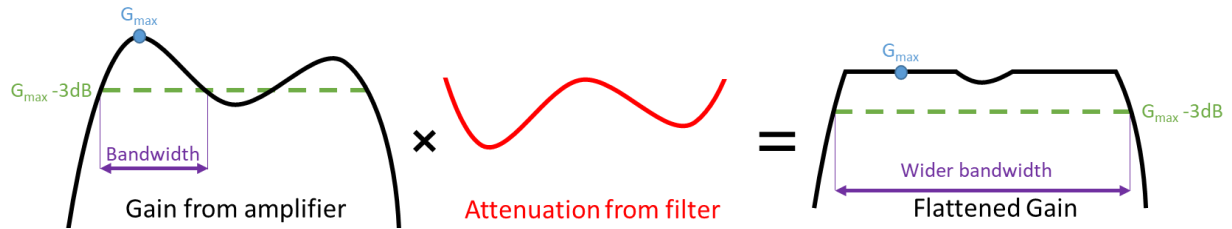


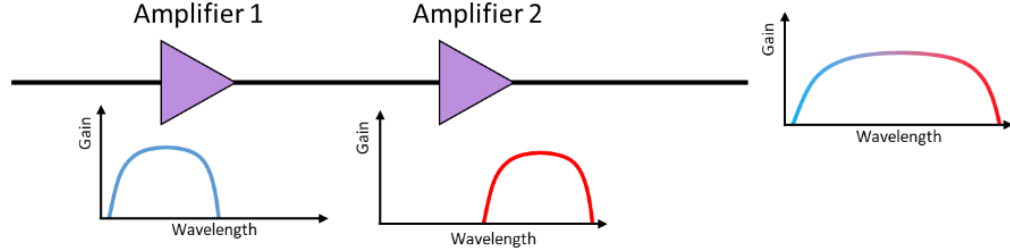
Figure 44. Illustration of Gain truncation.

A drawback of this method is that the maximal gain, like the overall gain, decreases over the bandwidth. This technique can be used for EDFA to flatten their optical bandwidths [47]. Some researchers tried to put this idea into application for SOAs without success, because of the high complexity or the bad reproducibility of the proposed options including integrated filters. For SOAs, the best solution is to couple the amplifier with other devices [79].

3.2. Multiple amplifiers

Another solution to enhance the gain bandwidth is to couple amplifiers. It is the most employed technique to enlarge amplification bandwidth of a device. Figure 45 illustrates this principle for cascaded and paralleled amplifiers.

Cascaded amplifiers:



Paralleled amplifiers:

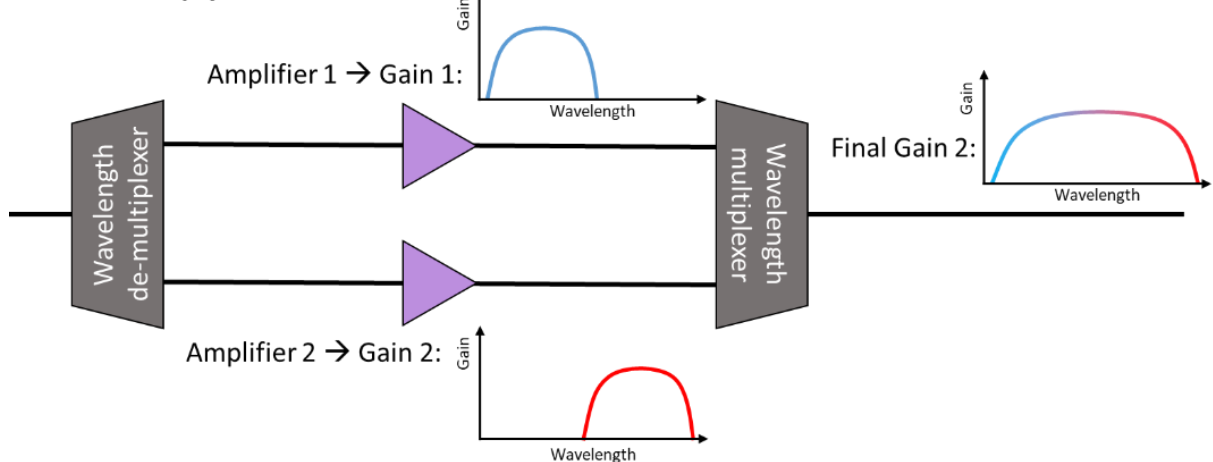


Figure 45. Bandwidth enlargement using several amplifiers.

The gain spectra must reach similar values and be offset from each other in terms of wavelength. Every combination of SOAs, EDFAs and Raman amplifiers can be achieved to create an hybrid amplifier [79, 80, 81]. One made of a SOA cascaded with a Raman amplifier is displayed in Figure 46.

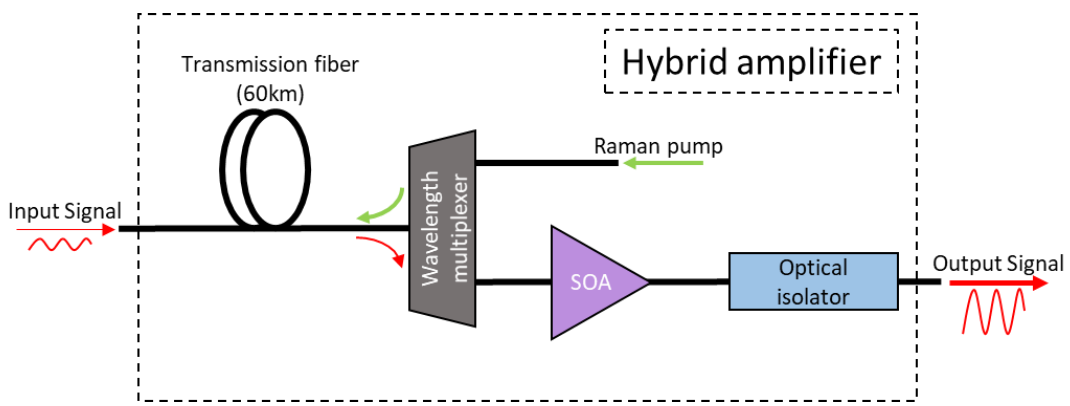


Figure 46. Scheme of a SOA-Raman hybrid amplifier [82].

It is composed of a Raman pump, a fiber coupler, an optical isolator, and the SOA which is the main amplifier. Its gain profile is extended by the Raman amplifier which compensates the gain losses at one side of the SOA's gain spectrum. In reference [83], this compensation occurs at the higher wavelengths. It enables to enlarge the bandwidth of around 40 nm, obtained from a narrow-bandwidth SOA, up to 70 nm. This type of amplifier could be used in Metro or Access networks [84].

For hybrid EDFA-Raman amplifiers illustrated in Figure 47, the configuration includes an EDFA, a Raman amplifier and a gain equalizer to enhance the gain flatness.

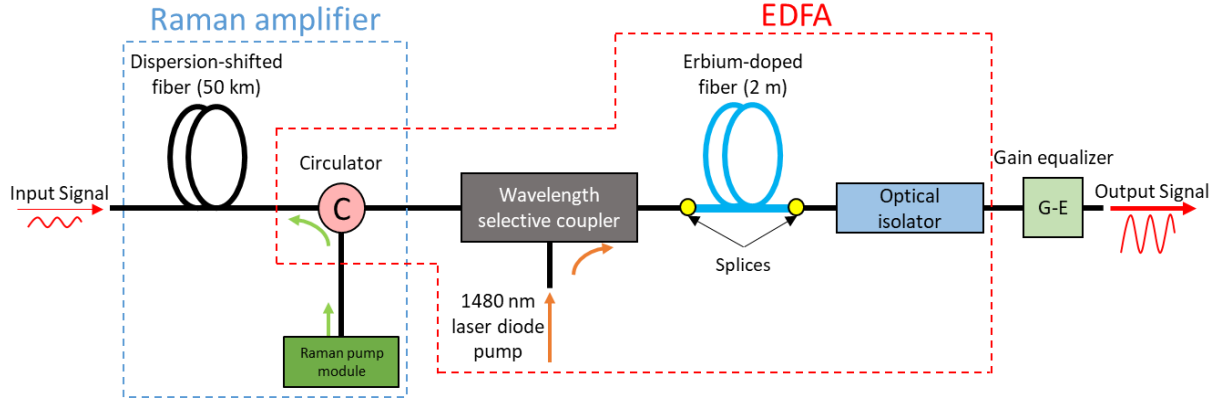


Figure 47. Example of hybrid EDFA-Raman amplifier architecture [85].

More complex configurations exist including an EDFA and two Raman amplifier units to provide multi-wavelength pumping [86]. In this configuration, the Raman amplifiers are also used to enlarge the EDFA's optical bandwidth from 30 nm to 80 nm. Some power consumption models are studied to integrate hybrid amplifiers in long-haul transmission systems [87].

Raman amplifiers can be pumped with several modules with different wavelengths. The architecture of this type of amplifier is displayed in Figure 48. It allows to generate several Raman gain spectra staggered from each other. The addition of these optical spectra can provide a wide bandwidth gain spectrum [52]. This technique requires many pump sources to provide a bandwidth of 100 nm, and this is a drawback in terms of device's consumption and compactness.

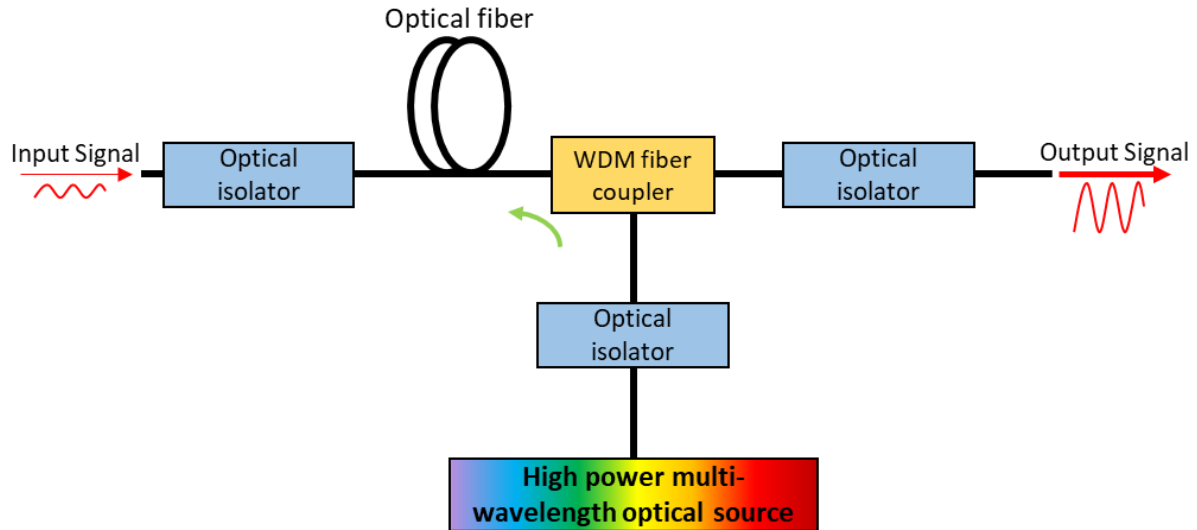


Figure 48. Raman amplifier using multi-wavelength pumps [81].

The multi-pumps Raman amplifier can be seen as a paralleled amplifier made of several single pump Raman amplifiers.

Similar configurations exist for xDFAs. Figure 49 shows the architecture of such an amplifier. Each amplifier has to provide gain in its well-defined bandwidth, and the addition of the signals enables to achieve large bandwidth amplification.

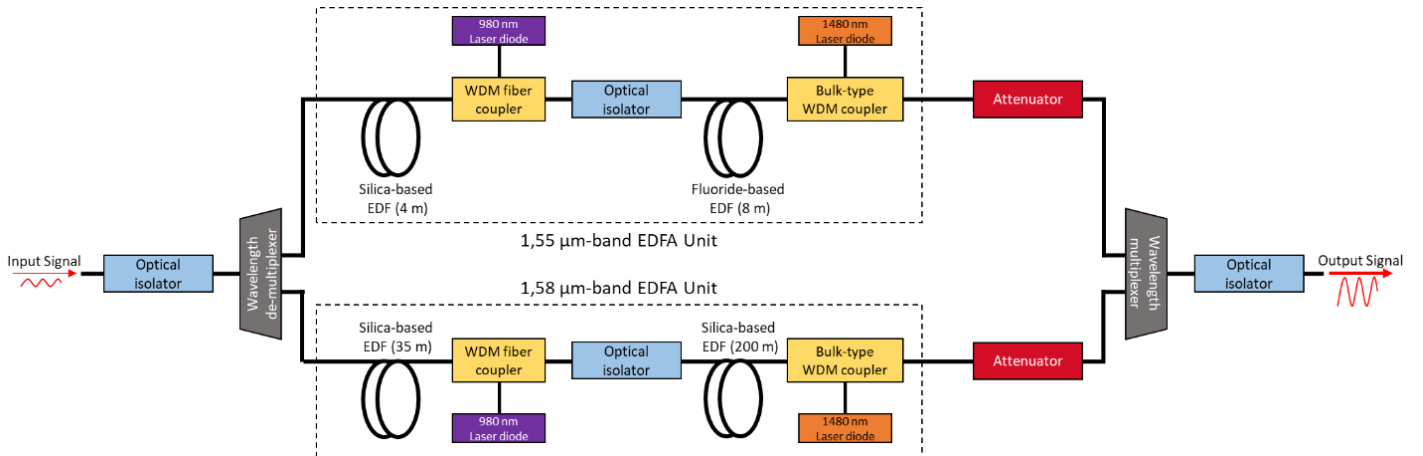


Figure 49. Paralleled EDFA architecture [80].

The use of several active devices to reach wideband amplification always faces consumption and compactness issues, giving SOAs an important argument for further developments.

3.3. Optical amplifiers state of the art

Figure 50 displays the performances of the different types of optical amplifiers taken from the literature. The presented performances are the maximum of gain and P_{sat} and the minimum of NF reached in the widest optical bandwidth.

For the O-Band amplification, three devices can be commented.

- The PDFA-SOA hybrid amplifier presents amplification, in the O-Band, from 1270 nm to 1360 nm. The main issue of this amplifier is its hybrid nature which is not compact and involves high energy consumption and high cost.
- The BDFA-based amplifiers cover less than the half of the O-Band. For the widest bandwidth device, the highlighted optical bandwidth does not take into account the -3 dB variation we presented in the section 2.3.2.6. It is not a valid solution for wideband amplification in the O-Band.
- The mentioned MQW based solution uses AlGaInAs compound and focused on the thermal aspect of the device instead of its wideband properties. Its optimal bandwidth is reached when operating at 75°C. It covers 40 nm of the O-Band, from 1270 nm to 1310 nm.

Consequently, for the O-Band, we want to develop a GaInAsP MQW-based SOA, providing an optical bandwidth of 100 nm, from 1260 nm to 1360 nm. The gain should be around 20 dB with a NF of less than 8 dB and a P_{sat} of more than 10 dBm. It would be the first time realization of GaInAsP MQW-based wideband SOA in this wavelength range.

In the C+L-Band, the situation is completely different. Figure 50 shows that wideband over more than 100 nm was already achieved with GaInAsP MQW-based SOAs. In this context, our work is to extend even more this bandwidth but also to enhance the devices' performances in terms of gain. We must provide flat gain of more than 20 dB, with NF of less than 8 dB and P_{sat} of more than 10 dBm.

This thesis follows previous developments made at III-V Lab. We describe them briefly in the next section and comment the key targets that are aimed at in the C+L-Band [79].

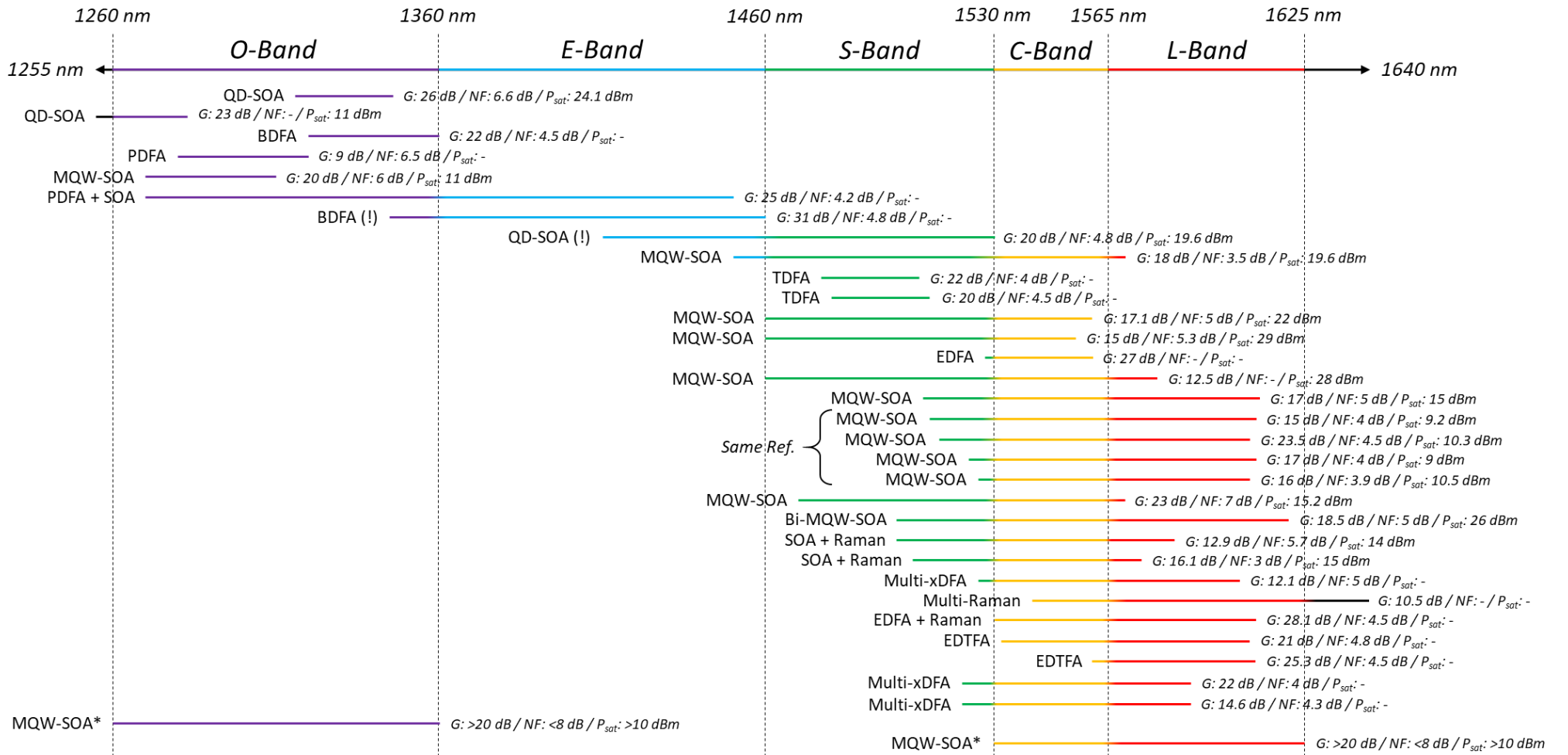


Figure 50. Optical amplifiers state of the art [88, 89, 41, 37, 90, 91, 92, 65, 68, 45] [44, 93, 94, 47, 95, 96, 79, 97, 98, 82] [83, 99, 53, 86, 34, 33, 100, 101].

3.4. Previous projects

During the past decade, four projects on wideband SOAs have been led at III-V Lab:

- ANR AROME, 2008-2010, (for : Amplificateur à semi-conducteur optique pour les Réseaux Optiques Métropolitains et Accès). This project was carried out in collaboration with the LPCNO (Laboratoire de Physique Chimie des Nano-Objets), Orange Labs, the LPN (Laboratoire de Photonique et de Nanostructures), the IEMN (Institut d'Electronique, de Microélectronique et Nanotechnologie) and the LTCI (Laboratoire de Traitement et Communication de l'Information). The AROME project proposed to produce, from design to fabrication, an SOA for 10 Gbit/s for in-line amplification in a coarse WDM network of 8 channels 20 nm apart. The targeted bandwidth was 150 nm with a maximal gain of 15 dB and a polarization dependency of less than 2 dB across the band. Additionally, the device should have a maximum NF of 9 dB and a P_{sat} of 10 mW.
- ANR UltraWIDE, 2010-2013 (Amplificateur intégré ultra-large-bande pour systèmes optiques WDM améliorés) was a collaboration between the III-V Lab, Alcatel-Lucent Bell Labs France, Kylia, Télécom SudParis, SUPELEC and ENIB (Ecole Nationale d'Ingénieurs de Brest). The aim of Ultrawide project was to improve the total capacity of WDM systems by increasing the amplified optical bandwidth. At that time, WDM communication systems used EDFAs with typical bandwidth of 32 nm. With this project, these amplifiers would be replaced by a 100 nm bandwidth device. This device, made of 2 high performance SOAs, would enable to reach over 20 dB for the gain, output power of around 25 dBm and NF of less than 7 dB.
- FUI CALIPSO, 2014-2017 (for, high CApacity ultra Large systems based on Integrated Powerful Semiconductor Optical amplifier). The III-V Lab participated in this project in collaboration with Nokia Bell Labs France, Kylia, Télécom SudParis and Egide. The objective was to obtain a SOA with a gain higher than 20 dB, output power of around 25 dBm and NF of less than 7,5 dB.
- FUI ABSOLU2, 2018-2021. The collaboration, for this project included the III-V Lab, APEX Technologies and the LPCNO. The aim of this project was to develop widely tunable lasers with an as-large-as-possible bandwidth in the C+L-band in priority, and optionally, in O-Band. These widely tunable lasers would be based on a RSOA to produce the gain spectrum over the wide bandwidth. These RSOA would have to reach a bandwidth wider than 100 nm, more than 15 dB of gain, and output power of more than 50 mW.

Since the AROME project, many ideas to reach wideband amplification were tested but only one was pursued in the following projects. This idea was to use large QWs with two electron bound states in order to provide stimulated emission for a larger number of transitions [79]. In this thesis, we pursue the idea of confining several carrier levels in the MQW. Our target is to enlarge the bandwidth, in the C+L-Band, and to apply this idea to the O-Band.

Consequently, for both of the studied bands, the targeted performances are summarized in Table 17, for the main parameters.

<i>Optical Band</i>	<i>Optical bandwidth</i>	<i>Gain</i>	<i>NF</i>	<i>P_{sat}</i>
C+L (1530 – 1625 nm)	> 100 nm	> 20 dB	< 8 dB	> 10 dBm
O (1260 – 1360 nm)	100 nm	20 dB	< 8 dB	> 10 dBm

Table 17. Targeted performances for the SOAs.

4. Conclusion

In the first section of this chapter, we explored the different applications in which wideband SOAs and RSOAs are required. These applications were telecommunications in both O and C+L-Bands, but also spectral measurement required in many domains and OCT, a medical application.

Then, we exposed the currently used amplifiers, xDFAs, Raman amplifiers and SOAs, giving their strengths and weaknesses. By focusing on the SOAs, we detailed their active region made of GaInAsP-based MQW in this work. We also defined the notions of gain, ASE power, NF, P_{sat} , polarization independency and optical bandwidth.

In the last section, we presented the different solutions involved in wideband amplification to compare them with wideband SOAs. We provided a state of the art to set the targets of our devices in terms of performances. We target to reach a bandwidth of 100 nm, with gain values of 20 dB or more, NF lower than 8 dB and P_{sat} of more than 10 dBm, in both wavelength ranges. Finally, we listed the previous projects led at III-V Lab that guided us to the development of thick QWs to achieve the wideband amplification by confining two electron levels in the MQW.

In the next chapter, we detail the conception steps required to design wideband SOA structures.

Bibliography

- [1] A. Sumits, "The history and future of internet traffic," Cisco, 28 August 2015. [Online]. Available: <https://blogs.cisco.com/sp/the-history-and-future-of-internet-traffic>. [Accessed 24 November 2022].
- [2] IEA, "Global trends in internet traffic, data centres workloads and data centre energy use, 2010-2020, IEA, Paris," IEA, 26 October 2022. [Online]. Available: <https://www.iea.org/data-and-statistics/charts/global-trends-in-internet-traffic-data-centres-workloads-and-data-centre-energy-use-2010-2020>. [Accessed 24 November 2022].
- [3] F. J. Effenberger, J.-i. Kani and Y. Maeda, "Standardization trends and prospective views on the next generation of broadband optical access systems," *IEEE Journal on selected areas in communications*, vol. 20, no. 6, pp. 773-780, 2010.
- [4] B. Clesca, "How low can fiber go?," OpticalCloudInfra, 17 April 2017. [Online]. Available: <http://opticalcloudinfra.com/index.php/2017/04/17/low-can-fiber-loss-go/>. [Accessed 24 November 2022].
- [5] K. Tsujikawa, K. Tajima and M. Ohashi, "Rayleigh scattering reduction method for silica-based optical fiber," *Journal of lightwave technology*, vol. 18, no. 11, pp. 1528-1532, 2000.
- [6] Z. Wang, H. Wu, X. Hu, N. Zhao, Q. Mo and G. Li, "Rayleigh scattering in few-mode optical fibers," *Scientific reports*, vol. 6, no. 35844, pp. 1-8, 2016.
- [7] Y. Chigusa, Y. Yamamoto, T. Yokokawa, T. Sasaki, T. Taru, M. Hirano, M. Kakui, M. Onishi and E. Sasaoka, "Low-loss pure-silica-core fibers and their possible impact on transmission systems," *Journal of lightwave technology*, vol. 23, no. 11, pp. 3541-3550, 2005.
- [8] Y. Tamura, H. Sakuma, K. Morita, M. Suzuki, Y. Yamamoto, K. Shimada, Y. Honma, K. Sohma, T. Fujii and T. Hasegawa, "Lowest-ever 0.1419-dB/km loss optical fiber," in *OFC*, San Diago, CA, USA, 2017.
- [9] ITU-T, "G.652 - Characteristics of a single-mode fibre and cable," 11/2016.
- [10] R. Ramaswami, K. N. Sivarajan and G. H. Sasaki, "Chapter 2 - Propagation of signals in optical fiber," in *Optical Networks* , Morgan Kaufmann, 2010, pp. 47-112.
- [11] M.-J. Li and D. A. Nolan, "Optical transmission fiber design evolution," *Journal of lightwave technology*, vol. 26, no. 9, pp. 1079-1092, 2008.
- [12] L. Marazzi, A. Boletti, P. Parolari, A. Gatto, R. Brenot and M. Martinelli, "Relative intensity noise suppression in reflective SOAs," *Optics communications*, vol. 318, pp. 189-188, 2014.
- [13] S.-J. Park, Y.-B. Choi, J.-M. Oh, S.-G. Koo and D. Lee, "An evolution scenario of a broadband access network using R-SOA-based WDM-PON technologies," *Journal of lightwave technology*, vol. 25, no. 11, pp. 3479-3487, 2007.
- [14] N. N. Cikan and M. Aksoy, "A review of self-seeded RSOA based on WDM PON," *Canadian journal of electrical and computer engineering*, vol. 42, no. 1, 2019.

- [15] T. Motaweh, *Modélisation et validation expérimentale de nouvelles structures SOA large bande et de techniques d'élargissement de la bande passante optique* (PhD thesis), Brest, France: Université de Bretagne occidentale, 2014.
- [16] B. J. Puttnam, G. Rademacher and R. S. Luís, "Space-division multiplexing for optical fiber communications," *Optica*, vol. 8, no. 9, pp. 1186-1203, 2021.
- [17] H. Yuan, M. Furdek, A. Muhammad, A. Saljoghei, L. Wosinska and G. Zervas, "Space-division multiplexing in data center networks: on multi-core fiber solutions and crosstalk-suppressed resource allocation," *J. opt. commun. netw.*, vol. 10, no. 4, pp. 272-288, 2018.
- [18] D. Soma, Y. Wakayama, S. Beppu, S. Sumita, T. Tsuritani, T. Hayashi, T. Nagashima, M. Suzuki, M. Yoshida, K. Kasai, M. Nakazawa, H. Takahashi, K. Igarashi, I. Morita and M. Suzuki, "10.16-peta-B/s dense SDM/WDM transmission over 6-mode 19-core fiber across the C+L band," *Journal of lightwave technology*, vol. 36, no. 6, pp. 1362-1368, 2018.
- [19] G. Rademacher, B. J. Puttnam, R. S. Luís, J. Sakaguchi, W. Klaus, T. A. Eriksson, Y. Awaji, T. Hayashi, T. Nagashima, T. Nakanishi, T. Taru, T. Takahata, T. Kobayashi, H. Furukawa and N. Wada, "10.66 peta-bit/s transmission over a 38-core-three-mode fiber," in *OFC*, San Diego, CA, USA, 2020.
- [20] R. Paschotta, "Optical Spectrum analyzers," RP photonics, [Online]. Available: https://www.rp-photonics.com/optical_spectrum_analyzers.html. [Accessed 04 January 2023].
- [21] R. A. Leitgeb and B. Baumann, "Multimodal optical medical imaging concepts based on optical coherence tomography," *Frontiers in physics*, vol. 6, no. 114, 2018.
- [22] Y. Xu, B. M. Williams, B. Al-Bander, Z. Yan, Y.-c. Shen and Y. Zheng, "Improving the resolution of retinal OCT with deep learning," in *Medical Image Understanding and Analysis*, 2018.
- [23] K. Bizheva, B. Tan, B. MacLelan, O. Kralj, M. Hajialamdar, D. Hileeto and L. Sorbara, "Sub-micrometer axial resolution OCT for in-vivo imaging of the cellular structure of healthy and keratoconic human corneas," *Biomedical optics express*, vol. 8, no. 2, pp. 800-812, 2017.
- [24] A. F. Fercher, W. Drexler, C. K. Hitzenberger and T. Lasser, "Optical coherence tomography - principles and applications," *Reports on progress in physics*, no. 66, pp. 239-303, 2003.
- [25] R. Paschotta, "Optical coherence tomography," rp-photonics, [Online]. Available: https://www.rp-photonics.com/optical_coherence_tomography.html. [Accessed 28 November 2022].
- [26] A. Kafar, S. Stanczyk, D. Schiavon, T. Suski and P. Perlin, "Review on optimization and current status of (Al,In)GaN superluminescent diodes," *ECS journal of solid state science and technology*, vol. 9, no. 015010, 2020.
- [27] R. Leitgeb, C. K. Hitzenberger and A. F. Fercher, "Performance of fourier domain vs. time domain optical coherence tomography," *Optical express*, vol. 11, no. 8, pp. 889-894, 2003.
- [28] W. Gao and X. Wu, "Differences between time domain and Fourier domain optical coherence tomography in imaging tissues," *Journal of microscopy*, vol. 268, no. 2, pp. 119-128, 2017.

- [29] R. Paschotta, J. Nilsson, A. C. Tropper and D. C. Hanna, "Ytterbium-doped fiber amplifiers," *IEEE journal of quantum electronics*, vol. 33, no. 7, pp. 1049-1056, 1997.
- [30] T. Klein and R. Huber, "High-speed OCT light sources and systems [invited]," *Biomedical optics express*, vol. 8, no. 2, pp. 828-859, 2017.
- [31] D. Rajan, "Analysis of 8 channel WDM network with EDFA," *International journal of scientific & engineering research*, vol. 7, no. 12, pp. 1446-1449, 2016.
- [32] T. Sakamoto, A. Mori, H. Masuda and H. Ono, "Wideband rare-earth-doped fiber amplification technologies - Gain bandwidth expansion in the C and L bands," *NTT technical review*, vol. 2, no. 12, pp. 38-43, 2004.
- [33] A. Mori, T. Sakamoto, K. Kobayashi, K. Shikano, K. Oikawa, K. Hoshino, T. Kanamori, Y. Ohishi and M. Shimizu, "1.58- μ m broad-band erbium-doped tellurite fiber amplifier," *Journal of lightwave technology*, vol. 20, no. 5, pp. 822-827, 2002.
- [34] M. Yamada, A. Mori, K. Kobayashi, H. Ono, T. Kanamori, K. Oikawa, Y. Nishida and Y. Ohishi, "Gain-flattened tellurite-based EDFA with a flat amplification bandwidth of 76 nm," *Photonics technology letters*, vol. 10, no. 9, pp. 1244-1246, 1998.
- [35] B. Min, H. Yoon, W. J. Lee and N. Park, "Coupled structure for wide-band EDFA with gain and noise figure improvements from C to L-band ASE injection," *IEEE photonics technology letters*, vol. 12, no. 5, pp. 480-482, 2000.
- [36] C.-H. Yeh, C.-C. Lee and S. Chi, "120-nm bandwidth erbium-doped fiber amplifier in parallel configuration," *IEEE photonics technology letters*, vol. 16, no. 7, pp. 1637-1639, 2004.
- [37] Y. Nishida, M. Yamada, T. Kanamori, K. Kobayashi, J. Temmyo, S. Sudo and Y. Ohishi, "Development of an efficient praseodymium-doped fiber amplifier," *IEEE journal of quantum electronics*, vol. 34, no. 8, pp. 1332-1339, 1998.
- [38] J. Mirza, S. Ghafoor, N. Habib, F. Kanwai and K. K. Qureshi, "Performance evaluation of praseodymium doped fiber amplifiers," *Optical review*, vol. 28, pp. 611-618, 2021.
- [39] A. Mori, Y. Ohishi, T. Kanamori and S. Sudo, "Optical amplification with neodymium-doped chalcogenide glass fiber," *Applied physics letters*, vol. 70, no. 10, pp. 1230-1232, 1997.
- [40] B. N. Samson, P. A. Tick and N. F. Borrelli, "Efficient neodymium-doped glass-ceramic fiber laser and amplifier," *Optics letters*, vol. 26, no. 3, pp. 145-147, 2001.
- [41] N. K. Thipparapu, A. A. Umnikov, P. Barua and J. K. Sahu, "Bi-doped fiber amplifier with a flat gain of 25 dB operating in the wavelength band 1320-1360 nm," *Optics letters*, vol. 41, no. 7, pp. 1518-1521, 2016.
- [42] V. Mikhailov, M. A. Melkumov, D. Inniss, A. M. Khegai, K. E. Riumkin, S. V. Firstov, F. V. Afanasiev, M. F. Yan, Y. Sun, J. Luo, G. S. Puc, S. D. Shenk, R. S. Windeler, P. S. Westbrook, R. L. Lingle, E. M. Dianov and D. J. DiGiovanni, "Simple broadband bismuth doped fiber amplifier (BDFA) to extend O-band transmission reach and capacity," in *OFC*, San Diego, CA, USA, 2019.

- [43] Y. Wang, N. K. Thipparapu, D. J. Richardson and J. K. Sahu, "Broadband bismuth-doped fiber amplifier with a record 115-nm bandwidth in the O and E bands," in *OFC*, San Diego, CA, USA, 2020.
- [44] T. Kasamatsu, Y. Yano and T. Ono, "Laser-diode-pumped highly efficient gain-shifted thulium-doped fiber amplifier operating in the 1480-1510-nm band," *IEEE photonics technology letters*, vol. 13, no. 5, pp. 433-435, 2001.
- [45] S. Aozasa, H. Masuda and M. Shimizu, "S-band thulium-doped fiber amplifier employing high thulium concentration doping technique," *Journal of lightwave technology*, vol. 24, no. 10, pp. 3842-3848, 2006.
- [46] W. J. Miniscalco, "Erbium-doped glasses for fiber amplifiers at 1500 nm," *Journal of lightwave technology*, vol. 9, no. 2, pp. 234-250, 1991.
- [47] M. Tachibana, R. I. Laming, P. R. Morkel and D. N. Payne, "Erbium-doped fiber amplifier with flattened gain spectrum," *IEEE photonics technology letters*, vol. 3, no. 2, pp. 118-120, 1991.
- [48] R. Paschotta, "Rare-earth-doped fibers," Rp-photonics, [Online]. Available: https://www.rp-photonics.com/rare_earth_doped_fibers.html. [Accessed 29 November 2022].
- [49] R. H. Stolen and E. P. Ippen, "Raman gain in glass optical waveguide," *Applied physics letters*, vol. 22, no. 276, pp. 276-278, 1973.
- [50] M. N. Islam, "Raman amplifiers for telecommunications," *IEEE journal of selected topics in quantum electronics*, vol. 8, no. 3, pp. 548-559, 2002.
- [51] H. Kidorf, K. Rottwitt, M. Nissov, M. Ma and E. Rabarijaona, "Pump interactions in 100-nm bandwidth raman amplifier," *IEEE photonics technology letters*, vol. 11, no. 5, pp. 530-532, 1999.
- [52] Y. Emori and S. Namiki, "100nm bandwidth flat gain raman amplifiers pumped and gain-equalized by 12-wavelength-channel WDM high power laser diode," in *OFC*, San Diego, CA, USA, 1999.
- [53] T. Naito, T. Tanaka, K. Torii, N. Shimojoh, H. Nakamoto and M. Suyama, "A broadband distributed raman amplifier for bandwidths beyond 100 nm," in *OFC*, Anaheim, CA, USA, 2002.
- [54] W. F. Kosonocky and R. H. Cornely, "GaAs laser amplifiers," *IEEE Journal of quantum electronics*, Vols. QE-4, no. 4, pp. 125-131, 1967.
- [55] G. Eisenstein and L. W. Stulz, "High quality antireflection coatings on laser facets but sputtered silicon nitride," *Applied optics*, vol. 23, no. 1, pp. 161-164, 1984.
- [56] G. Eisentstein, L. W. Stulz and L. G. Van Uitert, "Antireflection coatings on semiconductor laser facets using sputtered lead silicate glass," *Journal of lightwave technology*, Vols. LT-4, no. 9, pp. 1373-1375, 1986.
- [57] N.-N. Feng, G.-R. Zhou and W.-P. Huang, "Space mapping technique for design optimization of antireflection coatings in photonic devices," *Journal of lightwave technology*, vol. 21, no. 1, pp. 281-285, 2003.

- [58] R. E. Nahory, M. A. Pollack, W. D. J. Johnston and R. L. Barns, "Band gap versus composition and demonstration of Vergard's law for In_{1-x}GaxAsyP_{1-y} lattice matched to InP," *Applied physics letters*, vol. 33, no. 7, pp. 659-661, 1978.
- [59] I. Vurgaftman, J. R. Meyer and L. R. Ram-Mohan, "Band parameters for III-V compound semiconductors and their alloys," *Applied physics review*, vol. 89, no. 11, pp. 5815-5875, 2001.
- [60] H. Hillmer and S. Marcinkevičius, "Ultrafast modulation of 1.55-μm QW laser structures: optically detected carrier dynamics, limiting mechanisms, and applications," in *ICONO '98: Fundamental Aspects of Laser-Matter Interaction and New Nonlinear Optical Materials and Physics of Low-Dimensional Structures*, Moscow, RUSSIA, 1998.
- [61] P. Hervé and L. K. J. Vandamme, "General relation between refractive index and energy gap in semiconductors," *Infrared Phys. Technol.*, vol. 35, no. 4, pp. 609-615, 1994.
- [62] S. W. Corzine, R.-H. Yan and L. A. Coldren, "Chapter 1 - Optical gain in III-V bulk and quantum well semiconductor," in *Quantum well lasers*, P. S. J. Zory, Ed., 1993, pp. 17-96.
- [63] M. Sugawara, H. Ebe, N. Hatori, M. Ishida, Y. Arakawa, T. Akiyama, K. Otsubo and Y. Nakata, "Theory of signal amplification and processing by quantum-dot semiconductor optical amplifiers," *Physical review B*, vol. 69, no. 235332, pp. 1-39, 2004.
- [64] L. H. Li, M. Rossetti, A. Fiore, L. Occhi and C. Velez, "Wide emission spectrum from superluminescent diodes with chirped quantum dot multilayers," *Electronics letters*, vol. 41, no. 1, pp. 41-43, 2005.
- [65] T. Akiyama, M. Ekawa, M. Sugawara, K. Kawaguchi, H. Sudo, A. Kuramata, H. Ebe and Y. Arakawa, "An ultrawide-band semiconductor optical amplifier having an extremely high penalty-free output power of 23 dBm achieved with quantum dots," *IEEE photonics technology letters*, vol. 17, no. 8, pp. 1614-1616, 2005.
- [66] P. Borri, S. Schneider, W. Langbein and D. Bimberg, "Ultrafast carrier dynamics in InGaAs quantum dot materials and devices," *Journal of optics A: pure and applied optics*, vol. 8, no. S33, pp. 33-46, 2006.
- [67] S. Dommers, V. V. Temnov, U. Woggon, J. Gomis, J. Martinez-Pastor, M. Laemmlin and D. Bimberg, "Complete ground state gain recovery after ultrashort double pulses in quantum dot based semiconductor optical amplifier," *Applied physics letters*, vol. 90, no. 033508, pp. 1-3, 2007.
- [68] K. Morito, S. Tanaka, S. Tomabechi and A. Kuramata, "A broad-band MQW semiconductor optical amplifier with high saturation output power and low noise figure," *IEEE photonics technology letters*, vol. 17, no. 5, pp. 974-976, 2005.
- [69] G. P. Agrawal and N. K. Dutta, *Semiconductor Lasers*, Springer, 1993.
- [70] E. P. O'Reilly and A. Ghiti, "Chapter 7 - Valence band engineering in quantum well lasers," in *Quantum well lasers*, P. S. Zory Jr., 1993, pp. 329-363.
- [71] M. Asada, A. Kameyama and Y. Suematsu, "Gain and intervalence band absorption in quantum-well lasers," *IEEE journal of quantum electronics*, Vols. QE-20, no. 7, pp. 745-753, 1984.

- [72] A. Haug, "Auger recombination in direct-gap semiconductors: band-structure effects," *Journal of physics C: solid state physics*, vol. 16, no. 21, pp. 4159-4172, 1983.
- [73] Y. Said, H. Rezig and A. Bouallegue, "Analysis of noise effects in long semiconductor optical amplifiers," *The open optics journal*, vol. 2, pp. 61-66, 2008.
- [74] T. Briant, P. Grangier, R. Tualle-Brouri, A. Bellemain, R. Brenot and B. Thédrez, "Accurate determination of the noise figure of polarization-dependent optical amplifier: theory and experiment," *Journal of lightwave technology*, vol. 24, no. 3, pp. 1499-1503, 2006.
- [75] D. M. Baney, P. Gallion and R. S. Tucker, "Theory and measurement techniques for the noise figure of optical amplifiers," *Optical fiber technology*, vol. 6, pp. 122-154, 2000.
- [76] T. Mukai, Y. Yamamoto and T. Kimura, "S/N and error rate performance in AlGaAs semiconductor laser preamplifier and linear repeater systems," *IEEE transactions on microwave theory and techniques*, Vols. MTT-30, no. 10, pp. 1548-1556, 1982.
- [77] Y. Yamamoto and K. Inoue, "Noise in amplifiers," *Journal of lightwave technology*, vol. 21, no. 11, pp. 2895-2915, 2003.
- [78] A. Crottini, F. Salleras, P. Moreno, M.-A. Dupertuis, B. Deveaud and R. Brenot, "Noise figure improvement in semiconductor optical amplifiers by holding beam at transparency scheme," *IEEE photonics technology letters*, vol. 17, no. 5, pp. 977-979, 2005.
- [79] A. Verdier, "Modélisation, conception, fabrication, caractérisation et valorisation d'amplificateurs optiques à semiconducteur de très large bande spectrale. (PhD Thesis)," Université de Toulouse, Toulouse, FRANCE, 2018.
- [80] M. Yamada, H. Ono, T. Kanamori, S. Sudo and Y. Ohishi, "Broadband and gain-flattened amplifier composed of a 1.55 μ m-band and a 1.58 μ m-band Er3+-doped fibre amplifier in a parallel configuration," *Electronics letters*, vol. 33, no. 8, pp. 710-711, 1997.
- [81] S. Namiki and Y. Emori, "Ultrabroad-band raman amplifiers pumped and gain-equalized by wavelength-division-multiplexed high-power laser diodes," *IEEE Journal on selected topics in quantum electronics*, vol. 7, no. 1, pp. 3-16, 2001.
- [82] P. P. Iannone, K. C. Reichmann, X. Zhou and S. Gray, "A discrete SOA-Raman hybrid amplifier with 80-nm bandwidth," in *ECOC*, Cannes, FRANCE, 2006.
- [83] K. C. Reichmann, P. P. Iannone, X. Zhou, N. J. Frigo and B. R. Hemenway, "240-km CWDM transmission using cascaded SOA raman hybrid amplifiers with 70-nm bandwidth," *IEEE photonics technology letters*, vol. 18, no. 2, pp. 328-330, 2006.
- [84] P. P. Iannone and C. Reichmann, "Hybrid SOA-Raman amplifiers for fiber-to-the-home and metro networks," in *OFC*, San Diego, CA, USA, 2008.
- [85] H. Masuda, S. Kawai and K. Aida, "Ultra-wideband hybrid amplifier comprising distributed Raman amplifier and erbium-doped fibre amplifier," *Electronics letters*, vol. 34, no. 13, pp. 1342-1344, 1998.
- [86] H. Masuda and S. Kawai, "Wide-band and gain-flattened hybrid fiber amplifier consisting of an EDFA and a multiwavelength pumped raman amplifier," *IEEE photonics technology letters*, vol. 11, no. 6, pp. 647-649, 1999.

- [87] L. Lundberg, P. A. Andrekson and M. Karlsson, "Power consumption analysis of Hybrid EDFA/raman amplifiers in long-haul transmission systems," *Journal of lightwave technology*, vol. 35, no. 11, pp. 2132-2142, 2017.
- [88] S. Liu, J. Norman, M. Dumont, D. Jung, A. Torres, A. C. Gossard and J. E. Bowers, "High-performance O-Band quantum-dot semiconductor optical amplifiers directly grown on a CMOS compatible silicon substrate," *ACS photonics*, vol. 6, pp. 2523-2529, 2019.
- [89] H. Wang, E. T. Aw, M. Xia, M. G. Thompson, R. V. Penty, I. H. White and A. R. Kovsh, "Temperature independent optical amplification in uncooled quantum dot optical amplifiers," in *OFC*, San Diego, CA, USA, 2008.
- [90] S. Tanaka, A. Uetake, S. Okumura, M. Ekawa, G. Nakagawa and K. Morito, "Uncooled, polarization-insensitive AlGaInAs MQW-SOA module operable up to 75°C with constant current," in *ECOC*, Geneva, SWITZERLAND, 2011.
- [91] B. Kanwal, A. Armghan, S. Ghafoor, A. Atieh, M. Sajid, T. Kausar, J. Mirza and Y. Lu, "Design and analysis of an O+E-Band hybrid optical amplifier for CWDM systems," *Micromachines*, vol. 13(11), no. 1962, pp. 1-13, 2022.
- [92] Y. Wang, N. K. Thipparapu, D. J. Richardson and J. K. Sahu, "Ultra-broadband bismuth-doped fiber amplifier covering 115-nm bandwidth in the O and E bands," *Journal of lightwave technology*, vol. 39, no. 3, pp. 795-800, 2021.
- [93] K. Morito and S. Tanaka, "Record high saturation power (+22 dBm) and low noise figure (5.7 dB) polarization-insensitive SOA module," *IEEE photonics technology letters*, vol. 17, no. 6, pp. 1298-1300, 2005.
- [94] P. W. Juodawlkis, J. J. Plant, W. Loh, L. J. Missaggia, K. E. Jensen and F. J. O'Donnell, "Packaged 1.5-μm quantum-well SOA with 0.8-W output power and 5.5-dB noise figure," *IEEE photonics technology letters*, vol. 21, no. 17, pp. 1208-1210, 2009.
- [95] P. W. Juodawlkis, J. J. Plant, R. K. Huang, L. J. Missaggia and J. P. Donnelly, "High-power 1.5-μm InGaAsP-InP slab-coupled optical waveguide amplifier," *IEEE photonics technology letters*, vol. 17, no. 2, pp. 279-281, 2005.
- [96] J. Renaudier, A. Carbo Mesenguer, A. Ghazisaeidi, P. Tran, R. Rios Muller, R. Brenot, A. Verdier, F. Blache, K. Mekhazni, B. Duval, H. Debregas, M. Achouche, A. Boutin, F. Morin, L. Letteron, N. Fontaine, Y. Frignac and G. Charlet, "First 100-nm continuous-band WDM transmission system with 115Tb/s transport over 100km using novel ultra-wideband semiconductor optical amplifier," in *ECOC*, Gothenburg, SWEDEN, 2017.
- [97] L. F. Tiemeijer, P. J. A. Thijs, T. van Dongen, J. J. M. Binsma, E. J. Jansen, S. Walczyk, G. N. van den Hoven and E. C. M. Pennings, "High-gain, high-power 1550-nom polarization independent MQW optical amplifier," *IEEE photonics technology letters*, vol. 8, no. 9, pp. 1142-1144, 1996.
- [98] A. Verdier, A. Carbo Meseguer, K. Mekhazni, F. Blache, C. Calo, M. Goix, B. Duval, C. Fortin, F. Martin, C. Gomez, F. Morin, A. Boutin, L. Letteron, H. Carrère, D.-F. Bendimerad, Y. Frignac, J. Renaudier, G. Charlet and R. Brenot, "Wideband material for low linewidth widely tunable laser and reach extender for optical access networks," in *OFC*, Los Angeles, CA, USA, 2017.

- [99] A. A. Al-Azzawi, A. A. Almukthar, P. H. Reddy, S. Das, A. Dhar, M. C. Paul, H. Arof, H. Ahmad and S. W. Harun, "An efficient wideband hafnia-bismuth erbium co-doped fiber amplifier with flat-gain over 80 nm wavelength span," *Optical fiber technology*, vol. 48, pp. 186-193, 2019.
- [100] B. A. Hamida, A. A. Latiff, X. S. Cheng, M. A. Ismail, W. Naji, S. Khan, W. Al-Khateeb, H. Ahmad and S. W. Harun, "Wideband and flat-gain amplifier using high concentration erbium doped fibers in series double-pass configuration," in *ICCCE*, Kuala Lumpur, Malaysia, 2012.
- [101] A. A. Al-Azzawi, A. A. Almukhtar, B. A. Hamida, S. Das, A. Dhar, M. C. Paul, H. Ahmad and S. W. Harun, "Wideband and flat gain series erbium doped fiber amplifier using hybrid active fiber with backward pumping distribution technique," *Results in physics*, vol. 13, no. 102186, 2019.

Figures

Figure 16. Growth of monthly internet data traffic from 2010 to 2020. Sources: IEA & Cisco blog.....	3
Figure 17. Long Haul, Metro and Access network illustration.	4
Figure 18. Evolution of the propagation losses in optical fiber [4].....	5
Figure 19. CD in commercially available optical fibers. Data from various vendors available in [9]....	6
Figure 20. Illustration of chromatic dispersion in function of its sign.	6
Figure 21. Optical fiber absorption and dispersion in standard single mode fiber [11].	7
Figure 22. Illustration of a passive optical network.	8
Figure 23. Amplification in a transmission line in the optical network.	9
Figure 24. Illustration of a wavelength division multiplexer system.	10
Figure 25. SDM fibers commonly used in optical data transmissions.	11
Figure 26. SDM and MDW merged systems scheme.	11
Figure 27. Optical spectrum analyzer's display.	12
Figure 28. Scheme of a scanning optical spectrum analyzer.....	12
Figure 29. Spectral absorption of water and tissues chromophores together with scattering [21].....	14
Figure 30. Relation between axial resolution and spectral bandwidth in OCT following Equation 1..	15
Figure 31. Erbium doped fiber amplifier [31].	16
Figure 32. Amplification mechanism in EDFA.	16
Figure 33. The different light scatterings.	18
Figure 34. Raman amplifier scheme.....	18
Figure 35. Semiconductor optical amplifier scheme.....	19
Figure 36. Reflective semiconductor optical amplifier scheme.	19
Figure 37. GaInAsP system with interest areas [58, 59].	19
Figure 38. Spontaneous and Stimulated emissions.	20
Figure 39. PiN structure, bandgaps and refractive indexes.	21
Figure 40. Overlap between optical mode and active region in the case of a buried structure.	21
Figure 41. Bulk, Quantum Well, Multiple Quantum Wells, Quantum Wire, Quantum Dot schemes. .	22
Figure 42. Saturation output power illustration.....	25
Figure 43. Gain optical bandwidth representation.	26
Figure 44. Illustration of Gain truncation.....	27
Figure 45. Bandwidth enlargement using several amplifiers.	28
Figure 46. Scheme of a SOA-Raman hybrid amplifier [82].....	28
Figure 47. Example of hybrid EDFA-Raman amplifier architecture [85].	29
Figure 48. Raman amplifier using multi-wavelength pumps [81].....	29
Figure 49. Paralleled EDFAs architecture [80].	30
Figure 50. Optical amplifiers state of the art [88, 89, 41, 37, 90, 91, 92, 65, 68, 45] [44, 93, 94, 47, 95, 96, 79, 97, 98, 82] [83, 99, 53, 86, 34, 33, 100, 101].	32

Tables

Table 12. The optical bands' wavelength ranges.	7
Table 13. Required performance for optical amplifier depending on its role in the transmission line [15].	9
Table 14. Optical medical imaging comparison in terms of resolution and penetration.	14
Table 15. Gain media in swept lasers and some of their characteristics.	15
Table 16. Dopants used for optical fiber doped amplifiers [48].....	17
Table 17. Targeted performances for the SOAs.....	33

Chapter 2 – Conception of Semiconductor Optical Amplifiers

In this second chapter, we detail the conception steps of our devices, based on large GaInAsP MQW-based active regions. The first section focuses on the active areas to define the MQWs' characteristics (composition, strain, thickness) for wideband amplification. Then, we discuss the complete structure and review the literature dedicated to refraction indices models to design the surrounding layers. We finalize the conception of our devices by implementing a newly developed Super Lattice (SL) slab which enables a single mode behavior with large devices' dimensions. Six structures are designed to study the performances of SOAs as a function of the optical confinement in their MQW.

In this work, SOAs and RSOAs are based on the same epitaxy structure. To simplify the comprehension of this chapter, we refer to SOA only.

1. Active region simulation

The first step of SOA conception is the design of its active region. The freedom offered by III-V semiconductors for band structure engineering enables the tunability of the polarization sensitivity, the optical bandwidth and the material gain.

1.1. Band structure engineering

With a high control of the material growth given by the epitaxy techniques, we can artificially modify the electronic structure of the material to suit the device specifications [1]. This property was firstly used to reduce the threshold current density of lasers in 1986 [2, 3]. Nowadays, the modifications cover a wider spectrum of parameters. Band structure engineering can be used to improve efficiency, to reduce the temperature sensitivity of the device or to have better high speed performances. The band structure engineering can be applied for lasers as well as for amplifiers [4]. By tuning the compounds' compositions of the GaInAsP quaternary alloys grown on InP, we can tune both bandgap energy and strain. In this section, we will see how strain impacts the active region's properties.

1.1.1. Impact of strain over the bandgap energy

Strain depends on the lattice parameters of the grown material and the substrate. Figure 51 illustrates the two different types of strain, tensile and compressive.

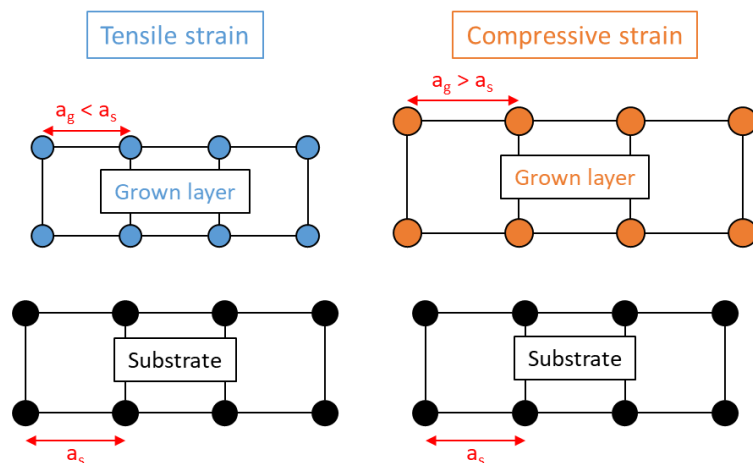


Figure 51. Illustration of tensile and compressive strain.

Following Equation 16, tensile strain is given by negative values, the substrate's lattice parameter being higher than the lattice parameter of the grown material. For compressive strain, this number is positive.

$$\text{Equation 16. } \varepsilon = \frac{a_g - a_s}{a_g}$$

Where:

- a_s , is the lattice parameter of the substrate, in our case InP.
- a_g , is the lattice parameter of the grown layer.

The lattice parameter, as well as its bandgap energy, depends on the material's composition. When lattice matched on InP, the $\text{Ga}_x\text{In}_{1-x}\text{As}_y\text{P}_{1-y}$ bandgap energy can be calculated with Equation 17 [5].

$$\text{Equation 17. } E_g(x, y) = 1.35 + 0.642x - 1.101y + 0.758x^2 + 0.101y^2 - 0.159xy + 0.28x^2y + 0.109xy^2$$

Strain is not taken into account in this equation as the lattice parameters are equal. To implement it, we must calculate its values in the plane of the epitaxial growth (ε_{xx} and ε_{yy}) and in the perpendicular (ε_{zz}) direction, with Equation 18 and Equation 19, respectively.

$$\text{Equation 18. } \varepsilon_{xx} = \varepsilon_{yy} = \varepsilon$$

$$\text{Equation 19. } \varepsilon_{zz} = -2 * \frac{C_{12}}{C_{11}} * \varepsilon$$

C_{11} and C_{12} are the elastic stiffness constants, given in Table 18, for the binary materials on which the GaInAsP alloys are based (GaAs, GaP, InAs and InP).

According to Bir and Pikus, the strain's impact on the energy can be considered as a hydrostatic component, which leads to an increase, or a decrease of the bandgap energy, and as a tetragonal term responsible for the light and heavy holes band edge splitting [6]. With tensile strain, the light hole band is the fundamental valence state, while with compressive strain, the heavy hole band is the top of the valence band. The band edge alignment of GaInAsP quantum well heterostructure is presented in Figure 52.

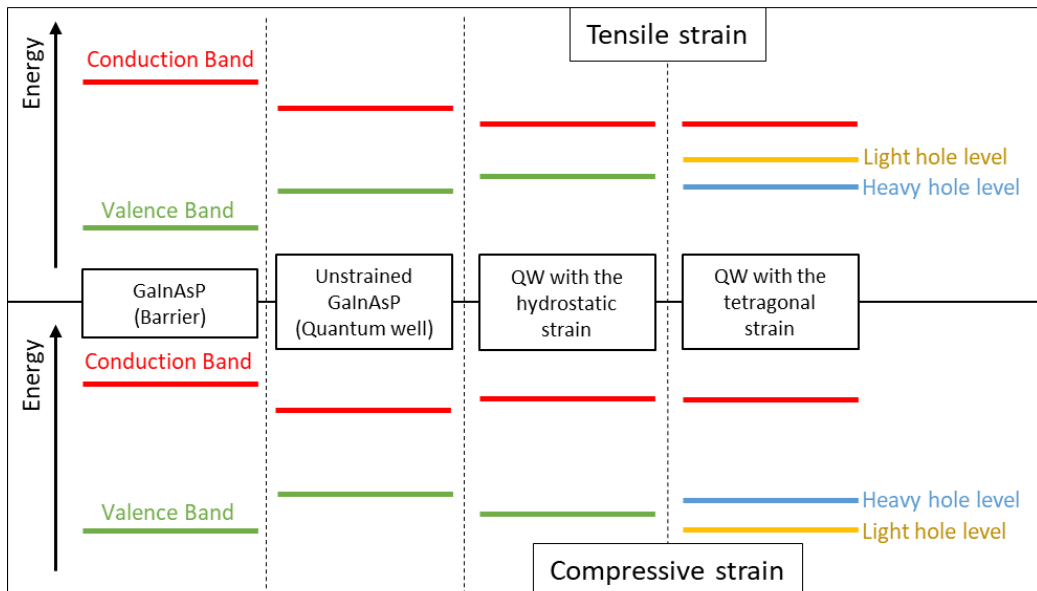


Figure 52. Band alignment of GaInAsP/GaInAsP QW under tensile and compressive strain [7].

The calculations of the strain's impact on the conduction band energy and the valence band energy of light and heavy holes are given by Equation 20, Equation 21 and Equation 22, respectively.

$$\text{Equation 20. } \delta E_c(x, y) = a_c(\varepsilon_{xx} + \varepsilon_{yy} + \varepsilon_{zz}) = 2a_c \left(1 - \frac{c_{12}}{c_{11}}\right) * \varepsilon$$

$$\text{Equation 21. } \delta E_{lh}(x, y) = a_v(\varepsilon_{xx} + \varepsilon_{yy} + \varepsilon_{zz}) - \frac{b}{2}(\varepsilon_{xx} + \varepsilon_{yy} + 2\varepsilon_{zz}) = 2a_v \left(1 - \frac{c_{12}}{c_{11}}\right) \varepsilon - b \left(1 + 2 \frac{c_{12}}{c_{11}}\right) \varepsilon$$

$$\text{Equation 22. } \delta E_{hh}(x, y) = a_v(\varepsilon_{xx} + \varepsilon_{yy} + \varepsilon_{zz}) + \frac{b}{2}(\varepsilon_{xx} + \varepsilon_{yy} + 2\varepsilon_{zz}) = 2a_v \left(1 - \frac{c_{12}}{c_{11}}\right) \varepsilon + b \left(1 + 2 \frac{c_{12}}{c_{11}}\right) \varepsilon$$

Where:

- a_c and a_v , are the conduction and valence band hydrostatic deformation potentials.
- b , is the valence band shear deformation potential.

These parameters are listed in Table 18 for the binary materials composing GaInAsP.

Parameter	GaAs	GaP	InAs	InP
$a(\text{\AA})$	5.6533	5.4505	6.0584	$a_s = 5.8688$
$C_{11} (10^{11} \text{dyn/cm}^2)$	11.879	14.050	8.329	10.110
$C_{12} (10^{11} \text{dyn/cm}^2)$	5.376	6.203	4.526	5.610
$a_c (eV)$	-7.17	-7.14	-5.08	-5.04
$a_v (eV)$	1.16	1.17	1.00	1.27
$b (eV)$	-1.7	-1.8	-1.8	-1.7

Table 18. Constants for strain impact calculation over GaInAsP bandgap energy.

To obtain the $\text{Ga}_x\text{In}_{(1-x)}\text{As}_y\text{P}_{(1-y)}$ parameters, we can apply Vegard's law (Equation 23) using the binary compounds' parameters (X_{GaAs} , X_{GaP} , X_{InAs} and X_{InP}).

$$\text{Equation 23. } X(x, y) = xy * X_{\text{GaAs}} + x(1 - y) * X_{\text{GaP}} + (1 - x)y * X_{\text{InAs}} + (1 - x)(1 - y) * X_{\text{InP}}$$

By combining Equation 20, Equation 21 and Equation 22 with the bandgap energy calculation of the unstrained material, we obtain Equation 24, for the electron-light hole transition and Equation 25, for the electron-heavy hole transition.

$$\text{Equation 24. } E_{c-lh}(x, y) = E_g(x, y) + \delta E_c(x, y) - \delta E_{lh}(x, y)$$

$$\text{Equation 25. } E_{c-hh}(x, y) = E_g(x, y) + \delta E_c(x, y) - \delta E_{hh}(x, y)$$

Strain modifies the valence band alignment, highlighting that heavy and light holes provide different bandgap energies. With its influence over the valence band, strain also impacts the polarization sensitivity of the material.

1.1.2. Polarization sensitivity

The relative positions of both valence bands results in two different light polarizations. Figure 53 displays an illustration for a better understanding of polarization. In the SOA, the signal propagates along the z-axis. The electromagnetic wave can either oscillate along the x-axis, in the TM mode or along the y-axis, in the TE mode.

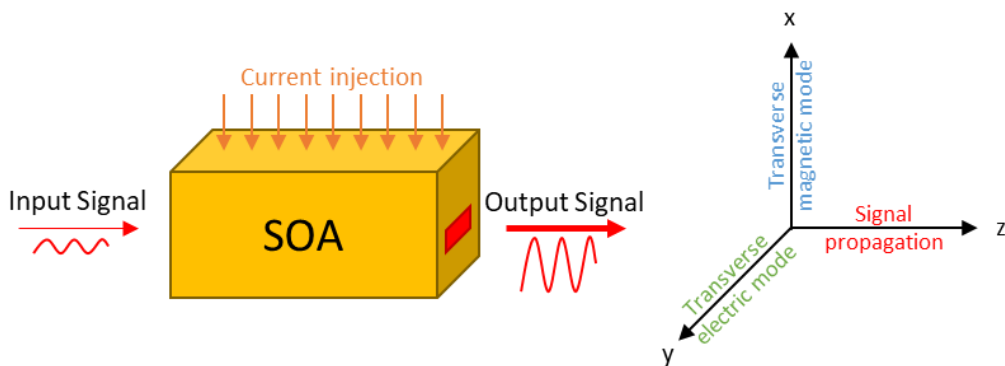


Figure 53. Signal propagation in the SOA with TE and TM polarization modes.

Recombination between electron and hole can be expressed with the dipole matrix element of Equation 26. In the case of electron-heavy hole recombination, it takes the form of the Equation 27. For electron-light hole recombination, we refer to Equation 28.

$$\text{Equation 26. } M_{nm}(k_\perp) = \langle \psi_m^C | \varepsilon \cdot p | \psi_n^V \rangle$$

$$\text{Equation 27. } M_{nm}(k_\perp) = \langle F_m^C | g_n^V \rangle \langle u_c | \varepsilon \cdot p | u_{v,h} \rangle$$

$$\text{Equation 28. } M_{nm}(k_\perp) = \langle F_m^C | f_n^V \rangle \langle u_c | \varepsilon \cdot p | u_{v,l} \rangle$$

In these equations, we have the following parameters:

- ψ_m^C and ψ_n^V , the bond state wave functions of carriers in the QWs for electron and hole, respectively.
- ε , the light polarization.
- p , the electron momentum.
- F_m^C , the envelope function of electron states.
- g_n^V and f_n^V , the envelope functions of heavy hole and light hole states, respectively.

The second terms of Equation 27 and Equation 28 depend on the wave polarization and the Bloch function of conduction and valence band edges. They are reported in Table 19 for the configuration exposed in Figure 53.

<i>Transition</i>	<i>Light propagation</i>	ε_x	ε_y	ε_z
<i>Electron-Heavy hole</i>	<i>x</i>	Impossible	$\frac{\Pi}{\sqrt{2}}$	$\frac{\Pi}{\sqrt{2}}$
	<i>y</i>	Forbidden	Impossible	$\frac{\Pi}{\sqrt{2}}$
	<i>z</i>	Forbidden	$\frac{\Pi}{\sqrt{2}}$	Impossible
<i>Electron-Light hole</i>	<i>x</i>	Impossible	$\frac{\Pi}{\sqrt{6}}$	$\frac{\Pi}{\sqrt{6}}$
	<i>y</i>	$\frac{2 * \Pi}{\sqrt{6}}$	Impossible	$\frac{\Pi}{\sqrt{6}}$
	<i>z</i>	$\frac{2 * \Pi}{\sqrt{6}}$	$\frac{\Pi}{\sqrt{6}}$	Impossible

Table 19. Selection rules for interband transitions given by [8], in $k_\perp = 0$.

With the signal propagation along the z-axis, TE mode, represented by ε_y , can be exhibited by both of the transitions. Only electron-light hole recombination can provide the TM mode, represented by ε_x .

The parameter Π , expressed in Equation 29, is related to the Kane matrix element, E_p , expressed in Equation 30.

$$\text{Equation 29. } \Pi = \frac{-i}{m_0} \langle S | p_x | X \rangle = \frac{-i}{m_0} \langle S | p_y | Y \rangle = \frac{-i}{m_0} \langle S | p_z | Z \rangle$$

$$\text{Equation 30. } E_p = 2 * m_0 * \Pi^2 (\approx 20 \text{ meV, whatever III-V material})$$

In these equations, we have:

- $|S\rangle, |X\rangle, |Y\rangle$ and $|Z\rangle$, the band edge Bloch functions of s-like conduction band and p-like valence band at Γ point in k-space.
- m_0 , the free electron mass.

To be polarization independent, a device must emit both TE and TM modes. At the device scale, this property can only be obtained with tensile strain in the active material. However, the polarization independency can be implemented through the chip packaging, using devices that have compressively

strained active layers. Figure 54 displays this type of packaging, requiring a single SOA to be polarization independent [9].

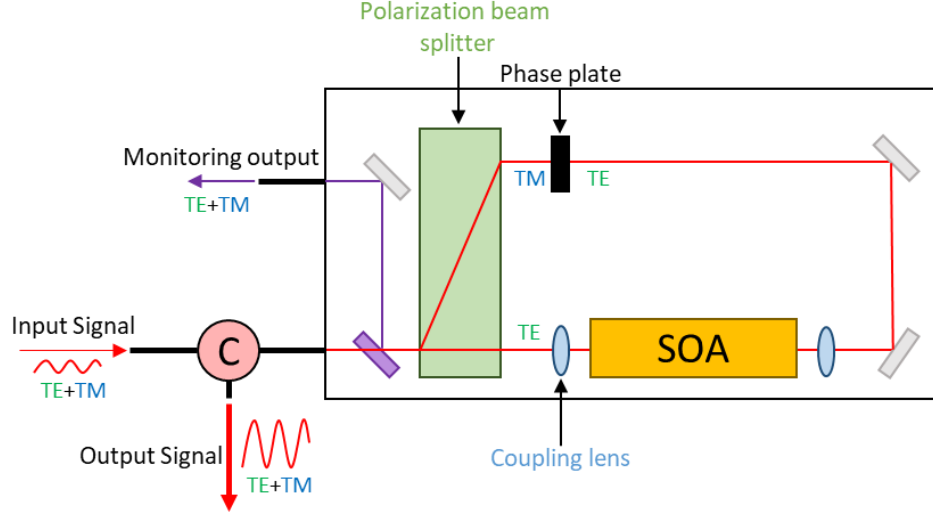


Figure 54. Polarization independent module using a single SOA.

In this module, the input signal is split according to its polarization. The TE mode signal is amplified through the SOA and then, rotated to TM mode. For TM mode, it is firstly rotated to TE mode before getting amplified. Both rotated signals are finally recombined in the output signal.

Another module architecture, using two SOAs, can be used as illustrated in Figure 55 [10].

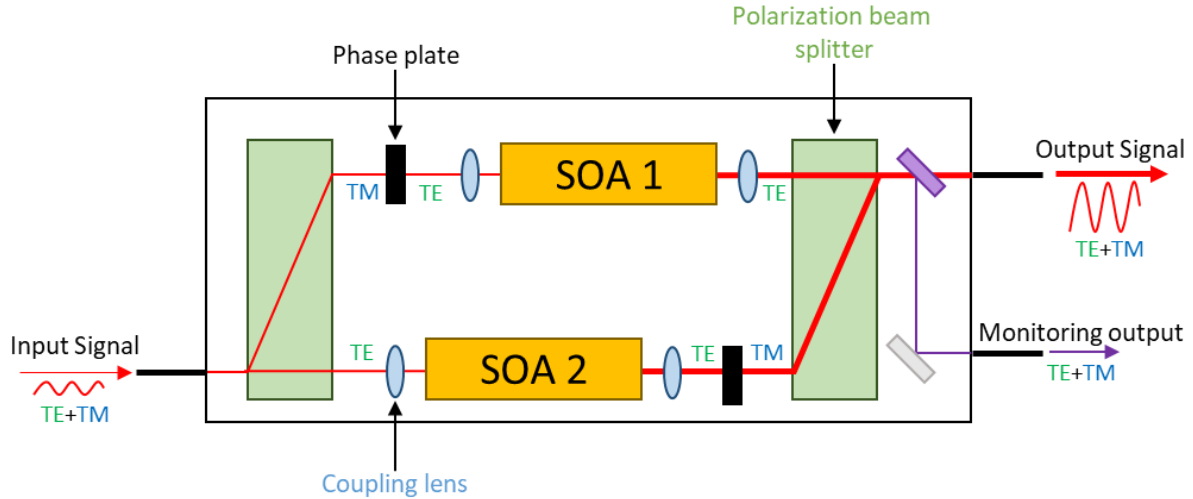


Figure 55. Polarization independent module using two SOAs.

We keep splitting and rotating the signal to amplify only TE mode with two SOAs. This architecture exhibits greater gain than the previous one. However, the two SOAs must have the same performances to equally amplify both of the polarizations.

The MQW of our structures are compressively strained. Consequently, one of these specific packaging is required to reach polarization independence. In the following section, we focus on the wideband amplification aspect of our devices.

1.2. Optical transitions in wideband amplification

In this section, we compare the use of narrow and large QWs in the context of wideband amplification. Then, we study the material gain through four parameters that are: (i) the QWs' bandgap energy, (ii) the strain in the MQW, (iii) the bandgap energy of the barriers and (iv) the QWs' thickness. This study is required to design the active region of our SOAs, in the next section.

1.2.1. Narrow quantum wells

In 2005, Morito, Tanaka, Tomabechi and Kuramata presented performances provided by a wideband SOA based on GaInAsP MQW [11]. With 5 nm thick QWs under 0.8% compressive strain, they reached a 120 nm bandwidth in the S+C-Band (from 1450 to 1570 nm). The chip gain was superior to 15 dB, the chip NF was under 4.5 dB and the P_{sat} was between 9 and 14 dBm.

By knowing the emitted wavelengths and the QWs' thickness and strain, we can find the active material's composition to electronically simulate the structure. With the simulation, we understand that a single electron level is confined. The optical bandwidth can only be enlarged with the transitions between the first electron level (e_1) and different hole levels (hh_n for heavy holes and lh_n for light holes).

Table 20 presents the different transition wavelengths of the structure. Transitions between e_1 and even heavy hole levels (e_1-hh_2 , e_1-hh_4 , ...) are forbidden because of the selection rules. Consequently, the amplification is only due to e_1-hh_1 and the wide bandwidth behavior comes from the band-filling of e_1 and hh_1 levels.

Transitions	Transition energy	Transition wavelengths
e_1-hh_1	0.795 eV	1586 nm
e_1-hh_2		Forbidden transition
e_1-lh_1	0.886 eV	1398 nm → Not in the spectrum
e_1-hh_3	0.945 eV	1311 nm → Not in the spectrum
e_1-hh_4		Forbidden transition

Table 20. Energy transitions wavelengths in simulated SOA structure.

A high current density must be injected to observe the wide gain bandwidth, thus, it is difficult to implement these SOAs in optical networks.

1.2.2. Large quantum wells

Large QWs allow the reduction of the injected current density by using several electron energy levels to provide recombination. By tuning the MQW's material in both wells and barriers, we can confine the second electron energy level (e_2) and enable a second transition at low injected current density.

In 1993, Miller and his coworkers used tensile strained QWs to obtain wide gain bandwidth of more than 92 nm [12]. The high tensile strain in the active material made the amplification mainly based on electron-light hole recombination. The presented bandwidth was reached for the TM polarization mode with a driving current of only 50 mA and provided a peak gain of 17 dB. A strain reduction could lead to a polarization insensitive device by tuning the material to get TE and TM gains around the same energy value [13].

With two confined electron levels, they obtained two distinct electronic transitions. Figure 56 illustrates the optical power behavior in function of the injected current. By increasing the current, gain reaches a saturation value at e_1-hh_1 wavelength while the optical bandwidth is enlarged by e_2-hh_2 . After observing a flat bandwidth, the second transition reaches higher gain values, at the expense of a bandwidth narrowing. The injection current giving the largest (or flattest) optical bandwidth is called flat gain current and noted I_m .

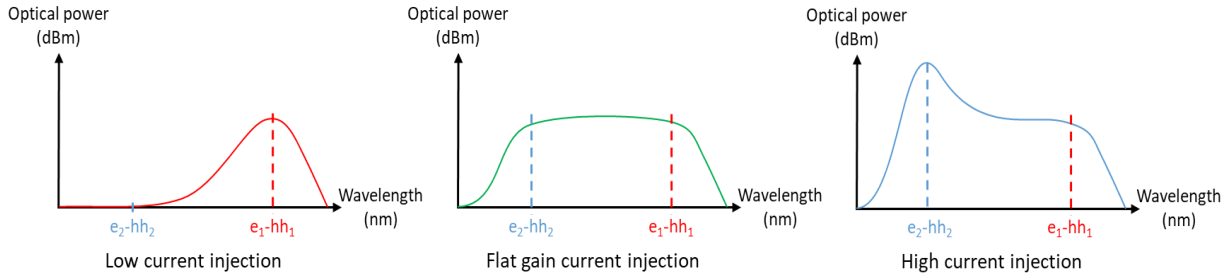


Figure 56. Gain behavior with injected current increase with two confined transitions.

The possibility to control the bandwidth's tilt with the injected current is useful in WDM long-haul transmission. The signal, amplified over a large bandwidth and passing through an optical fiber, generates Raman scattering. For bandwidths of more than 90 nm, in the C+L-Band, the shorter wavelengths transmission channels amplify the longer wavelengths ones. In the long haul telecommunications, the length of the fiber is long enough to modify the amplification spectrum during the transmission, as described in Figure 57. With a finely tuned injection current, the spectrum at the end of the fiber can also be the flattest possible.

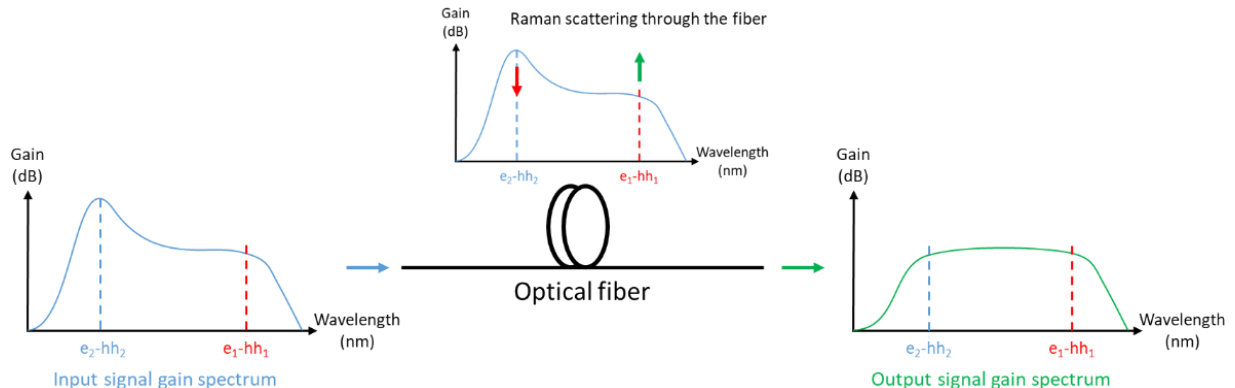


Figure 57. Raman scattering impact over amplification spectrum in long haul transmission system.

Our target is to reach wideband amplification over the C+L and O-Bands. Thus, we have to conceive our active regions with $e_1\text{-}hh_1$ at high L-Band wavelengths (1625 nm) and $e_2\text{-}hh_2$ in the low values of the C-Band (1530 nm). For O-Band, the first transition must be at 1360 nm and a second transition at 1260 nm. To set these wavelengths, we must study the notion of material gain.

1.2.3. Material gain

Material gain is directly related to the chip gain of the SOA, as mentioned in Chapter I (Equation 31).

$$\text{Equation 31. } G_{\text{chip}} = \exp^{[(\Gamma g_m(n) - \alpha(n)) * L]}$$

As G_{chip} is also involved in the calculation of the NF and P_{sat} , material gain is an important parameter to investigate in function of the energy that can be calculated with Equation 32 [14, 15, 16, 17].

$$\text{Equation 32. } g_m = \frac{e^2 \hbar}{m_0^2 n_0 c \epsilon_0} \frac{1}{\hbar \omega} \frac{1}{L} \left(1 - e^{\frac{1}{kT}(\hbar \omega - \Delta E_F)} \right) \sum_n \sum_m \int_0^{+\infty} \frac{k_\perp}{\pi} |M_{nm}(k_\perp)|^2 f(E_m^C(k_\perp) - E_F^C) \left(1 - f(E_F^V - E_n^V(k_\perp)) \right) \frac{\hbar \gamma_{\text{int}}}{(\hbar \omega - E_m^C(k_\perp) - E_n^V(k_\perp))^2 + (\hbar \gamma_{\text{int}})^2} dk_\perp$$

Where, we have:

- e , the electron charge.
- \hbar , the reduced Planck constant ($h/2\pi$).
- n_0 , the refractive index of the material.
- c , the speed of light.

- ϵ_0 , the permittivity of free space.
- ω , the optical angular frequency.
- L , the quantum well width.
- k , the Boltzmann's constant.
- T , the temperature.
- ΔE_F , the difference between the quasi-Fermi levels of conduction and valence band.
- n , the number of electron sub-bands.
- m , the number of hole sub-bands.
- $f(E_m^C(k_\perp) - E_F^C)$, the Fermi-Dirac conduction band occupancy number.
- $f(E_F^V - E_n^V(k_\perp))$, the Fermi-Dirac valence band occupancy number.
- $\gamma_{int} = \frac{1}{\tau_{int}}$, the reciprocal of intra-band relaxation time.
- $E_m^C(k_\perp)$, the carrier energies in the conduction band.
- $E_n^V(k_\perp)$, the carrier energies in the valence band.

The material gain's calculation requires the calculation of the quantum well band structure. Consequently, to optimize the material gain, we have to investigate 4 parameters:

1. The bulk material's bandgap energy of the material used in the QWs.
2. The strain involved in the quantum well material.
3. The band offset between the QWs and barriers.
4. The QWs' thickness.

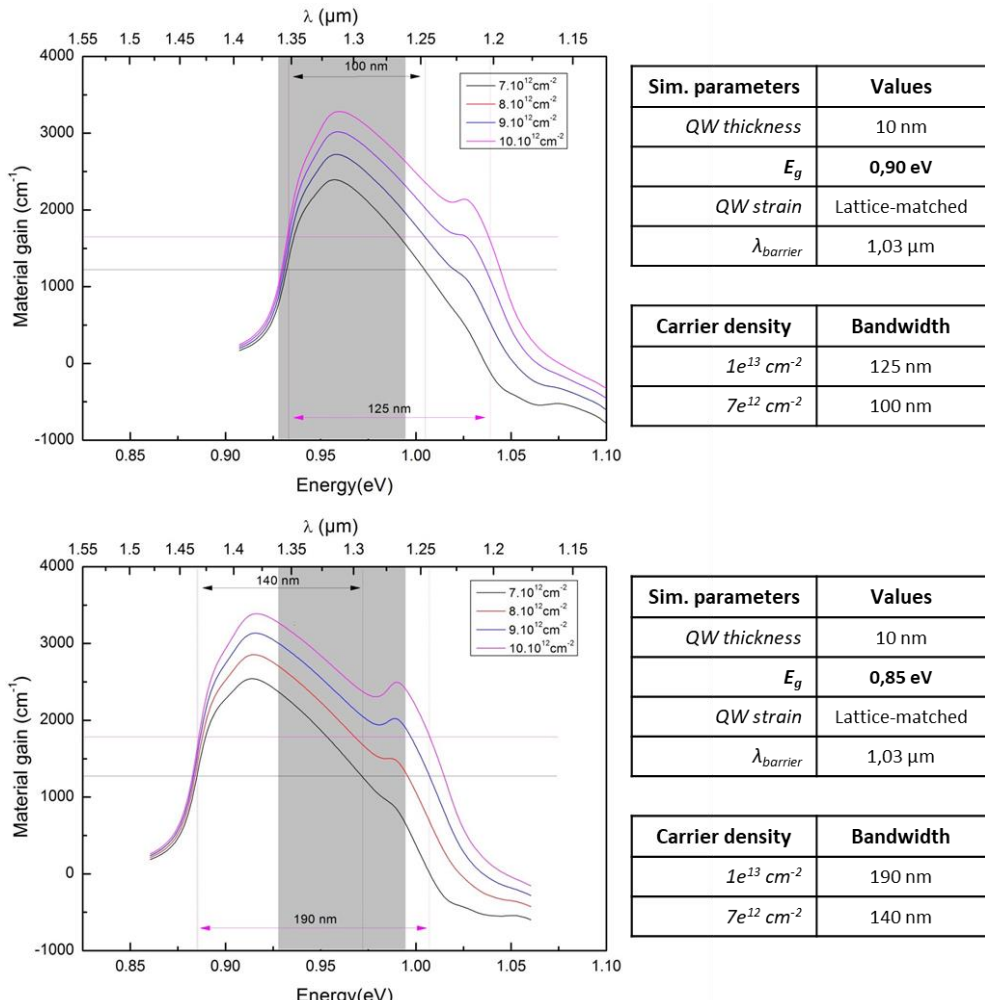


Figure 58. Simulations of g_m , for TE mode, in function of the bulk material's E_g set for QW.

Figure 58 displays the material gain calculation behavior in function of the first parameter, in the case of a O-band structure. In the graphs, the O-Band wavelengths are represented by the dark area and the curves represent the material gain in function of the carrier density. By modifying the bandgap energy of the material, we can adjust the gain peak provided by the fundamental transition in the low energy (or high wavelength) part of the band. The fundamental transition is particularly marked while the high energy transitions only have low contributions to the gain spectra, resulting in a limited bandwidth. To enhance their contributions, we have to modify the QWs' strain.

Figure 59 illustrates how the strain impacts the material gain. Two objectives have to be achieved at this step: (i) reach a flat material gain over the O-Band and (ii) keep the same optical bandgap energy for the quantum well.

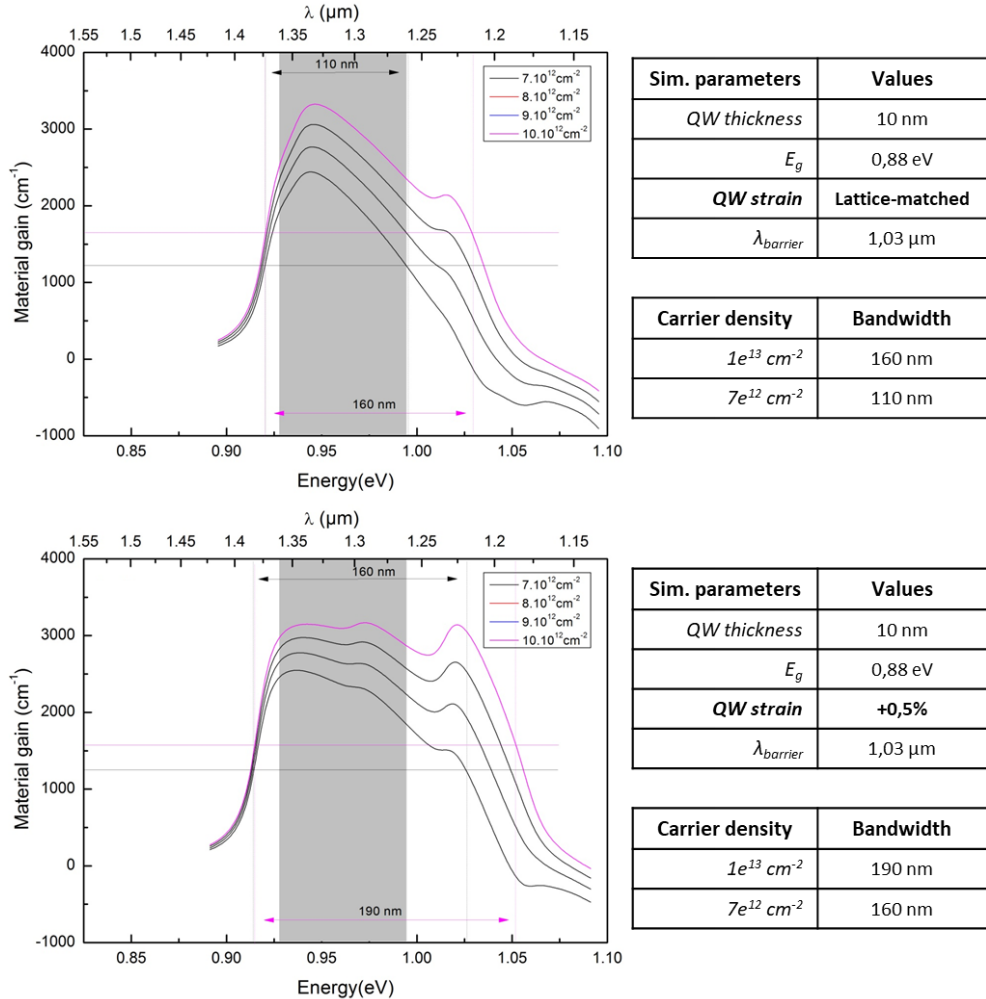


Figure 59. Simulations of g_m , for TE mode, in function of the strain incorporated in the QW.

Figure 60 shows the impact of different barrier compositions over the gain. With low bandgap energy barriers, the high energy transition disappears as the second electron level is poorly confined. Nonetheless, too high bandgap energy barriers could penalize the carriers' transport to the QWs. Thus, we must find a correct compromise.

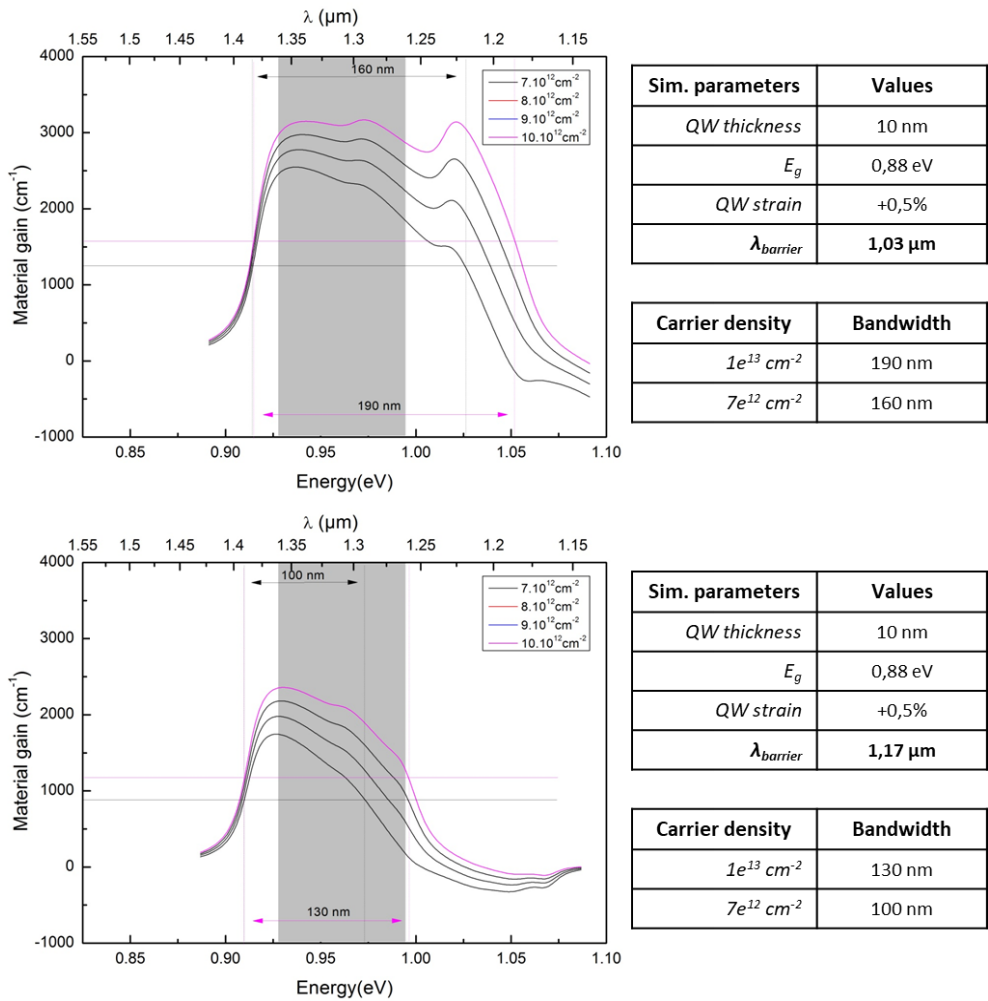


Figure 60. Simulations of g_{mb} for TE mode, in function of the band offset between barriers and QW.

The last parameter that can be adjusted is the thickness of the QWs. Equation 33 shows that the bound states energy (E_p) is linked to this thickness.

$$\text{Equation 33. } E_p = \frac{\hbar^2 * \pi^2}{2 * m^* * L^2} * p^2, p=1, 2, \dots$$

In Equation 33, we have the following parameters:

- \hbar is the reduced Planck constant ($h/2\pi$).
- m^* is the effective mass of the considered carrier (electron, light hole or heavy hole).
- L is the quantum well thickness.
- p is the considered bound state.

From this formula, we expect that the energy difference between e_1-hh_1 and e_2-hh_2 drastically increases by reducing the quantum well thickness. Figure 61 illustrates this behavior, but also shows that the material gain at high energy is considerably reduced by the lower carriers' confinement. This lower confinement can be detrimental for the optical bandwidth.

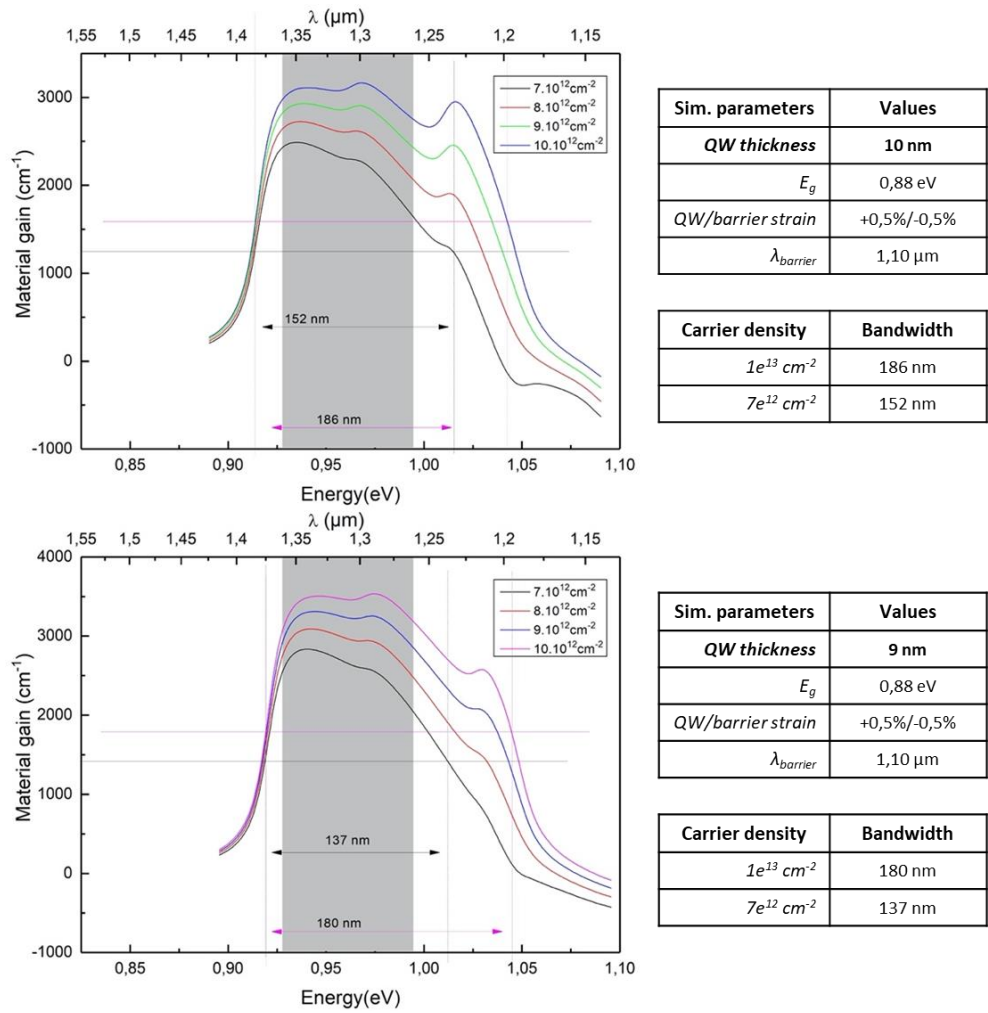


Figure 61. Simulations of g_m , for TE mode, in function of the QW thickness.

By knowing the behavior of the material gain in function of the presented parameters, we can design the active regions of our SOAs.

1.3. Designed active regions

The active regions are grown by GSMBE, which will be described in the next chapter. In order to take advantage of the precise composition control and the sharp interfaces that can be achieved with this technique, we must correctly design the MQW. The group-III elements must remain constants during the growth, and the composition difference between QWs and barriers has to be managed by the group-V elements.

In the C+L-Band, previous works made at III-V Lab set the GaInAsP alloy, lattice-matched on InP and emitting at 1.17 μm , noted $Q_{1.17}$ as the barriers' material. In the O-Band, we adapt this material to the targeted wavelengths, thus, we selected the GaInAsP alloy lattice-matched on InP and emitting at 1.03 μm , noted $Q_{1.03}$.

In this section, we set the thicknesses involved in the MQW, as well as the ratio between Arsenic (As) and Phosphorus (P) required in the QWs to cover the complete C+L-Band and O-Band with different structures.

1.3.1. C+L-Band active regions

In the C+L-Band, we electronically design two active regions.

The first is based on 14 nm thick and 1.23% compressively strained QWs. The theoretical energy difference between $e_1\text{-}hh_1$ and $e_2\text{-}hh_2$ is 76 meV which corresponds to a bandwidth of 146 nm. Figure 62 displays band alignment simulation of this structure.

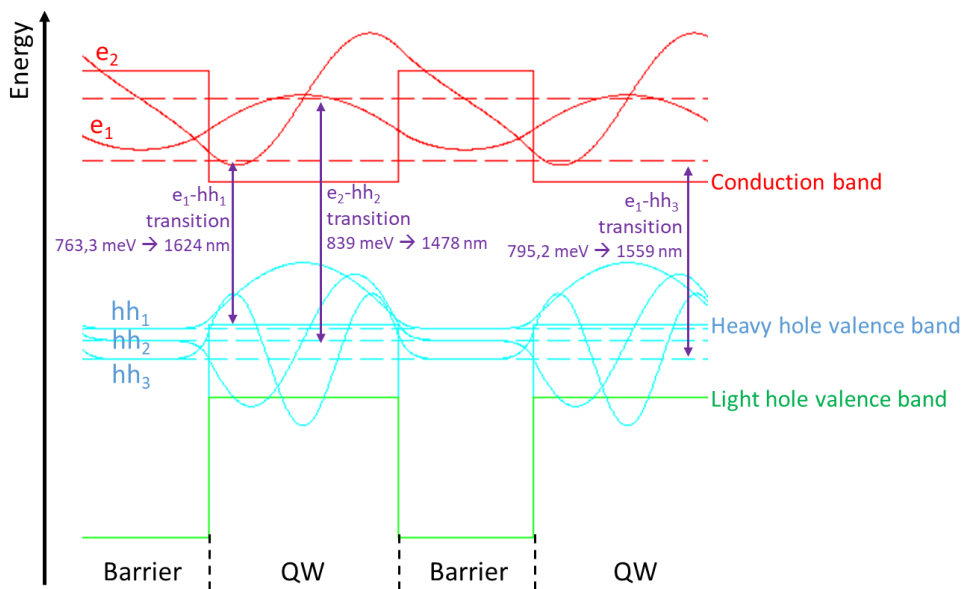


Figure 62. Band alignment simulation of the first C+L-Band active region.

Figure 63 presents the material gain calculated with this active region's characteristics. Losses are not taken into account in the material gain calculation, thus, it gives optimistic bandwidth values. Consequently, we set the difference between $e_1\text{-}hh_1$ and $e_2\text{-}hh_2$, from the band alignment simulation, as reference for this parameter.

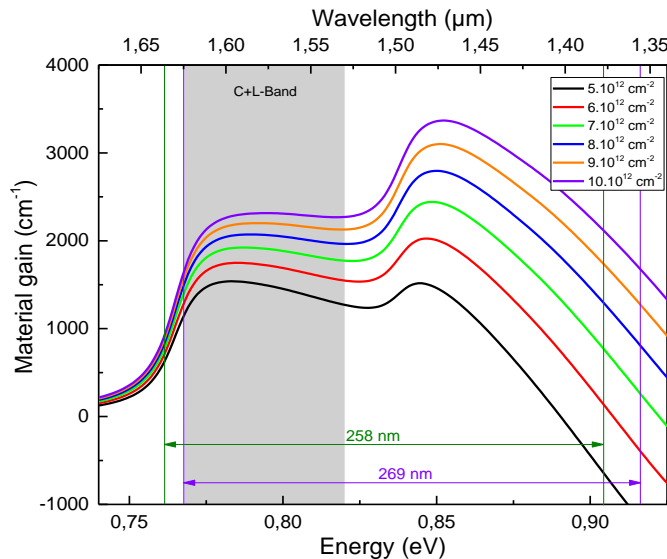


Figure 63. Calculation of g_m for TE mode, with the first C+L-Band active region design.

The second active region is designed to enlarge the theoretical energy difference between the optical transitions. To do this, we reduced the QWs' thickness to 11 nm with a compressive strain of 1.27%. Figure 64 illustrates the band alignment simulation of this structure.

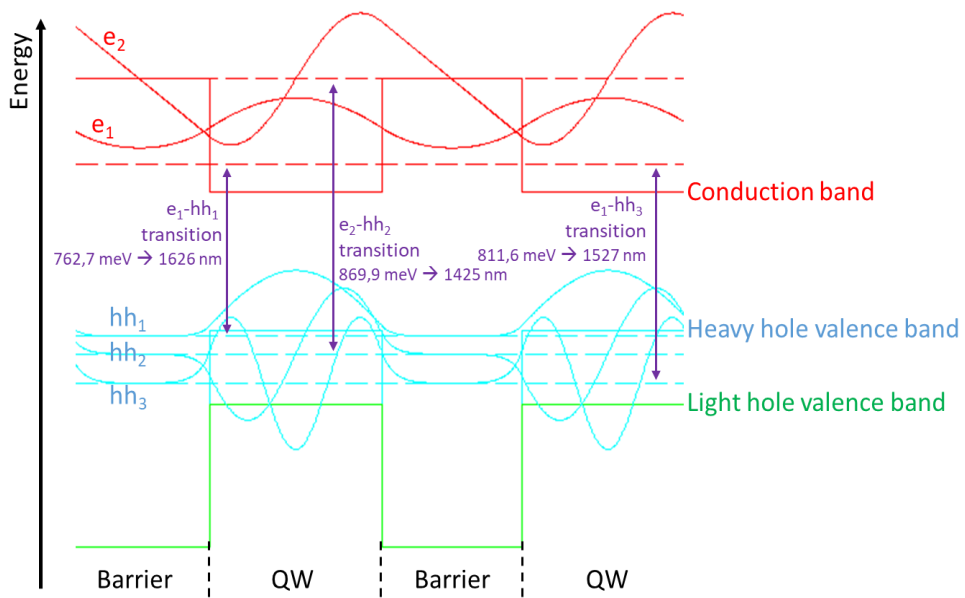


Figure 64. Band alignment simulation of the second C+L-Band active region.

We observe that the second electron level is poorly confined, at the limit of the barrier energy. The theoretical bandwidth reaches 201 nm. We also calculated the material gain, visible in Figure 65.

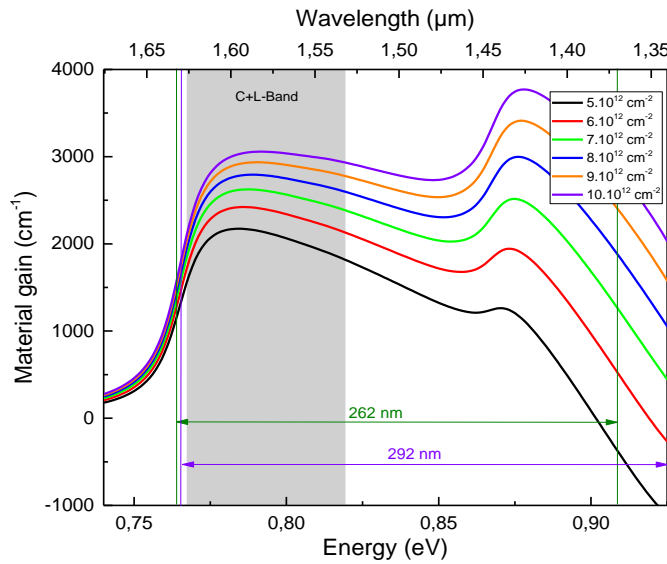


Figure 65. Calculation of g_m , for TE mode, with the second C+L-Band active region design.

The information about the designed active regions, for the C+L-Band, are summarized in Table 21.

<i>Characteristics</i>	<i>Design A</i>	<i>Design B</i>
<i>QW thickness</i>	140 Å	110 Å
<i>Barrier thickness</i>	100 Å	90 Å
<i>QW strain</i>	+1.23 %	+1.27 %
<i>Barrier strain</i>	Lattice-matched	Lattice-matched
e_1-hh_1 energy	763.3 meV	762.7 meV
e_1-hh_3 energy	795.2 meV	811.6 meV
e_2-hh_2 energy	839.0 meV	869.9 meV
e_1-hh_1 wavelength	1624 nm	1626 nm
e_1-hh_3 wavelength	1559 nm	1527 nm
e_2-hh_2 wavelength	1478 nm	1425 nm
<i>Theoretical bandwidth</i>	146 nm	201 nm

Table 21. C+L-Band active region designs.

1.3.2. O-Band active region

For the O-Band, we design a single structure.

In comparison with C+L-Band, the QWs' bandgap energy is higher, thus we must design the active region with higher bandgap energy barriers. Q_{1.03} was selected as barriers' material to have a sufficient band offset to confine the carriers in the QWs.

Wideband amplification in O-Band is also harder to achieve. For a same energy difference between two optical transitions, the wavelength bandwidth will be shorter in O-Band than in C+L-Band. This is visible with Equation 34 and Equation 35.

$$\text{Equation 34. } \lambda = \frac{h*c}{E}$$

$$\text{Equation 35. } \Delta\lambda = \frac{h*c}{E_1 * E_2} * \Delta E$$

Where:

- λ is the photon wavelength.
- $\Delta\lambda$ is the optical bandwidth in terms of wavelength.
- h is the Planck constant.
- c is the speed of light.
- E is the photon energy.

- E_1 and E_2 are the photon energy of the considered transitions.
- ΔE is the optical bandwidth in terms of energy.

With these equation, we understand that an energy difference of 100 meV gives a bandwidth of around 200 nm in L-Band, while it gives a bandwidth of around 140 nm in the O-Band.

Our O-Band design is based on 11 nm thick QWs under a 1.20% compressive strain. As shown in Figure 66, $e_1\text{-}hh_1$ is set at 1361 nm and $e_2\text{-}hh_2$ at 1230 nm, resulting in a theoretical bandwidth of 131 nm.

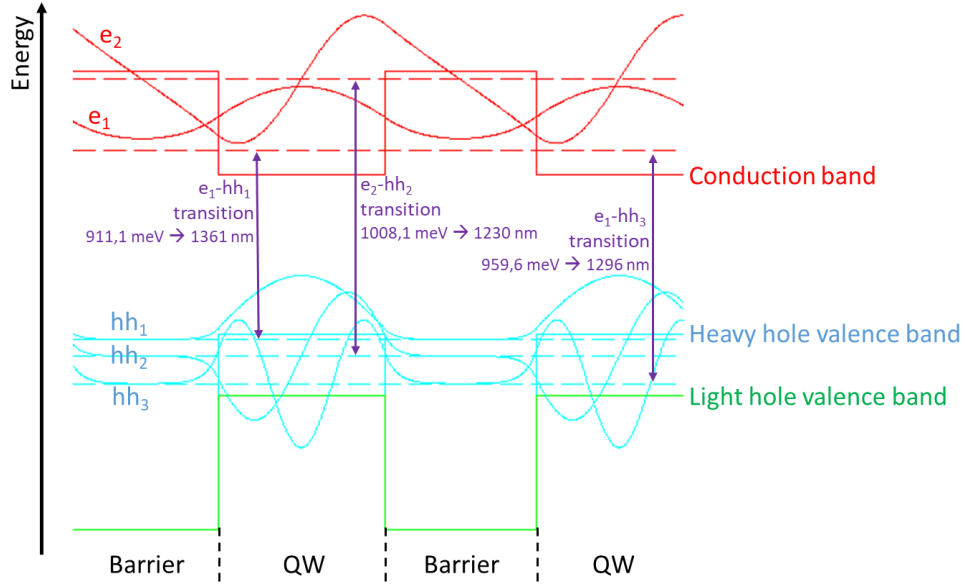


Figure 66. Band alignment simulation of the O-Band active region.

Figure 67 displays the material gain calculation of this structure and Table 22 summarizes the characteristics of our O-Band active.

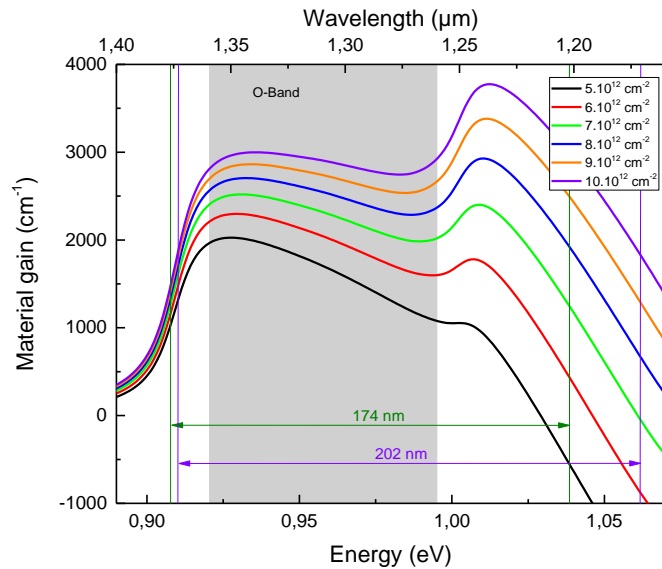


Figure 67. Calculation of g_m , for TE mode, with the O-Band active region design.

<i>Characteristics</i>	<i>Design O</i>
<i>QW thickness</i>	110 Å
<i>Barrier thickness</i>	100 Å
<i>QW strain</i>	+1.20 %
<i>Barrier strain</i>	Lattice-matched
<i>e₁-hh₁ energy</i>	911.1 meV
<i>e₁-hh₃ energy</i>	959.6 meV
<i>e₂-hh₂ energy</i>	1008.1 meV
<i>e₁-hh₁ wavelength</i>	1361 nm
<i>e₁-hh₃ wavelength</i>	1296 nm
<i>e₂-hh₂ wavelength</i>	1230 nm
<i>Theoretical bandwidth</i>	131 nm

Table 22. O-Band active region design.

From previous studies led on C+L-Band, we know that the theoretical bandwidth is always wider than the measured bandwidth at the end of the fabrication process. For this reason, we targeted wider bandwidth than the required 95 nm in C+L-Band and the 100 nm of the O-Band.

The designed active regions have to be implemented in a device structure to obtain SOAs. The next section describes the structure involved in the fabrication process that has to be taken into account for the optical simulations.

1.4. SOA structure

Optical, thermal and electrical properties of the devices can be optimized following their structure. The four main structures currently used in commercial applications are presented in Figure 68.

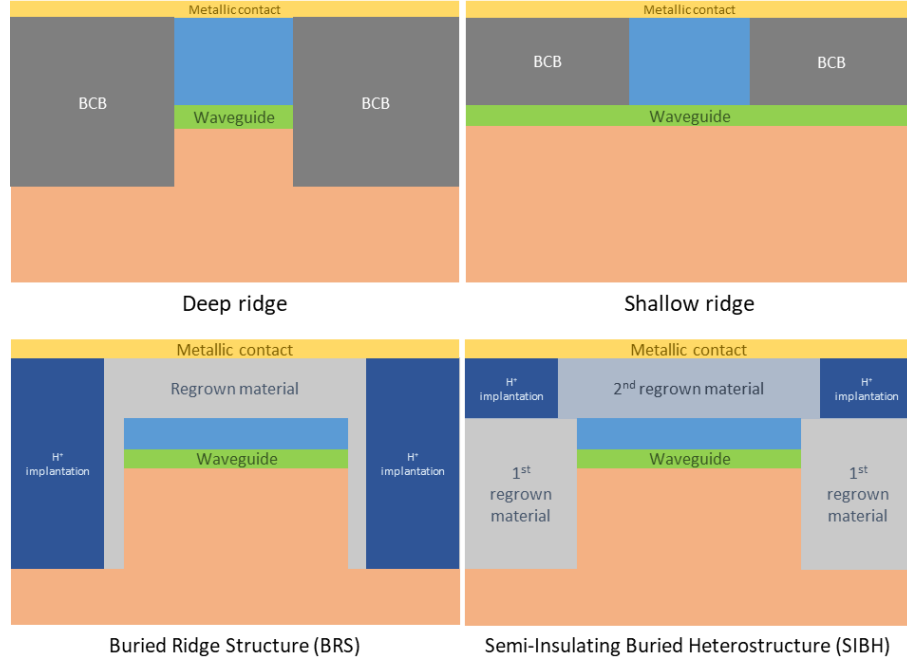


Figure 68. Illustration of the different ridge structures.

Each of them presents advantages and drawbacks, listed in Table 23.

	<i>Advantages</i>	<i>Drawbacks</i>
Deep ridge	<ul style="list-style-type: none"> ➢ Single epitaxy required ➢ High optical confinement ➢ High-speed modulation-compatible 	<ul style="list-style-type: none"> ➢ Very high series resistance (15 Ω) ➢ Very bad thermal dispersion ➢ Not taper-compatible
Shallow ridge	<ul style="list-style-type: none"> ➢ Single epitaxy required ➢ No electric leakage ➢ High-speed modulation-compatible ➢ Active zone not etched 	<ul style="list-style-type: none"> ➢ High series resistance (10 Ω) ➢ Bad thermal dispersion ➢ No simple taper implementation ➢ Not circular optical mode
Buried Ridge Structure (BRS)	<ul style="list-style-type: none"> ➢ Low series resistance (4 Ω) ➢ Good thermal dispersion ➢ Taper-compatible 	<ul style="list-style-type: none"> ➢ Epitaxy regrowth required ➢ Risk of current leakage at high injection ➢ Not high-speed modulation-compatible
Semi-Insulating Buried Heterostructure (SIBH)	<ul style="list-style-type: none"> ➢ Low series resistance (4 Ω) ➢ Good thermal dispersion ➢ High-speed modulation-compatible ➢ Low optical confinement in high absorption material ➢ Taper-compatible 	<ul style="list-style-type: none"> ➢ Epitaxy regrowths required ➢ Risk of current leakage at high injection

Table 23. Advantages and drawbacks of the ridge structures.

The selected structure for our devices is the SIBH, as it presents many advantages and limited drawbacks. Moreover, we have the facilities to achieve epitaxy regrowths. The SIBH fabrication process will be further detailed in Chapter III. With the electronically designed active regions and the structure involved in the SOA fabrication, we can focus on the optical simulations to design the complete structures.

2. Optical confinement simulation

We study the optical mode behavior in the structure with simulations using Fimmwave, a software edited by Photon Design. These simulations enable to set the optical confinement in the QWs (Γ_{QW}) by tuning the surrounding layers. The layers are defined by their dimensions (thickness and width) and their refractive indices. Figure 69 shows Fimmwave's interface after the creation of our SIBH structure.

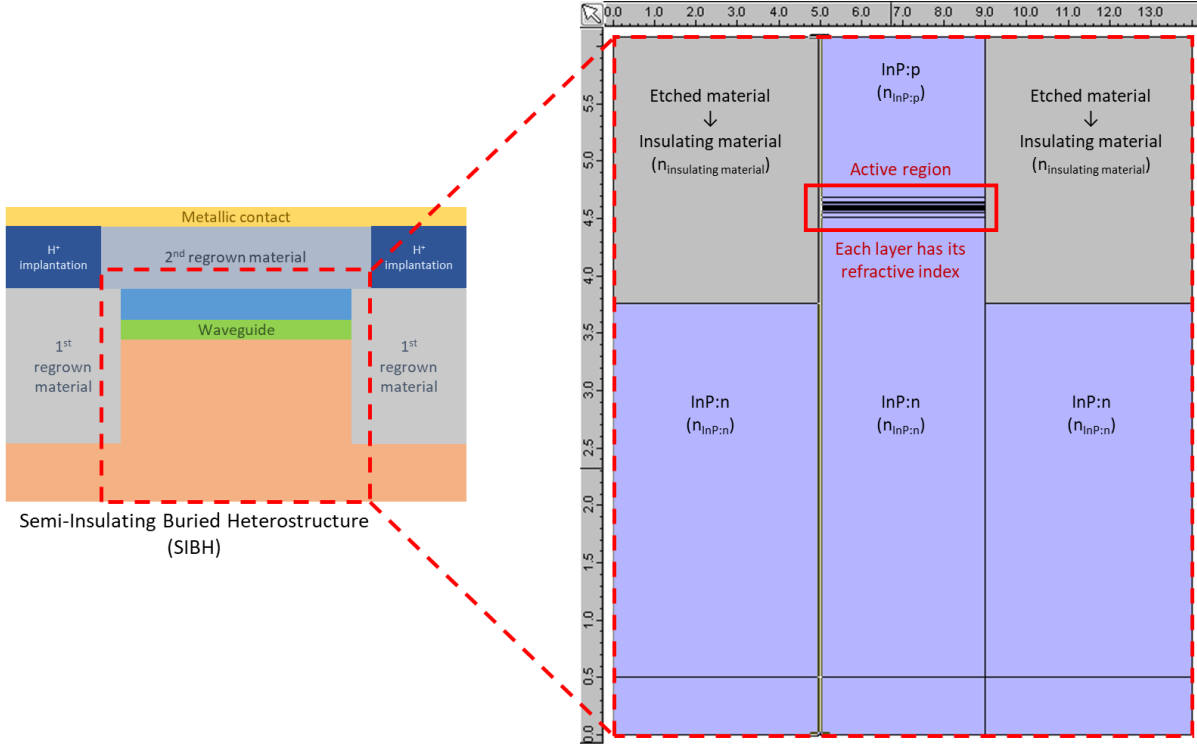


Figure 69. Fimmwave's interface for optical mode simulation creation.

In this section, we determine the refractive indices that are required for the optical simulation. This parameter depends on the material's composition as well as on the operating wavelength. We first focus on the refractive indices of the p- and n-doped InP compounds. Then, we review the literature toward the models used to calculate the refractive indices of GaInAsP alloys to determine our indices. Finally, we design a super-lattice based asymmetric claddings for our structures to set the values of Γ_{QW} .

2.1. Refraction indices in C+L- and O-Bands

In 1965, Pettit and Turner gave a first model to calculate the refractive index of InP depending on the incident wavelength, described by Equation 36 [18]. It is an application of the Sellmeier equation to InP.

$$\text{Equation 36. } n^2 = A + \frac{B\lambda^2}{\lambda^2 - C^2}$$

Where:

- A, B and C are constants set by Pettit and Turner to fit the experimental indices.
- λ is the wavelength of the desired input signal.

This equation shows that, in O-Band, the materials' refractive indices are different from the ones in C+L-Band. With this model, we set the refractive indices of undoped InP to be 3.205 at 1.3 μm , in the O-Band, and 3.166, at 1.55 μm , in the C+L-Band.

During the following decades, several models were developed to calculate the refractive indices of the GaInAsP compounds. In the following paragraphs, we will present a thorough review of these models,

with the view of (i) pointing the specificities of each approach, (ii) present their advantages and weaknesses and (iii) choose the most appropriate for our material description.

2.1.1. Interpolated Sellmeier equation

The Interpolated Sellmeier equation model requires the refractive indices of InP, GaAs, InAs and GaP calculated with Sellmeier equation (Equation 37) [19, 20].

$$\text{Equation 37. } n^2(\lambda) = A_i + \frac{B_i * \lambda^2}{\lambda^2 - C_i}$$

A_i , B_i and C_i are constants which depend on the considered binary material and are set to fit measurements. They are listed in Table 24, such that the wavelength has to be expressed in micrometers (μm).

<i>i</i>	<i>Material</i>	<i>A_i</i>	<i>B_i</i>	<i>C_i</i>	<i>f_i</i>
1	<i>GaAs</i>	8.950	2.054	0.390	xy
2	<i>GaP</i>	4.540	4.310	0.220	x(1-y)
3	<i>InAs</i>	7.790	4.000	0.250	(1-x)y
4	<i>InP</i>	7.255	2.316	0.3922	(1-x)(1-y)

Table 24. Sellmeier coefficients for binary compounds at room temperature.

These constants can be used in the Interpolated Sellmeier equation (Equation 38) to calculate the desired quaternary's refractive index.

$$\text{Equation 38. } n_q^2(\lambda) = \sum_{i=1}^4 \left(A_i + \frac{B_i * \lambda^2}{\lambda^2 - C_i} \right) * f_i = \sum_{i=1}^4 n_i^2(\lambda) * f_i$$

In this equation, f_i varies as a function of the $\text{Ga}_x\text{In}_{(1-x)}\text{As}_y\text{P}_{(1-y)}$ alloy's composition for each binary material as displayed in Table 24.

This model gives better approximations for materials emitting wavelengths that are lower than the one of the input signal, because they do not take the absorption band edge into account. If the studied material has its emitting wavelength near or in the absorption window, this method will not provide accurate refractive indices.

2.1.2. Single oscillator model

In 1971, Wemple and DiDomenico proposed the single-effective-oscillator model (Equation 39) to calculate the refractive indices at a defined photon energy, under the fundamental absorption edge [21].

$$\text{Equation 39. } n^2 - 1 = \frac{E_d * E_0}{(E_0^2 - (\hbar\omega)^2)}$$

Where:

- E_d , is the dispersion energy, which is related to interband optical transitions [22].
- E_0 , is the single oscillator energy.
- $\hbar\omega$, is the incident photon's energy.

Takagi proposed empirical Equation 40 and Equation 41 to calculate E_d and E_0 , taking into account direct and indirect-bandgap compounds [23]. The refractive indices of several "multinary" III-V compounds were calculated and compared with measurements.

$$\text{Equation 40. } E_0 = 1.80 * E_g + 0.90$$

$$\text{Equation 41. } E_d = 9.89 * E_0 * \alpha_{III} * \beta_V$$

α_{III} and β_V are coefficients depending on the III and V elements constituting the studied material, listed in Table 25.

Group-III element	α_{III}	Group-V element	β_V
Aluminum (Al)	0.76	Phosphorus (P)	0.82
Gallium (Ga)	1	Arsenic (As)	1
Indium (In)	1.08	Antimony (Sb)	1.26

Table 25. α_{III} and β_V coefficients [23].

Equation 40 was obtained plotting the single oscillator energy in function of the bandgap energy, for binary compounds that present direct and indirect transitions.

For Equation 41, the difficulty to directly link the dispersion energy to the bandgap, led the authors to express it with specific coefficients. They are supposed to be accurate for $\text{Al}_u\text{Ga}_{1-u}\text{In}_v\text{As}_{1-w-z}\text{P}_w\text{Sb}_z$, with Equation 42 and Equation 43.

$$\text{Equation 42. } \alpha_{III} = 0.76^u * 1.08^z$$

$$\text{Equation 43. } \beta_V = 0.82^w * 1.26^z$$

As we work with GaInAsP alloys, these equations can be simplified with $u = 0$ and $z = 0$.

Studies were also lead to further improve this model, implementing the temperature dependence on the three parameters E_g , E_0 and E_d . To do this, studies suggested to express E_0 and E_d as a function of the temperature dependent E_g [24, 25]. This dependence is visible through Equation 44, proposed by Varshni in [26]. In [24], we can find the implementation of Equation 44 to the expressions of E_0 and E_d proposed by Takagi to obtain Equation 45 and Equation 46.

$$\text{Equation 44. } E_g(T, y) = \left(1.421 - \frac{\alpha * T^2}{T + \beta}\right) - 0.72 * y + 0.12 * y^2$$

$$\text{Equation 45. } E_0(T, y) = 1.894 * E_g(T, y) + 0.8116$$

$$\text{Equation 46. } E_d(T, y) = 9.835 * E_g(T, y) + 15.455$$

Where, α and β are constants obtained by fitting the energy bandgap values of InP between 0 K and 300 K.

The single oscillator model gives reasonable results for photon energies well below the absorption edge in semiconductors. Like Sellmeier model, it neglects absorption effects, limiting the model's application when the incident energy is close to the material bandgap. Moreover, this model has been improved to give results that fit better measured values, as presented in Section 2.1.5.

2.1.3. Tanguy's model

In 1996, Tanguy presented a semi-empirical expression to calculate the refractive index (Equation 47). This model takes into account the excitonic effects and is accurate in the vicinity of the absorption threshold [27].

$$\text{Equation 47. } n^2 - 1 \approx \frac{a}{b - (E + i\Gamma)^2} + \frac{A\sqrt{R}}{(E + i\Gamma)^2} \left\{ \ln \frac{E_g^2}{E_g^2 - (E + i\Gamma)^2} + \pi \left[2 \cot \left(\pi \sqrt{\frac{R}{E_g}} \right) - \cot \left(\pi \sqrt{\frac{R}{E_g - (E + i\Gamma)}} \right) - \cot \left(\pi \sqrt{\frac{R}{E_g + (E + i\Gamma)}} \right) \right] \right\}$$

In this equation, the parameters are:

- a , the height of the absorption peak.
- b , the position of the absorption peak.
- Γ , the energy level broadening.
- A , the Kane momentum matrix element.
- R , the exciton binding energy.

Linear relationships between these parameters and the bandgap energies of $\text{Ga}_x\text{In}_{(1-x)}\text{As}_y\text{P}_{(1-y)}$ alloys, lattice-matched on InP, were proposed by Seifert and Runge to use this model more easily [28]. They are presented from Equation 48 to Equation 52.

$$\text{Equation 48. } a = 72.31936 + 12.77645 * E_g$$

$$\text{Equation 49. } b = 4.84111 + 4.65964 * E_g$$

$$\text{Equation 50. } \Gamma = -0.000691 + 0.00433 * E_g$$

$$\text{Equation 51. } A = -0.04534 + 2.11029 * E_g$$

$$\text{Equation 52. } R = -0.00115 + 0.00191 * E_g$$

This model being given for direct bandgap semiconductor in the vicinity of the absorption threshold will not be taken into account for the calculation of our refractive indices. We consider that the materials involved in our structures, except the QWs' one, have bandgap energies higher enough than the absorption edge energy. As far as the QWs' material is concerned, we use refractive index values that were previously established at III-V Lab.

2.1.4. Interpolation of polarizabilities model

Other researchers attempted to calculate the refractive indices of quaternary materials, for light radiation close to their bandgap energy. Nahory and Pollack proposed Equation 53 to calculate $\text{Ga}_x\text{In}_{(1-x)}\text{As}_y\text{P}_{(1-y)}$ at the material bandgap energy [29]. This equation is only available for quaternary compound lattice matched on InP, thus it only depends on y.

$$\text{Equation 53. } n(E_g) \approx 3.4 + 0.256 * y - 0.095 * y^2$$

To obtain this equation, they interpolated the values of the four binary constituents at their respective bandgap taken from [30]. The refractive indices on which this equation is based were obtained from a combination of reflection and transmission measurements.

Based on the same model, Olsen, Zamerowski, Smith and Bertin proposed other coefficients. They reached Equation 54 with the extrapolation of quaternary material from binary and compared their results with experimental data from vapor grown GaInAsP alloys [31].

$$\text{Equation 54. } n = 3.39 + 0.207 * y - 0.043 * y^2$$

They also implemented the aspect of strain effect, to open the model to the possibility to grow lattice-mismatched quaternary compounds on InP. However, the results obtained from this model does not directly rely on the quaternary composition, so we will not take them into account for our calculations. These equations also suffer a lack of physical justifications as they are mostly based on extrapolation.

Other equation was proposed by Burkhard, Dinges and Kuphal, based on the atomic polarizability, in Equation 55 [32].

$$\text{Equation 55. } n = 3.425 + 0.94 \Delta E + 0.952 * (\Delta E)^2 + (0.255 - 0.257 * \Delta E)y - (0.103 - 0.0952 * \Delta E)y^2$$

This equation is valid when the difference between the studied material's bandgap energy and the incident photon's energy is less than 0.2 eV ($\Delta E = E_g - E \leq 0.2 \text{ eV}$). Consequently, for the same reason as for Tanguy's model, it will not be used to determine our refractive indices.

2.1.5. Modified single oscillator model

In 1974, Afromowitz suggested a modified single oscillator model which provides a more realistic approach of the absorption for $\text{Ga}_{(1-x)}\text{Al}_x\text{As}$ compounds [33]. He presented a semi-empirical method for

the calculation of the room temperature refractive index at energies below the absorption edge, displayed by Equation 56.

$$\text{Equation 56. } n^2 - 1 = \frac{E_d}{E_0} + \frac{E_d * E^2}{E_0^3} + \frac{E_d * E^4}{2 * E_0^3 * (E_0^2 - E_g^2)} * \ln\left(\frac{2 * E_0^2 - E_g^2 - E^2}{E_g^2 - E^2}\right)$$

Where E represents the photon energy.

Utaka, Kobayashi and Suematsu proposed Equation 57 and the Equation 58 to calculate the E_0 and E_d parameters, respectively, to allow the use of the modified single oscillator model with GaInAsP-based material lattice-matched on InP [34]. These equations were obtained with an interpolation method applied to characteristics parameters derived from data on ternary compounds, GaInP and GaInAs, found in [22] and [33].

$$\text{Equation 57. } E_0 = 3.391 - 1.652 * y + 0.863 * y^2 - 0.123 * y^3$$

$$\text{Equation 58. } E_d = 28.91 - 9.278 * y + 5.626 * y^2$$

In both equations, y represents the As fraction of the $\text{Ga}_x\text{In}_{(1-x)}\text{As}_y\text{P}_{(1-y)}$ material, lattice-matched on InP. To integrate the strain's impact on the energy bandgap, Buus and Adams proposed to use Vegard's law to obtain E_0 and E_d for $\text{Ga}_x\text{In}_{(1-x)}\text{As}_y\text{P}_{(1-y)}$ alloys from their values for binary compounds [19].

Otherwise, Broberg and Lindgren proposed to implement a relation between x and y, displayed by Equation 59 [35].

$$\text{Equation 59. } x = \frac{0.1894 * y}{(0.4184 - 0.013 * y)}$$

They obtained Equation 60 and Equation 61 to calculate E_0 and E_d , respectively.

$$\text{Equation 60. } E_0 = 0.595 * x^2 * (1 - y) + 1.626 * x * y - 1.891 * y + 0.524 * x + 3.391$$

$$\text{Equation 61. } E_d = (12.36 * x - 12.71) * y + 7.54 * x + 28.91$$

The refractive indices calculated with these equations are in better agreement with measurements in the transparent region than the results obtained from Buus and Adams [35]. This model is a good candidate for the calculation of our refractive indices.

2.1.6. Dielectric function calculation model

A last model was proposed by Adachi to predict the refractive index of GaInAsP compounds, lattice-matched on InP [36]. In this method, the imaginary part of the dielectric function for direct band-to-band transitions is taken into consideration. It also exploits Kramers-Kronig relations to obtain Equation 62, where A and B parameters are given by Equation 63 and Equation 64. These parameters only take the As fraction into account while they are set for $\text{Ga}_x\text{In}_{(1-x)}\text{As}_y\text{P}_{(1-y)}$ lattice matched on InP, following Equation 65 from [37].

$$\text{Equation 62. } n^2 = A * \left[g\left(\frac{E}{E_g}\right) + 0.5 * \left(\frac{E_g}{E_g + \Delta}\right)^{\frac{3}{2}} * g\left(\frac{E}{E_g + \Delta}\right) \right] + B$$

$$\text{Equation 63. } A = 8.4 - 3.4 * y$$

$$\text{Equation 64. } B = 6.6 + 3.4 * y$$

$$\text{Equation 65. } x \approx 0.46 * y$$

With Δ , the spin-orbit splitting energy which is calculable with Equation 66 and $g(u)$, a function presented by Equation 67.

Equation 66. $\Delta = 0.119 + 0.30 * y - 0.107 * y^2$

Equation 67. $g(u) = \left(2 - (1+u)^{\frac{1}{2}} - (1-u)^{\frac{1}{2}}\right) * u^{-2}$

This model was used in the study of III-V semiconductors based on Al, Ga, In, P, As and Sb grown on InP, at 1.55 μm [38]. The study was led for compounds with bandgaps above 0.9 eV to avoid absorption edge effects. The A and B parameters can be obtained from Equation 63 and Equation 64 or by following Vegard's law using the A and B values of Table 26, taken from [38].

Binary constituent	A	B
GaAs	6.30	9.40
GaP	22.25	0.90
InAs	5.14	10.15
InP	8.40	6.60

Table 26. A and B parameters for GaInAsP system.

The dielectric function calculation model, can be improved by taking into account the temperature dependence of E_g [39].

This model also gave very good approximation of the dependence of refractive index on composition and wavelength in the transparent region, following the measurements and the comparison made by Broberg and Lindgren in [35].

According to this review, we have identified two models (the modified single oscillator and the dielectric function calculation models) as being usable for our indices calculations because, we need to find the $Q_{1.17}$ and the $Q_{1.03}$ refraction index with these models. The first two models do not provide accurate enough results to be considered, and for the models presented in sections 542.1.3 and 2.1.4, our quaternary compounds can be considered far from the absorption threshold. We will see in section 2.2 which one of the modified single oscillator or the dielectric function calculation models will be used. All the presented models are accurate for non-intentionally doped materials. However, some of the layers involved in our structure are doped to enhance the carriers' injection in the active region.

2.1.7. Influence of doping on the refractive index

The refractive index of a material can be modified because of the incorporation of impurities, such as dopants, in the material.

In 1981, Henry, Logan and Bertness calculated the contribution of free carriers in the change of refractive index, Δn , for GaAs material and proposed the following fitting Equation 68 [40].

Equation 68. $\Delta n = -\frac{r_0}{2*\pi*E_{number}^2*n} * \left(\frac{N}{m_e} + \frac{P}{m_h}\right)$

In this equation, we have:

- $r_0 = 2.82 \times 10^{-13}$ cm, the classical radius of an electron.
- E_{number} , the wave number of the incident photon given in cm^{-1} .
- n , the refractive index of the non-intentionally doped material.
- N and P , the density of dopants in the case of n-doping and p-doping, respectively.
- m_e , the electron mass.
- m_h , the hole mass.

In 1990, Bennett, Soref and Del Alamo estimated the variation of the refractive index for InP and GaInAsP caused by free carrier absorption with Equation 69, based on Equation 68, taking into account the mass of both light holes, m_{lh} , and heavy holes, m_{hh} [41].

$$\text{Equation 69. } \Delta n = -\frac{-6.9*10^{-22}}{n*E^2} * \left(\frac{N}{m_e} + P * \frac{m_{hh}^{1/2} + m_{lh}^{1/2}}{m_{hh}^{3/2} + m_{lh}^{3/2}} \right)$$

Even if the information given in [41] enables to calculate the impact on InP, it is not sufficient for GaInAsP alloys. Consequently, we completed Table 27 with information coming from several references [5, 41, 42].

	GaAs	GaP	InAs	InP
m_e/m_0	0.067	0.250	0.023	0.077
m_{hh}/m_0	0.500	0.670	0.400	0.600
m_{lh}/m_0	0.084	0.170	0.026	0.120

Table 27. Mass information for electron and holes in GaAs, GaP, InAs and InP.

This table gives information for binaries, thus, we must use Vergard's law to calculate the $\text{Ga}_x\text{In}_{(1-x)}\text{As}_y\text{P}_{(1-y)}$ parameters.

With Equation 69, we can calculate the refractive indices for our doped InP materials, following their doping type and levels. Their values are 3.160 and 3.165 for n- and p-doped InP, respectively, in the C+L-Band, and 3.193 and 3.196, respectively, in the O-Band.

2.2. Our refractive indices

In this section, we determine between the two selected models which one will be used to calculate the refractive indices of our GaInAsP alloys. However, the best way to access the refractive indices values of the grown materials is by measuring them by spectroscopic ellipsometry. It was done, at III-V Lab, for several quaternary compositions, at 1.55 μm and 1.30 μm . The results are listed in Table 28 and can be used in the optical simulation of our structures.

<i>Material</i>	<i>Photoluminescence peak wavelength (μm)</i>	<i>Refractive index at 1.55 μm</i>	<i>Refractive index at 1.3 μm</i>
<i>InP</i>	0.923	-	3.195
<i>Ga_{0.04}In_{0.96}As_{0.10}P_{0.90}</i>	0.974	3.210	-
<i>Ga_{0.07}In_{0.93}As_{0.14}P_{0.86}</i>	1.005	3.237	3.270
<i>Ga_{0.19}In_{0.81}As_{0.43}P_{0.57}</i>	1.205	3.349	3.426
<i>Ga_{0.27}In_{0.73}As_{0.56}P_{0.44}</i>	1.296	3.404	3.498

Table 28. *GaInAsP* alloys studied by spectroscopic ellipsometry at 1.55 μm .

We report, in Figure 70, the measured refractive indices as a function of the wavelength as well as the Broberg's and Adachi's models, at 1.55 μm . A linear regression from the measured values, given in Equation 70, is also reported.

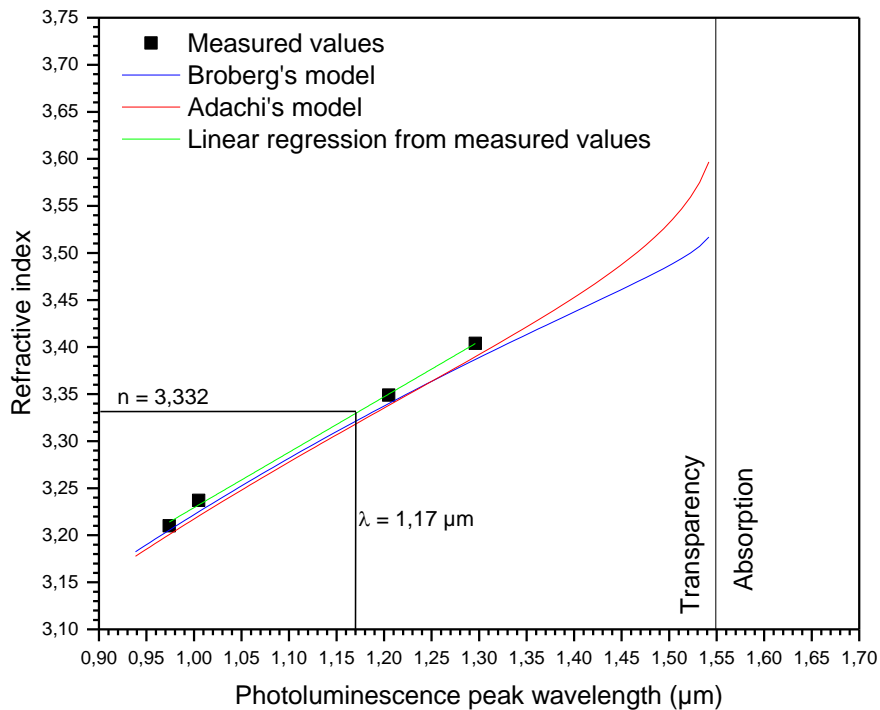


Figure 70. Refractive index of *GaInAsP* alloys measured by spectroscopic ellipsometry at 1.55 μm .

$$\text{Equation 70. } n = 2.643 + 0.589 * \lambda_{PL}$$

Both models taken from the literature provide slightly lower results than the measurements. However, they both show a linear behavior in the region of interest for Q_{1.17}. Consequently, we take the refractive index from the linear regression, which is 3.332 and can conclude that the initial models we had selected are well adjusted for our material.

For the InP layers, we used the model from Pettit and Turner and took into account their doping levels. For the quantum wells, as previously exposed, we use refractive index values that were previously established at III-V Lab.

We summarize the refractive indices involved in the C+L-Band simulations in Table 29.

Material	Refractive index
<i>Upper cladding: InP:p</i>	3.165
<i>Quantum wells</i>	3.550
<i>Barrier: Q_{1.17}</i>	3.332
<i>Semi-insulating material</i>	3.170
<i>Lower cladding: InP:n</i>	3.160

Table 29. C+L-Band refractive indices.

In O-Band, we need to find the Q_{1.03} refractive index. We compared the values from measurements, reported in Table 28, with Broberg's and Adachi's models, in Figure 71, with an operating wavelength of 1.30 μm. We observe that the modified single oscillator model fits correctly our measurements. Consequently, we pick the refractive index value for the barrier's material from this model, which is 3.295.

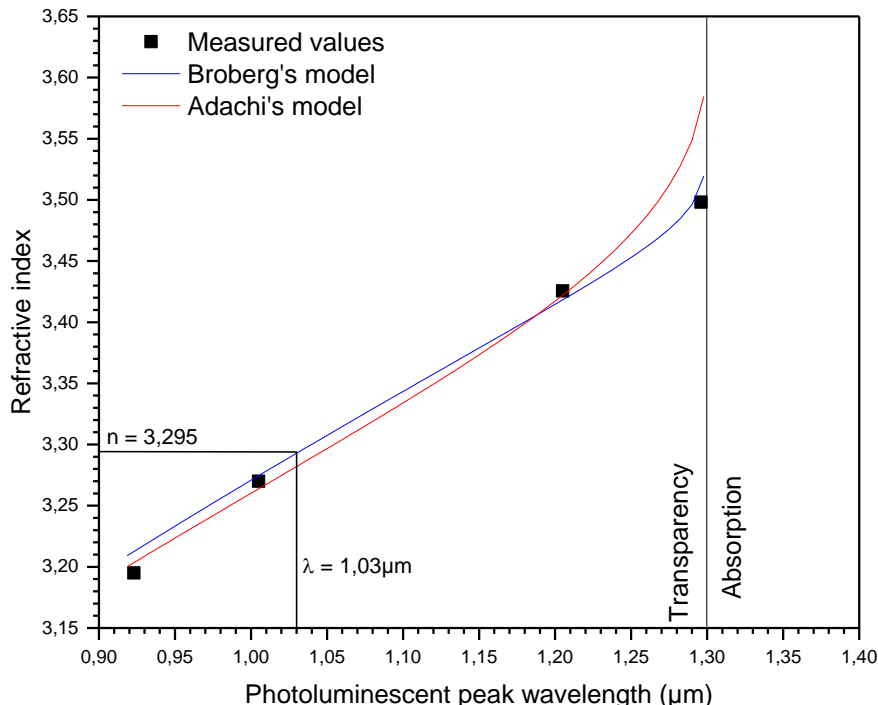


Figure 71. Refractive index of GaInAsP alloys measured by spectroscopic ellipsometry at 1.3 μm.

The refractive indices we use for O-Band simulations are listed in Table 30.

Material	Refractive index
<i>Upper cladding: InP:p</i>	3.196
<i>Quantum wells</i>	3.540
<i>Barrier: Q_{1.03}</i>	3.295
<i>Semi-insulating material</i>	3.198
<i>Lower cladding: InP:n</i>	3.193

Table 30. O-Band refractive indices.

With the refractive indices of the materials involved in the structure, we have the possibility to study the optical mode behavior to design our SOAs.

2.3. Asymmetric cladding

The p-doped layers that constitute the top layers of the structure are known to cause high propagation losses because of the IVBA, which depends on the hole density in this material [43, 44, 45]. To counter this effect, asymmetric structures with n-doped layers were developed. The aim of these layers is to decrease the optical confinement in the p-doped layer (Γ_p) by attracting the optical mode downwards, as shown in Figure 72.

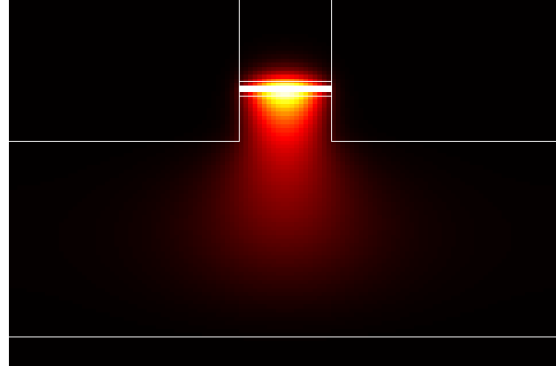


Figure 72. Optical mode simulation with asymmetric cladding.

Reducing Γ_p also reduces Γ_{QW} . It results in higher P_{sat} and lower NF, through the population inversion factor, but also in a lower gain [46]. With the asymmetric cladding, the device becomes a Slab-Coupled Optical Waveguide (SCOW) and we can use large dimensions during the conception, keeping a single mode behavior [47, 48, 49]. Without the slab, a large dimension waveguide would be detrimental in terms of performances because it would provide a multiple mode behavior.

The drawback of wide active regions is that they require higher injection current to provide sufficient carrier density to generate gain. Additionally, there is still a limit in the enlargement of the active region. It still can provide high optical confinement values for other optical modes, as shown in Figure 73, leading to a multi-mode device. The fabrication process of our devices set the width of the waveguides at three main values: 4 μm , 4.5 μm and 5 μm .

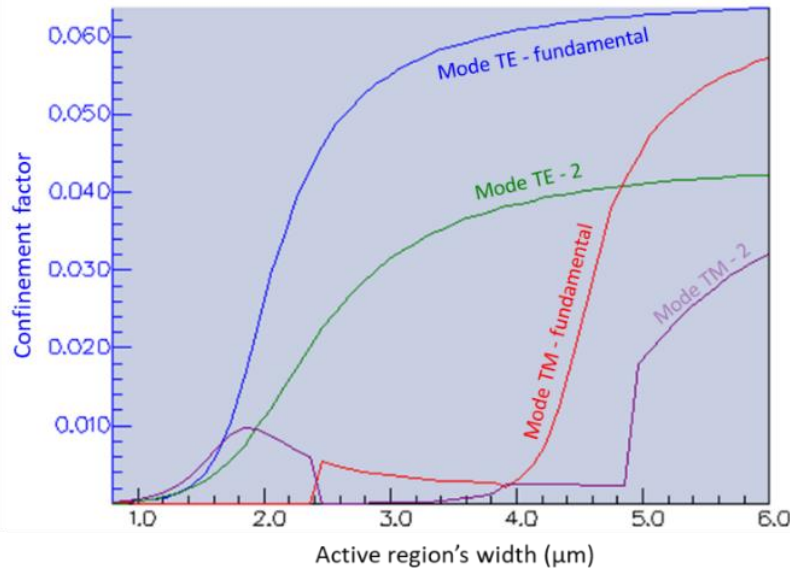


Figure 73. Optical mode confinement in function of the active region width.

Previous developments on C+L-Band SOAs led to the use of Q_{1.03} as unique material for the slab [50]. Here, we develop the idea of a super-lattice slab, illustrated in Figure 74.

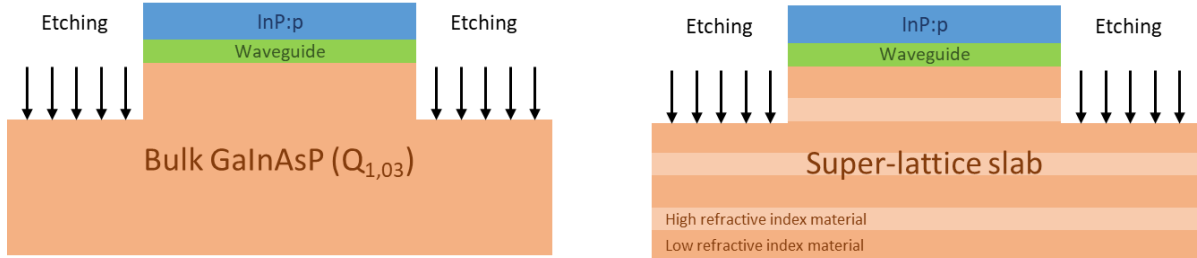


Figure 74. Bulk slab and super-lattice slab illustrations.

This SL is a succession of low refractive index material (InP:n) with high refractive index material ($Q_{1.17}$ in the C+L-Band and $Q_{1.03}$ in the O-Band) that is seen by the optical mode as a bulk material.

This type of structure has advantages over bulk material for the fabrication process. During epitaxy, the growth of a thick bulk material can easily lead to the apparition of dislocations if the growing material is not exactly lattice-matched on the substrate. Moreover, during the fabrication's etching step, monitored by reflectometry, the material difference between the layers enables a better control of the etching depth. This aspect will be further detailed in Chapter III.

The complete thickness of this bottom cladding was 4 μm in the previous developments [50]. To enable comparison with the previous results, we set the complete thickness of our SL slab to be around the same thickness. In terms of composition, we define the percentages of InP and $Q_{1.17}$ in the slab to reach desired values depending on Γ_{QW} . Finally, we calculate the thicknesses that enable to respect this composition in the slab. We have to choose low enough values to avoid impacts of the super-lattice configuration on the optical mode profile. This way, we set the slab configuration for every active regions previously designed, as shown in Table 31.

	C+L-Band	O-Band
QW thickness	140Å	110Å
Complete slab thickness	4.015 μm	4.015 μm
%InP	47 %	57 %
%$Q_{1.17}$ (or %$Q_{1.03}$)	53 %	43 %
Slab period	55 nm	55 nm
InP thickness	26 nm	32 nm
$Q_{1.17}$ or $Q_{1.03}$ thickness	29 nm	23 nm

Table 31. Slab configurations for each designed active region.

Other layers are involved in the control of Γ_{QW} , the Separate-Confinement Heterostructure (SCH) layers. They surround the MQWs and their first role is to enhance the electronic confinement in the active region. However, they also contribute to the optical confinement in the active zone [51]. Their material is the same as the barriers, $Q_{1.17}$ in C+L-Band and $Q_{1.03}$ in O-Band. By varying their thickness, we will study two values of Γ_{QW} for each structure to compare their behaviors with “high” and “low” optical confinement. The set thicknesses are listed in Table 32.

	C+L-Band		O-Band
QW thickness	140Å	110Å	110Å
“High” Γ_{QW}	80 nm	80 nm	75 nm
“Low” Γ_{QW}	60 nm	63 nm	55 nm

Table 32. SCH thicknesses for the different structures.

The etching depth is the last parameter to control the optical mode behavior. Indeed, as can be observed in Figure 75, this value impacts the optical confinement of the fundamental mode, which increases at the beginning of the etching.

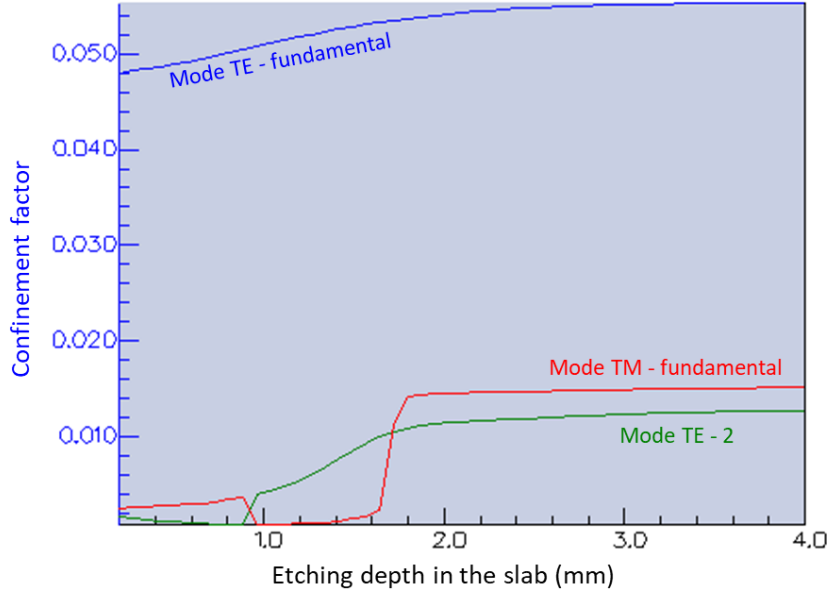


Figure 75. Etching depth impact over the optical confinement modes in the active region.

However, it also impacts the optical confinement of the other modes. Figure 76 shows the apparition of a second mode in the case of a too deep etching.

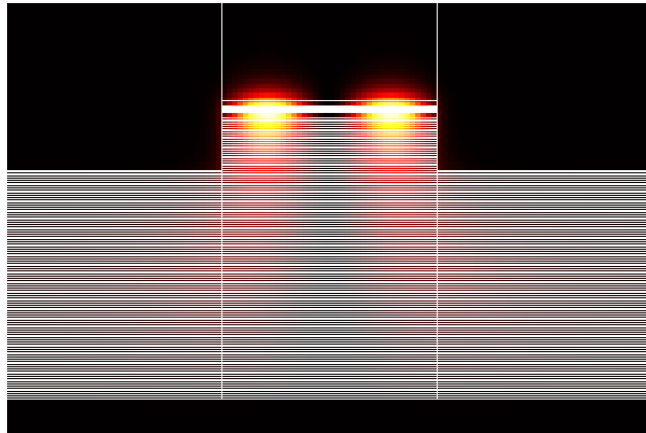


Figure 76. Second mode simulation in SOA SIBH structure.

The etching depth value must be well defined and respected during the etching step of the fabrication process to avoid a multimodal behavior of the device. The optimized etching depths, in the slab, for every structure, are set to be between 700 μm and 750 μm .

In the conclusion of this chapter, we summarize the set characteristics and the Γ_{QW} for each structure that was designed in this work.

3. Complete designs of C+L and O-Bands devices

According to the modeling, we have designed 4 devices in C+L-Band and 2 in O-Band. Their structures are summarized in the tables below.

3.1. C+L-Band structures

A first simulation campaign led us to the conception the structures presented in Table 33 and Table 34, for the C+L-Band.

Layer	Material	Thickness	Repetition
<i>Top cladding</i>	InP:p	200 nm	-
<i>SCH</i>	GaInAsP ($\lambda=1.17 \mu\text{m}$)	80 nm ¹ / 60 nm ²	-
<i>Quantum Well</i>	GaInAsP	140 Å	4
<i>Barrier</i>	GaInAsP ($\lambda=1.17 \mu\text{m}$)	100 Å	3
<i>SCH</i>	GaInAsP ($\lambda=1.17 \mu\text{m}$)	80 nm ¹ / 60 nm ²	-
<i>Slab</i>	GaInAsP:n ($\lambda=1.17 \mu\text{m}$)	29 nm	73
<i>Slab</i>	InP:n	26 nm	73
<i>Buffer</i>	InP:n	500 nm	-

Table 33. Growth structure based on the 140 Å-thick quantum well active region.

Layer	Material	Thickness	Repetition
<i>Top cladding</i>	InP:p	200 nm	-
<i>SCH</i>	GaInAsP ($\lambda=1.17 \mu\text{m}$)	80 nm ¹ / 63 nm ²	-
<i>Quantum Well</i>	GaInAsP	110 Å	4
<i>Barrier</i>	GaInAsP ($\lambda=1.17 \mu\text{m}$)	90 Å	3
<i>SCH</i>	GaInAsP ($\lambda=1.17 \mu\text{m}$)	80 nm ¹ / 63 nm ²	-
<i>Slab</i>	GaInAsP:n ($\lambda=1.17 \mu\text{m}$)	23 nm	73
<i>Slab</i>	InP:n	32 nm	73
<i>Buffer</i>	InP:n	500 nm	-

Table 34. Growth structure based on the 110 Å-thick quantum well active region.

In both tables, the superscript 1 is for “high” values of optical confinement in QWs, while the superscript 2 is for the structures providing a lower Γ_{QW} . The etching depth was set to be 750 nm in the slab for the first structure and 700 nm in the second, to keep a single mode behavior in our structures.

A second simulation campaign was led after the growth of these structures, that will be detailed in Chapter III, to calculate the Γ_{QW} , fitting the grown structures’ characteristics. We simulated the three different ridge widths that we had set for the fabrication process and the results are listed in Table 35.

<i>QW thickness</i>	<i>Simulated Γ_{QW} for “Thick” SCH</i>			<i>Simulated Γ_{QW} for “Thin” SCH</i>		
	4 μm	4.5 μm	5 μm	4 μm	4.5 μm	5 μm
140 Å	5.20 %	5.33 %	5.42 %	3.16 %	3.38 %	3.55 %
110 Å	5.88 %	5.97 %	6.04 %	4.16 %	4.34 %	4.46 %

Table 35. Optical confinement values obtained for our grown structures.

3.2. O-Band structures

The designed structure for O-Band SOAs are presented in Table 36. The etching depth of this structure is set to be 750 nm in the super-lattice slab.

Layer	Material	Thickness	Repetition
<i>Upper cladding</i>	InP:p	200 nm	-
<i>Superior SCH</i>	GaInAsP ($\lambda=1.03 \mu\text{m}$)	75 nm ¹ / 55 nm ²	-
<i>Quantum Well</i>	GaInAsP	110 Å	4
<i>Barrier</i>	GaInAsP ($\lambda=1.03 \mu\text{m}$)	100 Å	3
<i>Inferior SCH</i>	GaInAsP ($\lambda=1.03 \mu\text{m}$)	75 nm ¹ / 55 nm ²	-
<i>Slab</i>	GaInAsP:n ($\lambda=1.03 \mu\text{m}$)	29 nm	73
<i>Slab</i>	InP:n	26 nm	73
<i>Buffer</i>	InP:n	500 nm	-

Table 36. Growth structure based on the O-Band quantum well active region's design.

The calculated optical confinements in the QWs, fitting the grown structures' characteristics, are visible in Table 37.

<i>QW thickness</i>	<i>Simulated Γ_{QW} for "Thick" SCH</i>			<i>Simulated Γ_{QW} for "Thin" SCH</i>		
	4 μm	4.5 μm	5 μm	4 μm	4.5 μm	5 μm
110 Å	4.63 %	4.79 %	4.95 %	2.90 %	3.13 %	3.30 %

Table 37. Optical confinement simulated for the O-Band structures.

The next Chapter will describe the epitaxy steps and fabrication process of these structures to obtain the SOAs and RSOAs.

4. Conclusion

In this chapter, we studied the strain's impact on the band structure and the polarization sensitivity of the devices. We compared the wideband amplification with narrow and large QWs. We also studied the impact of the QWs' bandgap energy, thickness and strain, as well as the impact of the band offset between QWs and barriers on the material gain. These simulations enabled us to design three active regions for wideband amplification (two in C+L-Band, one in O-Band). We exposed the SOAs' structure to realize the optical simulations of the devices. For these simulations, we reviewed the literature in order to select models to determine the refractive indices of our materials. We conceived a super-lattice slab that enables more stability during the epitaxial growth and a more accurate etching. Finally, we designed the complete structures of the devices which were grown, processed and characterized, and presented in Chapter III and IV.

Bibliography

- [1] E. Yablonovitch and E. O. Kane, "Band structure engineering of semiconductor lasers for optical communications," *Journal of lightwave technology*, vol. 6, no. 8, pp. 1292-1299, 1988.
- [2] E. Yablonovitch and E. O. Kano, "Reduction of the lasing threshold current density by the lowering of valence band effective mass," *Journal of lightwave technology*, Vols. LT-4, no. 5, pp. 504-506, 1986.
- [3] A. R. Adams, "Band-structure engineering for low-threshold high-efficiency semiconductor lasers," *Electronics letters*, vol. 22, no. 5, pp. 249-250, 1986.
- [4] P. J. A. Thijs, L. F. Tiemeijer, J. J. M. Binsma and T. van Dongen, "Progress in long-wavelength strained-layer InGaAs(P) quantum-well semiconductor lasers and amplifiers," *IEEE journal of quantum electronics*, vol. 30, no. 2, pp. 477-499, 1994.
- [5] J. Minch, S. H. Park, T. Keating and S. L. Chuang, "Theory and experiment of In_{1-x}Ga_xAs_yP_{1-y} and In_{1-x-y}Ga_xAl_yAs long-wavelength strained quantum-well lasers," *IEEE journal of quantum electronics*, vol. 35, no. 5, pp. 771-782, 1999.
- [6] G. L. Bir and G. E. Pikus, *Symmetry and strain induced effects in semiconductors*, New York: Wiley, 1974.
- [7] H. Carrère, S. R. Joshya, Q. Hochart, C. Calò, X. Marie, O. Delorme, A. Balocchi and A. Wilk, "Materials for wide-band amplification," in *13th International Symposium on Communication Systems, Networks and Digital Signal Processing (CSNDSP)*, Porto, PORTUGAL, 2022.
- [8] G. Bastard, *Wave mechanics applied to semiconductor heterostructures*, 1990.
- [9] K. Morito and S. Tanaka, "Record high saturation power (+22 dBm) and low noise figure (5.7 dB) polarization-insensitive SOA module," *IEEE photonics technology letters*, vol. 17, no. 6, pp. 1298-1300, 2005.
- [10] J. Renaudier, A. Arnould, A. Ghazisaeidi, D. Le Gac, P. Brindel, E. Awwad, M. Makhsian, K. Mekhazni, F. Blache, A. Boutin, L. Letteron, Y. Frignac, N. Fontaine, M. Achouche and D. Neilson, "Recent advances in 100+nm ultra-wideband fiber-optic transmission systems using semiconductor optical amplifiers," *Journal of lightwave technology*, vol. 38, no. 5, pp. 1071-1079, 2020.
- [11] K. Morito, S. Tanaka, S. Tomabechi and A. Kuramata, "A broad-band MQW semiconductor optical amplifier with high saturation output power and low noise figure," *IEEE photonics technology letters*, vol. 17, no. 5, pp. 974-976, 2005.
- [12] B. I. Miller, U. Koren, M. A. Newkirk, M. G. Young, R. M. Jopson, R. M. Derosier and M. D. Chien, "Tensile-strained InGaAs/InGaAsP quantum-well optical amplifiers with a wide spectral gain region at 1.55 μm," *IEEE photonics technology letters*, vol. 5, no. 5, pp. 520-522, 1993.
- [13] P. Koonath, S. Kim, W.-J. Cho and A. Gopinath, "Polarization-insensitive quantum-well semiconductor optical amplifiers," *IEEE journal of quantum electronics*, vol. 38, no. 9, pp. 1282-1290, 2002.

- [14] S. L. Chuang, J. O'Gorman and A. F. J. Levi, "Amplified spontaneous emission and carrier pinning in laser diodes," *IEEE Journal of quantum electronics*, vol. 29, no. 6, pp. 1631-1639, 1993.
- [15] S. L. Chuang, "Optical gain of strained wurtzite GaN quantum-well lasers," *IEEE journal of quantum electronics*, vol. 32, no. 10, pp. 1791-1800, 1996.
- [16] W. L. Li, Y. K. Su and D. H. Jaw, "The influences of refractive index dispersion on the modal gain of a quantum-well laser," *IEEE journal of quantum electronics*, vol. 33, no. 3, pp. 416-423, 1997.
- [17] P. M. Enders, "Enhancement and spectral shift of optical gain in semiconductors from non-Markovian intraband relaxation," *IEEE journal of quantum electronics*, vol. 33, no. 4, pp. 580-588, 1997.
- [18] G. D. Pettit and W. J. Turner, "Refractive index of InP," *Journal of applied physics*, vol. 36, p. 2081, 1965.
- [19] J. Buus and M. J. Adams, "Phase and group indices for double heterostructure lasers," *Solid-state and electron devices*, vol. 3, no. 6, pp. 189-195, 1979.
- [20] M. S. Whalen and J. Stone, "Index of refraction of n-type InP at 0.633- μm and 1.15- μm wavelengths as a function of carrier concentration," *Journal of applied physics*, vol. 53, no. 6, pp. 4340-4343, 1982.
- [21] S. H. Wemple and M. DiDomenico Jr., "Behavior of the electronic dielectric constant in covalent and ionic materials," *Physical review B*, vol. 3, no. 4, pp. 1338-1351, 1971.
- [22] T. Takagi, "Refractive index of Ga_{1-x}In_xAs prepared by vapor-phase epitaxy," *Japanese journal of applied physics*, vol. 17, no. 10, pp. 1813-1817, 1978.
- [23] T. Takagi, "Dispersion parameters of the refractive index in III-V compound semiconductors," *Japanese journal of applied physics*, vol. 21, no. 3, pp. L167-L169, 1982.
- [24] D. Melati, A. Waqas, A. Alippi and A. Melloni, "Wavelength and composition dependence of the thermo-optic coefficient for InGaAsP-based integrated waveguides," *Journal of applied physics*, vol. 120, no. 21, pp. 1-8, 2016.
- [25] A. Waqas, D. Melati, Z. Mushtaq, B. S. Chowdhry and A. Melloni, "An improved model to predict the temperature dependence of refractive index of InP-based compounds," *Wireless personal communications*, vol. 95, pp. 607-615, 2017.
- [26] Y. P. Varshni, "Temperature dependence of the energy gap in semiconductors," *Physica*, vol. 34, no. 1, pp. 149-154, 1967.
- [27] C. Tanguy, "Refractive index of direct bandgap semiconductors near the absorption threshold: Influence of excitonic effects," *IEEE journal of quantum electronics*, vol. 32, no. 10, pp. 1746-1751, 1996.
- [28] S. Seifert and P. Runge, "Revised refractive index and absorption of In_{1-x}GaxAs_yP_{1-y} lattice-matched to InP in IR-transparent and absorption region," *Optical materials express*, vol. 6, no. 2, pp. 629-639, 2016.

- [29] R. E. Nahory and M. A. Pollack, "Threshold dependence on active-layer thickness in InGaAsP/InP D.H. lasers," *Electronics letters*, vol. 14, no. 23, pp. 727-729, 1978.
- [30] B. O. Seraphin and H. E. Bennett, "Chapter 12 - Optical constants," in *Semiconductors and semimetals, Volume 3*, Willardson, R. K.; Beer, Albert C., 1967, pp. 499-543.
- [31] G. H. Olsen, T. Z. Zamerowski, R. T. Smith and E. P. Bertin, "InGaAsP quaternary alloys: composition, refractive index and lattice mismatch," *Journal of electronic materials*, vol. 9, no. 6, pp. 977-987, 1980.
- [32] H. Burkhard, H. W. Dinges and E. Kuphal, "Optical properties of In_{1-x}GaxP_{1-y}As_y, InP, GaAs, and GaP determined by ellipsometry," *Journal of applied physics*, vol. 53, no. 1, pp. 655-662, 1982.
- [33] M. A. Afromowitz, "Refractive index of Ga_{1-x}Al_xAs," *Solid state communications*, vol. 15, no. 1, pp. 59-63, 1974.
- [34] K. Utaka, K.-I. Kobayashi and Y. Suematsu, "Lasing characteristics of 1,5-1,6 μm GaInAsP/InP integrated twin-guide lasers with first order distributed Bragg reflectors," *IEEE journal of quantum electronics*, Vols. QE-17, no. 5, pp. 651-658, 1981.
- [35] B. Broberg and S. Lindgren, "Refractive index of In_{1-x}GaxAs_yP_{1-y} layers and InP in the transparent wavelength region," *Journal of applied physics*, vol. 55, no. 9, pp. 3376-3381, 1984.
- [36] S. Adachi, "Refractive indices of III-V compounds: key properties of InGaAsP relevant to device design," *Journal of applied physics*, vol. 53, no. 8, pp. 5863-5869, 1982.
- [37] R. E. Nahory, M. A. Pollack, W. D. Johnston and R. L. Barns, "Band gap versus composition and demonstration of Vegard's law for In_{1-x}GaxAs_yP_{1-y} lattice matched to InP," *Applied physics letters*, vol. 33, no. 7, pp. 659-661, 1978.
- [38] M. Guden and J. Piprek, "Material parameters of quaternary III-V semiconductors for multilayer mirrors at 1,55 μm wavelength," *Modelling and simulation in materials science and engineering*, vol. 4, no. 4, pp. 349-357, 1996.
- [39] J.-P. Weber, "Optimization of the carrier-induced effective index change in InGaAsP waveguides - Application to tunable Bragg filters," *IEEE journal of quantum electronics*, vol. 30, no. 8, pp. 1801-1816, 1994.
- [40] C. H. Henry, R. A. Logan and K. A. Bertness, "Spectral dependence of the change in refractive index due to carrier injection in GaAs lasers," *Journal of applied physics*, vol. 52, no. 7, pp. 4457-4461, 1981.
- [41] B. R. Bennett, R. A. Soref and J. A. Del Alamo, "Carrier-induced change in refractive index of InP, GaAs, and InGaAsP," *IEEE journal of quantum electronics*, vol. 26, no. 1, pp. 113-122, 1990.
- [42] S. L. Chuang, "Appendix K - Electronic properties of Si, Ge, and a few binary, ternary, and quaternary compounds," in *Physics of Optoelectronic devices*, New York, Wiley, 1995, p. 709.
- [43] C. H. Henry, R. A. Logan, F. R. Merritt and J. P. Luongo, "The effect of intervalence band absorption on the thermal behavior," *IEEE journal of quantum electronics*, Vols. QE-19, no. 6, pp. 947-952, 1983.

- [44] H. C. Casey Jr. and P. L. Carter, "Variation of the intervalence band absorption with hole concentration in p-type InP," *Applied physics letters*, vol. 44, no. 1, pp. 82-83, 1984.
- [45] G. N. Childs, S. Brand and R. A. Abram, "Intervalence band absorption in semiconductor laser materials," *Semiconductor science and technology*, vol. 1, no. 2, pp. 116-120, 1986.
- [46] P. W. Juodawlkis, J. J. Plant, W. Loh, L. J. Missaggia, K. E. Jensen and F. J. O'Donnell, "Packaged 1,5- μm quantum-well SOA with 0,8-W output power and 5,5-dB noise figure," *IEEE photonics technology letters*, vol. 21, no. 17, pp. 1208-1210, 2009.
- [47] E. A. J. Marticatili, "Slab-coupled waveguides," *Bell system technical journal*, vol. 53, no. 11, pp. 645-674, 1974.
- [48] P. W. Juodawlkis, J. J. Plant, W. Loh, L. J. Missaggia, F. J. O'Donnell, D. C. Oakley, A. Napoleone, J. Klamkin, J. T. Gopinath, D. J. Ripin, S. Gee, P. J. Delfyett and J. P. Donnelly, "High-power, low-noise, 1,5- μm slab-coupled optical waveguide (SCOW) emitters: physics, devices, and applications," *IEEE journal of selected topics in quantum electronics*, vol. 17, no. 6, pp. 1698-1714, 2011.
- [49] J. N. Walpole, J. P. Donnelly, P. J. Taylor, L. J. Missaggia, C. T. Harris, R. J. Bailey, A. Napoleone, S. H. Groves, S. R. Chinn, R. Huang and J. Plant, "Slab-coupled 1,3- μm semiconductor laser with single-spatial large-diameter mode," *IEEE photonics technology letters*, vol. 14, no. 6, pp. 756-758, 2002.
- [50] A. Verdier, "Modélisation, conception, fabrication, caractérisation et valorisation d'amplificateurs optiques à semiconducteur de très large bande spectrale. (PhD Thesis)," Université de Toulouse, Toulouse, FRANCE, 2018.
- [51] S. H. Groves, "InGaAs/GaInAsP/GaInP strained-layer quantum well separate-confinement heterostructures grown by OMVPE," *Journal of crystal growth*, vol. 124, no. 1-4, pp. 747-750, 1992.

Figures

Figure 51. Illustration of tensile and compressive strain.....	35
Figure 52. Band alignment of GaInAsP/GaInAsP QW under tensile and compressive strain [7].	36
Figure 53. Signal propagation in the SOA with TE and TM polarization modes.	37
Figure 54. Polarization independent module using a single SOA.	39
Figure 55. Polarization independent module using two SOAs.....	39
Figure 56. Gain behavior with injected current increase with two confined transitions.	41
Figure 57. Raman scattering impact over amplification spectrum in long haul transmission system...	41
Figure 58. Simulations of g_m , for TE mode, in function of the bulk material's E_g set for QW.	42
Figure 59. Simulations of g_m , for TE mode, in function of the strain incorporated in the QW.....	43
Figure 60. Simulations of g_m , for TE mode, in function of the band offset between barriers and QW. 44	44
Figure 61. Simulations of g_m , for TE mode, in function of the QW thickness.....	45
Figure 62. Band alignment simulation of the first C+L-Band active region.	46
Figure 63. Calculation of g_m , for TE mode, with the first C+L-Band active region design.....	47
Figure 64. Band alignment simulation of the second C+L-Band active region.	47
Figure 65. Calculation of g_m , for TE mode, with the second C+L-Band active region design.	48
Figure 66. Band alignment simulation of the O-Band active region.....	49
Figure 67. Calculation of g_m , for TE mode, with the O-Band active region design.....	49
Figure 68. Illustration of the different ridge structures.	51
Figure 69. Fimmwave's interface for optical mode simulation creation.....	52
Figure 70. Refractive index of GaInAsP alloys measured by spectroscopic ellipsometry at $1.55\mu\text{m}$...	59
Figure 71. Refractive index of GaInAsP alloys measured by spectroscopic ellipsometry at $1.3\mu\text{m}$	60
Figure 72. Optical mode simulation with asymmetric cladding.....	61
Figure 73. Optical mode confinement in function of the active region width.....	61
Figure 74. Bulk slab and super-lattice slab illustrations.....	62
Figure 75. Etching depth impact over the optical confinement modes in the active region.....	63
Figure 76. Second mode simulation in SOA SIBH structure.	63

Tables

Table 18. Constants for strain impact calculation over GaInAsP bandgap energy.	37
Table 19. Selection rules for interband transitions given by [8], in $k_\perp = 0$	38
Table 20. Energy transitions wavelengths in simulated SOA structure.	40
Table 21. C+L-Band active region designs.	48
Table 22. O-Band active region design.	50
Table 23. Advantages and drawbacks of the ridge structures.	51
Table 24. Sellmeier coefficients for binary compounds at room temperature.	53
Table 25. α_{III} and β_V coefficients [23].	54
Table 26. A and B parameters for GaInAsP system.....	57
Table 27. Mass information for electron and holes in GaAs, GaP, InAs and InP.	58
Table 28. GaInAsP alloys studied by spectroscopic ellipsometry at $1.55 \mu\text{m}$	59
Table 29. C+L-Band refractive indices.	60
Table 30. O-Band refractive indices.....	60
Table 31. Slab configurations for each designed active region.	62
Table 32. SCH thicknesses for the different structures.	62
Table 33. Growth structure based on the 140 \AA -thick quantum well active region.	64
Table 34. Growth structure based on the 110 \AA -thick quantum well active region.	64
Table 35. Optical confinement values obtained for our grown structures.....	64
Table 36. Growth structure based on the O-Band quantum well active region's design.	65
Table 37. Optical confinement simulated for the O-Band structures.	65

Chapter 3 – Molecular Beam Epitaxy of wideband SOA and technological process fabrication

Having established the epitaxial structures in both C+L and O bands for the realization of SOAs and RSOAs, this chapter focuses on the devices fabrication. Both MBE and MOCVD epitaxy techniques are performed at different steps of the process. We give a short description of the equipment involved in the fabrication and the rationale behind their use.

It has to be noticed that the epitaxy process of the C+L-Band SOA has been initially developed on the R100 reactor late 2016. Since then and up to 2020, several attempts at reiterate the growth of 2016 structures have been unsuccessful. A lack of reactor availability due to multiple reactor failures have been proven difficult to sustain a comprehensive and coherent approach.

We can mention the following epitaxy reactors involved in this work:

- The GSMBE reactor R100-type, a RIBER modified V100 from Thermo VG Scientific, to grow the main structures.
- An horizontal Aixtron AIX200/4, for the regrowth of the InP:Fe SIBH, well established so called 2-step process.
- A close-coupled showerhead MOCVD reactor from Aixtron, for the InP:Fe regrowth of the 1-step SIBH process, more recently developed at III-V Lab.
- Finally, a RIBER MBE412 gas-source MBE reactor installed last year at III-V Lab, into which the R100-developed processes have been transferred. This MBE system is equipped with a broad range of state-of-the-art *in situ* characterization tools.

GSMBE reactor specificities are shared, especially for the growth of GaInAsP-based quaternary compounds, for which the control of the As/P ratio is a key parameter. Specific calibration procedures of the Building Blocks (BB) (Bulk materials, Slabs and Active layers) are described, involving RHEED, curvature measurement as *in situ* tools and XRD and PL, as non-destructive characterization tools. Growth conditions of the $\text{Ga}_{0.36}\text{In}_{0.64}\text{As}_{0.77}\text{P}_{0.23}$ quaternary alloy, being situated in the miscibility gap of the GaInAsP/InP phase diagram is discussed. Additional characterizations, such as photocurrent measurement and time-resolved PL, allowing to further assess physical properties of MBE material are performed.

A grand total of 21 epiwafers, based on the 2 O-band and the 4 C+L-band designs have been grown. Our MBE reactor being multi-wafer, sister-wafers of the same run have been processed using either the 1-step SIBH or 2-step SIBH technology. Possible failures during the fabrication have been taken into account, considering that the 1-step SIBH is not yet fully mature and the 2-step SIBH requires a significantly large number of steps.

Pros and cons of each design are explained. Pre-MOCVD regrowth SIBH fabrication are described. A short description of the regrowth process of MOCVD-grown InP:Fe and InP:Zn is discussed. We also give a short description of the back-end process for both SOA and RSOA devices.

Finally, 15 epiwafers have been fully processed, allowing to compare the different designs and technologies carried-out and potentially define the premises of a pilot-line production capability for the III-V Lab.

1. Epitaxy techniques

In this section, we present the MOCVD technique and discuss the architectures of the reactors used for the regrowth steps. Then, we focus on MBE and more specifically GSMBE, which is the technique used to grow our main structures, containing the super lattice slab, the SCH layers, the MQW and a thin top cladding layer. We also detail the GSMBE reactors involved in the SOA and RSOA developments.

1.1. Metal-Organic Chemical Vapor Deposition for SIBH process

MOCVD was developed in the end of the 1960s, by Manasevit [1]. It uses metalorganic precursors for group-III elements, based on organic alkyls radicals (C_nH_{2n+1})_x. Trimethylindium (TMIn), Trimethylgallium (TMGa) and Trimethylaluminum (TMAI) are the usual precursors. A carrier gas, Dihydrogen (H_2) is required to flow the precursors from their cylinders to the reaction chamber. The group-V elements are hydrides, Arsine (AsH_3) and Phosphine (PH_3). Typical growth temperatures for InP-based materials are in the 600 to 700°C range. Precursors' pyrolysis and subsequent crystallization occur at the surface of the heated substrate, as illustrated in Figure 77.

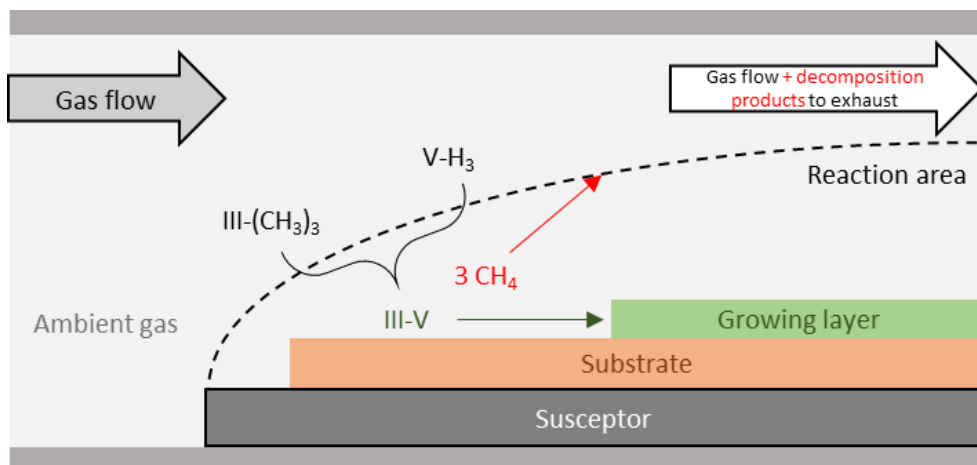


Figure 77. MOCVD growth principle [2].

The decomposition products, resulting from the pyrolysis are evacuated from the reactor, with the carrier gas. The pressures of operation in the MOCVD reactors can vary from 50 to 150 mbar for Low Pressure MOCVD (LPCVD) up to Atmospheric Pressure (APCVD).

MOCVD is well suited for the regrowth steps on patterned processed wafers. The high H_2 pressures in the growth chamber enhance the diffusion phenomena of the vapor phase reactive species at the substrate's surface. Moreover, at growth temperatures, the group-III elements cannot bind with the non-crystalline dielectric mask that protects the ridges, avoiding regrowth on the mask.

Two MOCVD systems have been used, in the context of the distinct SIBH fabrication process carried out on the MBE grown epiwafers. 1-step and 2-step SIBH fabrication processes will be further detailed.

1.1.1. AIX200/4 horizontal reactor for 2-step SIBH.

The architecture of the reactor involved in the 2-step SIBH process is schematized in Figure 78. The gas flow crosses the growth chamber horizontally while the substrate is rotating to provide a homogeneous deposition. The substrate is heated by Infrared (IR) radiations. Both this reactor and associated 2-step SIBH process are commonly used at the laboratory. It will provide a reference in terms of device performance to be compared with 1-step SIBH.

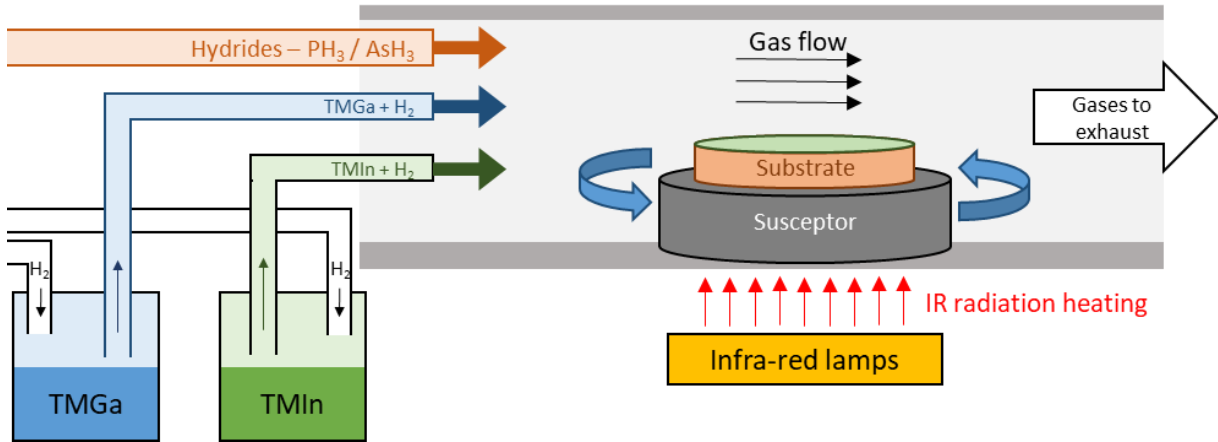


Figure 78. Schematic of a radial flow MOCVD reactor.

1.1.2. Closed-Coupled Showerhead (CCS) reactor

In the frame of the development of the 1-step SIBH process, we have been using a CCS reactor equipped with a water-cooled showerhead, from which the process gases are introduced over the entire surface, as shown in Figure 79. The substrates lie on a rotating and heating susceptor. Substrate temperature uniformity can be adjusted through three intertwined graphite heating areas.

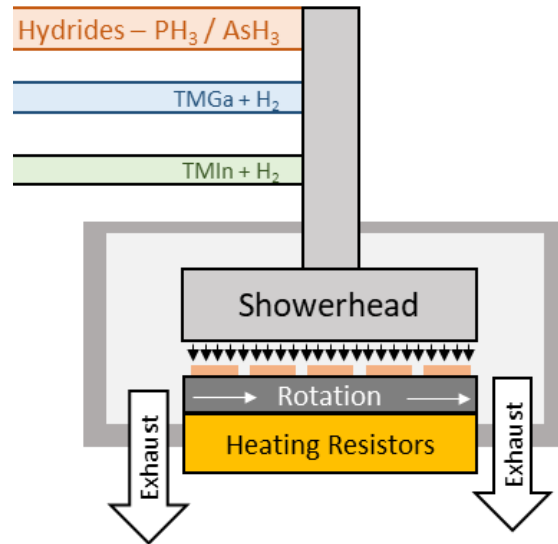


Figure 79. Schematic of a MOCVD growth chamber with a showerhead architecture.

1.2. Molecular Beam Epitaxy of InP and related materials

MBE, as we know it today, was invented in the 1960's, at Bell Laboratories, and developed in the 1970's by Arthur and Cho [3]. Since its invention, MBE has advanced as a process for synthesizing a wide range of high quality materials for high performance devices, including pseudomorphic High Electron Mobility Transistors (pHEMT), Heterojunction Bipolar Transistors (HBT), laser diodes, photodetectors and solar cells. During this time, MBE has evolved into an industrial production for a wide range of technologically important market applications. Early successes of a Research and Development (R&D) scale in demonstrating the creation of high purity materials with precise process control have prompted the development of larger systems capable of handling larger sizes and higher volumes of epiwafers.

While MOCVD is frequently used for the production of edge-emitting lasers, VCSELs and photodiodes, the MBE process is well suited for these devices' structures, where a high degree of process control, layer uniformity and interface sharpness increases the performances of the active layer in the device and the Distributed Bragg Reflector (DBR) epitaxial mirror stacks.

The choice of an epiwafers manufacturing process, for a particular device, depends on two main factors.

- The device's performance specifications may dictate the selection of a particular process. Epitaxial layer features achievable with the MBE process (abrupt and sharp interfaces, monolayer composition and doping control and high purity materials) may favor one production process over another, as these features impact device metrics, such as wavelength uniformity.
- When similar epitaxial features can be achieved with different growth techniques, the economic factors process yield and throughput may determine which process is best suited for a particular device.

Physical Vapor Deposition (PVD) techniques are known more for kinetically derived film properties and include deposition techniques, such as thermal evaporation, electron beam (e-beam) evaporation, sputtering and Pulsed Laser Deposition (PLD). MBE, traditionally a more kinetically driven growth regime, allows the control of individual layers of atoms. Chemical Vapor Deposition (CVD) is a growth technique that is dominated by thermodynamics rather than kinetics. From an epitaxial growth point of view, MBE compares most readily to MOCVD process for the growth of devices structures. In significant contrast to MBE, the MOCVD process occurs under a flow of high purity gas pressures ranging from a few Torr to around one atmosphere. MBE occurs at very low pressures, such that the atoms and molecules do not undergo any gas-phase interactions prior to arriving at the substrate's surface. In other words, the mean-free path of the molecules is significantly longer than the effusion source to substrate distance. The higher operating pressure of the MOCVD process requires consideration of the impact on the process performance from gas-phase transport and reaction, diffusion and convection.

Measurement and control of the growth process in MOCVD can include optical pyrometers, for temperature measurement, reflectometers, for real-time measurements of film thickness, as well as for growth rate and substrate curvature measurements during the growth. Advantages of the MOCVD process include high growth rates (from 2 up to 4 $\mu\text{m/h}$) for improved throughput. The MOCVD process also features more frequent but shorter maintenance cycles, depending on the reactor design. In contrast, a MBE production cycle can involve several thousand runs over 6 to 12 months, but the maintenance cycle can last a month or more from the end of one production campaign to the beginning of the next one. Disadvantages of the MOCVD process include: (i) the presence of hydrogen and carbon in the growth environment, which can be detrimental to the performance of the devices' structure, (ii) the pump/purge nature of metalorganic gasses, which can impact interfaces' qualities and (iii) higher process temperatures for the thermally driven chemical reactions. These higher temperatures can cause diffusion of epitaxial layer's constituents through layers and across interfaces, impacting the device's

performance. Additionally, while *in-situ* measurement can provide information about the growth process and the device structure, detailed surface analysis of the film during the growth, commonly achieved with Reflection High Energy Electron Diffraction (RHEED) in MBE, cannot be readily performed.

Further differences between MBE and MOCVD will be given in later sections.

1.2.1. MBE reactor design

MBE uses solid sources for every element that are thermally evaporated Ultra High Vacuum (UHV) to enable the growth. Group-III elements are evaporated in a directional monoatomic beam to reach the substrate's surface and crystallize by interacting with group-V elements [4]. The substrates are positioned on a heating and rotating substrate manipulator. The growth temperature is controlled by a thermocouple sensor at the back side of the substrate. As it does not represent the growth surface's temperature precisely, a pyrometer is usually implemented to monitor the growth temperature, through black body temperature measurement. More recently, band-edge thermometry has been developed to increase accuracy of substrate's temperature determination. The latter technique is viewport's coating independent, unlike pyrometry, providing a significant advantage. Its main drawback is the inability to accurately measure small bandgap material, such as antimonides. The rotation, in addition to a careful sources design, enables the deposition of homogeneous layers in terms of thickness and composition. The reactor operation, especially its sources, brings another degree of liberty in terms of uniformity, even if, at first order, design is the primary factor.

The atomic diffusion lengths of the species on the substrate's surface, which is function of their activation energies and the substrate's temperature, have to be taken into account to enable the growth of high crystalline quality material. Figure 80 shows the three types of growth that can occur [5].

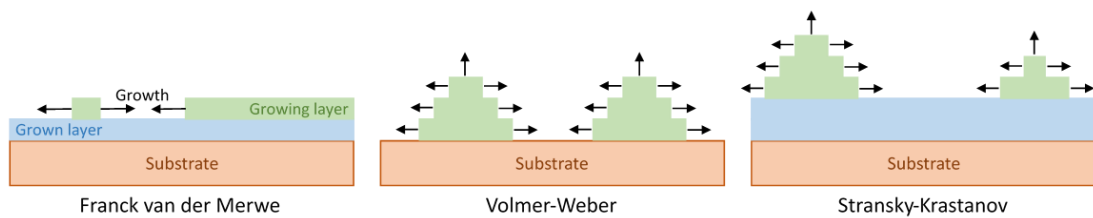


Figure 80. Types of crystalline growth.

- *The Franck-van-der-Merwe growth* is a layer by layer growth, happening when the atoms have enough energy to be incorporated at the edge of the growing layer. This growth mode provides the highest material quality. This growth is promoted by the use of low growth temperature, preventing the kinetic migration of the adatoms at the wafer's surface.
- *The Volmer-Weber growth* occurs when the substrate's temperature is too low or the incident atom flux insufficient. It leads to the growth of 3D islands that multiply until stabilization, and then, grow and coalesce to form layers.
- *The Stransky-Krastanov growth* appears after the others because of the strain energy accumulation in the layer. This type of growth can be useful to grow QDs based devices.

Our process does not involve Stransky-Krastanov growth type since all epilayers have been grown lattice matched or with a low strain ($\approx 1\%$).

To monitor the growth, MBE systems have been historically equipped with *in situ* characterization tools, such as:

- RHEED, to characterize the crystalline structure of the surface, as well as the V/III flux ratio and to measure the growth rates.
- Pyrometer, an optical measurement of the substrates' temperature.
- Mass spectrometry, to monitor the growth's environment.
- Beam flux monitor, made of a retractable ion gauge that can be moved in front of the substrates, to measure the Beam Equivalent Pressure (BEP) of each flux.

Low residual doping levels, synonymous to high purity layers can be reached by MBE. Moreover, the growth rates are slower than for the other techniques. It enables a high control over the grown layers' thicknesses and a high sharpness for the interfaces. These properties are key advantages in the growth of high quality material in MQW based structures.

1.2.2. Group-III elements' sources

Homogeneity of the layers depends on the growth chamber's architecture and the cell's characteristics. A large distance between cells and substrate gives a better thickness uniformity. This distance being limited, the geometry of the cells' crucibles has to be adapted to reach an optimized evaporation solid angle.

However, these crucibles can cause morphologic defects during the growth. Gallium and Indium cells are known to suffer material condensation at the top of their crucibles. By falling back in the source, the "cold" droplets are spread over the substrate [6]. The crucibles, usually made of Pyrolytic Boron Nitride (pBN) to be resistant against corrosion and high temperatures (900 to 1200°C), are thus coupled to heated inserts, as shown in Figure 81.

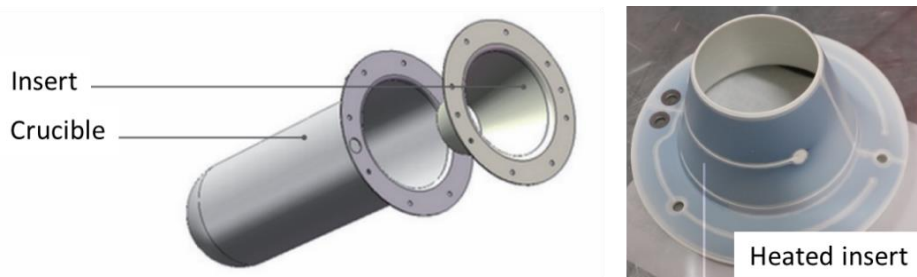


Figure 81. Schematic of a crucible and its heated insert.

The temperature control of these two parts limits the materials' condensation and the probability of source related defect apparition. The design of such conical inserts enables a good run-to-run reproducibility (with very small or no week-to-week temperature adjustments to keep the same flux) and good thickness and composition uniformities as the plume of evaporated materials can be precisely adjusted and provide a better than $\pm 1\%$ uniformity all over a given surface, also depending on the cell-to-platen length.

1.2.3. Group-V elements' sources

MOCVD and GSMBE are two prevailing growth techniques for producing high quality GaInAsP material. As and P are supplied for these techniques from AsH_3 and PH_3 gas. Due to the high toxicity of these gases, extensive and costly safety precautions must be taken.

1.2.3.1. Valved cracker phosphorus cell

Alternatively, Solid Source Molecular Beam Epitaxy (SSMBE) of GaInAsP, where As and P are supplied by subliming solid As and P, has been proven to be a reliable technique too. Since toxic solids are inherently easier to control than toxic gases, the safety hazards and costs of solid group-V sources are considerably less important than the gas group-V sources ones. Growth of GaInAsP, by SSMBE, began in the 1970s, but did not progress far due to difficulties related to the growth of arsenide phosphide materials. It was not until the introduction of group-V valved cracker sources, As in 1990 and P in 1991, that SSMBE research of GaInAsP moved forward once again. Since 1991, high quality GaInAsP material and lasers have been grown by SSMBE. Current design of valved cracker RIBER phosphorus cell is given in Figure 82.

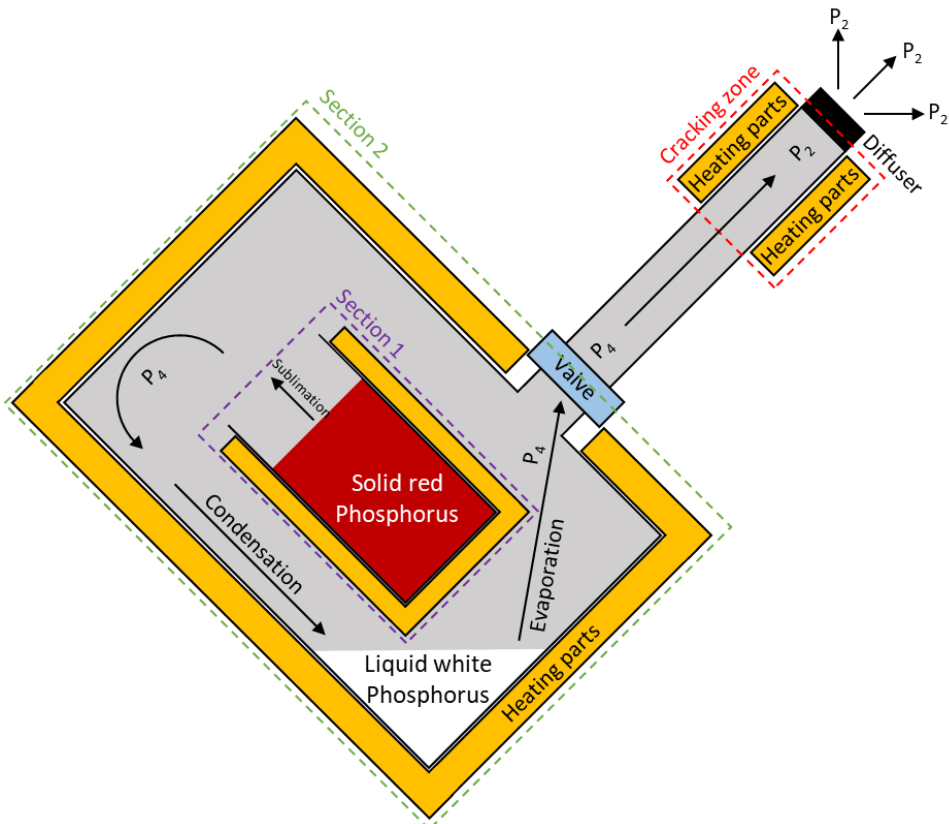


Figure 82. Simplified schematic of a valved cracker cell [7].

Vapor pressures of the 3 different allotropes of phosphorus are shown in Figure 83. Design of the cell takes advantage of the properties of red and white phosphorus [7, 8, 9].

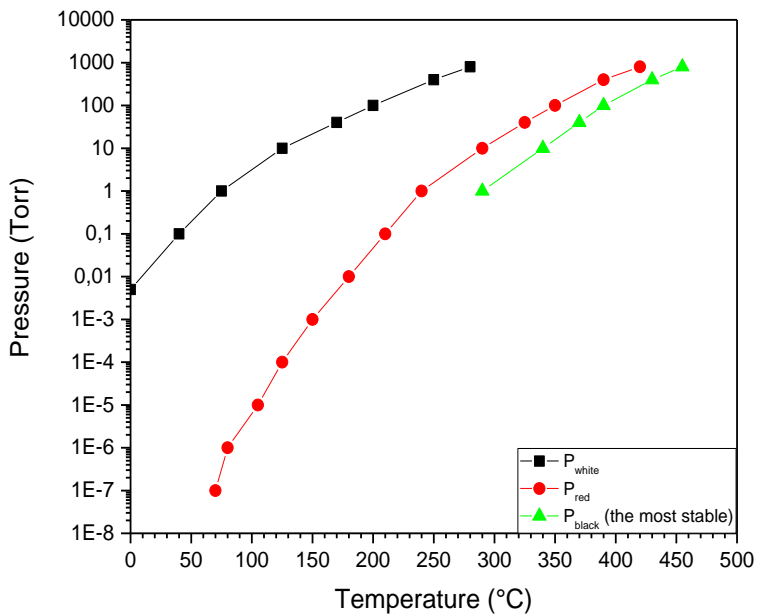


Figure 83. Phosphorus allotropes vapor pressures.

A P_4 phosphorus beam is issued from the sublimation of the red phosphorus (P_{red}) allotrope in a Al_2O_3 ceramic crucible at a temperature of about 300 to 350°C. P_4 condensation occurs under the white phosphorus (P_{white}) allotrope in the cell condenser. Several hours of sublimation/condensation are necessary to produce enough phosphorus for few tens of InP based structures' run. P_{red} to P_{white} conversion efficiency is pretty high. Three cells with different capacities are currently available: 40 cc,

250 cc and 1200 cc. In a single 2-inch capacity reactor, such phosphorus cell with a 40 cc capacity enables the growth of 400 μm . It has been noticed that, contrary to highly corrosive elements, such as As and Sb, P is not. It allows the use of commercial needle valves and fully leak-tight valves. It is consequently possible to isolate the reservoir part of the cell from the reactor to replenish it during the growth.

White phosphorus is re-evaporated at a temperature between 100 to 150°C under P_4 through a high precision needle valve and the cracking zone at 900 to 1000°C to ensure a close to 100% cracking efficiency of P_4 into P_2 [10]. This cell exhibits a good run-to-run reproducibility and a perfect flux stability, making SSMBE a viable technique for the growth of phosphorus-based materials [11, 8].

1.2.3.2. *GaP decomposition source*

At about the same period than valved cracked sources development a safer alternative was available (without highly flammable P_{white} production nor PH_3 gas use). Figure 84 shows a schematic view of GaP decomposition source, generating P_2 flux on one hand and a small Ga flux on the other hand, the latter being trapped in a baffle [12]. The process of producing P_2 is made easier by the respective vapor pressures of P and Ga at a given temperature. P_2 vapor pressure being a couple of order of magnitude higher than the Ga one.

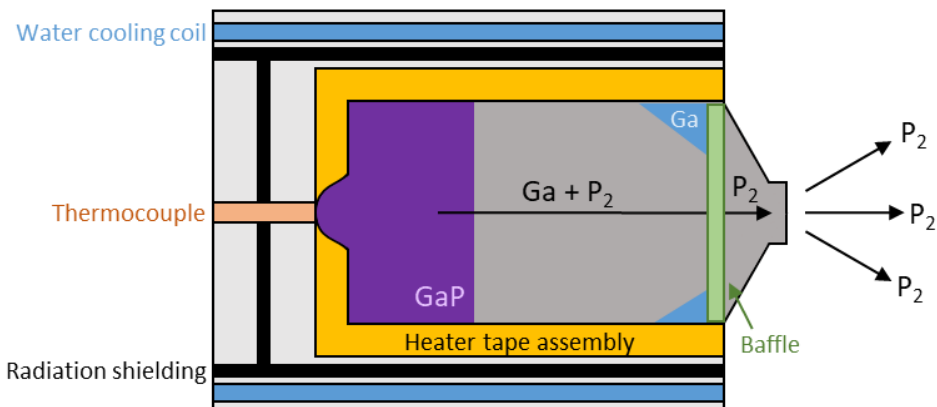


Figure 84. Simplified schematic of GaP source of phosphorus [12].

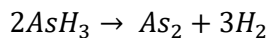
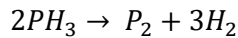
Nonetheless, this cell induces a potential incorporation of Ga in the layer, and the P flux varies strongly with the remaining quantity of GaP in the crucible. This cell was only marginally used.

1.3. Gas-Source Molecular Beam Epitaxy

GSMBE was developed, in 1974, at Bell Laboratories, by Morris and Fukui, with the integration of two gas lines to an MBE system to replace solid sources by gaseous sources [13].

The GSMBE method used at the laboratory is using AsH_3 and PH_3 as primary sources for As_2 and P_2 and solid elemental sources for Ga, In, Al and dopants (Beryllium (Be), Silicon (Si)). It is being used for the growth of numerous device structures, notably lasers and photodiodes. This method allows to grow high crystalline quality III-V compound semiconductors, regardless of the complexity of devices.

GSMBE is an alternative approach to conventional MBE in which the effusion cells of the MBE system are replaced by cracking sources capable of cracking selected molecular gases as molecular beams. A typical system includes a toxic gas manifold and the MBE system must be augmented with additional UHV pumping to exhaust the large quantities of H_2 produced by the cracking of gaseous hydrides.



In volume, cracking of AsH_3 or PH_3 is producing 3 times more H_2 than As_2 or P_2 .

The major strength of GSMBE is in the use of only one group-V source for both As and P. The single beam flux, containing premixed As and P in the cracker cell, makes the compositional control precise and reproducible, using a baratron transducer to adjust independently both gas pressures [14]. Moreover, the hydride sources are replenishable without venting the reactor. The beam fluxes remain constant throughout the lifetimes of the gas supplies. Another advantage is its ability to maintain excellent control over the compositional homogeneity for the growth of ternary and quaternary compounds.

The choice of gas source instead of solid source, where the growth environment is filled with high quantities of H_2 , has another major interest feature. H_2 allows for a better diffusion of adatoms on the surface of the epilayer. Consequently, it permits to improve the regrowth process on patterned processed epiwafers (Butt-joint, grating planarization) and avoids the undesired selective area growth (SAG) effect usually observed in MOCVD regrown epiwafers. The drawback of such high quantities of H_2 being the potential incorporation of hydrogen in the structures, passivating p-type dopants.

A major disadvantage remains the use of toxic and pyrophoric hydrides, though in much smaller quantities than what is required in MOCVD. Table 38 shows typical quantities of gases used during MOCVD and GSMBE processes.

InP based alloys	MBE	MOCVD
PH_3 (and/or AsH_3)	From 10 to 15 sccm	300 sccm
H_2 (carrier gas)	0*	12000 sccm
Growth temperatures	From 400 to 500°C	From 600 to 700°C

* no additional H_2 is required in MBE to carry the atoms onto the wafer's surface even though significant quantities of H_2 fill the chamber. Typical pressure during growth is the low 10^{-5} Torr range.

Table 38. Comparison of gas usage and growth temperatures between GSMBE and MOCVD for the growth of InP based alloys.

1.3.1. Updated and retrofitted V100 reactor

The MBE system initially used is a RIBER modified vintage V100 reactor retrofitted with two CT10-flat cryopumps, having a combined hydrogen pumping speed of 12000 l/s. Figure 85 and Figure 86 are schematic and cross section of the MBE reactor. Apart from diffusion pumps, cryopumps are the most efficient at pumping hydrogen. They must sustain periodic regeneration to outgas trapped H_2 onto the sorbent material, which is typically a porous solid, such as activated charcoal or zeolite. Regeneration cycles have to be performed every 12 μm or more of InP. The growth environment is surrounded by a

main Liquid Nitrogen (LN₂) cryopanel. A turbomolecular pump backed by a multi-stage roots roughing pump is situated behind a LN₂ cooled trap to capture P pumped from the growth chamber before it enters the roughing pump. This pump is not used during process, but as backup pump during the cryopumps regeneration and periodic main cryopanel regeneration. Due to the pyrophoric nature of phosphorus, care must be taken when removing cryopumps and cryopanels from the MBE system. To allow for controllable disposal of phosphorus, the smaller LN₂ cooled trap (Cold Finger) can be isolated and separated from the machine under a nitrogen atmosphere for cleaning in a fume hood. A preventing bake is also performed to transfer residual P_{white} into a scrubber.

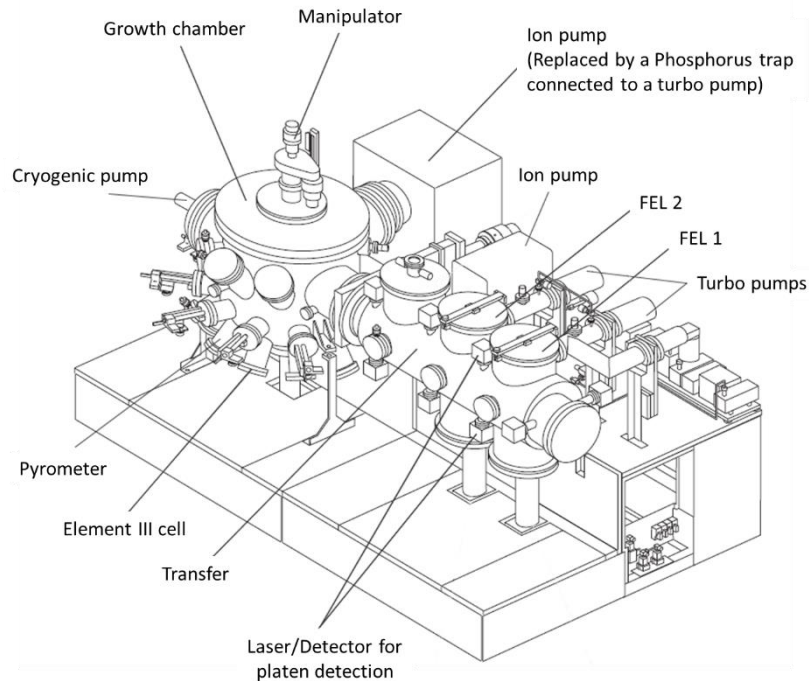


Figure 85. Typical solid source "1994" V100 reactor schematic.

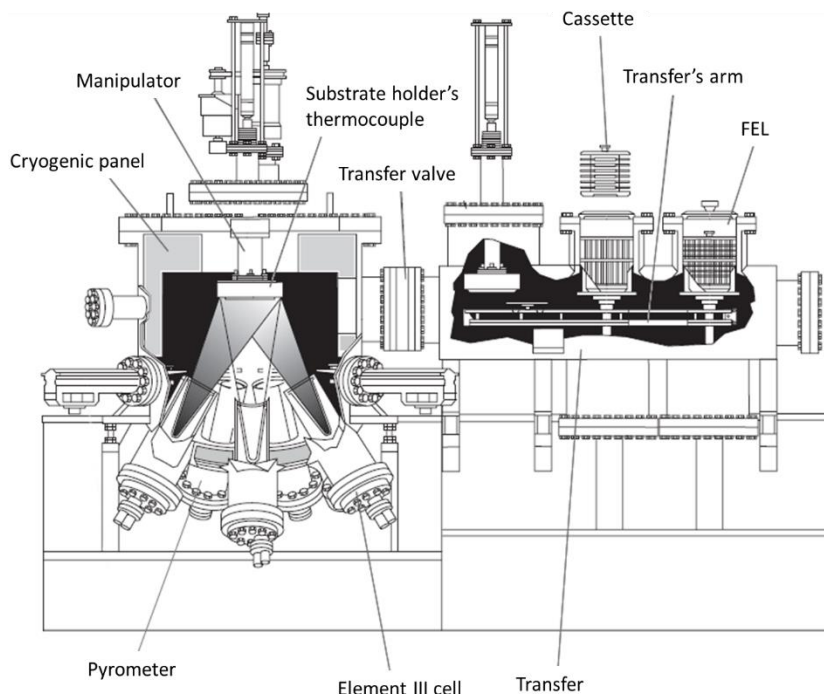


Figure 86. Cross section of the V100 reactor.

1.3.2. MBE412 reactor

After several years of service, the V100 has been replaced by a state of the art MBE reactor, the MBE412 from RIBER. This reactor has many advantages as compared to the V100:

- It can be equipped with 12 sources instead of 10 for the V100
 - For new materials
- Material consumption is reduced
 - Increasing campaign length
- Growth environment static cryogenic pumping is largely upgraded
 - Cryoshrouds are implemented around the substrate heater, the pumping well in addition to the main cryopanel, while there was only one cryopanel for the V100.
- Dynamic pumping is significantly higher as compared the V100
 - Increasing the duration between cryopumps regenerations and allowing to increase growth rate when necessary
 - Base pressure is one order of magnitude lower than it was in V100 (low 10^{-5} Torr in MBE412 and 10^{-4} Torr in V100, at identical hydrides cracking efficiency)
- Substrate heater is very reliable
 - Up and running for more than 500 runs
- Use of a low pressure injector, in opposition to the high pressure injector in V100
 - Faster switch
- Transfer is highly reliable
 - The reactor is currently operated 24/7 for as long as a year
- It can be upgraded with additional process chambers
 - Passivation for example (not included in our system)
- An additional growth chamber can be easily connected to the existing set up
 - Antimony, oxides, ... (not implemented yet)
 - Another AsP chamber to improve the throughput
- An additional preparation chamber has been equipped with a hydrogen plasma and a valved cracker phosphorus source for wafer preparation
- Reactor capacity is 3x2", 1x3", 1x4" (even if the V100 had a capacity of 3x3" and up to 1x6", uniformity was not optimized for such platen configurations)
- More importantly, this reactor has been equipped with multiple in-situ characterization tools such as stress and curvature measurement and band-edge thermometry, as shown in Figure 87

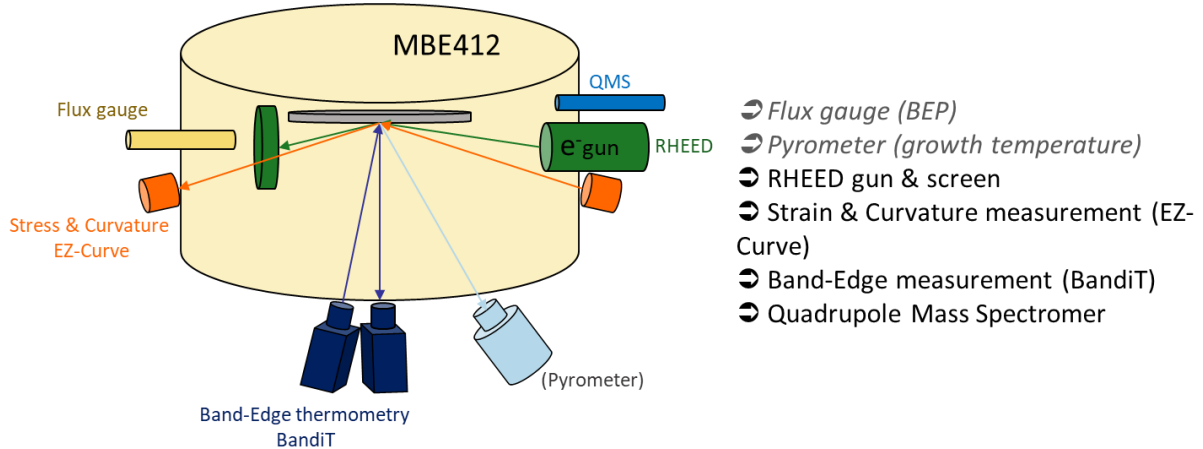


Figure 87. MBE412 set of in-situ characterization tools.

This new reactor is shown in Figure 88 and Figure 89. The central module of this system is the UHV cluster tool module, equipped with an ionic pump and connected to a Load-lock module, a storage, a plasma preparation chamber and the heart of the system, the III-AsP growth chamber.

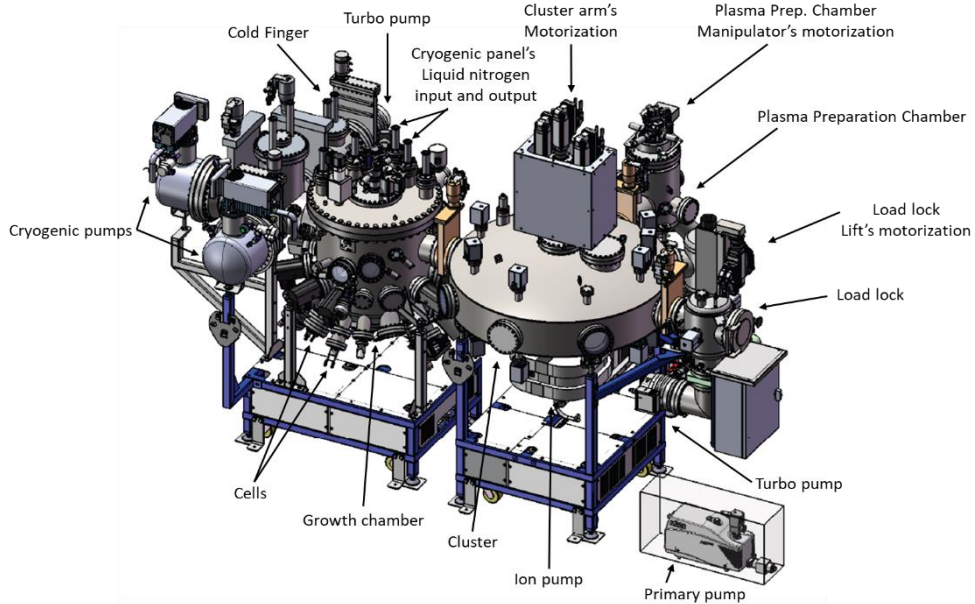


Figure 88. 3D drawing of the III-V Lab MBE412 reactor.

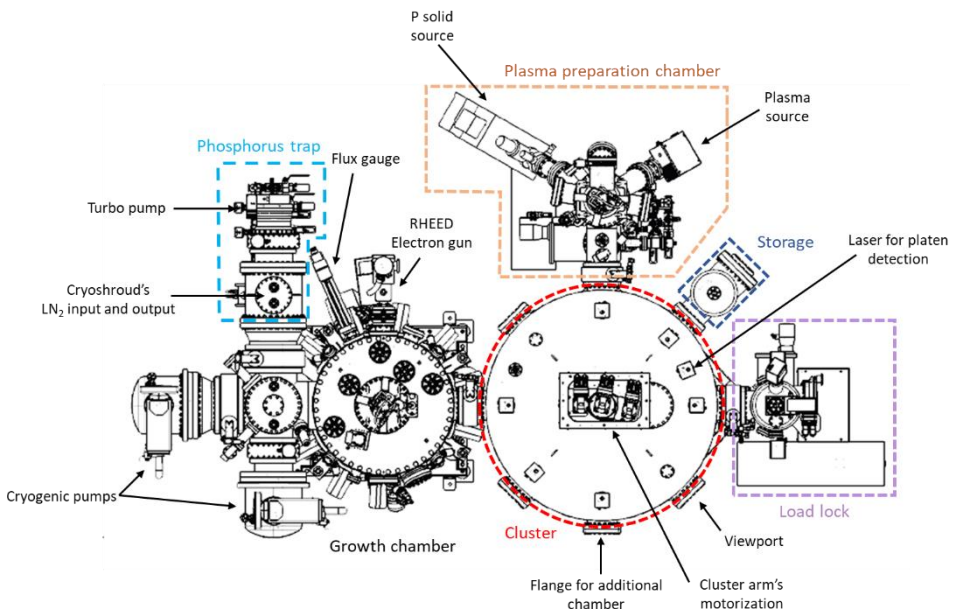


Figure 89. Top view of the III-V Lab MBE412 reactor.

The reactor has been qualified and the SOA growth process has been successfully transferred at the end of 2022, early 2023. The MBE412 has been proven to be in a position to provide excellent material quality and epiwafers in a reproducible manner very quickly after its commissioning.

Another significant improvement of the MBE412 is the RHEED, which was not implemented on the V100. All the characterization tools installed on the growth chamber allows for a better understanding of the growth conditions and a better production follow-up than what was possible in the V100. Even the Quadrupole Mass Spectrometer (QMS) located in the growth chamber helps us to follow in an appropriate manner how the process is running and eventually collect all necessary information in case of issue or failure. EZ-curve and BandiT tolls will be shortly described in the next sections.

2. MBE growth of GaInAsP quaternary alloys

Controlling the composition of $\text{Ga}_x\text{In}_{(1-x)}\text{As}_y\text{P}_{(1-y)}$ compounds can be difficult because of the different incorporation efficiencies of As and P and the dissimilar dependence of these efficiencies on growth parameters. In general, under normal growth conditions, any increase in Ga, or in growth rate, increases the P sticking probability relative to the As one. We also observed that, for particular alloys, the composition changes abruptly at a certain growth temperature. This effect is caused by a sudden change in the sticking coefficients of As and P, due to the surface reconstruction.

2.1. The issue of miscibility gap in the GaInAsP/InP system

Preparation of complex GaInAsP based device structures having different composition of GaInAsP layers can be difficult due to limited solid solubility of the components. The existence of a miscibility gap in the phase diagram of GaInAsP quaternary compound is well known [15]. According to thermodynamical calculations, unstable regions during the growth of the GaInAsP alloys lattice matched to InP can be found when the growth temperature is below 670 to 680°C. The thermal decomposition for lattice-matched alloy compositions, with As composition ranging roughly from 0.55 to 0.9, for materials with energy gaps corresponding to the wavelengths about 1.25 to 1.55 μm, can occur at growth temperature below 600°C. The instable region increases as the growth temperature decreases, as shown in Figure 90. As can be seen, there are important differences in the location of the boundary as calculated by several authors [16, 17, 18, 19]. The real position is still not well established.

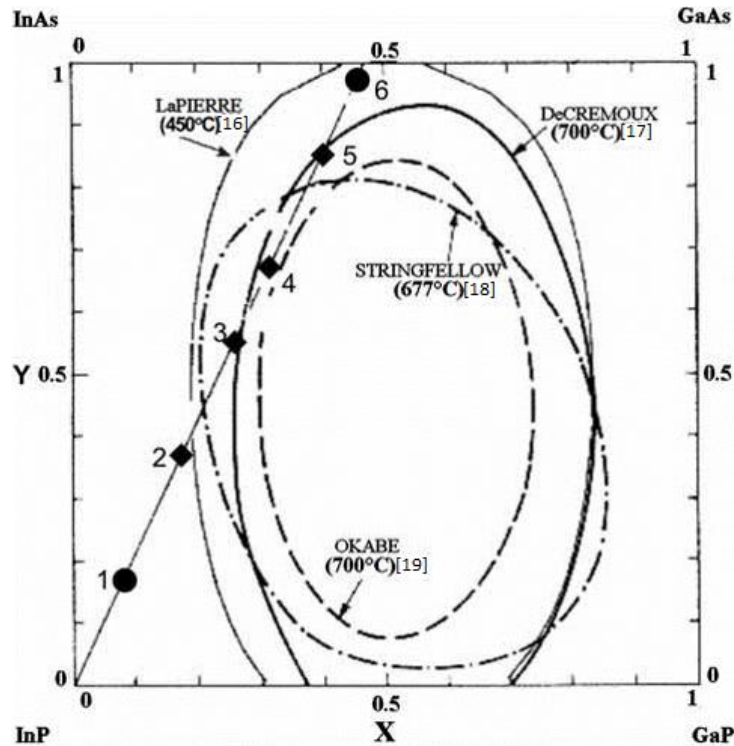


Figure 90. Boundaries of the $\text{Ga}_x\text{In}_{(1-x)}\text{As}_y\text{P}_{(1-y)}$ miscibility gap, as calculated by several authors [20].

MBE process, with temperatures varying between 440°C and 490°C could be prone to such behavior. Despite this miscibility gap, it is still possible to grow GaInAsP compounds on InP substrate over practically the entire composition range, from InP to lattice matched GaInAs. Indeed, the growth of lattice matched material reduce the probability to observe phase separation.

Although, the thermodynamical calculations are only valid for near equilibrium growth methods such as Liquid Phase Epitaxy (LPE) or MOCVD, evidence of a strong miscibility gap still exists for the quaternary composition corresponding to wavelengths in the middle of the 1000 to 1700 nm range. This

range has been experimentally shown to be closer to 1250 to 1600 nm, by GSMBE, which is a non-equilibrium growth method with a strong tendency to phase separation [21]. Careful selection of the optimum growth temperature is essential. As above mentioned, the effect of strain on material quality is also having a significant impact. Compressively strained epilayers should exhibit good structural quality.

In the C+L-Band structures, either the bulk materials are outside the unstable region (such as quaternary barriers and SCH or cladding), or nearby, such as the 0.7 to 1.0% compressively strained QW. But again, the 1% compressive strain can allow countering the effect of non-miscibility even though Photoluminescence (PL) study of such materials prone to phase separation exhibits broader spectra. As an example of such material quality variation, we can mention $\text{Ga}_{0.27}\text{In}_{0.73}\text{As}_{0.59}\text{P}_{0.41}$ and $\text{Ga}_{0.19}\text{In}_{0.81}\text{As}_{0.42}\text{P}_{0.58}$. The former is used in neither of our structures, the latter is the base material for many optoelectronic devices.

Keeping in mind these potential difficulties, equipment status and limitations, but also their strengths, we established growth conditions for the different BB of the epitaxial stack of the SOAs. We will briefly discuss standard calibration procedures, for each of the BB, followed by the growth conditions and the optimizations for the C+L as well as for the O-Band structures. Finally, we will discuss the growth process transfer from the V100 to the MBE412 system.

2.2. MBE reactor initial calibrations

An estimation of group-III element growth rate, is determined using the well-established RHEED technique and the specular beam intensity oscillations for both GaAs and InP on GaAs and InP substrates respectively. GaAs growth rate is being adjusted to the lattice parameter of InP, following Equation 71.

$$\text{Equation 71. } V_{GaAs/InP} = \frac{a_{InP}}{a_{GaAs}} * V_{GaAs/GaAs}$$

Where, a_{InP} and a_{GaAs} are the lattice parameters of InP and GaAs, respectively.

Typical RHEED setup is given in Figure 91. Accurate growth rates must be accurately verified using specific structures measured by means of PL and HRXRD. Both techniques are mandatory when quaternary alloys are considered.

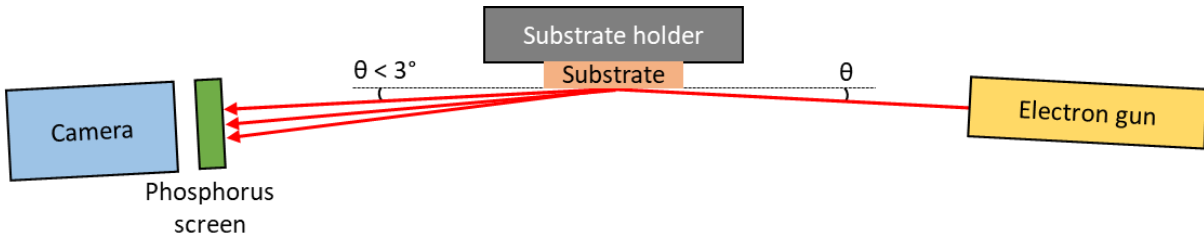


Figure 91. Schematic representation of a typical RHEED configuration.

GSMBE require a 20 keV RHEED electron gun (e-gun) due to relatively high hydrogen pressure during the process, preventing the electrons from reaching the fluorescent screen. Working pressures are 2 to 3 orders of magnitude higher in GSMBE than in SSMBE, for which usual e-gun are 12 keV.

The e-gun is at a grazing incidence angle to the substrate's surface and aligned with a fluorescent screen to collect the diffracted and reflected electrons. A camera enables the data acquisition of the specular beam's intensity oscillations, allowing to determine the incorporation rates [22]. These incorporation rates depend on the atomic fluxes. However, all the incident atoms do not participate in the growth. The species react differently with the surface, depending on their properties. Group-V elements have higher vapor pressure than group-III elements, so, they desorb from the substrate at lower temperatures. At usual growth temperatures (450 – 500°C for GaInAsP alloys), the group-III elements have a sticking coefficient close to unity, meaning that almost every atom coming from a cell participates in the growth. Figure 92 illustrates the growth of InP with a lack of phosphorus (low V/III ratio).

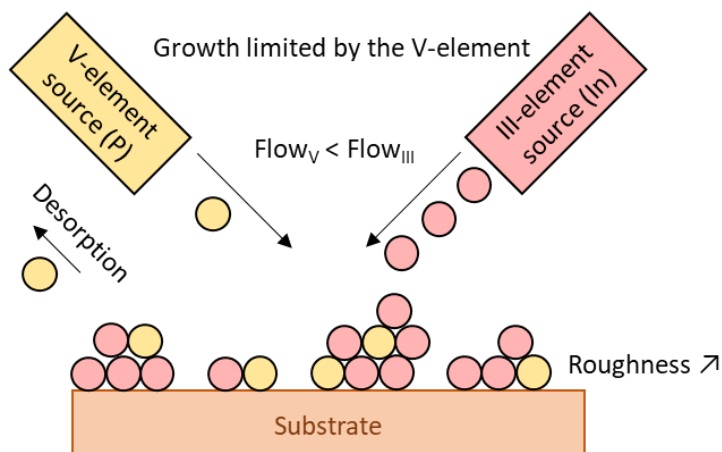


Figure 92. Growth with element III in excess ($V/III < 1$).

In this configuration, clusters are formed on the surface and increase the surface's roughness. These conditions are usually used in order to estimate fairly precisely the V/III flux detailed in the next section.

Figure 93 illustrates the growth with a V/III ratio > 1 . The growth proceeds layer-by-layer and the intensity of the specular beam oscillates with a period corresponding to the growth of one atomic layer as illustrated in Figure 94.

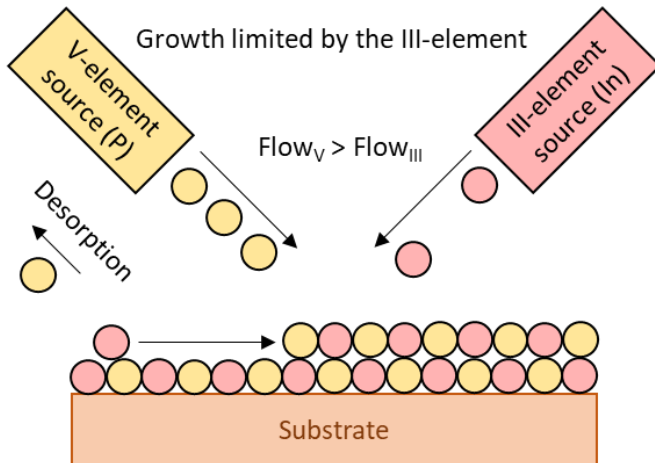


Figure 93. Growth with element V in excess ($V/III > 1$).

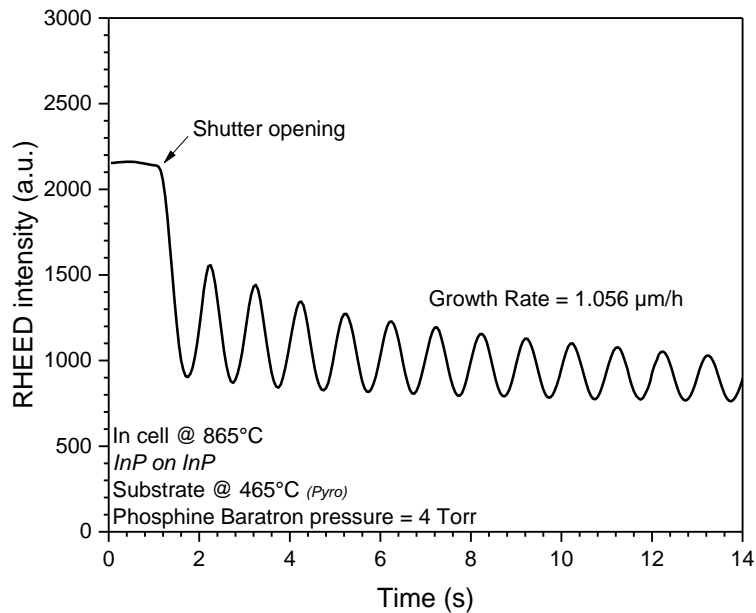


Figure 94. In incorporation rate measurement from RHEED oscillations.

2.2.1. Group-III elements

RHEED provides a unique tool for monitoring and controlling epitaxial growth by MBE. While the static RHEED intensities provide important information about substrate temperature, surface stoichiometry and the atomic arrangement of atoms on the surface, the dynamic behavior of RHEED intensities, obtained from recording the specular spot of the diffraction pattern, has been shown to be valuable, in quantifying the growth rate and qualitatively, providing insight into island formation and surface disorder during growth.

Oscillations, in both the intensity and width of RHEED beams, that are measured during MBE growth depend upon most growth parameters. The envelope of the intensity oscillations, for example, depends upon the flux ratios, the substrate's temperature, the sample's misorientation, the scattering geometry and the sample's flatness.

Substrate's temperature must be set low enough to avoid group-V element desorption and more importantly, limiting the diffusion length of adatoms on the surface, enhancing the oscillations. HRXRD and RHEED oscillation measurements performed for InP on the MBE412 are shown in Figure 95.

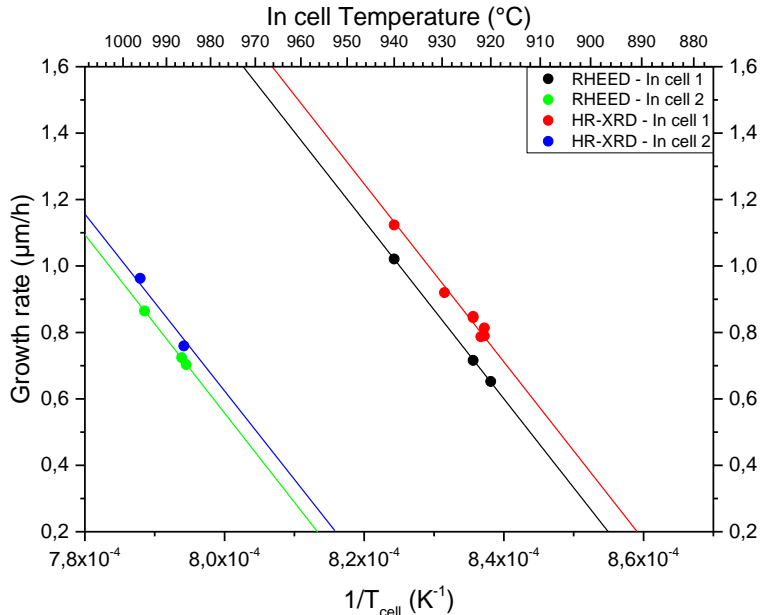


Figure 95. Arrhenius curves of two In cells growth rates as function of their temperatures.

Growth rate as a function of temperature can be fitted with an Arrhenius curve (Equation 72).

$$\text{Equation 72. } V_{III} = A * e^{\frac{-E_a}{kT}}$$

Where:

- V_{III} , is the growth rate of the source.
- A , is a coefficient varying in function of the cell geometry and the considered element.
- E_a , is the activation energy.
- k , is Boltzmann constant.
- T , is the cell's temperature.

High Resolution X-Ray Diffraction (HRXRD) of an InAsP/InP SL (Figure 96) allows to accurately determine InP growth rates. Growth rates discrepancy is related to the inaccuracy in positioning RHEED's electron beam at the center of the substrate.

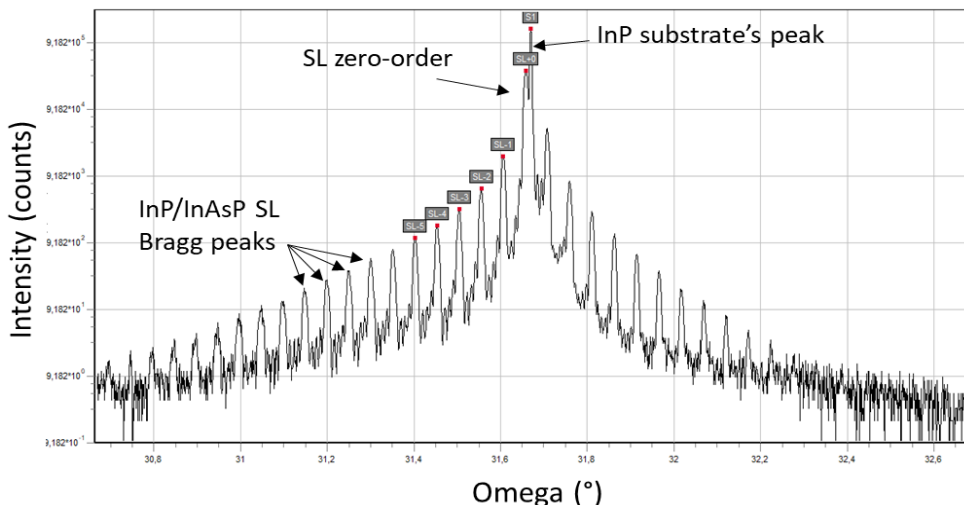


Figure 96. HR-XRD Omega-2-Theta curve of an InAsP/InP SL structure.

The SL period is given by Bragg's law (Equation 73).

$$\text{Equation 73. } \frac{1}{\Lambda} = \frac{2 * (\sin(\theta_n) - \sin(\theta_{n-1}))}{\lambda}$$

n peaks should be taken into account to increase accuracy, resulting in Equation 74.

$$\text{Equation 74. } \pm \frac{n}{\Lambda} = \frac{2 * (\sin(\theta_n) - \sin(\theta_{SL}))}{\lambda}$$

Where, Λ is the SL period, λ is the wavelength of incident X-ray, θ_n is the n^{th} -order peak in the omega-2-theta curve and θ_{SL} is the zero-order peak.

GaAs growth rate on InP can be extrapolated from a 200 nm thick GaInAs layer lattice matched or nearly lattice matched, characterized by HRXRD, as illustrated in Figure 97.

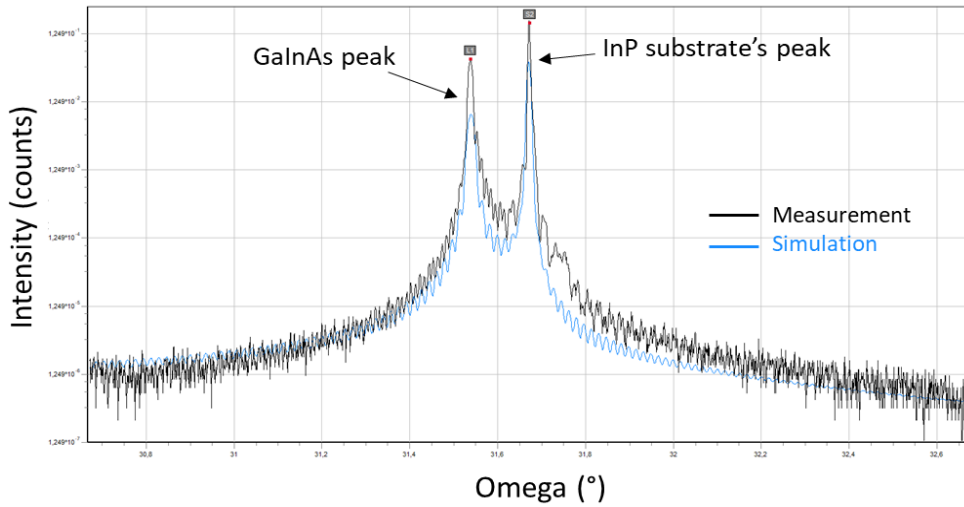


Figure 97. HR-XRD rocking curve of GaInAs/InP presenting a lattice-mismatch.

A more accurate and efficient solution to determine the growth rates of all group-III elements should be to grow GaInAs/AlInAs double SL structures, with different thicknesses and characterize them by HRXRD. In our particular case, even if we own an Al cell, at the time of the study, we did not melt the source's material, meaning we had to stick to the InAsP/InP SL and GaInAs bulk epilayers to evaluate growth rate by HRXRD.

2.2.2. V/III ratio and quaternary alloy growth conditions optimization

RHEED induced oscillations are also used to set the V/III ratio, as illustrated in Figure 98. At a given InP (or GaAs) growth rate, with V/III ratio above 1, reducing the phosphorus flux will allow to determine at which point, growth conditions switch from group-V element rich to group-III element rich. In the latter case, the growth is controlled by the group-III elements.

It has to be noticed that "flux" gauge and pressure gauge do not measure the real flux. For the flux gauge, we are measuring the BEP, which is easier to estimate and directly given by the "flux" monitoring. BEP is commonly given in Torr. It is depending on the flux gauge's orientation in regards of the cell's position. An atomic flux is given in atom/area/second, which is an absolute value. The difference is especially true in GSMBE, where large quantities of residual H₂ are not immediately pumped.

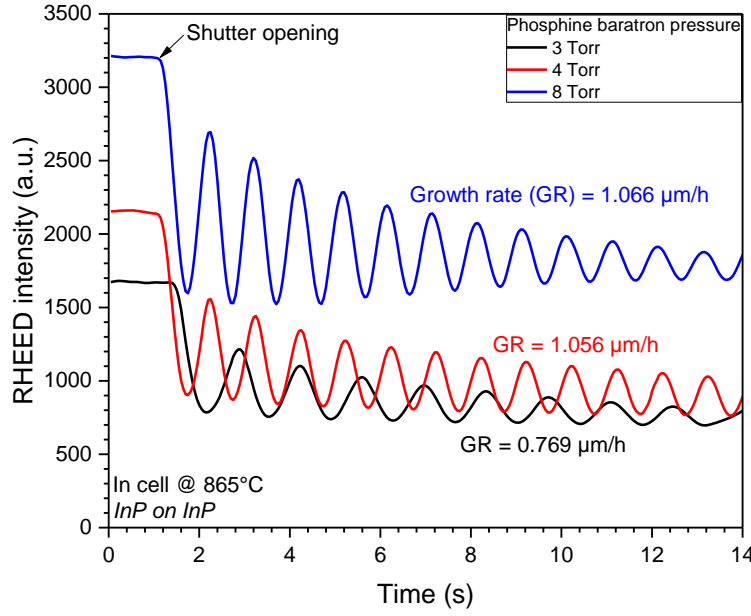


Figure 98. InP RHEED oscillations measured at different phosphine baratron pressures

We can determine a limit value under which the growth is driven by the group-V element, by plotting the obtained growth rates as function of the baratron pressure, like in Figure 99. Such study will allow to adjust the V/III ratio and determine the maximum growth rate that can be used. V/III flux ratio are within the usual range of operation.

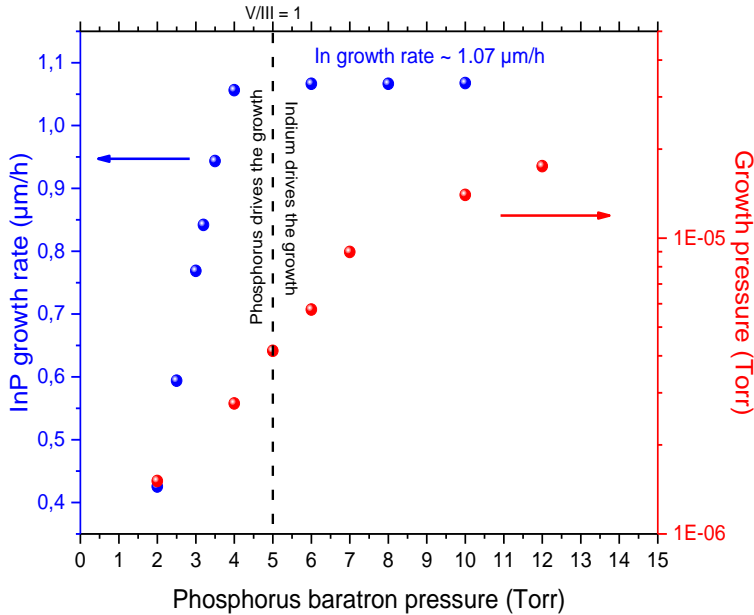


Figure 99. InP growth rates as function of phosphine baratron pressure.

PL measurement of quaternary alloys such as Q_{1.17} and Q_{1.03}, operated at 300K, will allow to accurately and practically adjust the right group-V element overpressure. PL mapping and uniformities of peak intensity and peak wavelength are the main parameters to check. Figure 100 exhibits very good wavelength and intensity uniformities measured on a Q_{1.17} quaternary alloy, grown on a centered 1x2" substrate, exhibiting 2 nm wavelength maximum variation and 5.1% intensity's standard variation for optimized growth conditions, with a 4 mm edge exclusion zone.

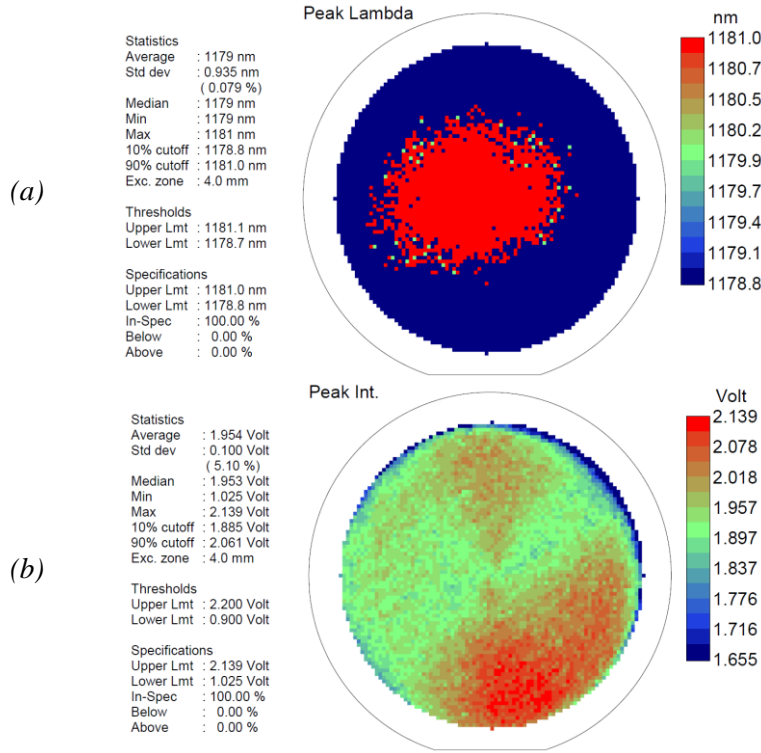


Figure 100. PL mapping of a Q_{1.17} quaternary alloy grown in a 1x2" platen configuration, illustrating (a) the peak wavelength and (b) the peak intensity uniformities.

Similarly, reasonably good uniformity results have been measured on a 3x2" platen configuration, with a peak wavelength standard deviation of 1.5 nm and a peak intensity standard deviation of 10% (Figure 101).

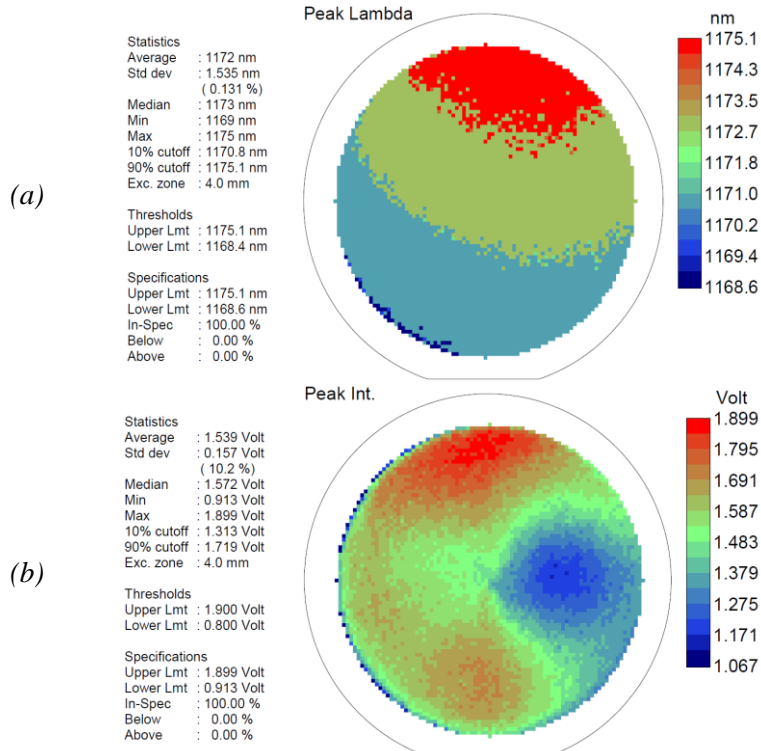


Figure 101. PL mapping of a Q_{1.17} quaternary alloy grown in a 3x2" platen configuration, illustrating (a) the peak wavelength and (b) the peak intensity uniformities.

2.3. GaInAsP quaternary alloys' growths, from bulk material to MQW based active zone

2.3.1. GaInAsP bulk material optimization

As previously stated, despite the large miscibility gap, MBE being a growth method under non-equilibrium conditions, it is possible to grow $\text{Ga}_x\text{In}_{(1-x)}\text{As}_y\text{P}_{(1-y)}$ alloys lattice matched to InP from InP to GaInAs with phosphorus mole fraction varying from 1 to 0. Figure 102 shows a panel of alloys ranging from $Q_{1.05}$ to $Q_{1.45}$ right into the unstable region, visible in Figure 103. $Q_{1.30}$ As content is about 59% and $Q_{1.45}$ As content is about 77%.

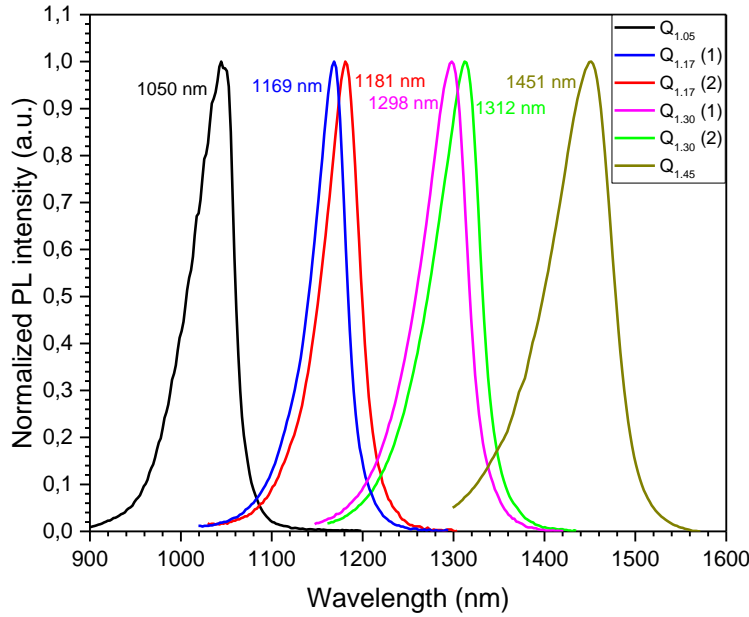


Figure 102. 300 K PL spectra of $Q_{1.05}$, $Q_{1.17}$, $Q_{1.30}$ and $Q_{1.45}$ quaternary alloys.

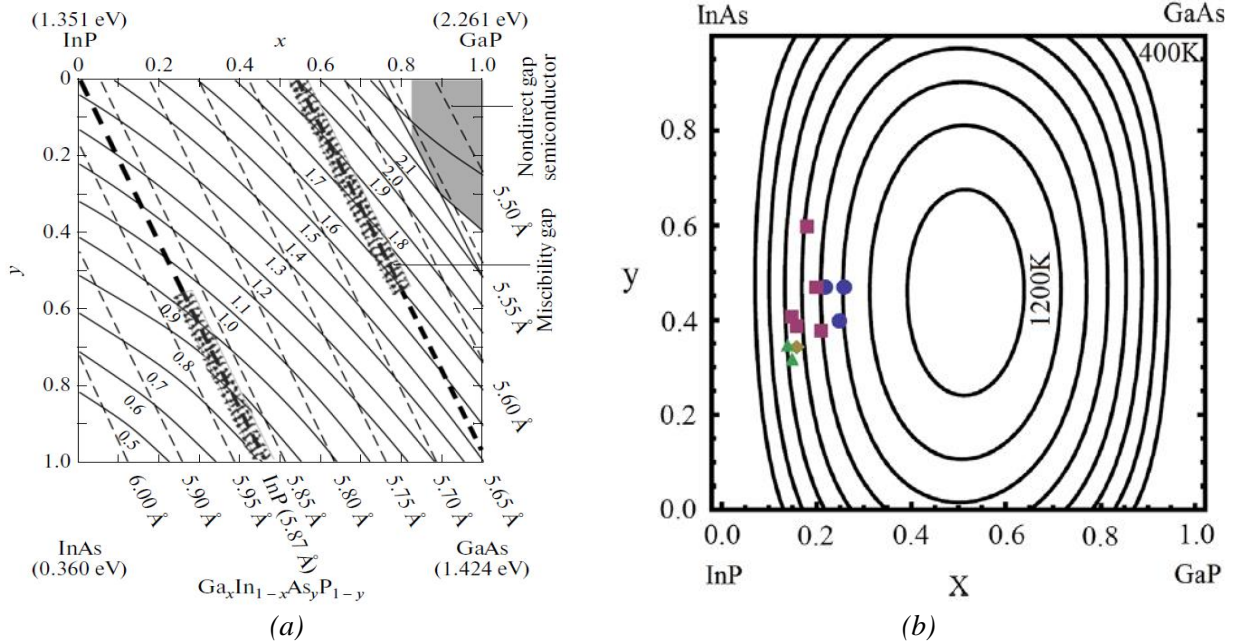


Figure 103. GaInAsP quaternary alloy bandgap variation with the lattice parameter. Dashed line along the InP lattice matched shows the unstable region, roughly ranging from an As content of 0.55 to 1.

Each individual growth conditions had to be adjusted in terms of V/III flux ratio and temperature to both maximize intensity and reduce FWHM. As can be observed in Figure 104, FWHM of alloys in the miscibility gap exhibit larger FWHM values as compared to lower As content alloys.

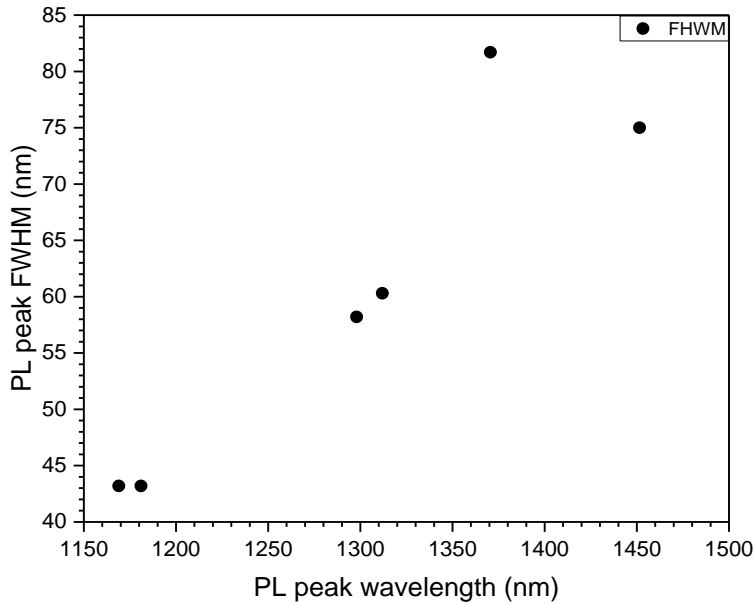


Figure 104. Quaternary alloys' FWHM as function of PL peak wavelength.

Composition control of the various alloys can be accurately adjusted by varying baratron transducer of AsH₃ and PH₃, as displayed in Figure 105.

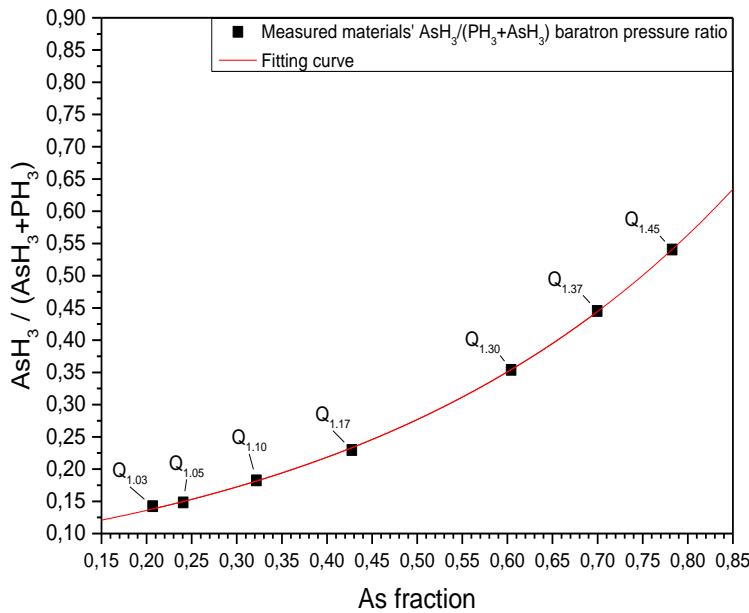


Figure 105. AsH₃/P_{total} baratron transducer pressure as function of the alloys' As concentration.

Growth temperature is the primary parameter to adjust in order to optimize the crystalline quality of the epilayers. As incorporation is depending on the temperature, the lower the temperature, the higher the As incorporation. Consequently, it is important to define the correct combination between Ga/In ratio, As/P ratio and temperature, requiring a fastidious optimization period. V100 was not a stable reactor, many problems inherent to its design made these parameters difficult to adjust and then, reproduced optimized growth conditions. However, the process transfer to MBE412 has been pretty straightforward. We have been able to quickly adjust growth conditions and stabilize them to be able to grow various wideband SOA structures, on this new reactor, thanks to the implementation of the band-edge thermometer apparatus.

The growth of our SOA structures requires the precise optimization of two quaternary compounds, the Q_{1,17} and Q_{1,03}, that are required:

- As a component of the SL slab, which is a Q_{1.17}/InP SL in the C+L-Band structures and a Q_{1.03}/InP SL in the O-Band structures
- In the SCH
- In the barrier, that should be slightly strain compensated by adjusting the As/P ratio, with a tensile strain of about -0.7%
- In the QW themselves, considering that the Ga/In ratio is kept constant between barriers and QW, with only the As/P ratio is significantly adjusted, to reach the 1% compressive strain targeted

To exhibit large bandwidths, our QW must be relatively large as compared to their laser counterparts. Also they can be thicker than their barriers. The active region could require compensating QW strain, with barriers under tensile strain, especially for C+L-Band structures. Indeed, the As concentration of their QW is relatively high, to reach the 1625 nm peak PL wavelength.

As/P ratio of the QW needs to be adjusted to reach e₁-hh₁ transition corresponding to the highest wavelengths of each band, 1625 nm, for the C+L-Band and 1360 nm, for the O-Band, at low excitation (during PL measurement) and low injection (for the device).

2.3.2. C+L-Band active region calibration

As illustrated in Figure 106, adjusting the AsH₃/PH₃ ratio, for the C+L-Band is requiring the use of an extended GaInAs photodetector, since the cut-off wavelength of a standard GaInAs detector is about 1.62 μm. The use of the wrong PL setup can lead to disastrous error. III-V Lab's PL bench is not equipped with such extended photodetector. We had thus to send calibration structures to LPCNO, to accurately determine their peak wavelength.

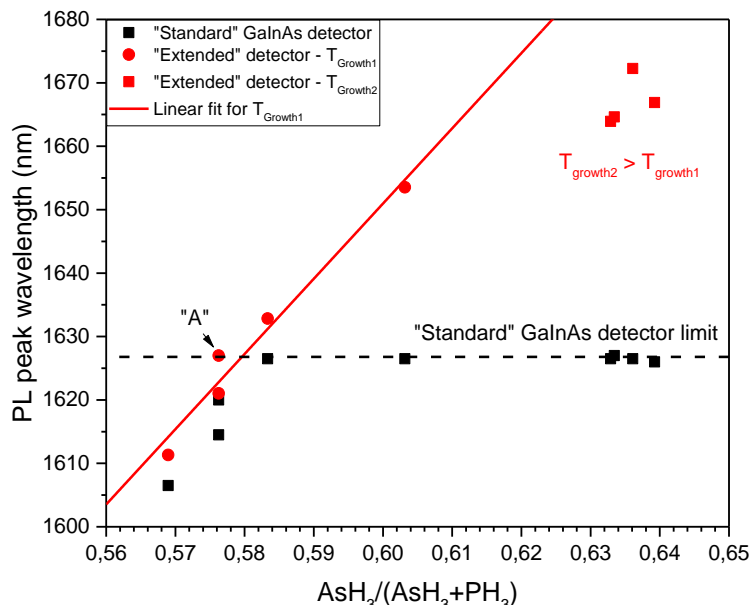


Figure 106. PL peak wavelengths measured with GaInAs and extended GaInAs detectors as a function of the AsH₃ baratron pressure.

Temperature dependence and competition between As and P incorporation are also highlighted. As incorporation has been significantly reduced at higher temperature. For efficiency purposes, temperature should be optimized first, then As/P ratio. An AsH₃/(PH₃+AsH₃) ratio of 0.577 corresponds to e₁-hh₁ target PL wavelength, represented by the wafer "A" in Figure 106. Figure 107 illustrates the effect of temperature's optimization on PL intensity, with an almost identical FWHM.

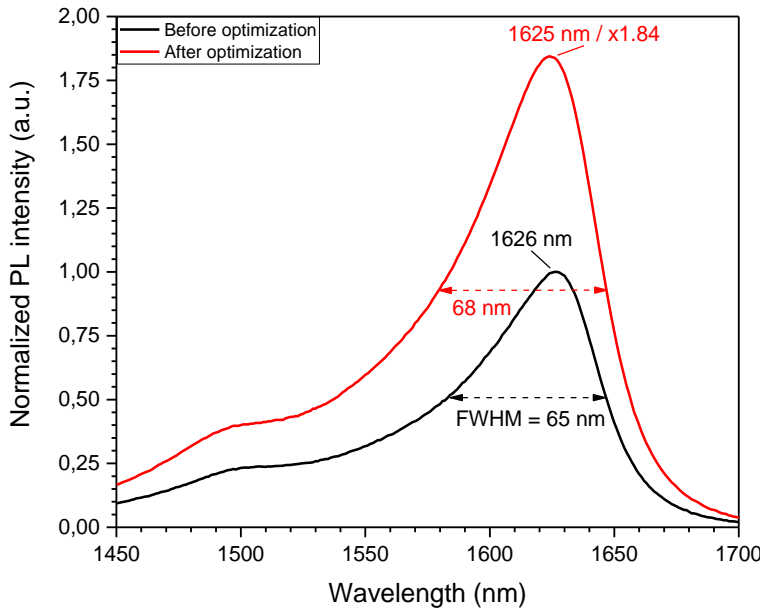


Figure 107. PL comparison between wavelength optimized and fully optimized growth conditions.

The $e_1\text{-}hh_1$ optical transition is clearly visible, but $e_2\text{-}hh_2$ cannot be discretized. Photocurrent measurements, performed at LPCNO, allowed us to observe additional electronic transitions. Figure 108 shows photocurrent response and PL spectra in relative to the transition energies calculations.

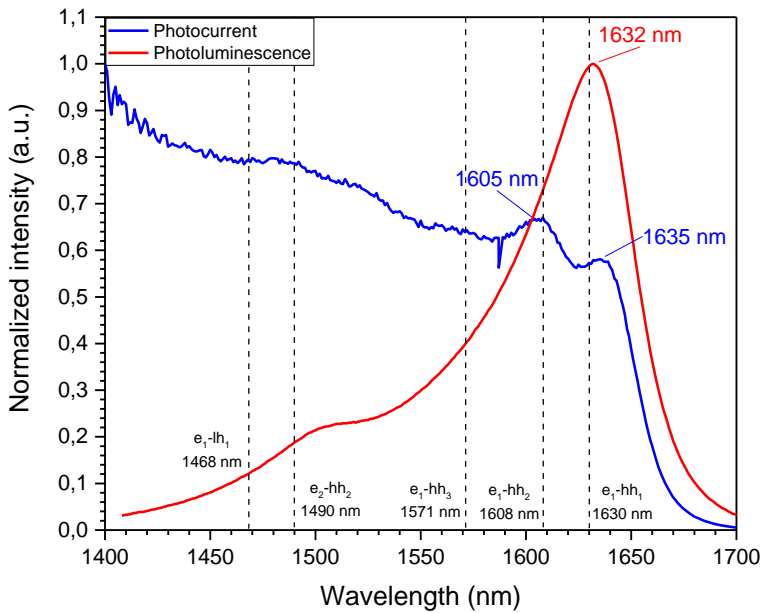


Figure 108. Photocurrent and PL measurements compared with the calculated transition wavelengths.

1650 nm photocurrent transition corresponds to the $e_1\text{-}hh_2$ forbidden transition. At high current injection, i.e. high electric field, we are in a flat band regime, as shown in Figure 109. In that case, the wave function overlap for type I QW is 100%. The probability of an $e_1\text{-}hh_1$ transition is maximum. At low current electric film, both valence and conduction bands are tilted. Consequently, the wave function overlap and transition probability between $e_1\text{-}hh_2$ is not zero anymore.

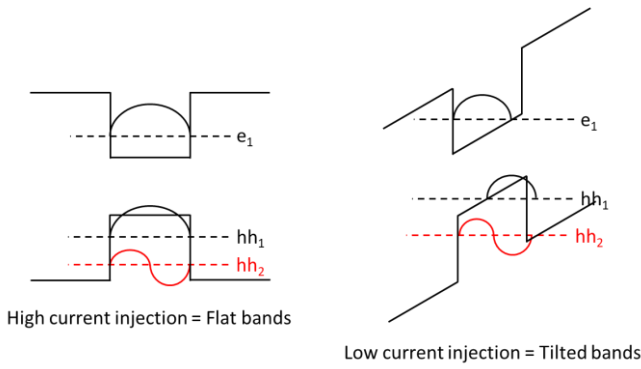


Figure 109. Wave function overlap in high and low injection regimes.

Variations in the photocurrent intensity can be assimilated to other transitions without accurate enough to provide exact values. The simulation seems to be in accordance with the photocurrent and the PL measures for the e_1-hh_1 and e_1-hh_2 transitions. For high energy transitions, the simulation seems to give optimistic values in terms of bandwidth.

The last BB of the structure is the GaInAsP (Q_{1.17})/InP SL slab lattice matched to InP. This under cladding has been characterized by HRXRD (Figure 110 (a)) and Electrochemical Capacitance Voltage (ECV) (Figure 110(b)). Target SL period is a bit smaller than expected, we have thus decided to increase the number of periods, instead of increasing the InP and GaInAsP thicknesses. Si doping is in good accordance with target.

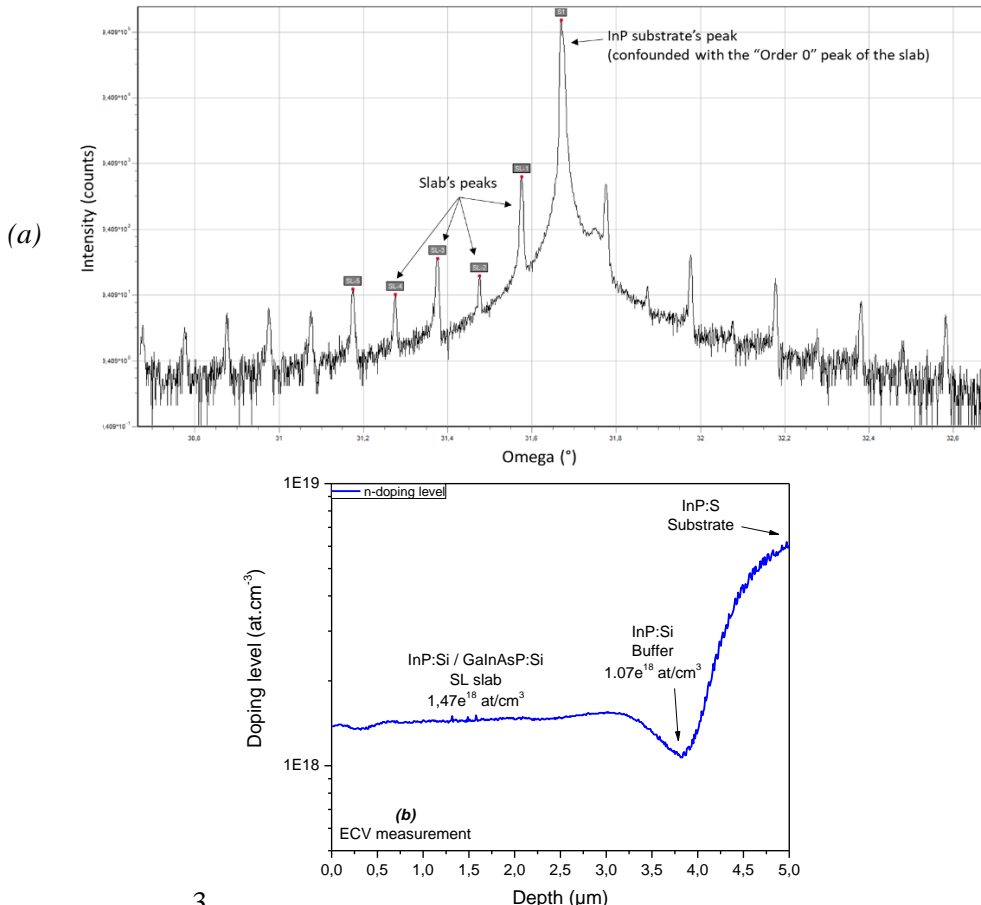


Figure 110. SL slab structure's (a) HRXRD diffractometer and (b) doping measurement.

3.1. C+L-Band full structure

Now that all the BB have been independently calibrated, characterized and stabilized, the next step has been to perform the growth of the full structures.

As a reminder, the SOA structures designed for the C+L-Band are given in Table 39 **Erreur ! Source du renvoi introuvable.** and Table 40 **Erreur ! Source du renvoi introuvable..**

Layer	Material	Thickness (Å)	Repetition
<i>Top cladding</i>	InP:Be	2000	-
<i>SCH</i>	GaInAsP (Q _{1.17})	800 or 600	-
<i>Quantum Well</i>	GaInAsP	140	4
<i>Barrier</i>	GaInAsP (Q _{1.17})	100	3
<i>SCH</i>	GaInAsP (Q _{1.17})	800 or 600	-
<i>Super-lattice slab</i>	InP:Si	290	73
<i>Super-lattice slab</i>	GaInAsP:Si (Q _{1.17})	260	73
<i>Buffer</i>	InP:Si	5000	-

Table 39. C+L-Band SOA structures based on 140 Å thick MQW, labelled "A1" for 800 Å thick SCH and "A2" for 600 Å thick SCH layers.

Layer	Material	Thickness (Å)	Repetition
<i>Top cladding</i>	InP:Be	2000	-
<i>SCH</i>	GaInAsP (Q _{1.17})	800 or 630	-
<i>Quantum Well</i>	GaInAsP	110	4
<i>Barrier</i>	GaInAsP (Q _{1.17})	90	3
<i>SCH</i>	GaInAsP (Q _{1.17})	800 or 630	-
<i>Super-lattice slab</i>	InP:Si	230	73
<i>Super-lattice slab</i>	GaInAsP:Si (Q _{1.17})	320	73
<i>Buffer</i>	InP:Si	5000	-

Table 40. C+L-Band SOA structures based on 110 Å thick MQW, labelled "B1" for 800 Å thick SCH and "B2" for 630 Å thick SCH layers.

We labelled the structures as follow:

- "A1" is the reference structure with 140 Å thick QWs and 800 Å thick SCH.
- "A2" is the reference structure with a lower optical confinement resulting from thinner 600 Å thick SCH.
- "B1" active region consists in 110 Å thick QWs, sandwiched by 800 Å thick SCH, to increase the optical bandwidth.
- "B2" is the low optical confinement variation of the previous structure with 630 Å thick SCH.

HRXRD omega-2-theta scans of the four above mentioned designs are displayed in Figure 111.

A summary of epitaxial structures' characteristics is given in Table 41. SL slab period, QW period and average QW strain are the parameters that could be extracted from HRXRD diffractometers.

Structure	A1	A2	Target A1/A2	B1	B2	Target B1/B2
MQW period (Å)	239.0	235.7	240	198.4	193.1	200
Slab period (Å)	534.1	518.9	550	515.9	517.3	550
Number of period	76	76	73	77	78	73
Slab thickness (µm)	4.059	3.944	4.015	3.972	4.035	4.015
Q_{1.17} mismatch (%)	Lattice-matched					
MQW mismatch (%)	+1.083	+1.087	+1.23	+1.090	+1.072	+1.27

Table 41. HRXRD results for the C+L-Band structures.

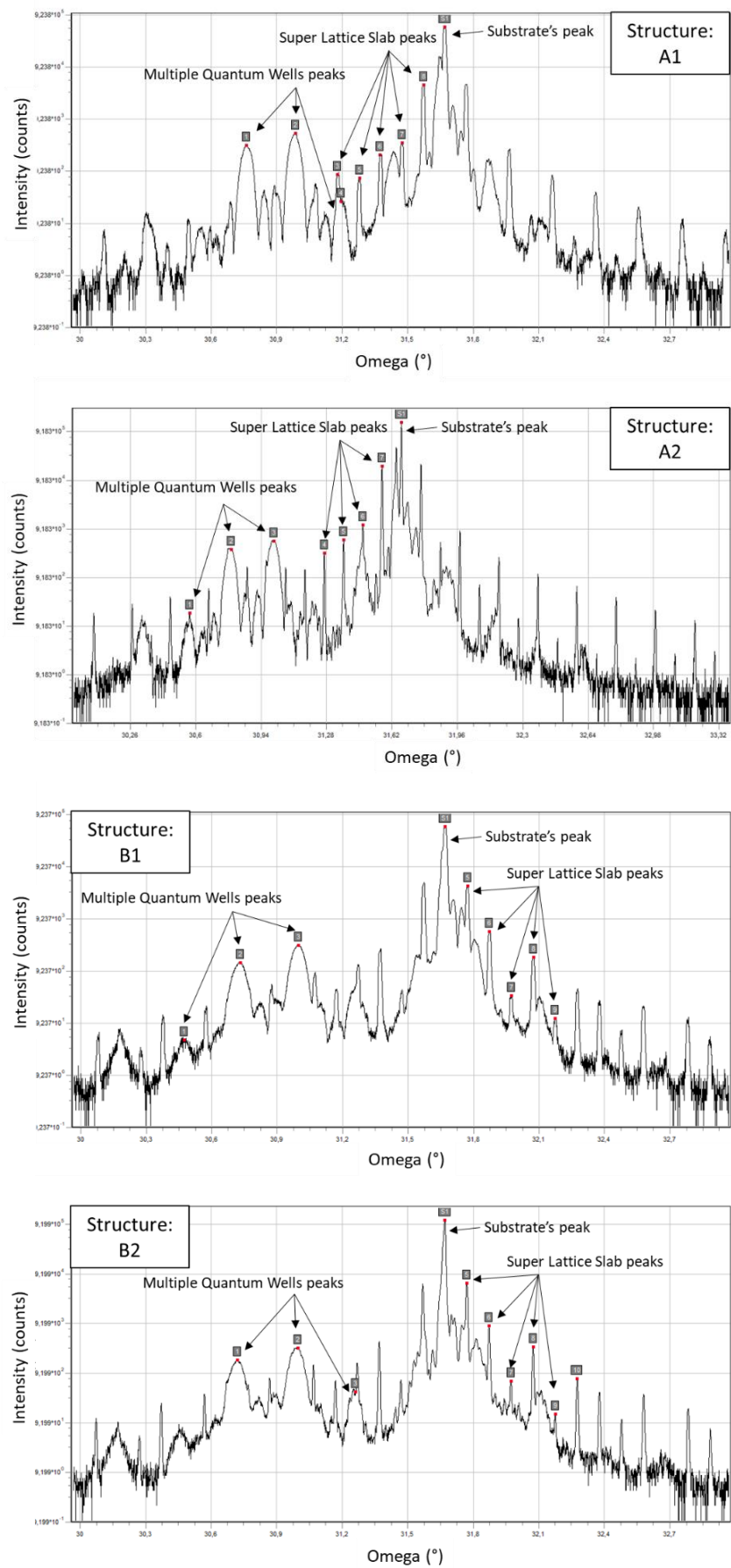


Figure 111. HRXRD diffractometers measured from the C+L-Band structures.

MQW being thinner than expected, the device bandwidth should be larger than expected, with a lower QW optical confinement, resulting in a reduced gain, at the device scale. The actual structures were used in the second simulation campaign mentioned in Chapter II.

QW average strain is also lower than targeted structure, resulting in a discrepancy, in terms of composition, in comparison with target and in a slight shift in PL. The PL measurement performed at LPCNO, with extended GaInAs photodetector are shown in Figure 112.

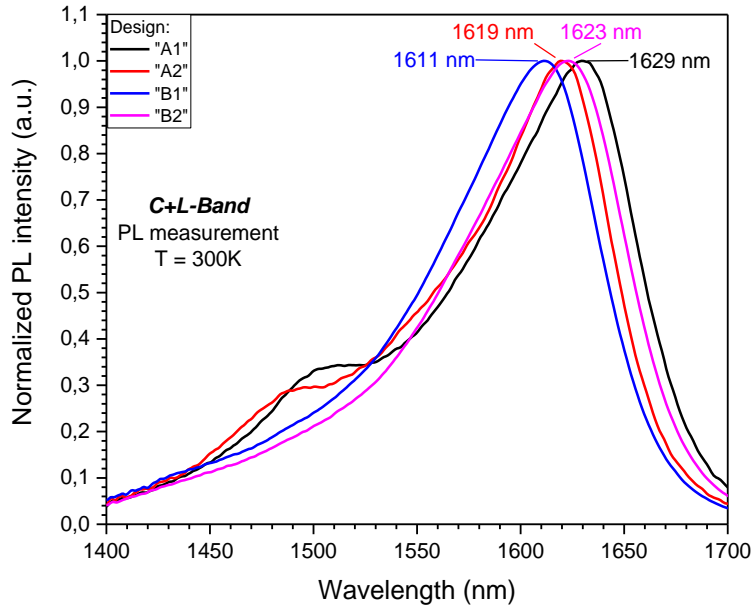


Figure 112. PL measurements of the C+L-Band structures made with extended GaInAs detector.

These measurements clearly indicate the $e_1\text{-}hh_1$ transition's wavelength of the structures. However, we do not have the possibility to discretize wavelength value for the $e_2\text{-}hh_2$ transition. Broad shoulder at lower wavelength is indeed typical for larger QW structures A1 and A2. As a consequence, to complete the set of characterization, we used another PL setup, equipped with a high power excitation laser to enhance $e_2\text{-}hh_2$ transition, using a standard GaInAs detector. Figure 113 exhibits PL measurements performed on the same structures, allowing to extract a wavelength for $e_2\text{-}hh_2$.

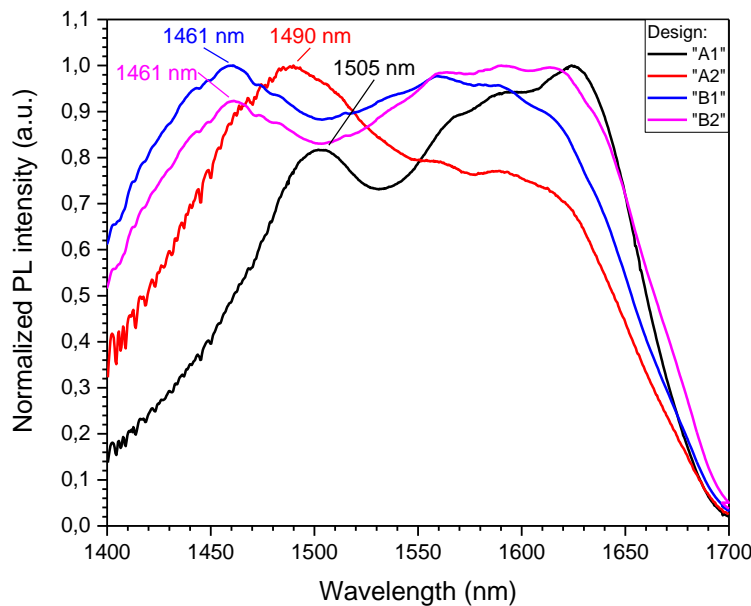


Figure 113. PL measurements of the C+L-Band structures with a high power laser.

Optical bandwidth extracted from the two PL setup are shown in Table 42**Erreur ! Source du renvoi introuvable.**, including the experimental and target transitions $e_1\text{-}hh_1$ and $e_2\text{-}hh_2$.

<i>Structure</i>	<i>A1</i>	<i>A2</i>	<i>A Sim.</i>	<i>B1</i>	<i>B2</i>	<i>B Sim.</i>
<i>e₁-hh₁ wavelength (nm)</i>	1629	1619	1624	1611	1623	1626
<i>e₂-hh₂ wavelength (nm)</i>	1505	1490	1478	1461	1461	1425
<i>Opt. Bandwidth (nm)</i>	124	129	146	150	162	201

Table 42. PL results from the C+L-Band structures.

A larger discrepancy to the targeted structure is observed on the B1 and B2 structures. The $e_2\text{-}hh_2$ transition shows a more substantial difference in each case.

All structures have been grown in a multi-wafer configuration (3x2"), in order to follow different fabrication processes that will be presented in Section 4.1. Now, we can focus on the O-Band structures' growths.

3.2. O-Band material growth

O-band targeted structures are given in Table 43.

Layer	Material	Thickness (Å)	Repetition
<i>Top cladding</i>	InP:Be	200	-
<i>Sup. SCH</i>	GaInAsP ($Q_{1.03}$)	750 or 550	-
<i>Quantum Well</i>	GaInAsP	110	4
<i>Barrier</i>	GaInAsP ($Q_{1.03}$)	100	3
<i>Inf. SCH</i>	GaInAsP ($Q_{1.03}$)	750 or 550	-
<i>Super-lattice slab</i>	InP:Si	290	73
<i>Super-lattice slab</i>	GaInAsP:Si ($Q_{1.03}$)	260	73
<i>Buffer</i>	InP:Si	5000	-

Table 43. O-Band SOA structures based on 110 Å thick MQW, labelled "O1" for 750 Å thick SCH and "O2" for 550 Å thick SCH layers.

Like for the C+L-Band, we label the structures for clarity purposes:

- “O1” is the reference structure in the O-Band, with 110 Å thick QW and 750 Å thick SCH layers.
- “O2” corresponds to its low optical confinement variation with 550 Å thick SCH layers.

3.2.1. Growth conditions optimization in the unstable region

A first batch of O-Band calibration structures have been grown using the same growth conditions as for the C+L-Band structures. But it has proven to be less straightforward than anticipated. These structures exhibited poor PL intensities as compared to their C+L counterparts. Moreover, we observed slight cross-hatch dislocation lines highlighted using a Fast Fourier Transform (FFT) filter, as shown in Figure 114.

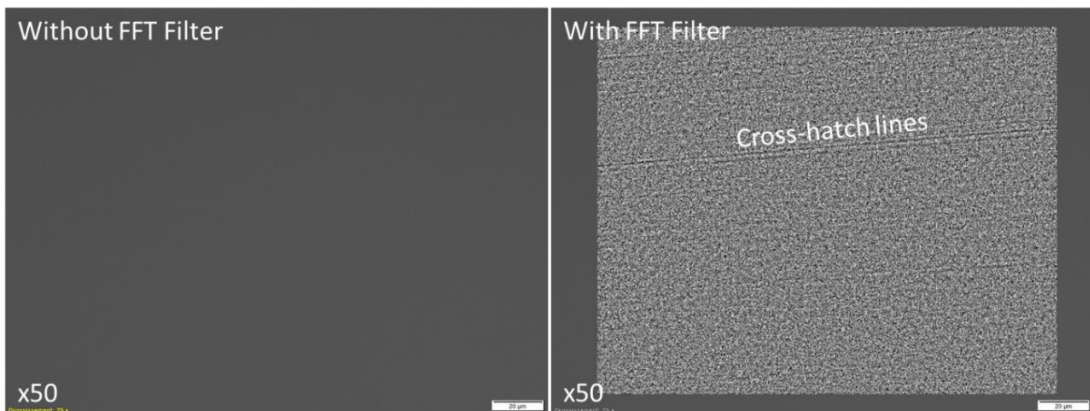


Figure 114. Microscope pictures of O-Band calibration without and with FFT filter.

The calibration structures are SL slab free to be able to focus only on the active region and not worry about a potential 4 μm thick under cladding, above critical thickness. Cross-hatch being the image at the surface of a wafer suffering a strain accumulation leading to relaxation, we initially checked the average QW strain of the calibration structure with HRXRD measurement (Figure 115).

Unexpectedly, the compressive strain of the MQW was limited to +0.724%, lower than the ones measured with the C+L-Band structures. This cannot explain the apparition of cross-hatch. However, QW composition is within the miscibility gap of GaInAsP compounds that we presented in Section 2.1. Consequently, this result illustrates the importance of the growth optimization for such O-Band structures.

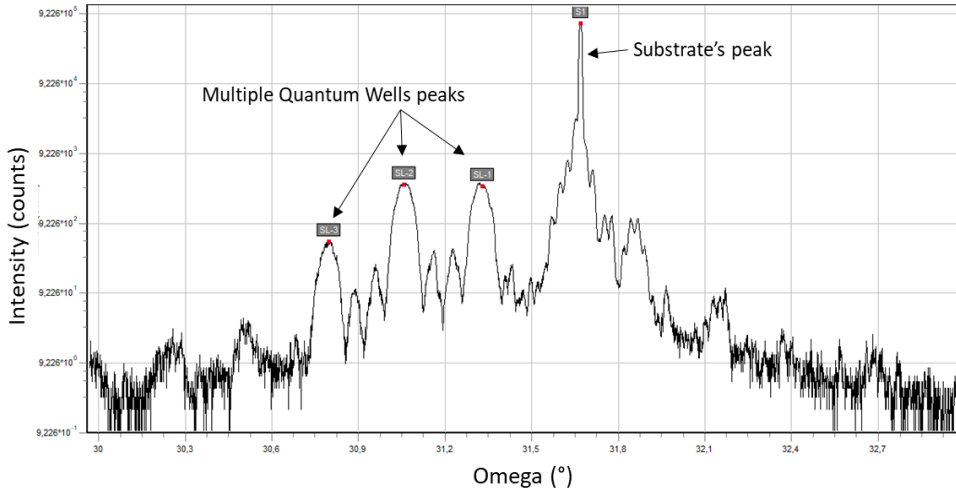


Figure 115. HRXRD diffractometer from the cross-hatched wafer.

As previously stated, InP and their related materials are extremely temperature sensitive, especially the ones in this unstable region, for which, further optimizations have to be carried out [23].

Cross-hatch has been also highlighted on the PL mapping, as shown in Figure 116, where PL peak intensity was null. We suppose that cross-hatch is issued from some kind of quick phase separation of GaInAsP, since thickness of the QW is very thin.

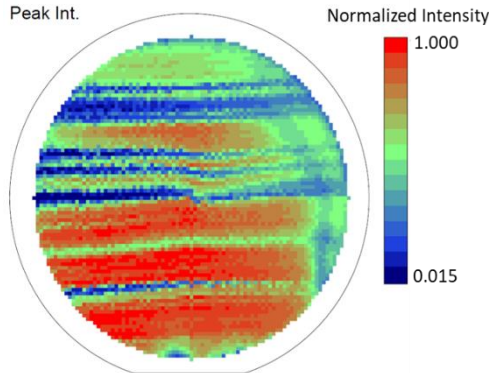


Figure 116. PL mapping of the O-Band calibration wafer presenting cross-hatch.

In the following structures, growth temperature of the active region has been reduced to reduce decomposition probability, in addition to an increased V/III flux ratio and a slightly reduced growth rate [24, 25]. Incremental optimized growth conditions allow us to grow good quality material, totally cross-hatch free, as confirmed by the PL peak intensity mapping, presented in Figure 117.

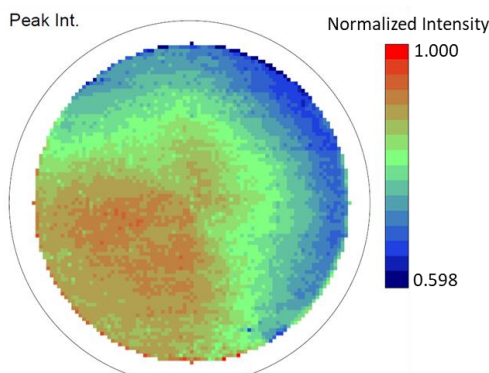


Figure 117. PL intensity peak mapping of an O-Band calibration wafer grown with strain compensation.

The 1363 nm e_1-hh_1 transition wavelength was measured on this wafer with a standard deviation of 0.148%, corresponding to 2.012 nm.

After the growth of the O-Band structures, their material characteristics were measured. In the next section, we will compare these measurements with the targeted values set with the simulations.

3.2.2. O-Band SOA full structure epitaxy

The last building difficulty being resolved, both variations of the O-Band SOA were grown. HRXRD diffractometers of the structures (Figure 118) allow us to extract the MQW and Slab periods, as well as the QW average strain. A summary of the extracted parameters is given in Table 44.

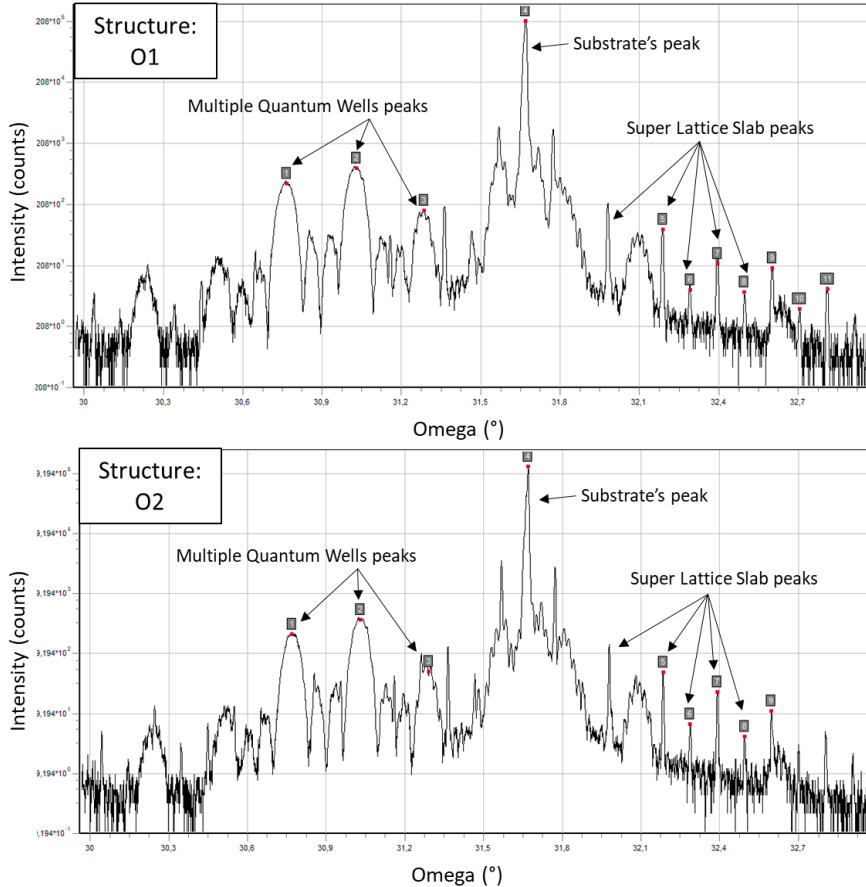


Figure 118. HRXRD diffractometers of the complete O-Band structures.

<i>Structure</i>	<i>O1</i>	<i>O2</i>	<i>Target O1/O2</i>
<i>MQW period (Å)</i>	201	201	210
<i>Slab period (Å)</i>	499.4	502.2	550
<i>Number of period</i>	79	79	73
<i>Slab thickness (µm)</i>	3.945	3.967	4.015
<i>MQW mismatch (%)</i>	+0.990	+1.007	+1.20

Table 44. Results extracted from the HRXRD measurements of the O-Band structures.

Observations are similar to C+L-Band structures, with thinner QW and a reduced QW strain. Composition discrepancies impact the energy transitions. PL measurements are shown in Figure 119, using both PL setup, and the e_1-hh_1 and e_2-hh_2 wavelengths, for both designs are summarized in Table 45.

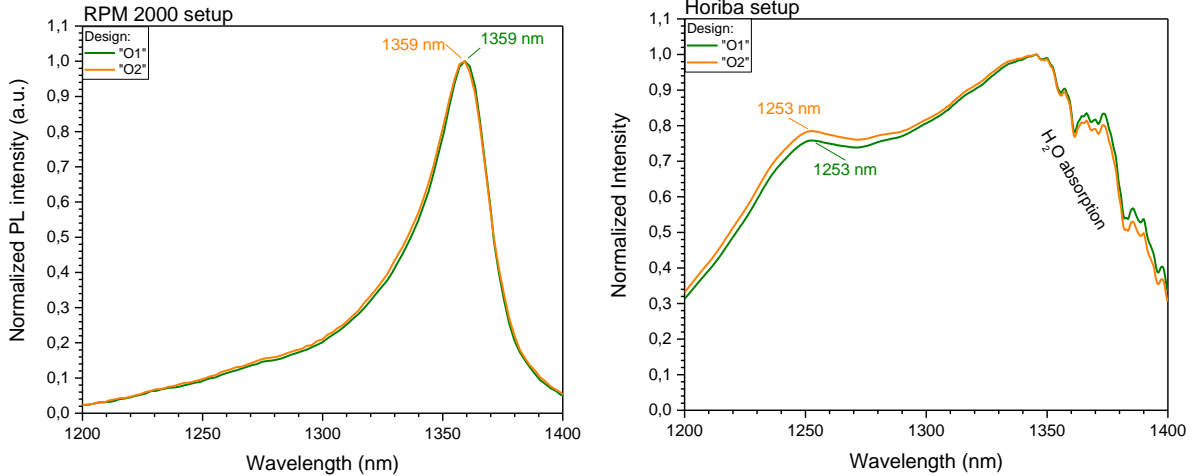


Figure 119. PL measurements of the O-Band structures with both PL setups.

Structure	O1	O2	O Sim.
<i>e₁-hh₁ wavelength (nm)</i>	1359	1361	
<i>e₂-hh₂ wavelength (nm)</i>	1253	1230	
<i>Opt. Bandwidth (nm)</i>	106	131	

Table 45. PL results of the O-Band structures compared with the calculated target.

As it could be foreseen from HRXRD measurement, e₂-hh₂ transition is red-shifted by 23 nm, resulting in narrower optical bandwidths. However, it is interesting to note that both of the structures give exactly the same values, showing the reproducibility of the epitaxy.

The material parameters of both O-Band structures are summarized in Table 46.

	Structure	O1	O2
HRXRD	<i>MQW period (Å)</i>	201	201
	<i>Slab period (Å)</i>	499.4	502.2
	<i>MQW mismatch (%)</i>	+0.990	+1.007
PL	<i>e₁-hh₁ wavelength (nm)</i>	1359	1359
	<i>e₂-hh₂ wavelength (nm)</i>	1253	1253
	<i>Bandwidth (nm)</i>	106	106

Table 46. Material characterization results of the O-Band structures.

Structures were grown on a 3x2" platen to further study both SIBH processes developed at III-V Lab. The fabrication processes and the regrowth steps will be further detailed, in Section 4.

3.3. O-Band SOA growth process transfer to the MBE412 reactor

All above discussed epiwafers have been grown in the V100 reactor with difficulty because of the lack of *in-situ* characterization tools (no RHEED, nor nothing else) and the reactor's instability and failures.

It was consequently of great importance for the laboratory to transfer growth process on the new MBE412 reactor. O-Band wideband SOA epitaxy being more difficult to perform, we have decided to focus on these specific structures.

As mentioned at the beginning of the chapter, the MBE412 growth chamber is equipped with 2 *in-situ* characterization tools allowing us to monitor and finally optimize the growth.

- Band-edge thermometry, for absolute growth temperature measurement (kSA BandiT)
 - The bandgap measurement is not impacted by the interferences related to the viewport coating or any IF reflection into the growth chamber.
- Stress and curvature measurement (RIBER EZ-Curve, initially developed by A. Arnoult from LAAS laboratory in Toulouse, FRANCE)
 - The setup provides unrivalled high responsivity and high accuracy, even as compared to its competitors (kSA MOS or Laytec). Even short period SL or QD can be monitored.

BandiT allowed us to converge very quickly on growth temperature. This is a very powerful tool too, of much better interest as compared to standard black-body temperature measurement pyrometer. BandiT, combined with InP deoxydation RHEED observation, gave us the opportunity to accurately adjust the temperature of each BB of the SOA. We monitored, with EZ-Curve, the stress of the calibration structure detailed in Table 47.

Layer	Material	Thickness (Å)	Repetition	Comment
<i>Top cladding</i>	InP:Be	180	-	
<i>Sup. SCH</i>	GaInAsP (Q _{1.03})	700	-	
<i>Quantum Well</i>	GaInAsP	110	4	PL wavelength = 1.36 μm (e ₁ -hh ₁) + 1% compressive strain
<i>Barrier</i>	GaInAsP (Q _{1.03})	100	3	Under tensile strain compensation of lattice matched
<i>Inf. SCH</i>	GaInAsP (Q _{1.03})	700	-	
<i>Buffer</i>	InP:Si	3000	-	
<i>Substrate</i>	InP:S	500 μm		

Table 47. Calibration structure monitored during its growth with EZ-Curve.

Wafer strain is shown in Figure 120, where every single growth step can be extracted.

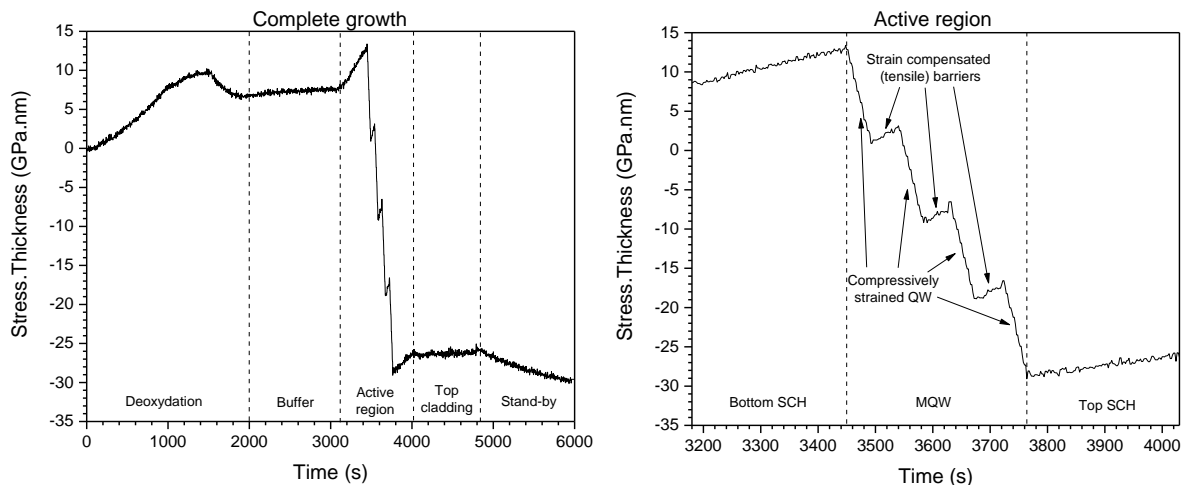


Figure 120. Real-time stress measurement of a slab-less SOA. Full structure and focus on the active zone.

The temperature increases during the substrate's deoxydation (RHEED pattern in Figure 121). During this step, the stress variations are caused by temperature modifications. The wafer is under tensile strain during the temperature increase and various substrate temperature ramps can be easily spotted.

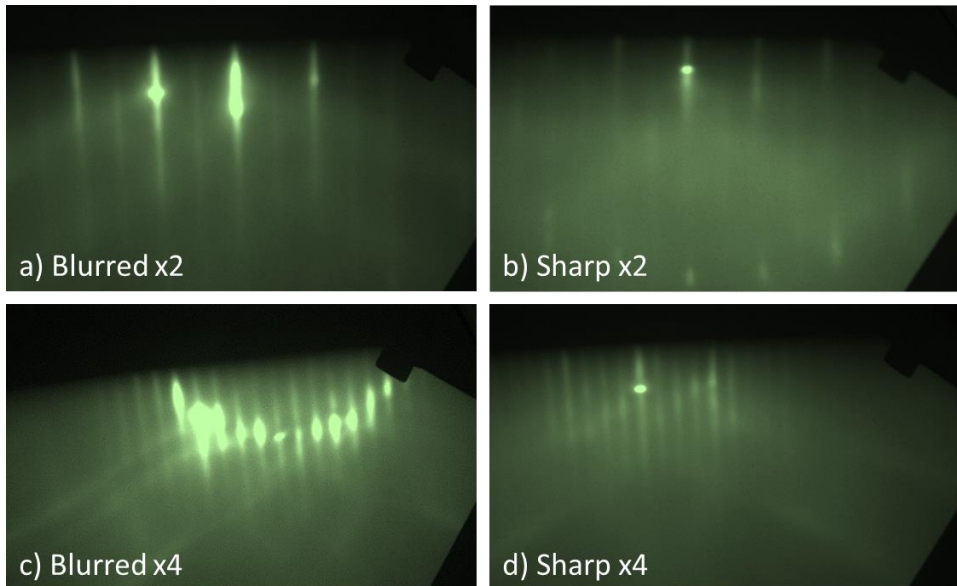


Figure 121. Evolution of the reconstructions observed with RHEED during the deoxydation.

A compressive strain is then observed when the temperature decreases.

During the InP:Si growth, tensile strain is slightly building up. It is related to the slow substrate's temperature increase caused by the silicon cell, heated at more than 1250°C.

The Q_{1.03} SCH is significantly more tensile strained. It has to be noticed that the strain measured at growth temperature must be adjusted to obtain its actual value at room temperature. A layer exhibiting tensile strain at growth temperature will be closer to its matching conditions at room temperature.

The response time of the apparatus is short enough to measure the thin layers, like the MQW region. As expected in this area, the barriers are slightly under tensile strain and the QW are under stronger compressive strain.

EZ-Curve provides real-time strain which can be calculated following Equation 75.

$$\text{Equation 75. } \varepsilon = \frac{\Delta y / \Delta x}{v * E'}$$

Where, ε is the strain, $\Delta y / \Delta x$ is the slope in GPa.nm/s, v is the growth rate in nm/s and E' is the biaxial modulus of the epilayer. The quaternary alloy's biaxial modulus can be calculated using Vergard's law, from binary compounds, listed in Table 48, in GPa.

InP	GaAs	InAs	GaP
95.31 GPa	119.8 GPa	79.08 GPa	149.3 GPa

Table 48. Biaxial moduli of the binary compounds involved in GaInAsP quaternary alloy.

A -0.057% tensile strain is obtained from the bottom SCH, and a -0.029%, for the top SCH. The difference is related to a temperature change during the epilayer growth. The substrate's temperature is increased during bottom SCH growth and increased during top SCH growth.

In the MQW region, the QWs are under an average compressive strain of +0.982% and the barriers are grown with an average tensile strain of -0.126%.

This structure has been fully characterized by HRXRD (Figure 122) and PL (Figure 123 & Figure 124).

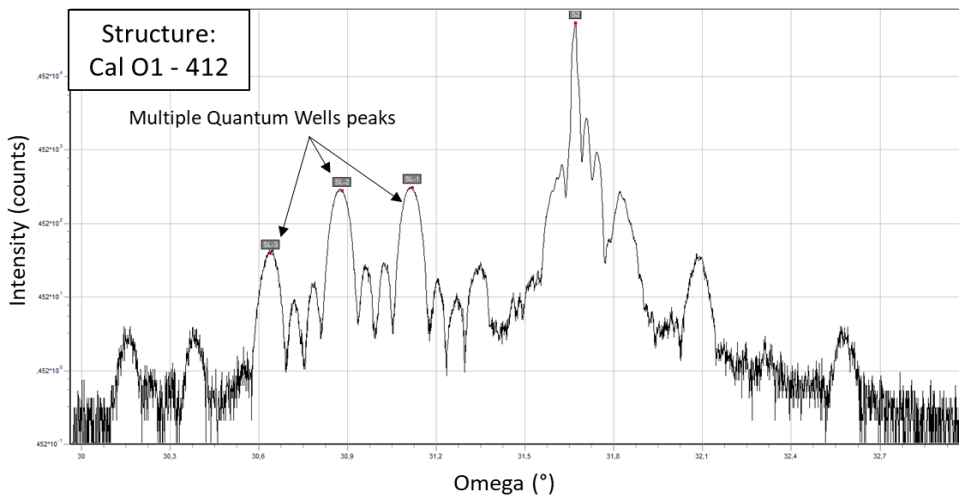


Figure 122. HRXRD diffractometer of the O-Band calibration wafer grown in the MBE412.

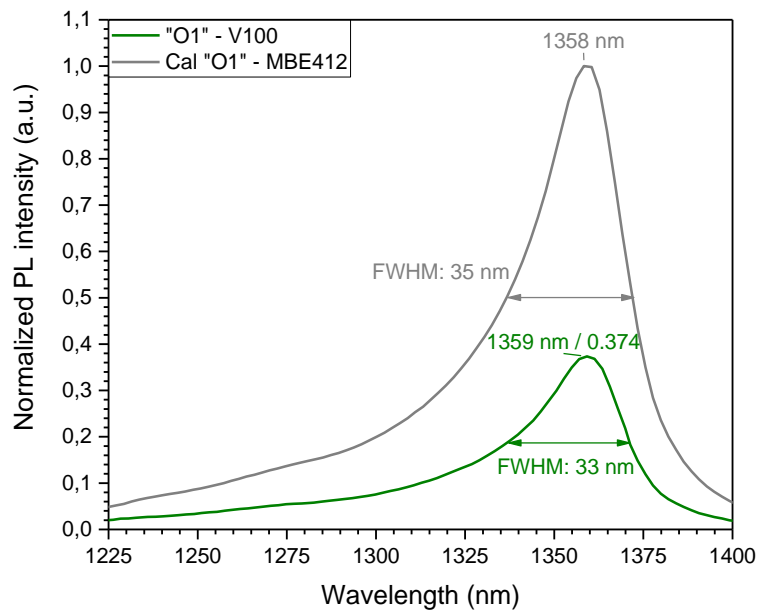


Figure 123. PL results of MBE412 SOA calibration wafer compared with processed wafer.

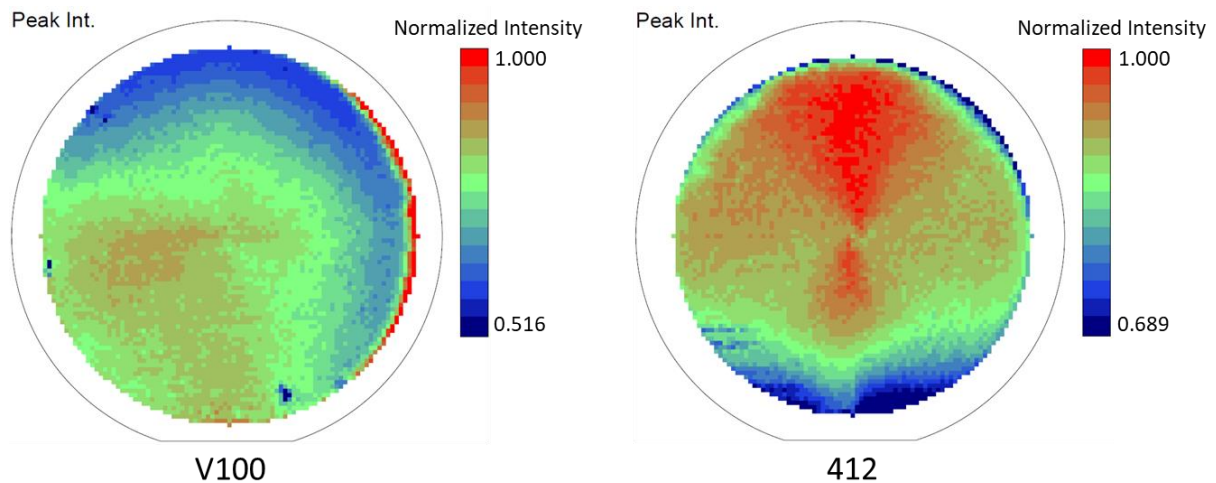


Figure 124. Mapping PL of O-Band structures grown by V100 and MBE412 reactors.

From HRXRD measurements, we obtain a 216 Å thick MQW period for a target of 210 Å, corresponding to a difference of 2 ML. We also observe a +0.983% compressive strain in the QW, which was measured to be +0.982% with EZ-Curve.

A quick comparison with the same structure grown in the V100 is shown in Figure 123. A significant increase of the PL intensity, with the same FWHM can be observed. Only a couple of active region calibration structures have been required to adjust growth conditions and PL wavelength, i.e. the AsH₃/(PH₃+AsH₃) baratron pressure ratio.

In addition, in terms of homogeneity, we have been able to observe an improvement as compared to the V100, illustrated in Figure 124. At the time of the study, we have obtained the results summarized in Table 49.

	V100	MBE412
Peak PL wavelength standard deviation	0.186%	0.092%
Peak PL intensity standard deviation	10.60%	7.45%

Table 49. Standard deviations measured with PL mapping with V100 and MBE412 grown structures.

Following this material validation, C+L-Band and S+C-Band complete structures have been grown and are currently processed at III-V Lab. These structures are designed to follow the 1-step SIBH fabrication process, including both the 4 μm thick under cladding, the upper cladding and the contact layers.

On the MBE412, we have already developed the growth process of wideband SOA for O-Band to L-Band, including S- and C-Bands, as shown in Figure 125. Intermediate transitions on the S+C-Band are clearly spotted.

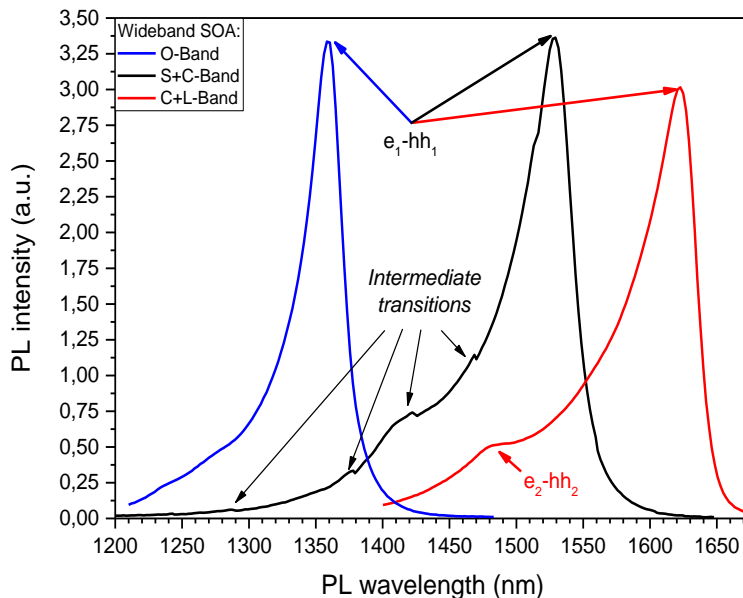


Figure 125. PL measurement of O-Band, S+C-Band and C+L-Band structures grown with the MBE412.

4. Fabrication processes

Two SIBH fabrication processes are developed at III-V Lab, “2-step SIBH” and “1-step SIBH”. Both processes consist in burying the ridges in semi insulating InP material. They enable to obtain a circular mode at the devices’ outputs, a more efficient heat sinking than the other technologies (BRS, Deep Ridge and Shallow Ridge) and lower absorption losses.

Main objective is to compare these two SIBH processes through the devices’ performances. In this section, we describe the different steps involved in each process.

4.1. SIBH processes descriptions

The 1-step SIBH, developed at III-V Lab, is born from a necessity to simplify the classical process that is the 2-step SIBH. The processes’ names come from the number of epitaxy regrowths required to complete the structures. The 1-step SIBH enables to reduce the number of required epitaxial regrowth steps, by including the p-doped top cladding layer to the base structure and to avoid the H⁺ implantation step. Figure 126 presents two Scanning Electron Microscopy (SEM) pictures of the structures’ sections at the end of the processes. We can observe the different growth steps.

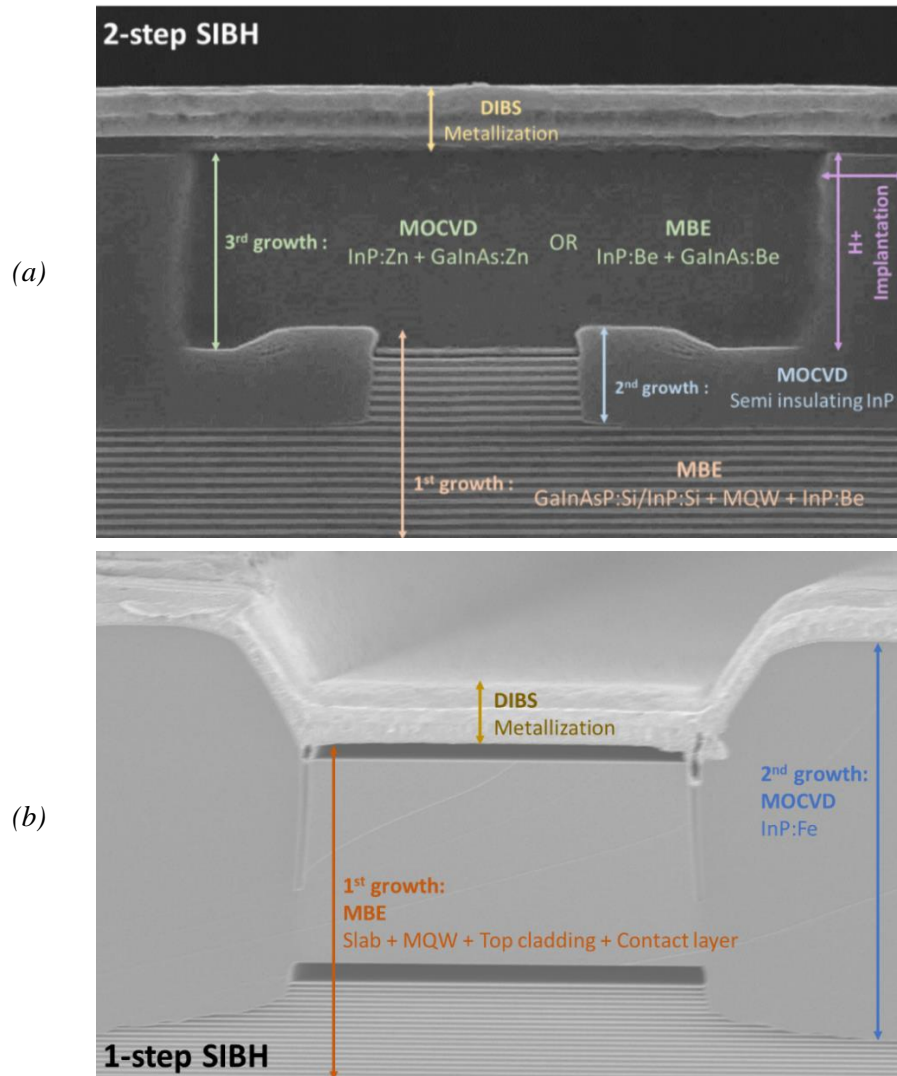


Figure 126. SEM picture of (a) a 2-step SIBH and (b) a 1-step SIBH structures.

These pictures show the remaining layers to achieve a 1-step SIBH process. Indeed, the stack representing the “1st growth” is much thicker for the 1-step than for the 2-step SIBH. For this last process, the thickness of the semi insulating InP needed to be increased, to improve the lateral diode resistance. However, this parameter is limited the slab etching that cannot be too deep, to keep the control of the optical mode profile. This issue can be solved by the 1-step SIBH which requires thicker regrowth with the implementation of the p-doped cladding layer in the base structure. The 1-step SIBH can be only achieved with a precise control of the regrowth conditions and by avoiding overgrowths, indicated by the green arrows in Figure 127. We now have two options in terms of process to manufacture the SOA structures. They are schematized in Figure 127 (a) for the 2-step SIBH and in Figure 127 (b) for the 1-step SIBH.

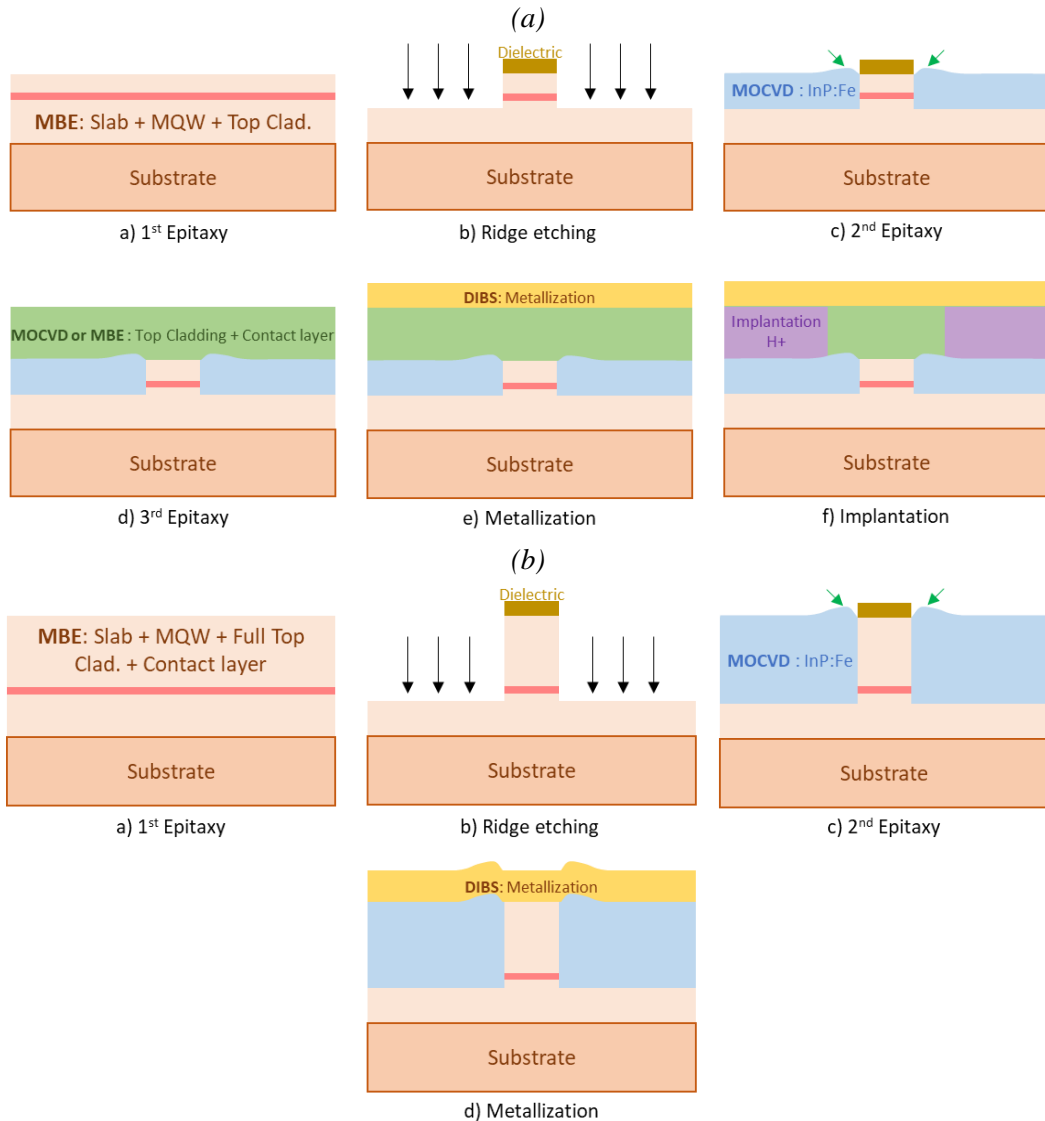


Figure 127. Schematizes of (a) the 2-step SIBH and (b) the 1-step SIBH processes.

After these steps, for both processes, we must thin the substrate to deposit the other metallic contact on the substrate's side of the wafer. The absence of the implantation step, as well as the requirement of a single epitaxial regrowth are substantial time savings for the 1-step SIBH.

4.2. Wafers preparation for 1-step SIBH process

All 21 epiwafers wafers are well suited for 2-step SIBH. To undergo the 1-step SIBH process, the wafers must have complete top cladding and contact layers. To obtain them, we performed regrowths, by GSMBE, called “P-type regrowth”, as the layers are only p-doped. The layers, listed in Table 50, are the same for every wafer whatever its active region.

Layer	Material	Thickness (Å)	Doping levels (cm⁻³)
<i>Contact</i>	GaInAs:Be	2500	3x10 ¹⁹
<i>Transition</i>	GaInAsP:Be (Q _{1.17})	200	8x10 ¹⁸
<i>P-Cladding</i>	InP:Be	14000	From 1.2x10 ¹⁸ to 5x10 ¹⁸
<i>P-Cladding (Regrowth's buffer)</i>	InP:Be	1000	1.2x10 ¹⁸

Table 50. Regrown layers to obtain wafers for 1-step SIBH fabrication process.

To avoid any interaction between the signal and the metal, a 1.4 µm thick top cladding is required.

P-type dopants, such as Zinc (Zn) and Be are known for their temperature-sensitive diffusion characteristics. Zn is especially prone to diffusion, as compared to Be. That being said, the impact of high temperature MOCVD annealing can also modify the doping profile, both laterally and in the growth direction. We will briefly discuss the consequence of MOCVD regrowth on MBE epilayers.

Design	A1	A2	B1	B2	O2
Lattice mismatch (%)	-0.079	-0.053	-0.025	-0.019	-0.017

Table 51. Lattice mismatch between the new peak and the substrate for every wafer.

No wafer based on the O1 design was fabricated with the 1-step SIBH process, thus, none of them underwent the P-type regrowth. Once the regrowths and the verifications were achieved, the fabrication processes were performed.

4.3. Ridge etching

The fabrication steps for the ridge etching are schematized in Figure 128.

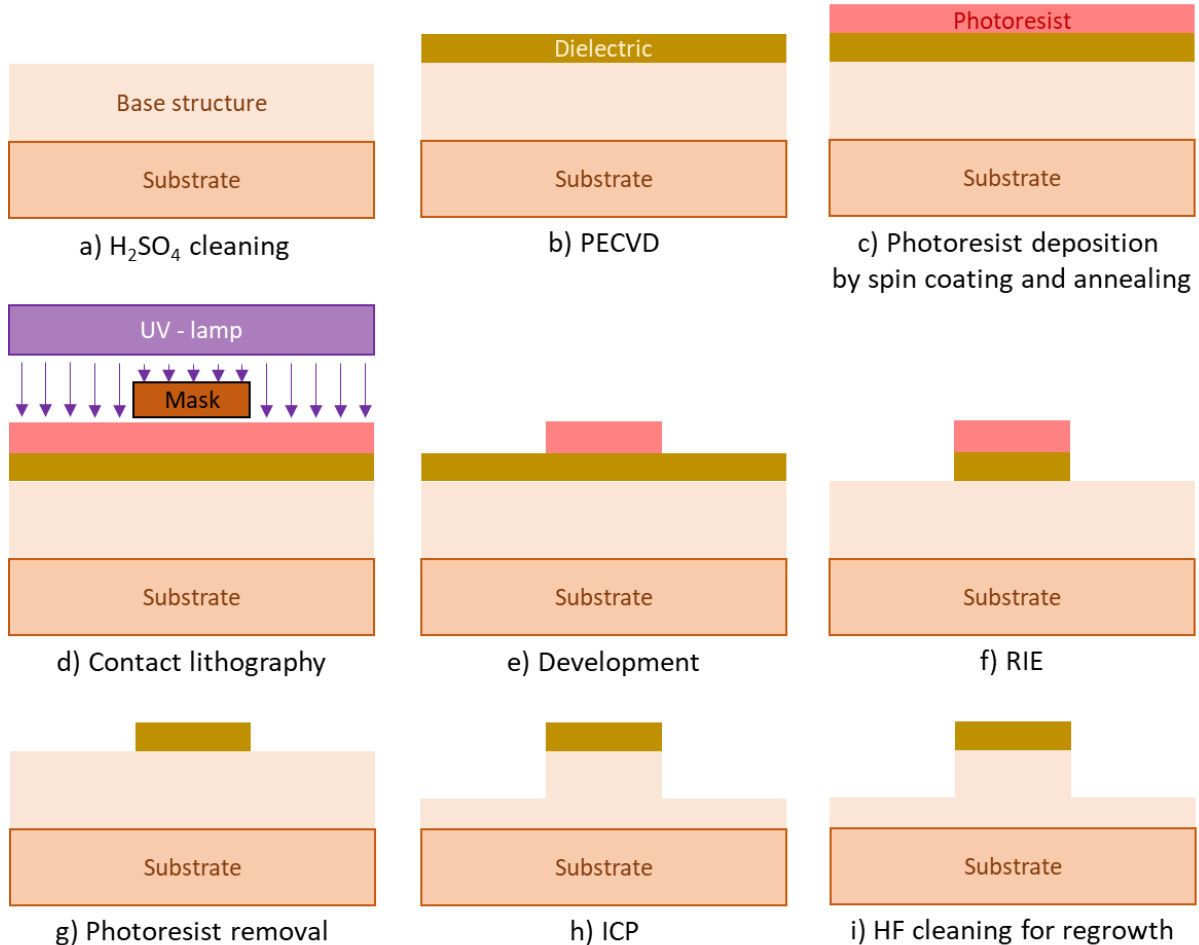


Figure 128. Fabrication steps for the ridges definition in the structures.

First, a chemical deoxydation using sulfuric acid (H_2SO_4) is performed, followed by a dielectric deposition of $1.1 \mu\text{m}$ over the wafer. This deposition is performed using Plasma Enhanced Chemical Vapor Deposition (PECVD) with a Nextral D200 system. The thickness of the deposited layer is estimated by ellipsometry. Then, a contact photolithography is required to protect the wafer with photoresist to etch the ridges. The unprotected surface undergoes a first Reactive-Ion Etching (RIE) to remove the dielectric, with a Nextral E100 system. The plasma used during this step is a mix of SF_6 , CHF_3 and O_2 , which only impacts the dielectric, without damaging the III-V material. This etching is monitored with a reflectometry measurement. We can observe the oscillations resulting from the interferences between: (i) the light reflected at the surface of the dielectric we etch and (ii) the light reflected at the interface between the dielectric and the semiconductor. This step is considered as finalized when the reflectometry displays a flat curve.

The photoresist, at the top of the remaining dielectric, is removed and the wafer is chemically cleaned before the III-V materials' etching, using an Inductively Coupled Plasma (ICP). The top of the ridges is still protected by a dielectric layer that defines the ridges' geometry. For the ICP etching as well, the process is monitored by reflectometry. This step is crucial for every wafer, because the etching depth impacts the optical mode behavior, as described in Chapter II. In Figure 129, representing the reflectometry curves corresponding to the etching of two different structures, we can observe why the super-lattice configuration of the slab is interesting.

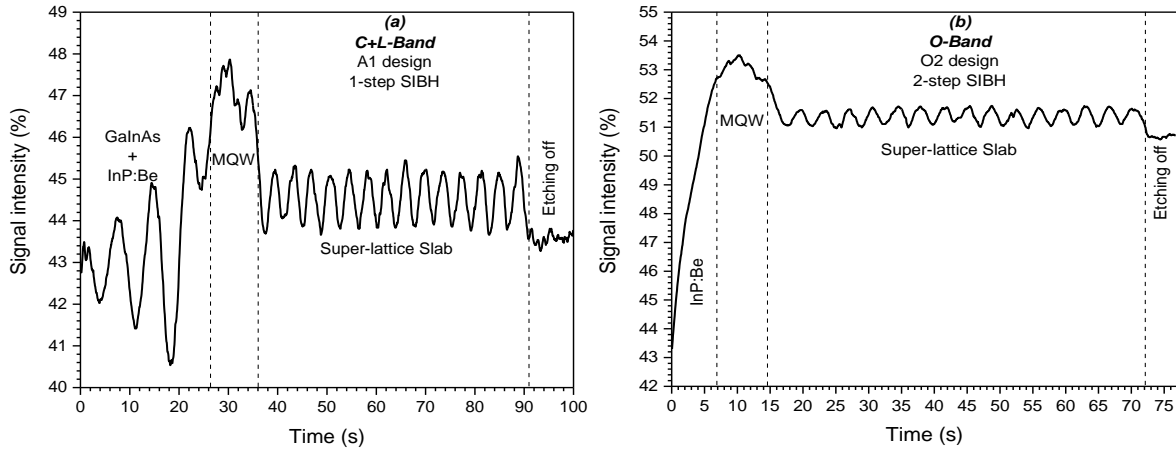


Figure 129. Reflectometry curve from the ICP etching of (a) a C+L-band wafer following the 1-step SIBH process and (b) a O-band wafer following the 2-step SIBH process.

By monitoring the etching by reflectometry, we can observe the different materials involved in the structures. As shown in Figure 129 (a), the time required before the etching of the MQW is higher because, there is a thick InP:Be cladding. Figure 129 (b) represents the etching of a 2-step SIBH wafer, as the layer etched before the MQW is the thin p-doped top cladding. In both curves, the most important section is the one corresponding to the etching of the super-lattice slab. The increase of intensity corresponds to the etching of InP and the decrease, to the etching of the quaternary compound. It is also important to note that the oscillation amplitude is reduced for the O-band structures, due to the lower composition difference between InP and Q_{1.03} than between InP and Q_{1.17}. For a bulk slab, the depth of the etching is harder to control. The homogeneity of the material does not provide these oscillations. Consequently, for a bulk slab, we can previously calculate the etching rate or we can place the measurement spot at the limit between a masked and an unmasked area to obtain the interferences related to the semiconductor's etching modulated by a second oscillation related to the dielectric mask erosion. In our case, the etching is easier to follow, we can stop the etching when the targeted number of oscillations is reached, with the measurement spot wherever on the unprotected semiconductor.

The next step is the regrowth of the semi-insulating material. The surface and the sides of the ridges are cleaned using diluted fluoric acid (HF). The top of the ridges must remain protected by dielectric to avoid semiconductor regrowth at their tops, as shown by the last illustration in Figure 128.

4.4. SIBH regrowth steps

The growth conditions are different between 1-step and 2-step SIBH. A chemical preparation using potassium hydroxide (KOH) and H₂SO₄ is performed to clean the wafers just before the epitaxy regrowth.

2-step SIBH regrowth process has been initially developed in an AIX200/4 reactor, described in Section 1.1.1. It is a well-established process, extremely reproducible. 1-step SIBH process has been more recently developed at III-V Lab, using a recently acquired CCS reactor (2017), described in Section 1.1.2. This reactor offers more versatility and growth pressure regime can be adapted.

The regrown layers are listed in Table 52 for 2-step SIBH.

Material	Thickness (Å)
<i>InP:Si</i>	2000
<i>InP:Fe</i>	Depends on the etching depth
<i>InP:Fe (Regrowth's buffer)</i>	500

Table 52. 2-step SIBH regrown layers.

The InP:Fe layer's thickness must be defined for every wafer, based on the III-V material etched by ICP, measured by profilometry coupled to ellipsometry to determine the thickness of the remaining dielectric at the top of the ridges. For 2-step SIBH, this layer thickness is usually around 1 μm.

Another important point that impact the SIBH regrowth is the ridge geometry of the RSOA devices: a soft curvature from one end to the other of the device's length provides high reflection on one side and reduces the reflection at the input/output facet. Consequently, further optimizations were led to enable a correct regrowth for both straight and curved devices.

4.4.1. Influence of the SIBH regrowth on SOA epilayers

At design level, it is important to evaluate the influence of the fabrication steps of the device following the first epitaxy, especially if the process involves more severe conditions than the initial ones. It is possible to anticipate the design or minimize their impact. Major repercussions are:

- Dopant diffusion (Zn and Be) in the growth direction and perpendicular to the growth direction (laterally).
 - Dopant diffusion in unintentionally doped active region (usually parallel to growth direction) or even in the semi insulating layers can seriously hinder the operation of the device or significantly limit its performances.
- QW intermixing
 - It usually prompts device wavelength blue shift.

We carried out high temperature annealing on different kind of epiwafers to assess the impact of MOCVD regrowth on MBE grown SOA structures.

Looking only at HRXRD diffractometers of 680°C SIBH overgrown SOA structures, we did not observe any major structural modification of underlying MBE epilayers, as shown in Figure 130, on both O-Band and C+L-Band designs.

Highly doped p-type GaInAs contact fully absorbing the PL signal, we could not check what could be the effect in terms of dopant diffusion at active region. We consequently chose to use a different approach:

- Use a Distributed Feedback (DFB) laser structure as reference, with a structure having undoped cladding layers and a second structure, in which these layers are doped.
- Perform a 680°C annealing under PH₃ gas for a couple of hours, in the AIX200/4 reactor, to simulate a top cladding regrowth.

Similarly to regrown SOA, we did not observe any difference by HRXRD, as illustrated in Figure 131.

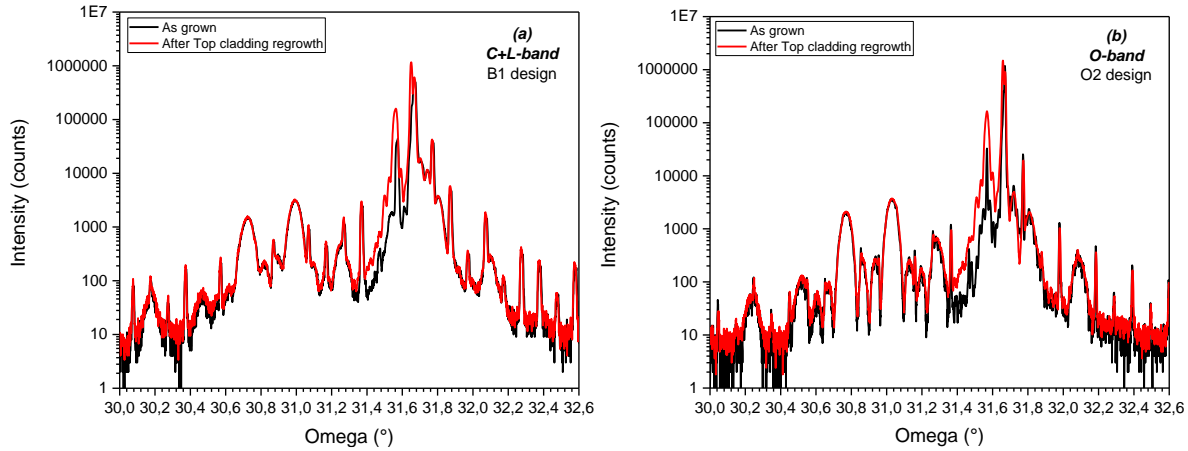


Figure 130. HRXRD diffractogram comparison before and after the p-type regrowth (a) for a C+L-Band and (b) for a O-Band structures.

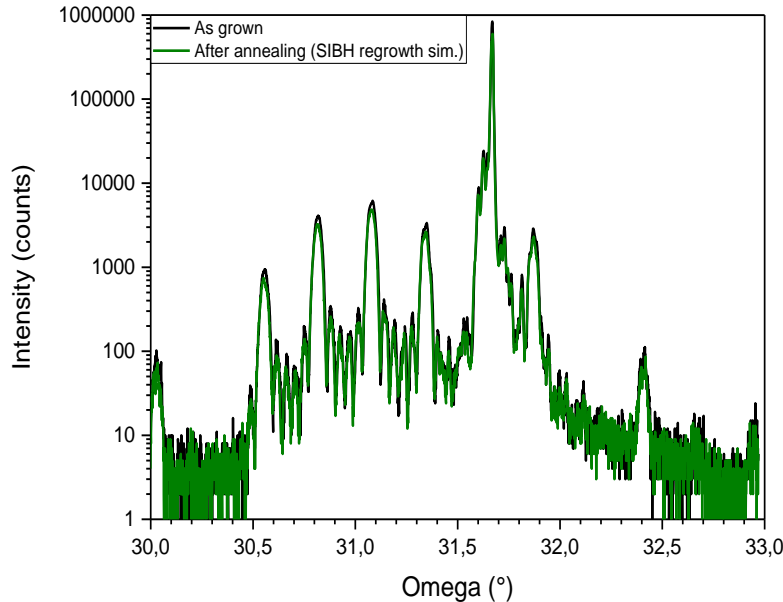


Figure 131. Omega-2-theta scan of a DFB laser structure as-grown, before annealing and after a 680°C annealing.

We observe a major wavelength shift of e_1-hh_1 transition, by about 20 nm, as we were expecting, in Figure 132. A positive impact has been a 20 to 25% increase in the PL intensity. The latter is related to the removal of non-radiative recombination centers from QW and QW to barrier interfaces.

Further annealing did not really highlight subsequent PL or HRXRD modification.

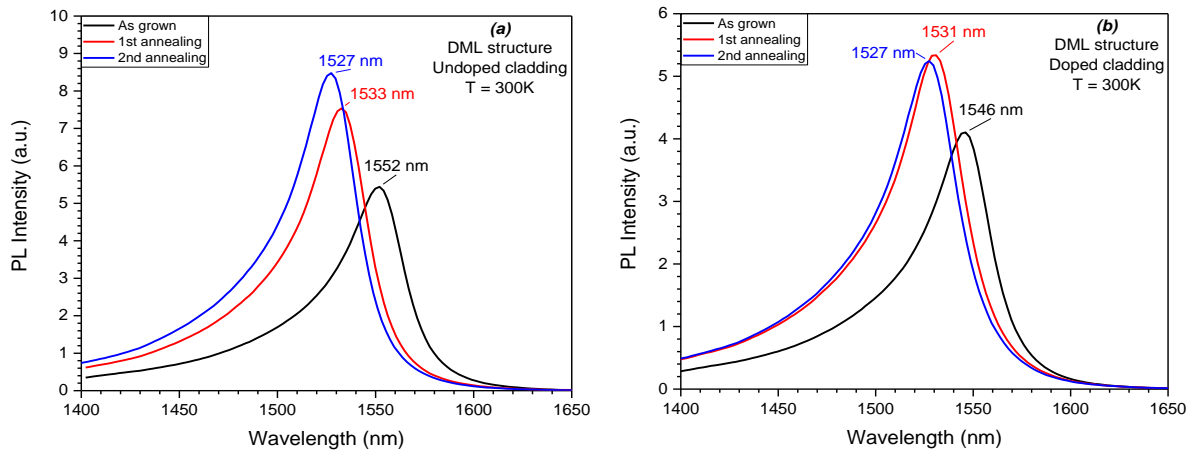


Figure 132. PL results of DML structures with (a) an undoped and (b) a doped cladding layers, before and after each annealing step, at ambient temperature.

Since we did not observe any change at the structural level (HRXRD), the intermixing, schematized in Figure 133, has been clearly put in evidence.

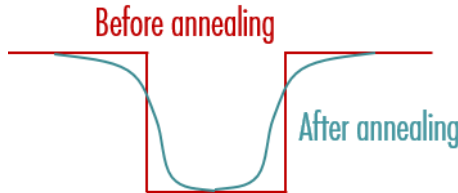


Figure 133. Schematic representation of the QW to barrier before and after the annealing.

The Ga/In inter diffusions at the QW to barrier interfaces lead to graded compositions. Consequently, the energy levels of the states confined to the graded bandgap QW are shifted upwards and we obtain a weaker carrier confinement.

4.4.2. Study of the impact of the SIBH regrowth on the active doping levels

The regrowths' temperatures, have also repercussions on the active doping levels of the structures. To study this phenomenon, we observed the Beryllium's behavior when the wafer undergoes annealing, still under PH₃ pressure. First, we grew a structure made of three InP layers with different doping levels and we performed Secondary Ion Mass Spectrometry (SIMS) and ECV analysis to compare the doping concentration and the active doping levels, before and after annealing (Figure 134).

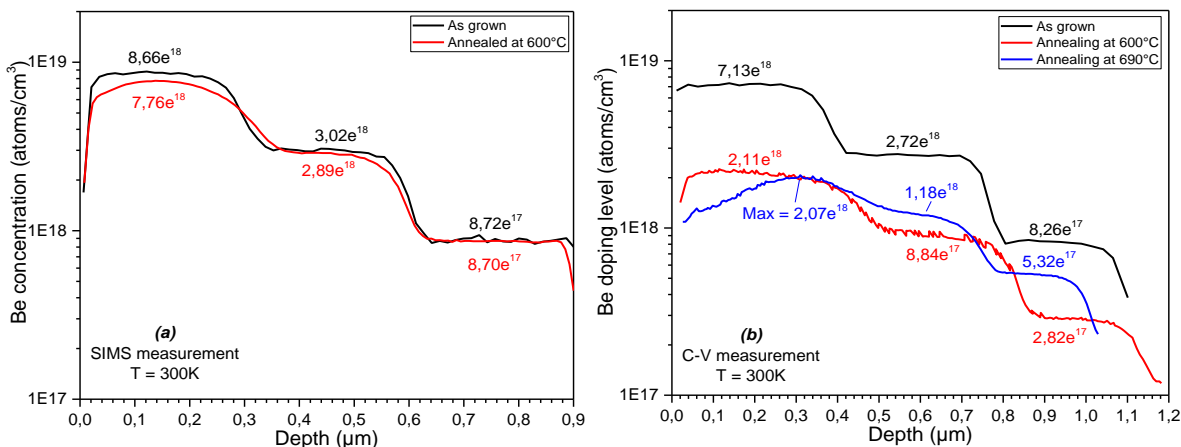


Figure 134. Analysis of a three InP:Be layers structure, as grown and after annealing, by (a) SIMS and (b) ECV measurements.

As-grown, we have a slight difference between the SIMS and ECV results because all the dopants, in the layers. It could be either a slight compensation effect, as Be, just like Al or Si, is prone to oxidation, and/or some hydrogen passivation effect, well known for p-type dopants. The same measurements were performed after an annealing at 600°C and 690°C. There is a clear evidence of a strong dopant deactivation. Be atom is considered as active when it is located in a substitutional site of the crystal, as shown in Figure 135.

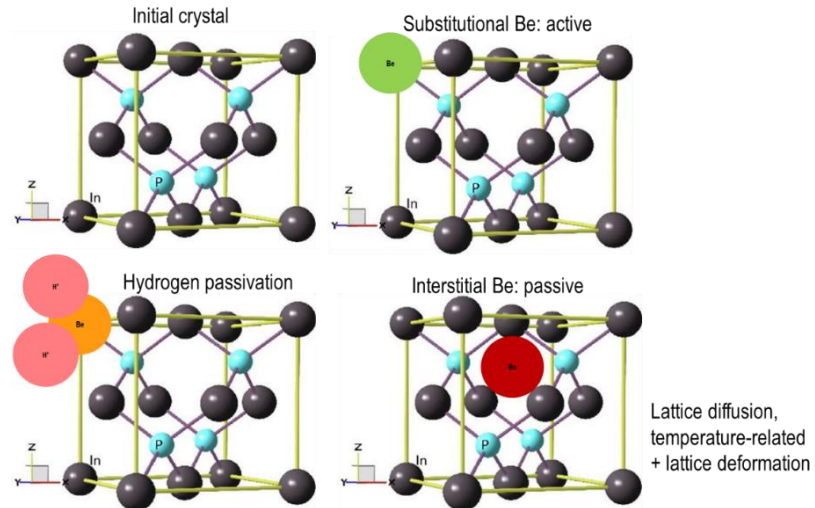


Figure 135. Illustration of the different Be-passivation processes.

If a Be atom suffers a hydrogen passivation, or, if it migrates to an interstitial site, it becomes passive. Consequently, it will be measured by SIMS, but inactive ECV-wise. With the annealing at 690°C, we also see that the high temperatures, comparable to an MOCVD regrowth, have an even more dramatic impact on the initial profile.

A reactivation procedure, performed at 500°C, does not enable to fully recover the initial active doping, as show on ECV profiles, in Figure 136. Disturbed profile resulting from the 690°C annealing is still visible after the reactivation procedure.

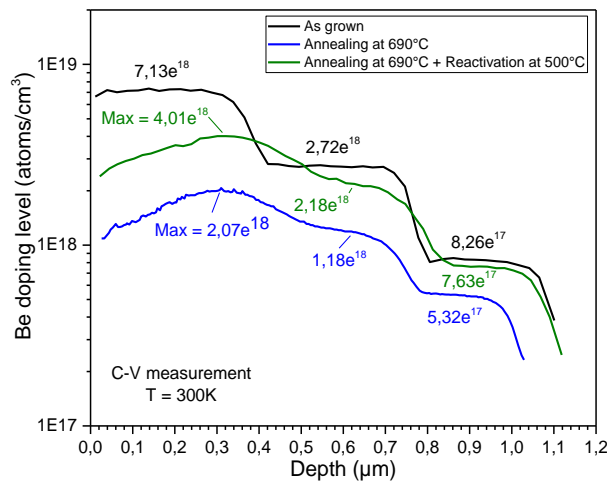


Figure 136. ECV profiles of InP:Be structures, as grown, after 690°C annealing and after reactivation procedure.

The same study was led with more complex structures, carried out on DFB laser and modulators, with many interfaces and we observed less prominent diffusion and deactivation phenomena than we did with the InP:Be reference structure. This study is not enough to conclude on the dopant deactivation/diffusion, since we can only characterize epilayers in the growth direction. Iron (Fe), Zn and even Be diffusion has been observed by SEM laterally, perpendicular to the growth direction.

4.5. Fabrication process finalization

After the SIBH regrowths, every wafer is chemically lift off to remove the dielectric from the top of the ridges. 1-step SIBH wafers are ready for the metal deposition step, while the 2-step SIBH wafers still require additional steps before their metallization.

Once the dielectric is removed, the 2-step SIBH wafers are cleaned with H_2SO_4 and processed by MOCVD for p-type regrowth. The layers of this second regrowth are detailed in Table 53.

Material	Thickness (\AA)	Doping levels (cm^{-3})
<i>GaInAs:Zn</i>	2500	3×10^{19}
<i>GaInAsP:Zn</i>	200	8×10^{18}
<i>InP:Zn</i>	14000	From 1.2×10^{18} to 5×10^{18}
<i>InP:Zn</i>	1000	1.2×10^{18}
<i>InP:Zn (Regrowth's buffer)</i>	200	1.2×10^{18}

Table 53. P-type regrowth for 2-step SIBH.

The p-type dopant used in MOCVD is Zn. This dopant has a much higher tendency to diffuse in the surrounding layers, motivating regrowth by GSMBE [26, 27]. Beryllium can also diffuse but at a lesser degree. Two wafers, one for each optical band (“A2” and “O1” designs), underwent the 2-step SIBH process with p-type regrowth performed in the V100 reactor by GSMBE.

We can now proceed with metallic contact deposition. To do this, the wafers are cleaned with sulfuric acid and two photoresists layers are applied. Then, a contact photolithography and development are performed to obtain a photoresist cap as schematized in Figure 137.

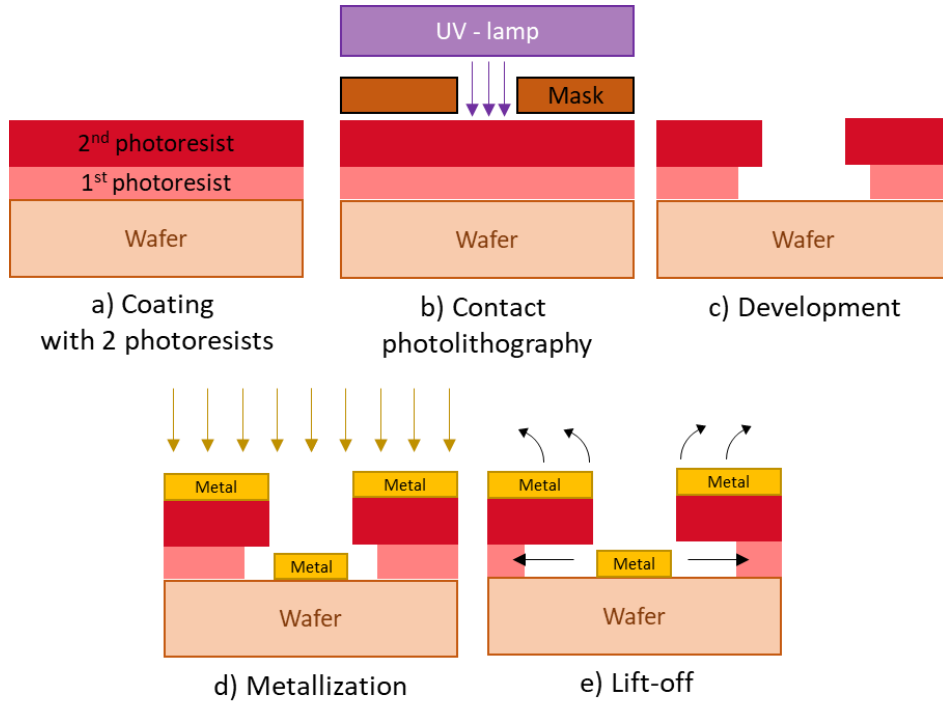


Figure 137. Lift off steps for metallization.

Once this cap is well defined, we can begin the metal deposition using Dual Ion Beam Sputtering (DIBS). This technique allows the deposition of metallic contact layers made of Platinum (Pt) and Gold (Au). After the deposition, the lift off step removes the photoresists and thus, the metal deposited over it.

At this stage, 2-step SIBH and 1-step SIBH are in different situations. The 1-step SIBH ridges are electrically separated by the semi-insulated material. However, the 2-step SIBH ridges are still linked by the P-type regrowth's layers. To obtain the required insulation, these wafers must be prepared for proton implantation.

A thick photoresist is applied on the wafers and a contact lithography is performed to remove the photoresist between the ridges. The implantation is an outsourced step for which we join a list of the energies required for the implantation that can be simulated with a dedicated software. Afterward, the wafers are cleaned to remove the photoresist and thinned them down to $120 \mu\text{m} +/- 10\mu\text{m}$. The last step is a metallic deposition at the side of the wafer that underwent the thinning to obtain a n-contact. This step is achieved by DIBS and consists in the deposition of Titanium (Ti), Pt and Au.

At this point of the fabrication process, the SOAs and the RSOAs are still all located on the plain wafer. We still need to cleave these devices, apply the anti-reflection coatings and select the ones that we will mount on carriers to obtain the final devices. These are the back-end steps, detailed in the next Section.

5. Back-end

FP cavities, SOAs and RSOAs are now fully processed. We must cleave devices' bars, apply facet coatings and operate a first series of measurements for each stripe (Power-Intensity (P(I)) / Voltage-Intensity (V(I)) / Far field / ASE spectra). Then, we select the devices to mount on carriers before their final characterizations, including gain, NF and P_{sat} measurements.

5.1. Preparation for the first measurements

Figure 138 presents a picture of a processed wafer on which we can localize the different devices that we will characterize.

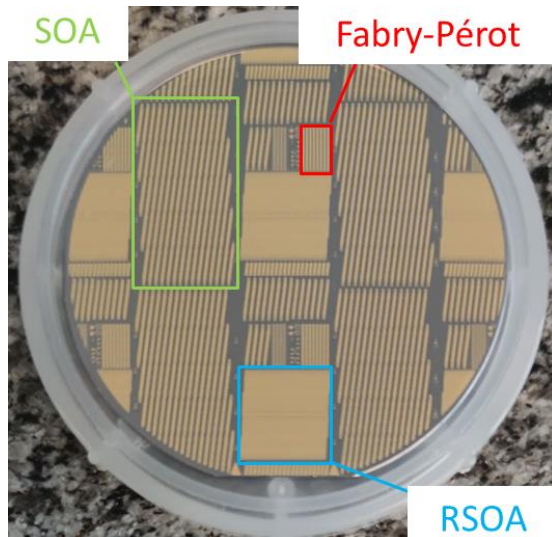


Figure 138. Picture of a processed wafer.

On each processed wafer, we have 2 mm long FP cavities that are perpendicular to the wafer's flat, to maximize reflections at their facets. This device is only cleaved in bars to be characterized by far-field, P(I) and V(I) measurements. The FPs do not require further back-end steps, thus, they enable to quickly verify that the fabrication process was correctly achieved.

The devices of interest for our works are the SOAs and RSOAs. They are positioned in several cells that also have to be cleaved to obtain components bars of the desired length. For the SOAs, their length is set at 4 mm to compensate the small optical confinement values (Γ) of the X2 designs. To avoid the reflections at their facets, the active regions are straight but tilted with an angle of 7° from the perpendicular to the flat. This tilt is the reason why we see large separations between the single devices. Indeed, the mask was optimized to allow cleaving without sacrificing the device's neighbors.

RSOAs can be seen as folded SOA, with a low reflectivity facet on one side and a high reflectivity facet on the other side. As illustrated by the Figure 139, it possesses a straight side which is perpendicular to the wafer's flat. On the other side, the waveguide is tilted to reach the same geometry as SOAs and reduce the reflections at its input/output facet. The length of this device is set at 2 mm, in order to make the signal go through 4 mm of semiconductor, like for the SOAs, with the reflection at one side.

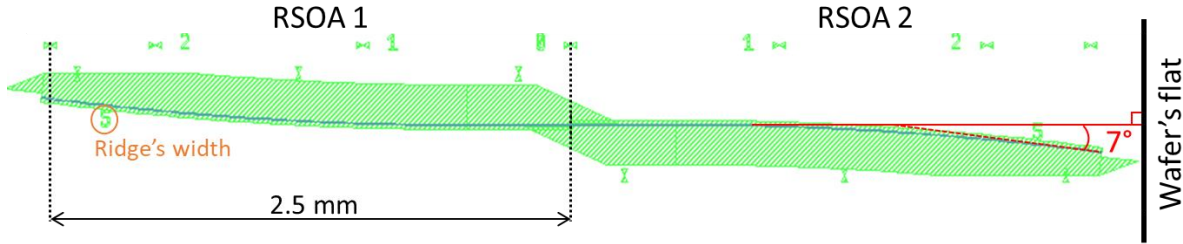


Figure 139. Schematize of the RSOA geometry.

Both SOAs and RSOAs must undergo a facet coating to reduce even more the reflections and avoid lasing effect.

The Anti-Reflection (AR) coatings at both of the SOAs' facets and at the tilted facet of the RSOAs consists of thin SiO₂ and TiO₂ layers depositions. The objective is to reduce the reflectivity under 0.1% at the facets. This coating is realized with a ion assisted electron beam evaporation system, that uses the evaporation principle of dielectric solid sources by electronic bombardment and an Argon (Ar) / Oxygen (O) plasma. The thin films' deposition is controlled by ellipsometry to measure the refractive index and the thickness of the layers. Their thicknesses depend on the refractive index of the semiconductor's waveguide and the operating wavelengths.

The RSOAs can be coated at their straight facets with a high-reflection (HR) coating to enhance its power by reducing the losses at this facet. The HR coatings are longer processes than the AR ones because they consist in the deposition of four successions of SiO₂ and TiO₂ layers. Each bi-layer divides the reflectivity of the facet by two. Consequently, this coating enables to reach until 93.75% of reflection. The typical thickness of the SiO₂ layers is 160 nm and for the TiO₂, it is 140 nm. However, the availability of the coating system led us to keep our RSOA with only an AR coating at the tilted side.

At this step, the optical and electrical characterization of the devices can be undertaken. We have to select the individual devices that can be mounted on carriers. The selection, based on degraded performances, is detailed in the next section.

5.2. Selection process of the individual devices

The first measurements operated after the coating are P(I) and V(I), as shown in Figure 140. The graphs represent the performances of SOA devices manufactured following the 2-step SIBH process and based on the B2 design.

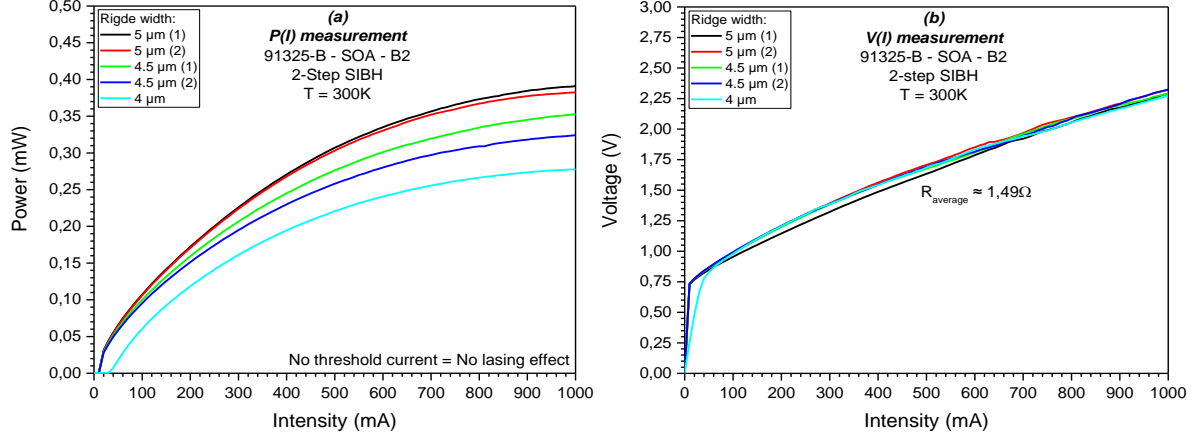


Figure 140. Results of 2-step SIBH SOAs, based on the B2 design, during (a) P(I) and (b) V(I) measurements.

For both measurements, the devices are electrically injected by direct polarization. We use an integrating sphere power meter as detector to obtain the total power of the device. The use of large detectors also limits the results dependency to the beam divergence. In the P(I) graph, we do not observe current thresholds, due to the removal of the reflections at each facet by the AR coatings.

V(I) is performed simultaneously with P(I). The results show a defect on the 4 μm wide ridge causing a shift of the power increase in the P(I) curve and a flexion point in its V(I) curve requiring a higher current. Consequently, this stripe can only provide 5 and 4.5 μm wide devices. To limit the number of devices to mount, we select the more powerful devices, in our case, the devices labelled “5 μm (1)” and “4.5 μm (1)”.

At this step, we can also have a first idea of the wavelengths corresponding to the $e_1\text{-}hh_1$ and $e_2\text{-}hh_2$ transitions, by measuring the ASE spectra. Indeed, the spontaneous emission occurs at the transitions’ wavelengths. To make this measurement, we inject current the same way as for P(I) and V(I). One of the facet is coupled to an optical fiber to maximize the collected optical power. This optical fiber is connected to a MS9710B Anritsu OSA which measures and displays the optical power for a selected range of wavelengths. The results at both facets should be equivalent as ASE is the same at both end of a symmetric waveguide. We measured the ASE spectra of the SOAs on bars, as presented in Figure 141. This measurement is performed at different injection currents to observe the optical bandwidth behavior.

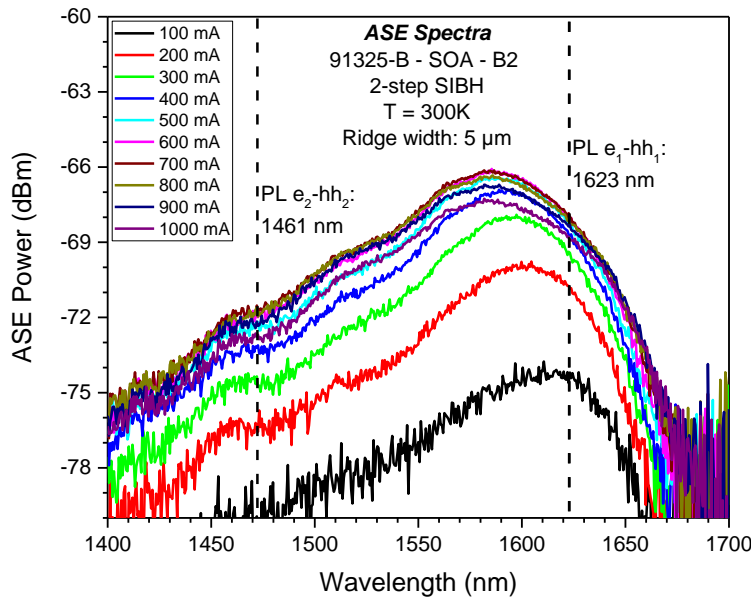


Figure 141. ASE spectra measurements from the 5 μm wide ridge 2-step SIBH SOA based on design B2 during the chip selection.

In comparison with the spectra described in the Chapter I, the ones measured with the device on stripe are degraded. In Figure 141, the impact of the thermal management on the $e_2\text{-}hh_2$ transition leads to low power exhibition, even at high current injection. However, we can already make a comparison with the wavelengths obtained by PL, in the Chapter III, represented with dashed straight lines. For both of the transitions, at high injection current, the PL measurement showed higher values than the ones visible with ASE spectra. This behavior can come from the QW intermixing related to the SIBH regrowth, or the band filling effect at high injection current.

This selection was operated with every processed wafer to obtain until 3 SOAs (5 μm – 4.5 μm – 4 μm) and 4 RSOAs (5 μm – 4.5 μm – 4 μm – 3 μm), in the best case. The selected components are cleaved and brazed on specific sub-mounts to improve the thermal management, as presented in Figure 142.

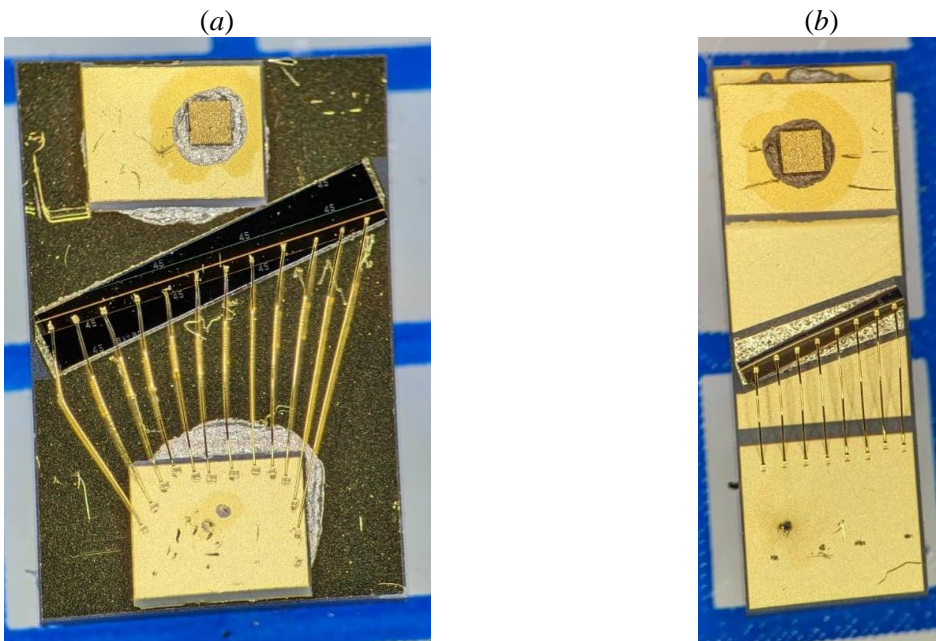


Figure 142. Pictures of mounted (a) SOA and (b) RSOA.

The device brazed on its sub-mount is called a “Chip on Carrier” (CoC). The sub-mounts comprise a thermistance close to the chip to measure the device’s temperature. This resistance serves as sensor for a Peltier module on which the CoC is placed during the characterizations.

Both SOAs and RSOAs CoC are fabricated to facilitate the electrical injection. Indeed, the devices are brazed on an electrode while a wire bonding connects their upper face to another electrode. This architecture facilitates the contacts with the electrical probes that are connected to a Keithley 2400 current source for the devices’ characterizations.

The SOAs and RSOAs being 7° -tilted, their light goes out of the semiconductor with an angle of 23° following Snell-Descartes law. Consequently, to facilitate the characterization and the modules’ mounting in which the devices can be involved, the SOAs and RSOAs are positioned with a 23° angle on the sub-mounts.

The devices can undergo Far Field imaging, ASE spectra, Gain, NF and P_{sat} characterization measurements. These characterizations and their results are discussed, in Chapter IV.

6. Conclusion

In this Chapter, we discussed the two techniques used for the fabrication process (SIBH), as well as the reactors involved in the growth of SOAs and RSOAs (GSMBE and MOCVD) and detailed some aspects of the MBE process transfer from the V100 to the new MBE412. We described the growth conditions and their optimizations to obtain device-grade material. Considering the large amount of epiwafers, devices and variations, sorting of devices must be carried out through ASE, Far Field imaging, P(I) and V(I) measurements.

21 wafers have been grown and 15 have been fully processed. A summary of the different designs and fabrication processes is given in Table 54.

GSMBE Wideband SOA Structures (V100)	1-step SIBH regrowth (CCS reactor)	2-step SIBH with MOCVD p-type regrowth (AIX 200/4 reactor)	2-step SIBH (AIX 200/4 reactor) with MBE P-type regrowth (V100)
<i>A1</i>	V	V	X
<i>A2</i>	V	V	V (A2R)
<i>B1</i>	V	V	X
<i>B2</i>	V	V	X
<i>O1</i>	X	V	V
<i>O2</i>	V	V	X

Table 54. C+L-Band structures grown and their specificities (fabrication process and P-type regrowth's epitaxy technique).

Combining MBE and MOCVD has been key to the fabrication of our devices, giving us the opportunity to compare and discuss 6 different structure designs and 3 fabrication processes and potentially gives some guidelines to follow, depending for device performance optimization.

Bibliography

- [1] H. M. Manasevit and W. I. Simpson, "The use of metal-organics in the preparation of semiconductor materials - I. Epitaxial Gallium-V compounds," *Journal of electrochemical society*, vol. 116, no. 12, pp. 1725-1732, 1969.
- [2] P. Legay, "Epitaxie localisée par jets chimiques sur substrats GaAs et InP (Ph.D thesis)," Université de Nantes, Nantes, FRANCE, 1998.
- [3] A. Y. Cho and J. R. Arthur, "Molecular Beam Epitaxy," *Progress in solid-state chemistry*, vol. 10, no. 3, pp. 157-191, 1975.
- [4] A. Wilk, "Réalisation par epitaxie par jets moléculaires d'une nouvelle structure laser III-V émettant à plus de 3 µm (Ph.D thesis)," Université de Montpellier II, Montpellier, FRANCE, 2000.
- [5] M. A. Herman and H. Sitter, Molecular Beam Epitaxy, Fundamental and current status, Springer-Verlag, 1989.
- [6] D. G. Schlom, W. S. Lee, T. Ma and J. S. Harris Jr., "Reduction of gallium-related oval defects," *Journal of vacuum science and technology B*, vol. 7, no. 2, pp. 296-298, 1989.
- [7] F. F. Briones, "Phosphorus effusion cell for molecular beam epitaxy". United States Patent US005431735A, 11 July 1995.
- [8] J. N. Baillargeon, A. Y. Cho, F. A. Thiel, R. J. Fischer, P. J. Pearah and K. Y. Cheng, "Reproducibility studies of lattice matched GaInAsP on (100)InP grown by molecular beam epitaxy using solid phosphorus," *Applied physics letters*, vol. 65, no. 2, pp. 207-209, 1994.
- [9] J. N. Baillargeon, A. Y. Cho and R. J. Fischer, "Evaluation of the performance and operating characteristics of a solid phosphorus source valved cracking cell for molecular beam epitaxy growth of III-V compounds," *Journal of vacuum science and technology B*, vol. 13, no. 64, pp. 65-68, 1995.
- [10] J. N. Baillargeon, K. Y. Cheng, A. Y. Cho and S. N. G. Chu, "All solid source molecular beam epitaxy growth of $\text{Ga}_x\text{In}_{1-x}\text{As}_y\text{P}_{1-y}/\text{InP}$ lasers using phosphorus and arsenic valved cracking cells," *Journal of vacuum science and technology B*, vol. 14, no. 3, pp. 2244-2247, 1996.
- [11] M. L. Dotor, P. Huertas, P. A. Postigo, D. Golmayo and F. Briones, "(InP)5/(Ga0.47In0.53As)5 superlattice confined 1.5 µm multiquantum well laser grown by all-solid source atomic layer molecular beam epitaxy," *Journal of the european optical society*, vol. 5, no. 10049s, pp. 1-4, 2010.
- [12] M. Pessa, M. Toivonen, M. Jalonens, P. Savolainen and A. Salokatve, "All-solid-source molecular beam epitaxy for growth of III-V compound semiconductors," *Thin solid films*, vol. 306, no. 2, pp. 237-243, 1997.
- [13] F. J. Morris and H. Fukui, "A new GaAs, GaP, and GaAs_xP_{1-x} vacuum deposition technique using arsine and phosphine gas," *Journal of vacuum science and technology*, vol. 11, no. 2, pp. 506-510, 1974.

- [14] L. Goldstein, C. Starck, J.-Y. Emery, F. Gaborit, D. Bonnevie, F. Poingt and M. Lambert, "Optoelectric devices by gas source molecular beam epitaxy," *Journal of crystal growth*, vol. 120, no. 1-4, pp. 157-161, 1992.
- [15] E. Kuphal, "Liquid phase epitaxy," *Applied physics A*, vol. 52, no. 6, pp. 380-409, 1991.
- [16] R. R. LaPierre, T. Okada, B. J. Robinson, D. A. Thompson and G. C. Weatherly, "Lateral composition modulation in InGaAsP strained layers and quantum wells grown on (100) InP by gas source molecular beam epitaxy," *Journal of crystal growth*, vol. 158, no. 1-2, pp. 6-14, 1996.
- [17] B. Decremoux, P. Hirth and J. Ricciardi, in *Proceedings of the 1980 international symposium on GaAs and related compounds*, Vienna, AUSTRIA, 1981.
- [18] G. B. Stringfellow, "Miscibility gaps in quaternary III/V alloys," *Journal of crystal growth*, vol. 58, no. 1, pp. 194-202, 1982.
- [19] K. Onabe, "Calculation of miscibility gap in quaternary InGaPAs with strictly regular solution approximation," *Japanese journal of applied physics*, vol. 21, no. 5, pp. 797-798, 1982.
- [20] V. A. Mishurnyi, A. Y. Gorbatchev, F. De Anda and J. Nieto-Navarro, "Influence of baking on the photoluminescence spectra of In_{1-x}Ga_xAs_yP_{1-y} solid solutions grown on InP substrates," *Revista mexicana de fisica*, vol. 50, no. Re3, pp. 216-220, 2004.
- [21] K. Tappura and J. Laurila, "Unstable regions in the growth of GaInAsP by gas-source molecular beam epitaxy," *Journal of crystal growth*, vol. 131, no. 3, pp. 309-315, 1993.
- [22] F. Turco, J. Massies and J. P. Contour, "Application de la technique des oscillations d'intensité de diffraction électronique en incidence rasante à la croissance des semi-conducteurs III-V par épitaxie par jets moléculaires," *Revue de physique appliquée*, vol. 22, no. 8, pp. 827-836, 1987.
- [23] M. Pessa, K. Tappura and A. Ovtchinnikov, "GaInAsP gas-source MBE technology," *Thin solid films*, vol. 267, no. 1-2, pp. 99-105, 1995.
- [24] K. Tappura and H. Asonen, "Growth of Ga_{0.29}In_{0.71}As_{0.61}P_{0.39} ($\lambda \approx 1.3 \mu\text{m}$) on InP by gas source molecular beam epitaxy," *Journal of crystal growth*, vol. 127, no. 1-4, pp. 217-220, 1993.
- [25] R. R. LaPierre, T. Okada, B. J. Robinson, D. A. Thompson and G. C. Weatherly, "Spinodal-like decomposition of InGaAsP/(100)InP grown by gas source molecular beam epitaxy," *Journal of crystal growth*, vol. 155, no. 1-2, pp. 1-15, 1995.
- [26] E. F. Schubert, C. J. Pinzone and M. Geva, "Phenomenology of Zn diffusion and incorporation in InP grown by organometallic vapor-phase epitaxy (OMVPE)," *Applied physics letters*, vol. 67, no. 5, pp. 700-702, 1995.
- [27] S. Koumetz, K. Ketata, M. Ihaddadene, E. Joubert, M. Ketata and C. Dubois, "Be diffusion in InGaAs/InP heterostructures grown by gas source molecular beam epitaxy," *Journal of crystal growth*, vol. 220, no. 1-2, pp. 46-50, 2000.

Figures

Figure 77. MOCVD growth principle [2].....	68
Figure 78. Schematic of a radial flow MOCVD reactor.....	69
Figure 79. Schematic of a MOCVD growth chamber with a showerhead architecture.	69
Figure 80. Types of crystalline growth.....	71
Figure 81. Schematic of a crucible and its heated insert.	72
Figure 82. Simplified schematic of a valved cracker cell [7].	73
Figure 83. Phosphorus allotropes vapor pressures.	73
Figure 84. Simplified schematic of GaP source of phosphorus [12].	74
Figure 85. Typical solid source "1994" V100 reactor schematic.	76
Figure 86. Cross section of the V100 reactor.	76
Figure 87. MBE412 set of in-situ characterization tools.	77
Figure 88. 3D drawing of the III-V Lab MBE412 reactor.	78
Figure 89. Top view of the III-V Lab MBE412 reactor.	78
Figure 90. Boundaries of the $\text{Ga}_x\text{In}_{(1-x)}\text{As}_y\text{P}_{(1-y)}$ miscibility gap, as calculated by several authors [20].	79
Figure 91. Schematic representation of a typical RHEED configuration.	81
Figure 92. Growth with element III in excess ($\text{V}/\text{III} < 1$).	81
Figure 93. Growth with element V in excess ($\text{V}/\text{III} > 1$).	82
Figure 94. In incorporation rate measurement from RHEED oscillations.	82
Figure 95. Arrhenius curves of two In cells growth rates as function of their temperatures.	83
Figure 96. HR-XRD Omega-2-Theta curve of an InAsP/InP SL structure.	83
Figure 97. HR-XRD rocking curve of GaInAs/InP presenting a lattice-mismatch.	84
Figure 98. InP RHEED oscillations measured at different phosphine baratron pressures	85
Figure 99. InP growth rates as function of phosphine baratron pressure.	85
Figure 100. PL mapping of a $\text{Q}_{1.17}$ quaternary alloy grown in a $1 \times 2"$ platen configuration, illustrating (a) the peak wavelength and (b) the peak intensity uniformities.	86
Figure 101. PL mapping of a $\text{Q}_{1.17}$ quaternary alloy grown in a $3 \times 2"$ platen configuration, illustrating (a) the peak wavelength and (b) the peak intensity uniformities.	86
Figure 102. 300 K PL spectra of $\text{Q}_{1.05}$, $\text{Q}_{1.17}$, $\text{Q}_{1.30}$ and $\text{Q}_{1.45}$ quaternary alloys.	87
Figure 103. GaInAsP quaternary alloy bandgap variation with the lattice parameter. Dashed line along the InP lattice matched shows the unstable region, roughly ranging from an As content of 0.55 to 1.	87
Figure 104. Quaternary alloys' FWHM as function of PL peak wavelength.	88
Figure 105. $\text{AsH}_3/\text{P}_{\text{total}}$ baratron transducer pressure as function of the alloys' As concentration.	88
Figure 106. PL peak wavelengths measured with GaInAs and extended GaInAs detectors as a function of the AsH_3 baratron pressure.....	89
Figure 107. PL comparison between wavelength optimized and fully optimized growth conditions... ..	90
Figure 108. Photocurrent and PL measurements compared with the calculated transition wavelengths.	90
Figure 109. Wave function overlap in high and low injection regimes.....	91
Figure 110. SL slab structure's (a) HRXRD diffractometer and (b) doping measurement.	91
Figure 111. HRXRD diffractometers measured from the C+L-Band structures.	93
Figure 112. PL measurements of the C+L-Band structures made with extended GaInAs detector.	94
Figure 113. PL measurements of the C+L-Band structures with a high power laser.	94
Figure 114. Microscope pictures of O-Band calibration without and with FFT filter.	96
Figure 115. HRXRD diffractometer from the cross-hatched wafer.	97
Figure 116. PL mapping of the O-Band calibration wafer presenting cross-hatch.	97
Figure 117. PL intensity peak mapping of an O-Band calibration wafer grown with strain compensation.	97

Figure 118. HRXRD diffractometers of the complete O-Band structures.	98
Figure 119. PL measurements of the O-Band structures with both PL setups.	99
Figure 120. Real-time stress measurement of a slab-less SOA. Full structure and focus on the active zone.	100
Figure 121. Evolution of the reconstructions observed with RHEED during the deoxydation.	101
Figure 122. HRXRD diffractometer of the O-Band calibration wafer grown in the MBE412.	102
Figure 123. PL results of MBE412 SOA calibration wafer compared with processed wafer.	102
Figure 124. Mapping PL of O-Band structures grown by V100 and MBE412 reactors.	102
Figure 125. PL measurement of O-Band, S+C-Band and C+L-Band structures grown with the MBE412.	103
Figure 126. SEM picture of (a) a 2-step SIBH and (b) a 1-step SIBH structures.	104
Figure 127. Schematizes of (a) the 2-step SIBH and (b) the 1-step SIBH processes.	105
Figure 128. Fabrication steps for the ridges definition in the structures.	107
Figure 129. Reflectometry curve from the ICP etching of (a) a C+L-band wafer following the 1-step SIBH process and (b) a O-band wafer following the 2-step SIBH process.	108
Figure 130. HRXRD diffractogram comparison before and after the p-type regrowth (a) for a C+L-Band and (b) for a O-Band structures.	110
Figure 131. Omega-2-theta scan of a DFB laser structure as-grown, before annealing and after a 680°C annealing.	110
Figure 132. PL results of DML structures with (a) an undoped and (b) a doped cladding layers, before and after each annealing step, at ambient temperature.	111
Figure 133. Schematic representation of the QW to barrier before and after the annealing.	111
Figure 134. Analysis of a three InP:Be layers structure, as grown and after annealing, by (a) SIMS and (b) ECV measurements.	111
Figure 135. Illustration of the different Be-passivation processes.	112
Figure 136. ECV profiles of InP:Be structures, as grown, after 690°C annealing and after reactivation procedure.	112
Figure 137. Lift off steps for metallization.	113
Figure 138. Picture of a processed wafer.	115
Figure 139. Schematize of the RSOA geometry.	116
Figure 140. Results of 2-step SIBH SOAs, based on the B2 design, during (a) P(I) and (b) V(I) measurements.	117
Figure 141. ASE spectra measurements from the 5 μm wide ridge 2-step SIBH SOA based on design B2 during the chip selection.	118
Figure 142. Pictures of mounted (a) SOA and (b) RSOA.	118

Tables

Table 38. Comparison of gas usage and growth temperatures between GSMBE and MOCVD for the growth of InP based alloys	75
Table 39. C+L-Band SOA structures based on 140 Å thick MQW, labelled "A1" for 800 Å thick SCH and "A2" for 600 Å thick SCH layers.	92
Table 40. C+L-Band SOA structures based on 110 Å thick MQW, labelled "B1" for 800 Å thick SCH and "B2" for 630 Å thick SCH layers.	92
Table 41. HRXRD results for the C+L-Band structures.	92
Table 42. PL results from the C+L-Band structures.....	95
Table 43. O-Band SOA structures based on 110 Å thick MQW, labelled "O1" for 750 Å thick SCH and "O2" for 550 Å thick SCH layers.	96
Table 44. Results extracted from the HRXRD measurements of the O-Band structures.....	98
Table 45. PL results of the O-Band structures compared with the calculated target.....	99
Table 46. Material characterization results of the O-Band structures.	99
Table 47. Calibration structure monitored during its growth with EZ-Curve.	100
Table 48. Biaxial moduli of the binary compounds involved in GaInAsP quaternary alloy.....	101
Table 49. Standard deviations measured with PL mapping with V100 and MBE412 grown structures.	103
Table 50. Regrown layers to obtain wafers for 1-step SIBH fabrication process.	106
Table 51. Lattice mismatch between the new peak and the substrate for every wafer.....	106
Table 52. 2-step SIBH regrown layers.	109
Table 53. P-type regrowth for 2-step SIBH.....	113
Table 54. C+L-Band structures grown and their specificities (fabrication process and P-type regrowth's epitaxy technique).	120

Chapter 4 – Devices’ characterizations

This chapter is dedicated to the description of optical and electrical characterization of the materials and device modeled and fabricated during the three years of this project. In a first section, we compare the performances of the different designs with devices manufactured following the 2-step SIBH process. To do this, we study their far field mode profiles to ensure a great coupling efficiency. Then, we measure the ASE and gain spectra to determine the optical bandwidths of the devices. We also discuss their NF and the saturation output power. Then, we study the same performances from the devices manufactured with the newly developed 1-step SIBH process. During this work, seven 2-step SOAs, four 1-step SOAs, three 2-step RSOAs and two 1-step RSOAs were studied for a total of sixteen devices. This study covers the C+L-Band amplifiers and the O-Band devices. These latter are fully characterized and we demonstrate the first wideband SOA operating in this wavelength range based on a GaInAsP MQW structure. These analyzes also enable us to compare the performances obtained with the different fabrication processes and conclude on which fabrication process is more adapted to the SOAs and RSOAs’ manufacturing.

1. 2-step SIBH devices’ performances

In this section, we focus on the devices fabricated with the 2-step SIBH process which is the reference in terms of SOA fabrication in the laboratory.

1.1. Far field imaging

1.1.1. Measurement bench

A precise method to obtain an image of the optical mode outside the SOA consists in performing far field imaging of the output beam. The set up consists of an array of photodiodes which measures the light power passing through a thin slot placed between the detector and the SOA facet (Figure 143).

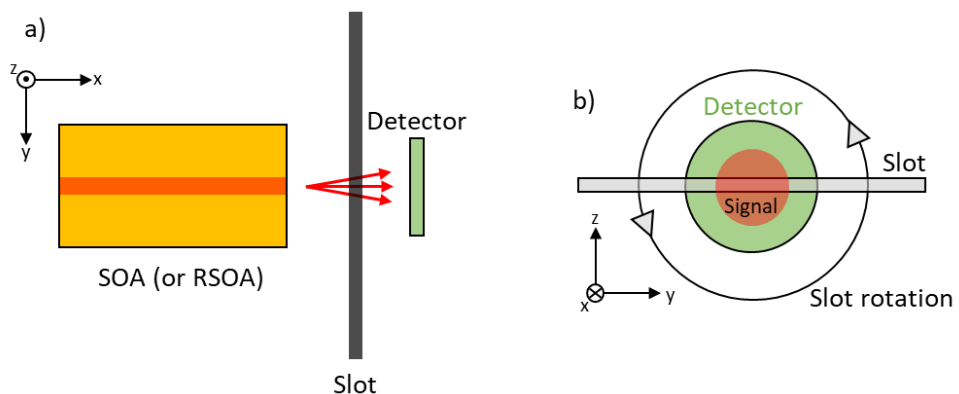


Figure 143. Schematic representation of the far field measurement setup (a) from above and (b) from the front of the detector and slot.

To generate the beam, the SOA is directly electrically polarized via the PiN diode electrodes. There is no optical signal injected at the input facet, in order to only detect the ASE signal’s profile which indicates the mode behavior of the device.

At the outside facet of the SOA, the optical beam begins to diverge from the waveguide mode geometry. The rotation of the slot enables the acquisition of the 2D profile of the optical mode. The divergence angles are obtained by comparing two profiles measured at different distances from the detector (Figure 144) and by using Equation 76.

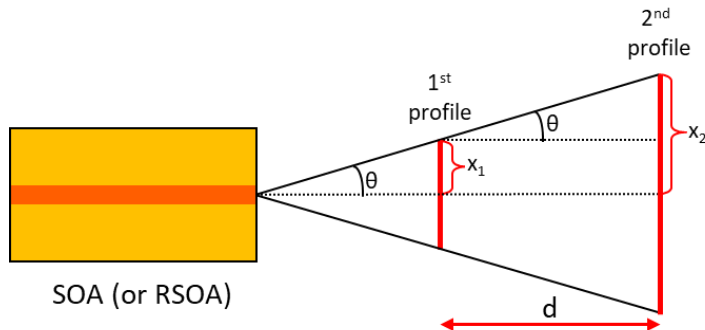


Figure 144. Schematic of the divergence angle calculation.

$$\text{Equation 76. } 2\theta = 2 * \arctan \left(\frac{x_2 - x_1}{d} \right)$$

Where:

- 2θ is the divergence angle.
- d is the distance between the measurements.
- x_i represents the half of the considered value for mode profile's size.

The far field distribution of a circular mode is Gaussian. As shown in Figure 145, we calculate the divergence angle for half of the output signal power from the FWHM of the intensity as function of the profile size.

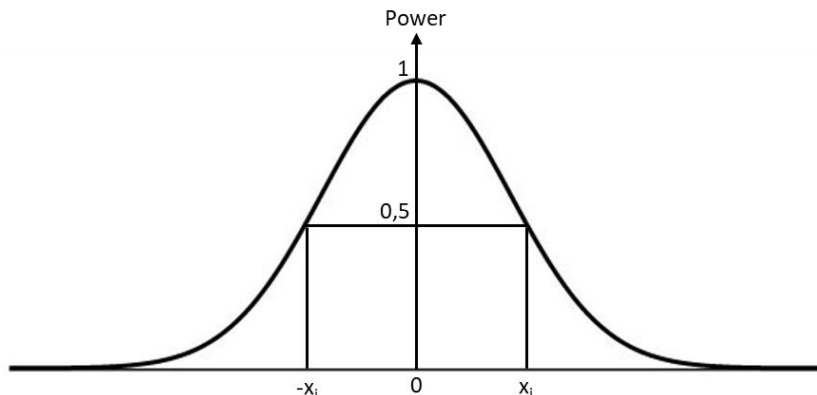


Figure 145. Gaussian fit showing the determination of x_i for the divergence angle calculation.

1.1.2. Results

Figure 146 shows the experimental curves of the far field measurement at 0 and 90° (horizontal and vertical slot, respectively), for every C+L-Band design. Measurements are done at 1 A, for the 4.5 μm wide and 4 mm long SOAs and at 500 mA for the 2 mm long RSOA, to compare their results at the same current density.

For the RSOAs, their lower exhibited powers result in noisier curves, which is detrimental to calculate the FWHM value correctly. The RSOAs based on the B2 design could not be measured due to degraded facets.

These curves and their FWHM values cannot be compared directly because they depend on the relative positions of the detector and the device. However, the larger FWHM values obtained for the vertical axis show an elliptical form of the mode profile. Finally, the SOAs designed with low optical confinement (X2 designs) present a shoulder. This enlargement is even more visible with the slot rotation enabling to observe the 2D mode profiles, given in Figure 147.

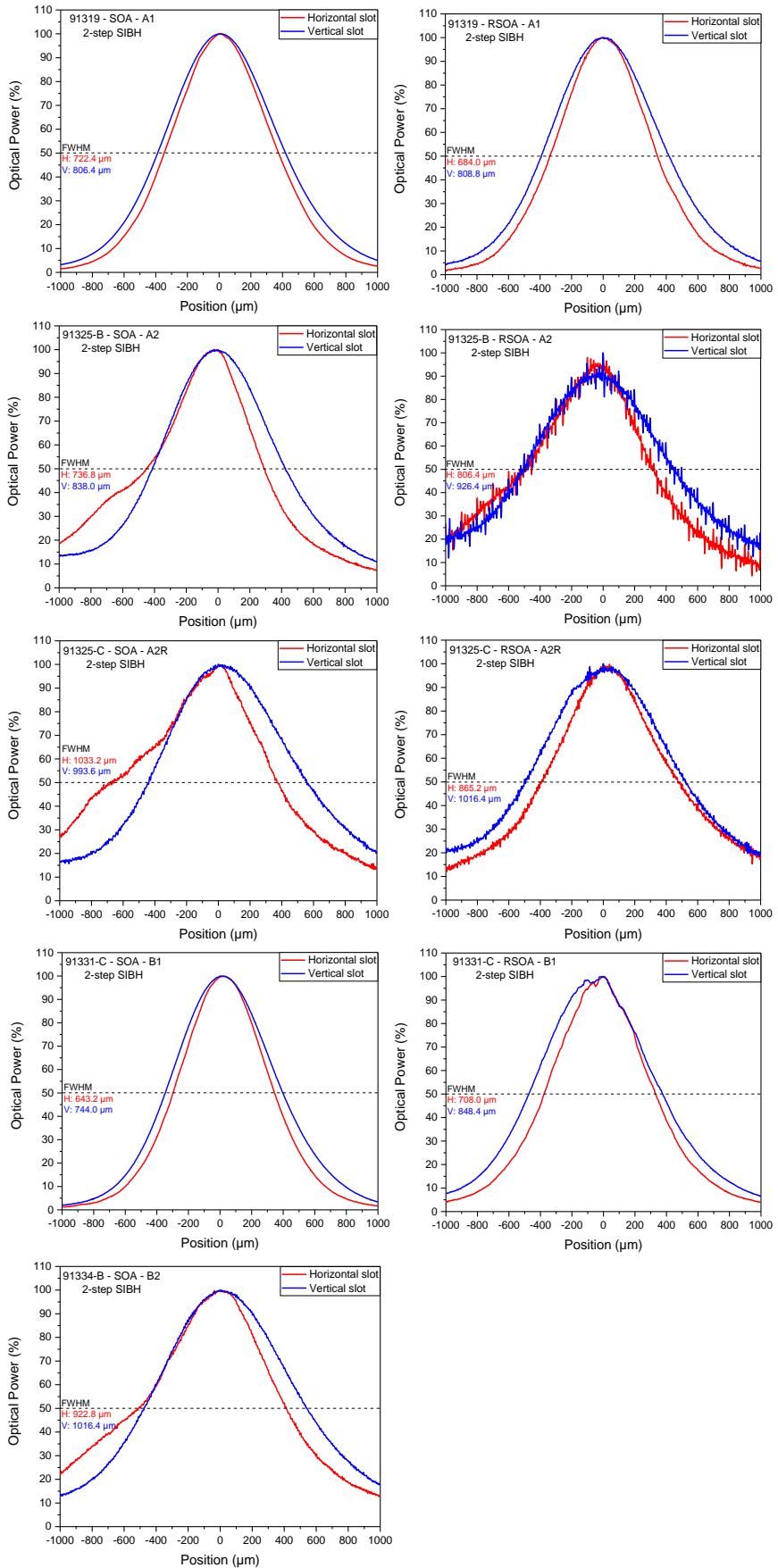


Figure 146. Mode profile horizontal and vertical sections, from SOAs on the left and RSOAs on the right.

This behavior can result from the presence of a second mode emitted by our device, which would not be consistent with our simulations. However, these simulations were operated at $1.55\text{ }\mu\text{m}$ for the C+L-Band and $1.31\text{ }\mu\text{m}$ for the O-Band. Consequently, this second mode can be generated by the shortest wavelengths. A last possibility is that the far field profile is a combination between a spontaneous emission, with a random direction, large along the horizontal axis, and the ASE, represented by the highest intensity peak and that does not provide enough optical power to reduce the impact of the spontaneous emission during the measurement. For the SOAs, the measurements are performed at both of the facets to verify if one of them was not damaged during the back-end steps.

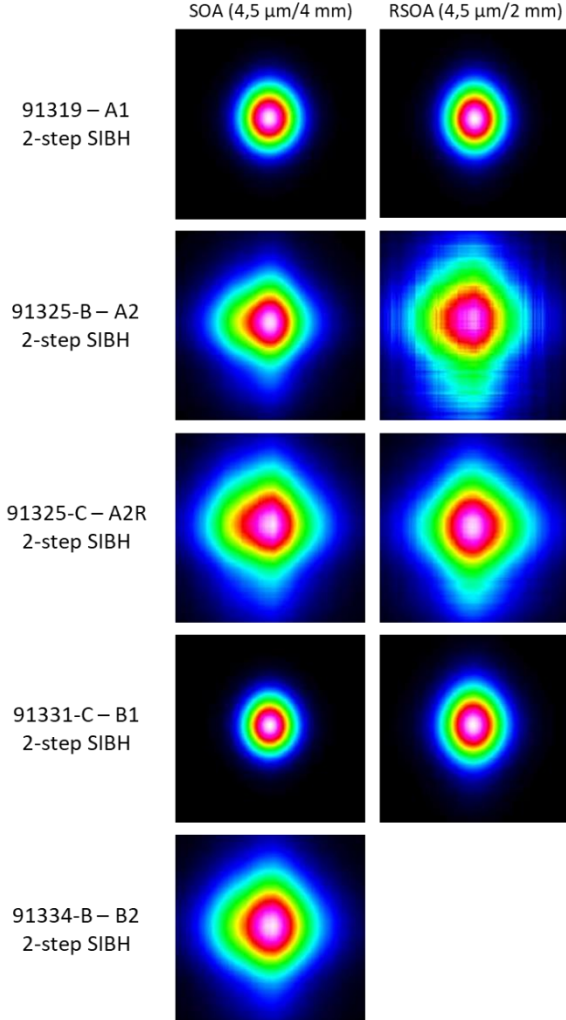


Figure 147. 2D mode profiles measured from the 2-step SIBH SOAs, at 1 A, on the left and RSOAs, at 500 mA, on the right.

In Figure 147, white and red indicate high optical power and blue low optical power. The elliptic behavior of the mode profile is clear for the devices designed to reach high optical confinements (X1 designs). Even if the others show an enlargement on the horizontal axis, they still have profiles that allows great coupling with optical fibers. As seen with the curves, in Figure 146, the RSOAs display wider and noisier profiles than SOAs possessing the same design, except for the A1 and B1 designs which have high enough optical confinements to avoid profile deformation.

It is interesting to combine the far field measurements with the P(I) measurements to observe the profiles' evolutions with the injected current. Figure 148 and Figure 149 show the far field profiles and the optical output power measured with an integrating sphere detector for the A1 and A2 SOAs, respectively.

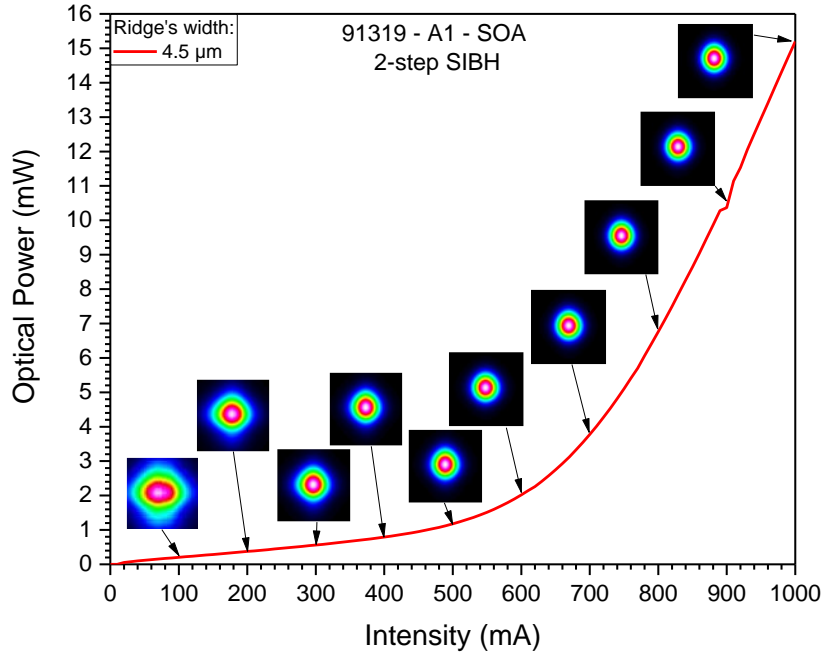


Figure 148. Comparison between $P(I)$ measurement (red line) and far field mode profile for SOA with design A1.

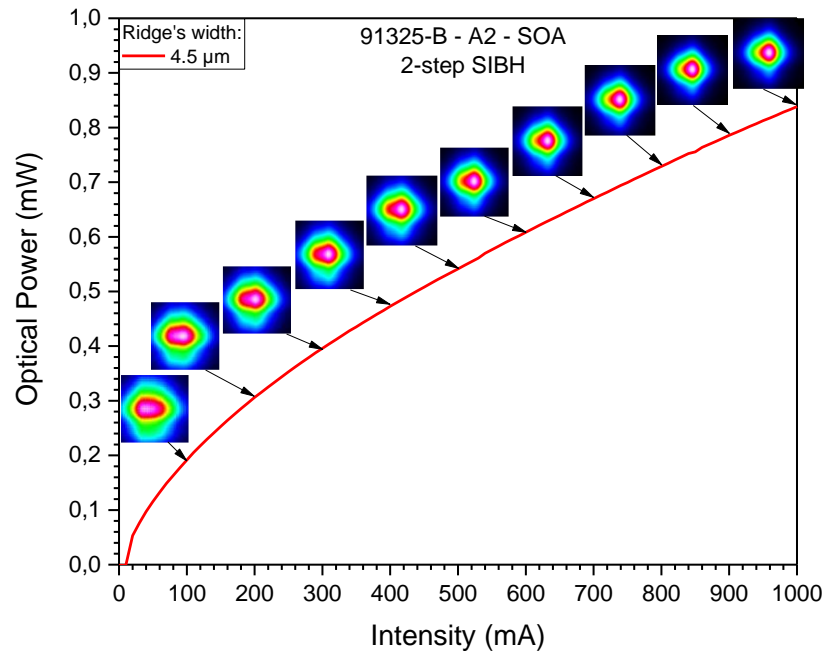


Figure 149. Comparison between $P(I)$ measurement (red line) and far field mode profile for SOA with design A2.

At low injected current, we observe only the ASE mode profiles that are blurred for both devices. By increasing the injected current, the beam is focused, resulting in an elliptical shape for the devices with high enough optical confinement, as shown in Figure 148. For the others, the ASE mode profile is still visible and causes the horizontal enlargement (Figure 149).

We can observe that the mode profile of the SOA based on the A2 design at 1A is similar to the one of the SOA based on the A1 design at 200 mA. Consequently, with higher output power, obtained by increasing the optical confinement or the injected current values (without losses caused by temperature), the low optical confinement devices' profiles tend to be similar to the high optical confinement devices' ones.

For the O-band, the 2D far field profiles are displayed in Figure 150. The 2-step SIBH RSOA based on the O2 design did not exhibit enough power to be further studied.

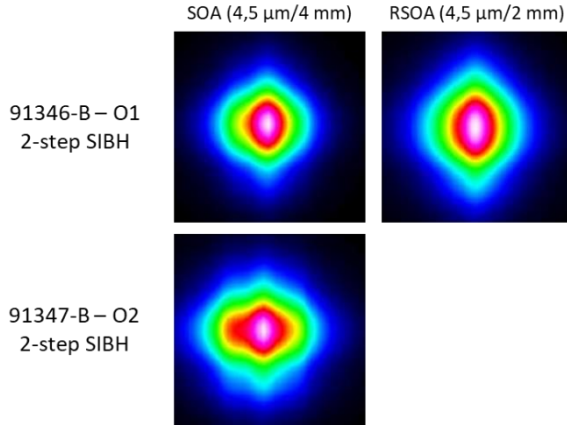


Figure 150. 2D mode profile from 2-step SIBH SOAs and RSOA operating in O-Band.

The same behavior as for the C+L-Band devices is observed with even more enlargement following the horizontal axis, for the O2 design.

Two far field measurements, made at different distances from the detector, allow to measure the beam divergence, as explained in the previous section. The calculated values are listed in Table 55 for each device at 500 mA.

Design	SOA		RSOA	
	Horizontal axis	Vertical axis	Horizontal axis	Vertical axis
A1	10.94°	12.83°	10.32°	12.62°
A2	15.29°	14.51°	9.22°	7.78°
A2R	13.82°	13.97°	11.36°	15.18°
B1	10.53°	12.63°	10.66°	13.18°
B2	10.92°	12.83°	-	-
O1	12.48°	12.18°	10.28°	16.02°
O2	11.04°	14.24°	-	-

Table 55. Beam divergence angles (2θ) at FWHM for 2-step SIBH devices at 500 mA for every device.

These values are great for optical fiber coupling. The A2 RSOA shows low values due to its lack of optical output power which did not allowed a correct measurement of its FWHM values to determine the divergence angles.

The great coupling efficiency between the devices and optical fibers is required for the next device characterization, ASE spectra measurements.

1.2. ASE Spectra

Spontaneous emission occurs at the wavelengths corresponding to the optical transitions, thus, an SOA's bandwidth can be first assessed by measuring the ASE spectra. However, ASE and gain spectra can be different if the device is subject to Longitudinal Spacial Hole Burning (LSHB). This phenomenon results in a variation of the carrier density throughout the waveguide with a maximum in the middle of the device and minimums at its facets. Without LSHB, ASE and gain spectra have similar shapes, but usually shifted currents. Stimulated emission has a higher carrier consumption than spontaneous emission, meaning that higher injected current is required to obtain the same level filling.

During the ASE spectra measurement, the SOA is electrically injected by direct polarization. The device is coupled at one facet with an optical fiber by maximizing the collected optical power. The fiber is then connected to an OSA. In the C+L-Band, the ASE power is measured from 1450 nm to 1650 nm, while, for the O-Band, from 1225 nm to 1400 nm.

1.2.1. C+L-Band

Figure 151 and Figure 152 show the different ASE spectra measured from the C+L-Band SOAs with design A (14 nm thick QW) and design B (11 nm thick QW), respectively.

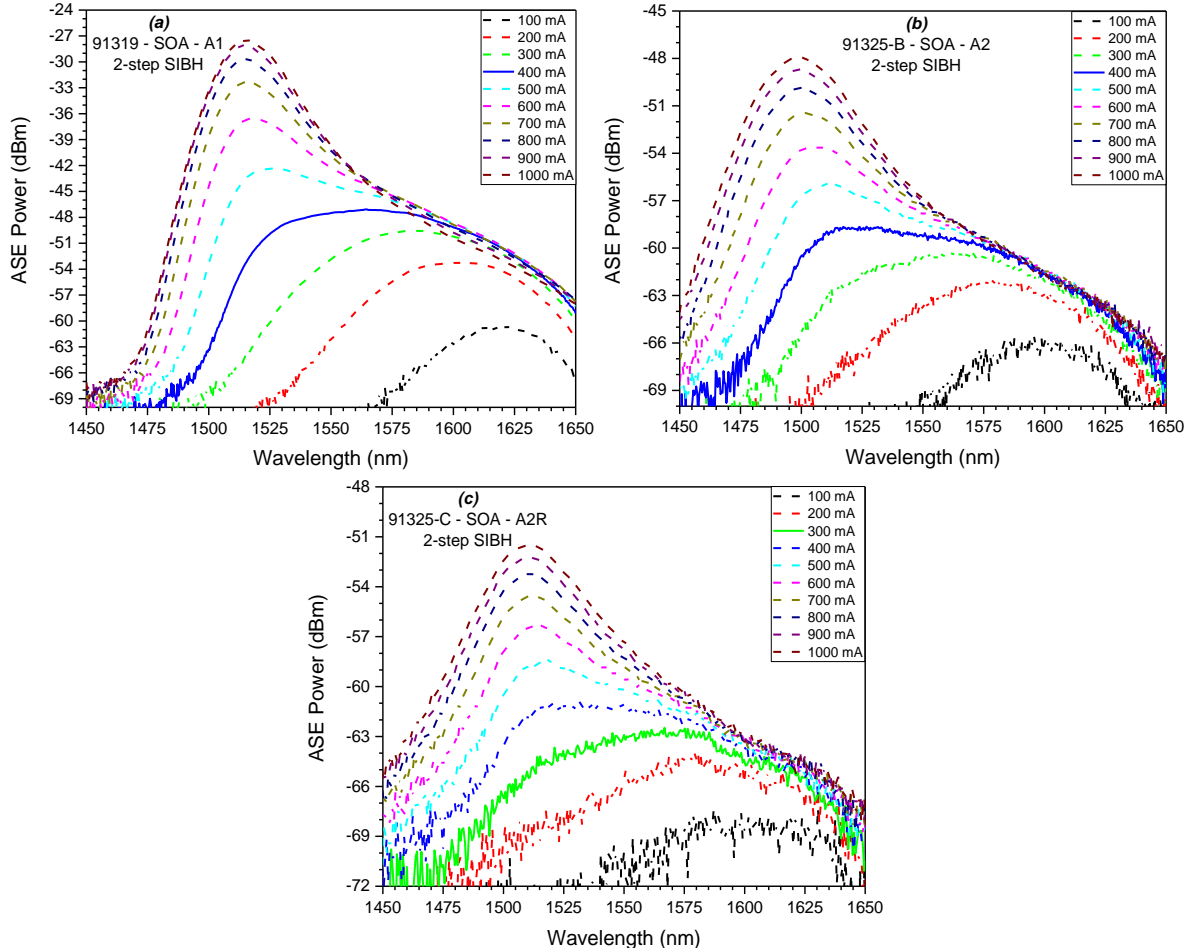


Figure 151. ASE Spectra measured from 2-step SIBH SOAs based on (a) the A1 design, (b) the A2 design, (c) the A2R design.

The measured ASE power depends on the coupling efficiency which is not taken into account during the measurements. The ASE spectra enable to obtain an approximate value for the optical bandwidth, which is determined with the same condition as the gain optical bandwidth. The A1 design SOA, reaches a maximal ASE optical bandwidth of 85 nm (1524 – 1609 nm) at 400 mA (corresponding to a current

density of 1.11 kA/cm^2). For the A2 design, this optical bandwidth reaches 102 nm (1496 – 1598 nm), for the same injected current density. However, for an injected current of 300 mA (0.83 kA/cm^2), this design shows a 101 nm wide bandwidth, better covering the C+L-Band (1512 – 1613 nm). At 300 mA (0.83 kA/cm^2), the similar A2R design exhibits its maximal ASE bandwidth of 109 nm (1508 – 1617 nm).

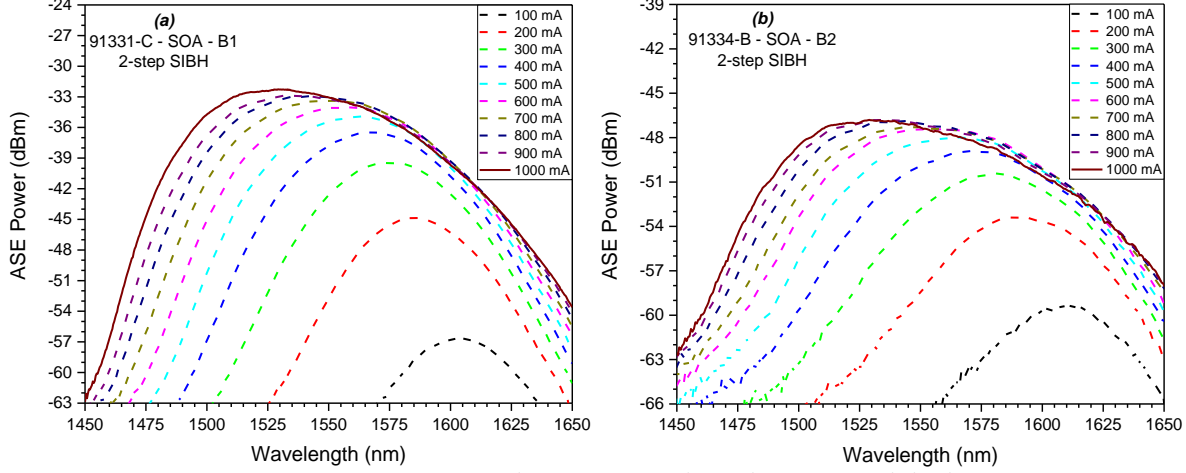


Figure 152. ASE Spectra measured from SOAs with (a) design B1 and (b) design B2.

Contrary to the 14 nm thick QW designs, the $e_2\text{-}hh_2$ transition is not visible with the 11 nm thick QW based designs. This is due to a less efficient confinement of the second electronic level in the MQW. Consequently, the injected current required to reach the widest ASE optical bandwidth is higher, 1 A (2.78 kA/cm^2) for both designs. The SOA fabricated following the B1 design exhibits a 77 nm wide bandwidth (1497 – 1574 nm), while the B2 design shows a 99 nm bandwidth (1493 – 1592 nm).

Figure 153 displays these curves for the RSOA devices fabricated with design A. The ASE spectra from the RSOA with the B1 design is presented in Figure 154.

The smaller size of the RSOAs enables to observe the ASE behavior at higher injected current densities. The RSOA with the A1 design shows a laser effect around 1513 nm, with an injected current of 500 mA (2.78 kA/cm^2), which was not the case or the SOA. Moreover, with too high injected currents, the RSOAs' performances are degraded because of the thermal management which is not as great as for the SOAs.

For the A1 design, the flattest ASE curve is reached at 200 mA (1.11 kA/cm^2), for an ASE optical bandwidth of 94 nm (1524 – 1617 nm). For the A2 and A2R RSOAs, the injected current must be 250 mA (1.39 kA/cm^2) and 300 mA (1.67 kA/cm^2) to reach bandwidths of 126 nm (1500 – 1626 nm) and 123 nm (1504 – 1627 nm), respectively.

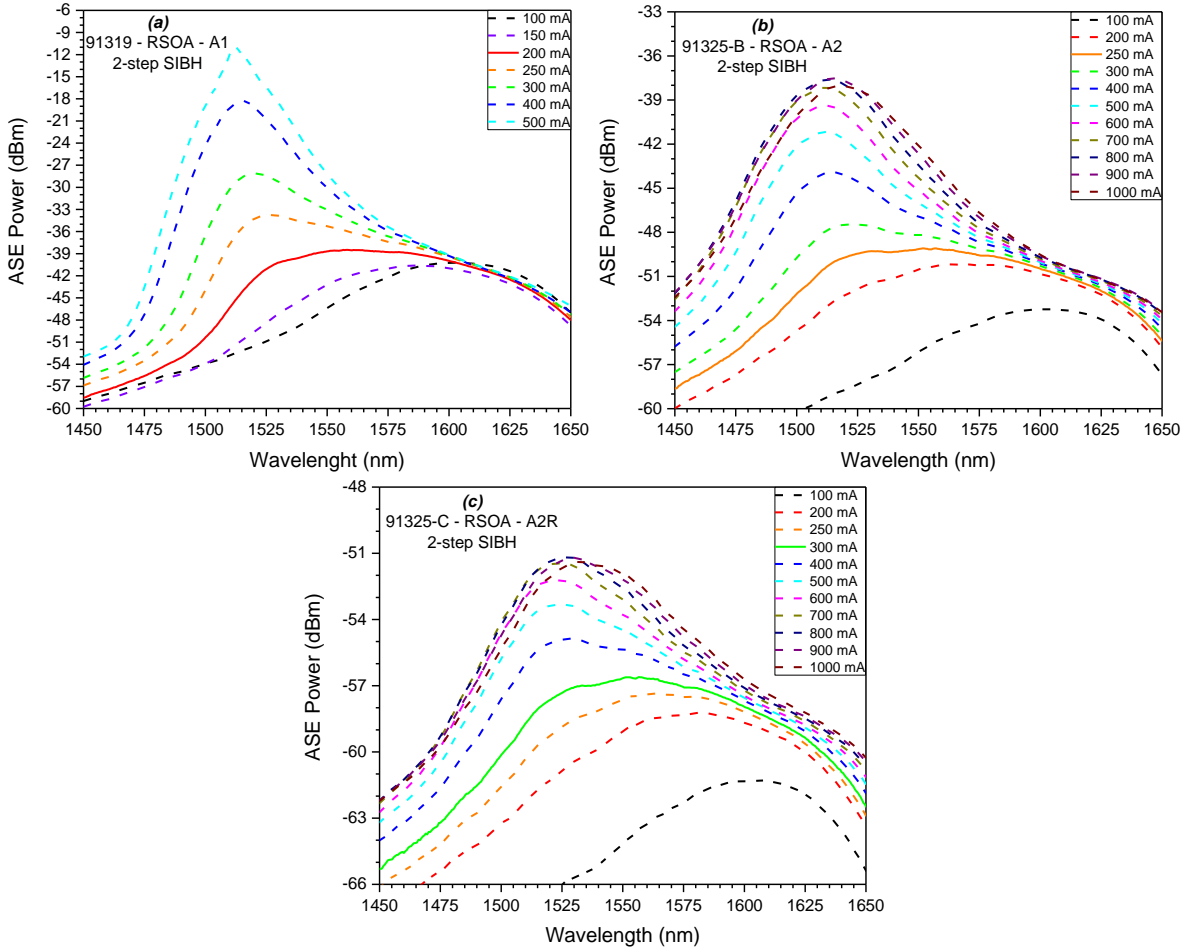


Figure 153. ASE spectra measured from RSOAs with (a) design A1, (b) design A2 and (c) design A2R.

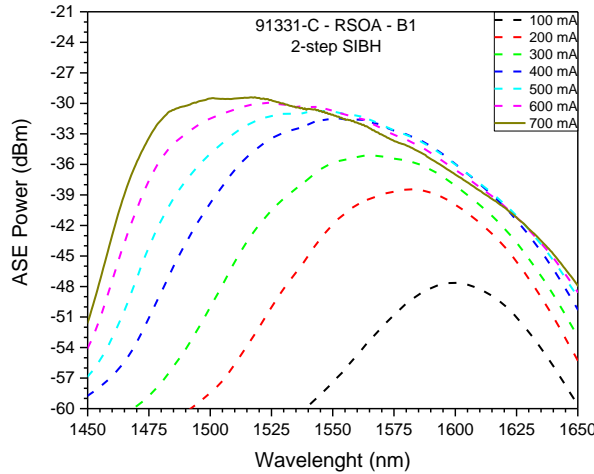


Figure 154. ASE spectra measured from RSOA with design B1.

The B1 design shows a higher contribution of the higher energy transitions with the RSOA device, thanks to the higher injected current densities. It exhibits its widest bandwidth of 88 nm (1477 – 1565 nm) at 700 mA (3.89 kA/cm²).

We observed all the C+L-Band ASE spectra measured for the devices based on 4,5 μ m wide ridges manufactured following the 2-step SIBH process. In the next section, we focus on the 2-step SIBH fabricated O-Band devices.

1.2.2. O-Band

The O-Band SOAs' ASE spectra are presented in Figure 155.

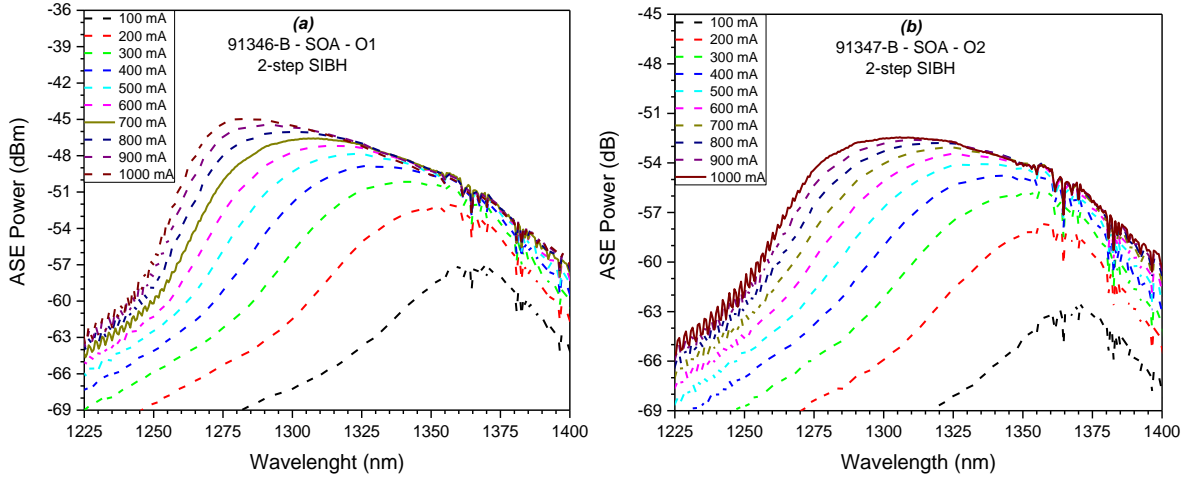


Figure 155. ASE Spectra measured from O-Band SOAs, based on (a) O1 design and (b) O2 design.

Both designs for the O-Band show an ASE behavior similar to the B designs of the C+L-Band, which possess the same QW thickness. The better confinement given by the larger SCH layers of the O1 design enables a higher participation of the e_2 - hh_2 transition in the ASE spectra. Its maximal ASE bandwidth is 79 nm (1277 – 1356 nm), reached at 700 mA (1.94 kA/cm^2). For the O2 design, the widest bandwidth requires an injected current of 1 A (2.78 kA/cm^2) and covers 91 nm (1270 – 1361 nm). This value could be more important with higher current densities and without the atmosphere's absorption impacting the highest wavelengths of the O-Band.

The more important participation of the high energy transitions, for the O1 design, is even more visible with the RSOA that enables measurements at higher current densities, as shown in Figure 156.

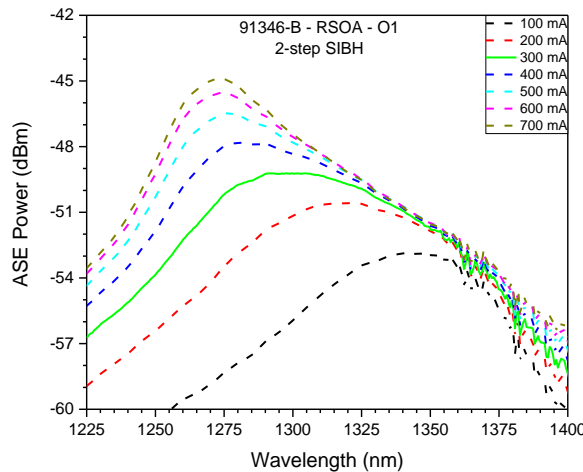


Figure 156. ASE spectra measured from the O1 design RSOA.

The higher energy transition appears at lower injected current density than for the C+L-Band designs possessing 11 nm thick QW. It shows a better electronic confinement of the e_2 level and reduces the device's consumption. This RSOA offers a 95 nm wide ASE bandwidth (1260 – 1355 nm), for an injected current of 300 mA (1.67 kA/cm^2).

1.2.3. Results

The largest optical bandwidths extracted from the ASE spectra are listed in Table 56 and Table 57, for SOAs and RSOAs, respectively.

Design	SOA						
	A1	A2	A2R	B1	B2	O1	O2
Flat ASE current (mA)	400	300	300	1000	1000	700	1000
Flat ASE current density (kA/cm²)	1.11	0.83	0.83	2.78	2.78	1.94	2.78
Simulated Bandwidth (nm)		146		201		131	
PL Bandwidth (nm)	124		129		150	162	106
ASE Optical Bandwidth (nm)	85	101	109	77	99	79	91
Lower limit (nm)	1524	1512	1508	1497	1493	1277	1270
Upper limit (nm)	1609	1613	1617	1574	1592	1356	1361

Table 56. ASE performances measured from 2-step SIBH SOAs.

Design	RSOA					
	A1	A2	A2R	B1	O1	
Flat ASE current (mA)	200	250	300	700	300	
Flat ASE current density (kA/cm²)	1.11	1.39	1.67	3.89	1.67	
Simulated Bandwidth (nm)		146		201	131	
PL Bandwidth	124		129		150	106
ASE Optical Bandwidth (nm)	94	126	123	88	95	
Lower limit (nm)	1523	1500	1504	1477	1260	
Upper limit (nm)	1617	1626	1627	1565	1355	

Table 57. ASE performances measured from 2-step SIBH RSOAs.

In general, we observe that RSOAs exhibit lower ASE powers and wider optical bandwidths in the C+L-Band. Moreover, the flat ASE current density is higher for the designs based on 11 nm thick QW because of the lower electronic confinement of the e₂ level.

The bandwidths are narrower and cover smaller wavelengths than expected from the simulations. The measured bandwidths have difficulties to reach 100 nm, while the simulations gave us much larger values with the gain material and the simulated structure in Chapter II. This difference comes from the absorption and recombination phenomena that are not taken into account during the simulations but affect the spectra widths. The measured bandwidths are also lower than the bandwidths obtained from the photoluminescence measurements, in Chapter III. Indeed, the optical power exhibited by the e₁-hh₁ transition is limited at high current density. The bandwidth is thus narrower because of the e₂-hh₂ transition's prominence (Ax designs) or shifted to smaller wavelengths (Bx and Ox designs).

To obtain the exact device bandwidths, we must study their gain spectra as explained in Chapter I.

1.3. Gain Spectra - G

ASE spectra is related to the devices' gain, but the exact optical bandwidth of the devices is given by the gain spectra. In this section, we describe the measurement bench used to measure the gain, the NF and the saturation output power by taking into account the coupling losses. Consequently, the presented values correspond to the chip performances.

1.3.1. Measurement bench

Gain measurement is more complex than ASE spectra measurement because it requires an input signal at a given wavelength. The setup is presented in Figure 157 and Figure 158, for SOAs and RSOAs' configurations, respectively.

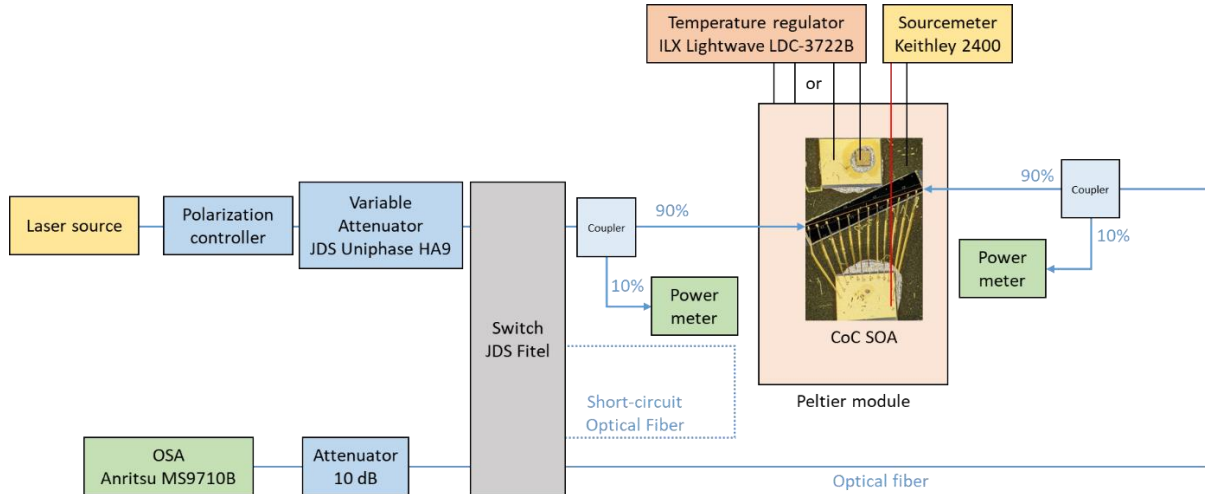


Figure 157. Schematic representation of the optical gain measurement setup, with a SOA CoC.

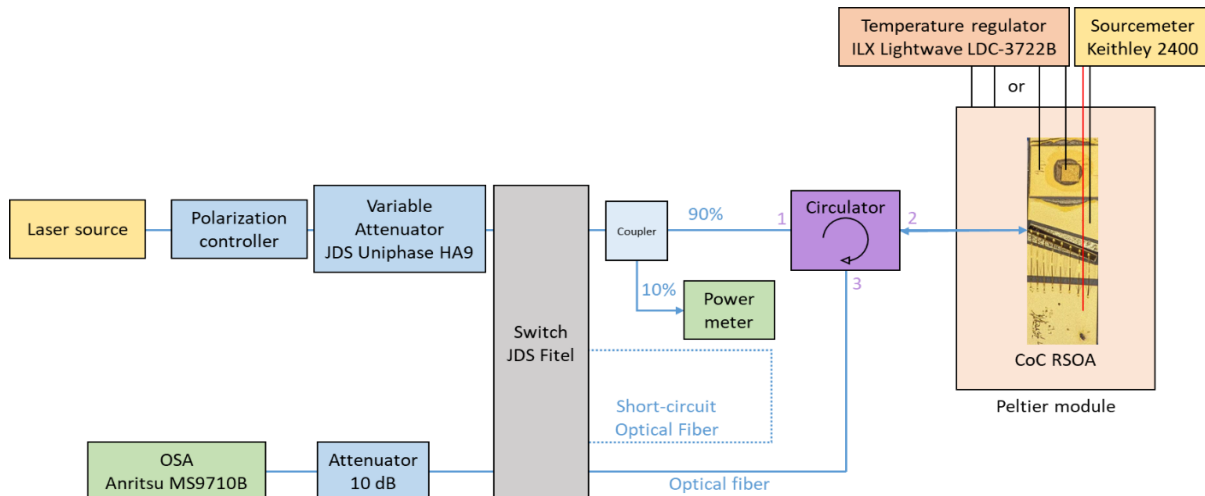


Figure 158. Schematic representation of the optical gain measurement setup, with a RSOA CoC.

These representations comprise three blocks, the input block, the (R)SOA main block and the output block that are connected with an optical switch from JDS Fitel. This switch can link the (R)SOA block to the others, to allow the measurement of both devices.

The input block comprises a tunable laser source that provides the input signal. The source is different for the C+L-Band, with a tuning range between 1520 and 1610 nm, and the O-Band, with a tuning range between 1260 and 1360 nm. Their maximum output power is 0 dBm, which limits measurements of our wideband devices, in terms of saturation output power. The input signal's polarization is then controlled

to only inject TE polarization in the device and a HA9 variable attenuator from JDS Uniphase controls the input signal power level.

The (R)SOA, brazed on a carrier, is placed on a Peltier module managed by a ILX LDC-3722B controller with temperature information from the thermal resistance placed on the carrier or from the Peltier module itself. In the SOA configuration, two power meters are linked to the fiber to enable the coupling between the device and the optical fiber with the ASE power. The output optical fiber returns to the switch to reach the output block. For the RSOA, only one power meter is required as a single facet has the roles of input and output facet. Because of this, a circulator is required to short-circuit one coupler as shown in Figure 158.

The output block comprises a 10 dB attenuator and an Anritsu MS9710B OSA. The switch also allows to bypass the main block for direct measurement of injected source in SOA optical power and wavelength.

The gain measurement consists in measuring the ratio of output power over input power. The input power can be easily measured but the output power cannot because of the ASE power's impact. The ASE power must be subtracted from the read value of optical output power. From there, gain is calculated following Equation 77.

$$\text{Equation 77. } G = 10 * \log \left(\frac{P_{out}}{P_{in}} \right)$$

To be in the linear regime of our devices, the input signal's power is fixed at -25 dB for all gain and NF measurements. The coupling losses for all our devices are comprised between 1.5 and 2 dB. These values, depending on the wavelength, are taken into account to present the chips' performances.

1.3.2. C+L-Band

As laser tuning range of the source used for the input signal is limited in terms of wavelengths, thus, the measurements are operated from 1520 to 1610 nm. Figure 159 represents the Gain spectra of the C+L-Band SOA and Figure 160 the curves measured from RSOAs.

We begin with the SOAs and the A1 design which exhibits its flattest gain at an injected current of 500 mA (injected current density: 1.39 kA/cm²), with a maximum value of 25 dB at 1540 nm and a measured bandwidth of 90 nm (1520 – 1610 nm). We expect the SOA bandwidth to be a bit larger than 90 nm because its measured bandwidth is only limited by the laser tuning range. As for the ASE measurements, we observe the wideband behavior of the device, with the contribution of the higher energy transitions increasing with the current.

For the A2 design based SOA, the flattest gain is also reached at 500 mA (1.39 kA/cm²) with a lower maximum gain, caused by the lower optical confinement, of 10 dB. The bandwidth should again be larger than the 90 nm measured wavelength range. The A2R SOA presents higher injected current to reach a flat gain behavior. This value can be from 600 to 700 mA (1.67 to 1.94 kA/cm²) as the measured wavelengths do not allow to determine which current density exhibits the largest bandwidth. At these currents, the maximal gain values are 11 dB and 12 dB, respectively. Both A2 and A2R designs were supposed to show the same performances, thus, this difference can originate from fabrication process and illustrates the gain sensitivity to the fabrication conditions.

The thinner QW designs, B1 and B2, results are presented in Figure 159 (d) and (e). The B1 design exhibits its flattest gain at 700 mA (1.94 kA/cm²) in the measured wavelength range. Its maximal gain is 35 dB at 1560 nm and its bandwidth is 71 nm (1522 – 1593 nm). However, at higher injected current than 800 mA (2.22 kA/cm²), the low limit of the wavelength range belongs to the device's bandwidth, as the gain value remains within the -3 dB limit. The device can, thus, be considered promising for S+C-Band applications. The higher gain value results from the higher optical confinement. For the B2 design, the flattest gain reaches its maximum of 19 dB at 1560 nm, with an injected current of 800 mA (2.22

kA/cm^2) in the measured wavelength range. Its bandwidth is 90 nm, covering the complete measured wavelength range. Again, the higher current densities are amplifying wavelengths belonging to the S-Band. However, for the C+L-Band, the another interesting current is 700 mA (1.94 kA/cm^2), showing a bandwidth of 88 nm (1522 – 1610 nm). As the upper wavelength belongs to the bandwidth, we can expect the bandwidth to be wider, thus, to cover the complete C+L-Band. It has a maximal gain of 18 dB, at 1560 nm.

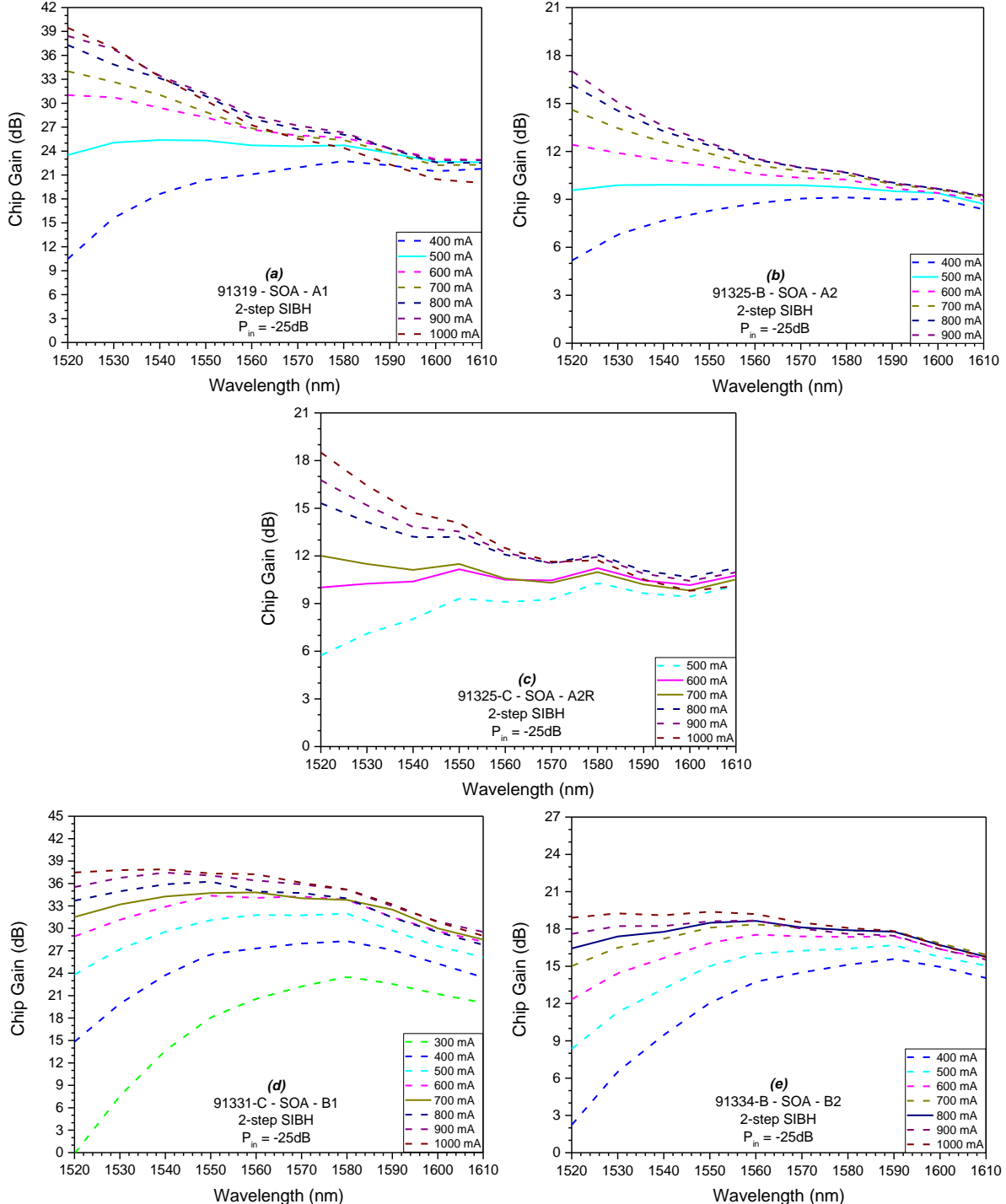


Figure 159. C+L-Band SOAs' Gain spectra from devices based on (a) A1, (b) A2, (c) A2R, (d) B1 and (e) B2 designs.

From these measurements, we observe that the gain values are consistent with the optical confinement in the active layers of the devices. More important, we see that the reduction of the QWs thickness is a

limited option to enlarge the bandwidth. In our case, the e_2 confinement is degraded. Consequently, the 11 nm thick QW based SOAs require high current densities to reach flat gain behavior. Finally, the gain behavior of these designs can be used in the C+L-Band at “low” current densities but allow S-Band amplification with higher current densities.

We also studied the gain features of the RSOA devices, as shown in Figure 160. However, only three devices were finalized, the ones based on designs A1, A2 and B1.

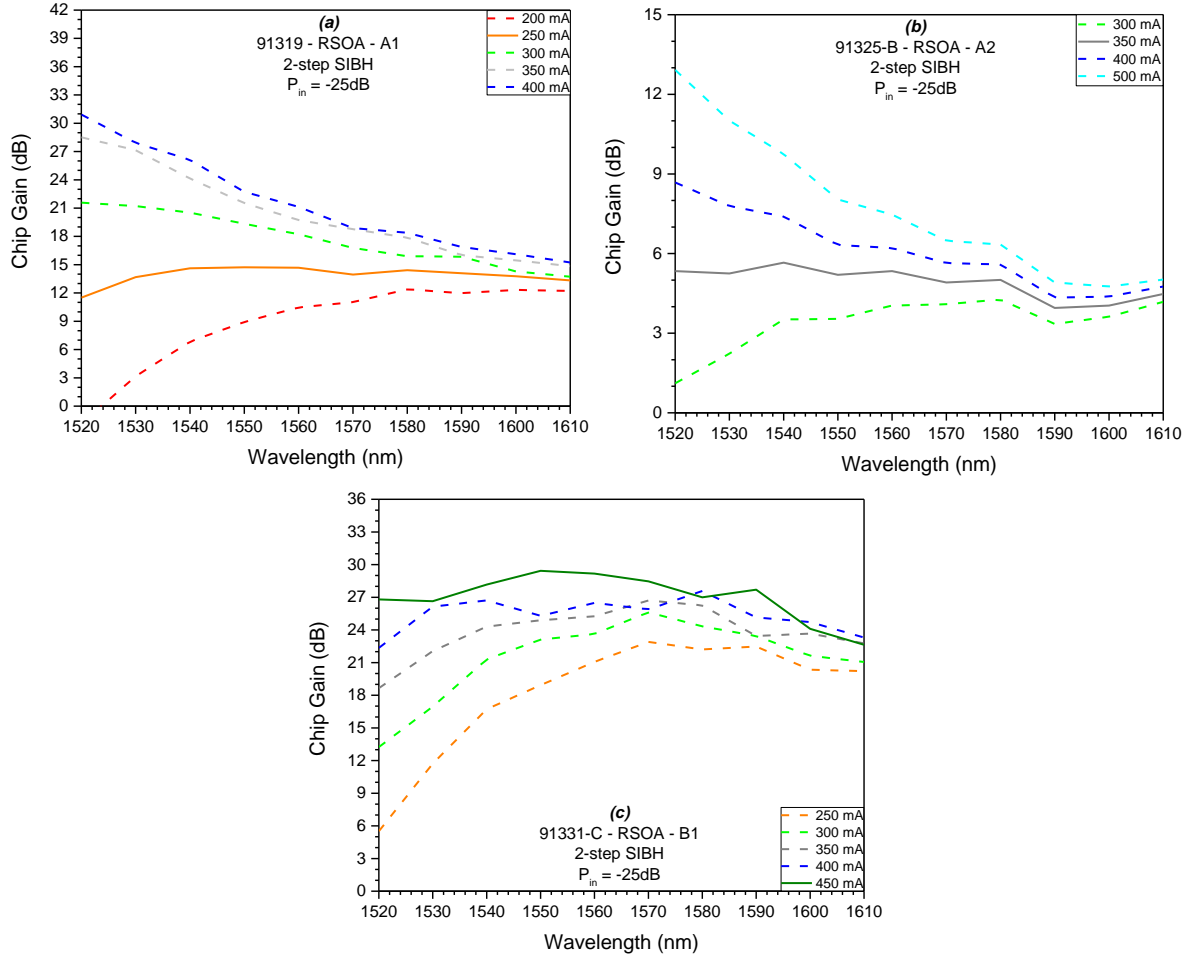


Figure 160. C+L-Band RSOAs' Gain spectra from devices based on (a) A1, (b) A2 and (c) B1 designs.

As expected from the ASE measurements, the RSOAs' gain values are lower than the SOAs' ones. The A1 RSOA shows its flattest gain at 250 mA (1.39 kA/cm^2), like the SOA, with a maximal gain of 15 dB at 1550 nm. Its measured bandwidth is 89 nm wide (1521 – 1610 nm). The A2 RSOA shows low gain values with a maximum of 6 dB at 1540 nm for an injected current of 350 mA (1.94 kA/cm^2). Its bandwidth also covers more than the measured wavelength range.

The B1 RSOA measurement was limited to 450 mA in terms of current injection. Consequently, the maximal measured bandwidth is 75 nm wide (1526 – 1601 nm) with a maximal gain of 27.5 dB, at 1580 nm, reached at 350 mA (1.94 kA/cm^2).

We can observe that the flattest gains are obtained at the same injected current densities for the SOAs and RSOAs fabricated with the same design. Contrary to ASE spectra observation, that showed larger bandwidths with RSOAs than SOAs, the bandwidths are similar for both devices.

1.3.3. O-Band

In the O-Band, the measured wavelength range covers the entire band, from 1260 nm to 1360 nm. Figure 161 shows the gain spectra obtained from both O-Band designs. The O-Band RSOA did not present gain, thus, we will only focus on the SOAs for the next measurements.

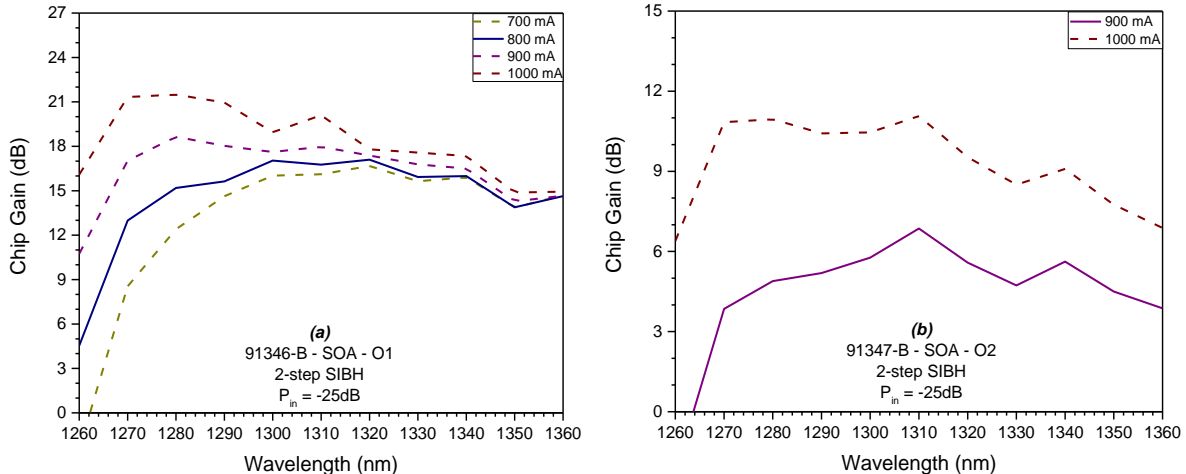


Figure 161. O-Band SOAs' Gain spectra based on (a) O1 and (b) O2 designs.

The O1 SOA do not enable a large enough amplification of the signal at the shortest wavelengths in the O-Band. However, it is the first demonstration of a wideband SOA amplifying in the O-Band, based on GaInAsP MQW. Its maximal measured bandwidth is 87 nm (1273 – 1360 nm), for an injected current of 800 mA (2.22 kA/cm²). The maximal gain value is 17 dB, at 1320 nm.

The maximal gain of the O2 SOA is limited to 7 dB, at 1310 nm, for its flattest gain, reached at 900 mA (2.50 kA/cm²). The measured maximal bandwidth is 90 nm (1270 – 1360 nm).

The O-Band SOAs are similar to the C+L-Band SOAs designed with 11 nm thick QWs. They require “high” injected current densities and exhibit limited bandwidths, probably due to both poor e₂ confinement in the MQW and a redshift resulting from bandgap renormalization.

1.3.4. Results

As far as amplification in C+L-Band is concerned, the values extracted from the graphs are listed in Table 58 and Table 59 for SOAs and RSOAs, respectively.

Design	SOA						
	A1	A2	A2R	B1	B2	O1	O2
Simulated optical confinement (%)	5.33	3.38	3.38	5.97	4.34	4.79	3.13
Flat gain current (mA)	500	500	600	700	800	800	900
Flat gain current density (kA/cm²)	1.39	1.39	1.67	1.94	2.22	2.22	2.50
Maximal gain (dB)	25	10	11	35	19	17	7
Optical bandwidth (nm)	90	90	90	71	90	87	90
Lower limit (nm)	1520	1520	1520	1522	1520	1273	1270
Upper limit (nm)	1610	1610	1610	1593	1610	1360	1360

Table 58. Gain performances from the 2-step SIBH SOAs.

	<i>RSOA</i>		
<i>Design</i>	<i>A1</i>	<i>A2</i>	<i>B1</i>
<i>Simulated optical confinement (%)</i>	5.33	3.38	5.97
<i>Flat gain current (mA)</i>	250	350	350
<i>Flat gain current density (kA/cm²)</i>	1.39	1.94	1.94
<i>Maximal gain (dB)</i>	15	6	27.5
<i>Optical bandwidth (nm)</i>	89	90	75
<i>Lower limit (nm)</i>	1521	1520	1526
<i>Upper limit (nm)</i>	1610	1610	1601

Table 59. Gain performances from the 2-step SIBH RSOAs.

The target of 20 dB is reached for three devices, the A1 SOA and the B1 SOA and RSOA. The B2 design SOA seems also to be a great design that still requires to be improved to reach higher gain at lower current. The B1 design shows a reduced bandwidth for a higher consumption than the A1 design, which is consequently better for the C+L-Band amplification.

For the O-Band amplification, the largest bandwidth is achieved with the O2 design, but the better gain of the O1 SOA makes it a better design. The O1 design is the first SOA based on GaInAsP MQW providing wideband amplification in the O-Band. The performances of our device is compared, in Table 60, to the ones found in the literature, exposed in Chapter I.

<i>Device</i>	<i>GaInAsP MQW-SOA</i>	<i>InAs/InGaAs QD-SOA</i>	<i>InGaAs QD-SOA</i>	<i>BDFA</i>	<i>PDFA</i>	<i>AlGaInAs MQW-SOA</i>	<i>PDFA + SOA</i>
<i>Max. flat gain (dB)</i>	17	26	23	22	9	20	25
<i>Bandwidth (nm)</i>	87	30	28	40	40	40	180
<i>Upper limit (nm)</i>	1273	1316	1255	1320	1280	1270	1270
<i>Lower limit (nm)</i>	1360	1346	1283	1360	1320	1310	1450
<i>Reference</i>	This work	[1]	[2]	[3]	[4]	[5]	[6]

Table 60. Gain comparison between the O1 device and the literature in terms of gain and bandwidth.

With this Table, we observe that the gain of our device needs to be increased. However, we also see that our O1 design based SOA provides a great solution for the optical amplification in the O-Band. Its bandwidth is the largest for a single device. The only solution found to have a wider bandwidth is a hybrid amplifier combining SOA and PDFA.

1.4. Noise Figure - NF

When measuring gain, the ASE power is also measured for each wavelength. Consequently, we can calculate the NF using Equation 78. Nevertheless, we must be careful to take into account the optical band (B_0), corresponding to the OSA filter bandwidth, which is its resolution.

$$\text{Equation 78. } NF = \frac{2*P_{ASE}}{G_{Chip}*\hbar v*B_0} + \frac{1}{G_{Chip}} = \frac{2*(G_{Chip}-1)*n_{sp}}{C_1*G_{Chip}}$$

With the used bench, the measurement is fully automatized to avoid mistakes when calculating the NF values and to take the coupling losses into account during the measurements.

1.4.1. C+L-Band

Figure 162 and Figure 163 show the NF of the C+L-Band SOAs and RSOAs, respectively, for different injected currents.

In every plot, the shorter wavelengths show higher NF than longer wavelengths. This is the result of the wavelength dependence of the population inversion factor, visible in Equation 78, which has its value between 0 and 1. The lower energy levels, i.e. the longest wavelengths, are more populated and show higher population inversion. This parameter's value increases when the carrier density decreases, explaining why NF is higher for high energy levels, i.e. the shortest wavelengths. Consequently, all SOAs and RSOAs' NF tend to a measured minimum at 1610 nm.

At the flat gain current densities and in the optical bandwidth observed in the previous section, the NF values are between 9.0 and 5.1 dB for the A1 SOA and between 7.5 and 5.1 dB, for the A2 SOA. The A2R SOA has a NF between 8.4 and 4.4 dB, at 600 mA (1.67 kA/cm²) and between 8.5 and 4.8 dB, at 700 mA (1.94 kA/cm²).

For the B1 SOA, the NF is between 8.2 and 5.8 dB and for the B2 SOA, it is between 6.9 and 5.1 dB.

For the RSOAs, the NF is higher for the same design. For the A1 design, the RSOA's NF is between 12.5 and 7.3 dB. Its value is between 10.4 and 7.2 dB for the A2 design and between 9.3 and 6.1 dB for the B1 design. These higher values are caused by the population inversion factor, which is impacted by the two paths of the signal in the device. For the A2 design the NF values are higher than its gain values that is detrimental for its use in systems.

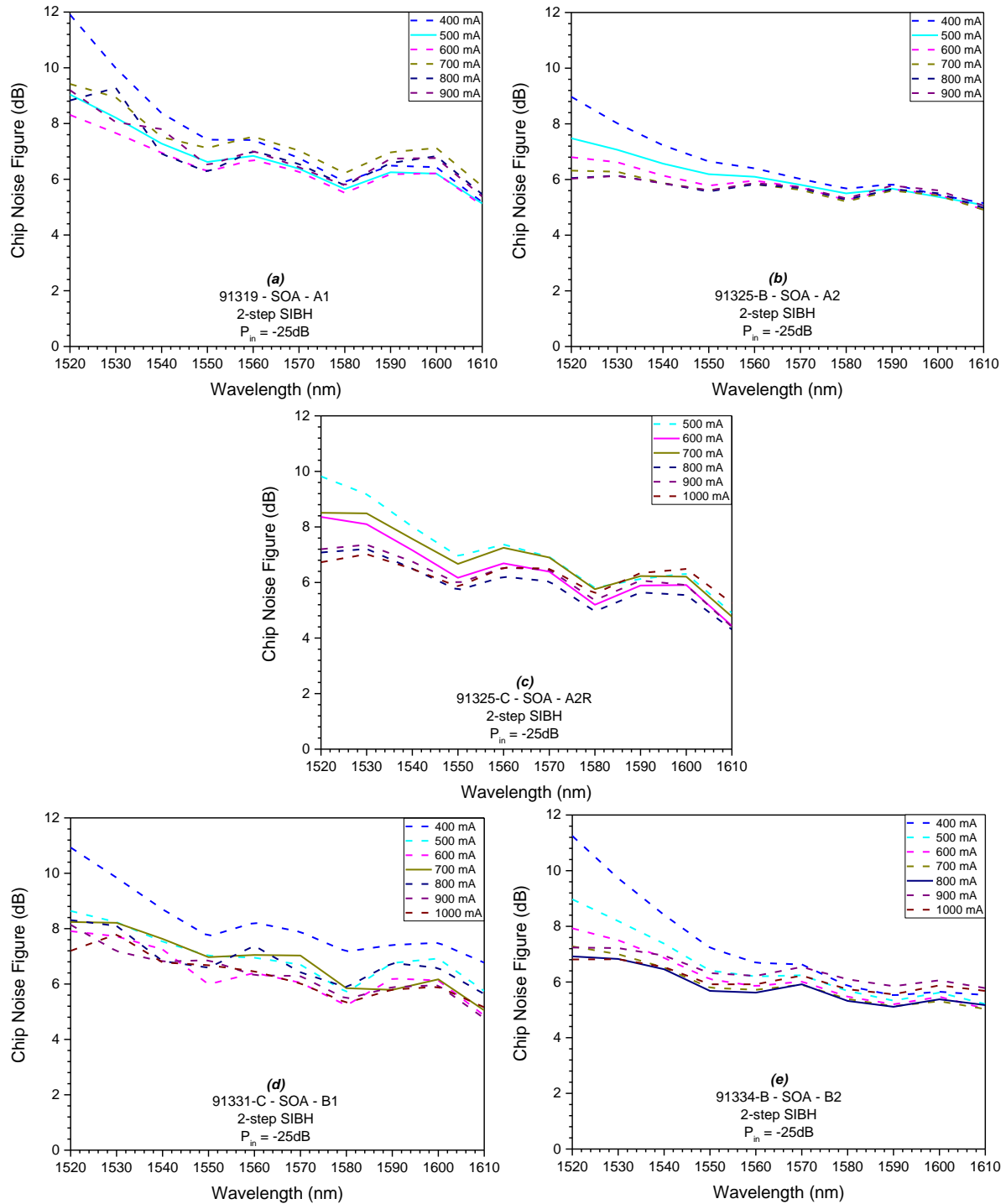


Figure 162. NF measured from C+L-Band SOAs, based on (a) A1, (b) A2, (c) A2R, (d) B1 and (e) B2 designs.

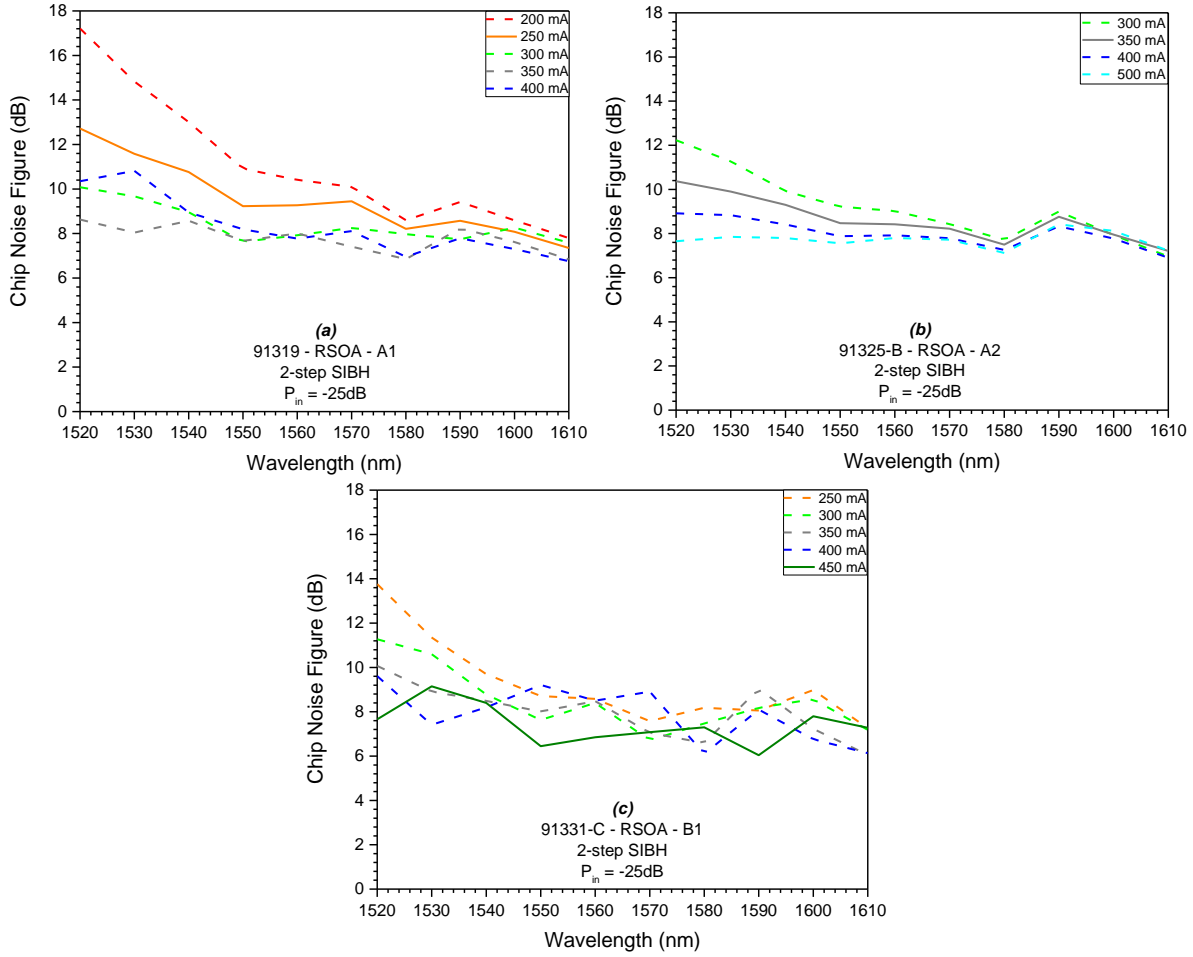


Figure 163. NF measured from C+L-Band RSOAs, based on (a) A1, (b) A2 and (c) B1 designs.

1.4.2. O-Band

The O-Band SOAs' NF are presented in Figure 164. Again, only the SOAs are studied because of the lack of gain of the RSOAs.

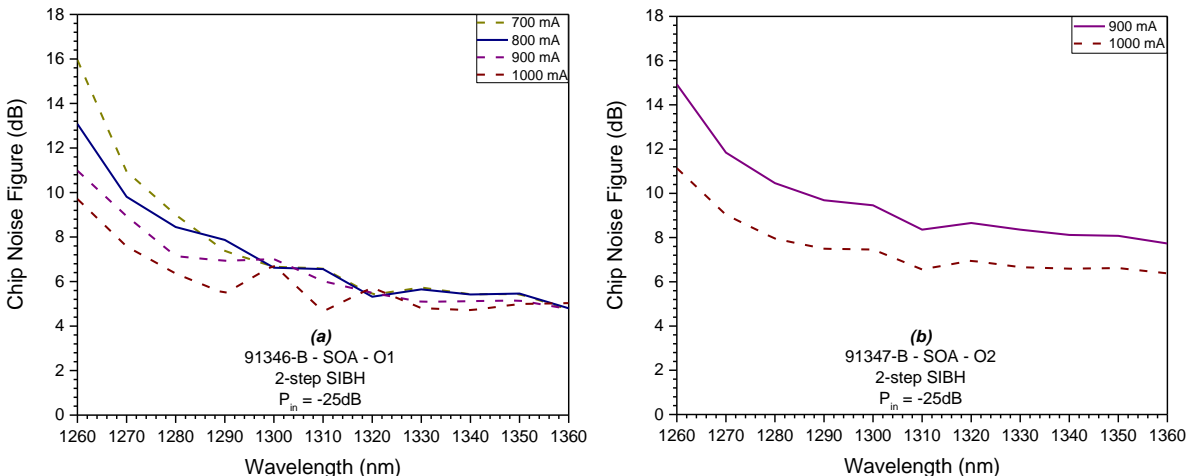


Figure 164. NF measured from O-Band SOAs, based on (a) O1 and (b) O2 designs.

In the optical bandwidths and at the flat gain current densities, the NF is between 9.4 and 4.8 dB, for the O1 design and between 9.0 and 7.7 dB, for the O2 design. The values observed for the O1 design are similar to the one measured in the C+L-Band. However, the O2 design shows high NF values, that are even higher than the gain values.

1.4.3. Results

The interesting NF values, concerning the flat gain current densities previously observed, are listed in Table 61 and Table 62 for SOAs and RSOAs, respectively.

Design	SOA						
	A1	A2	A2R	B1	B2	O1	O2
Flat gain current density (kA/cm²)	1.39	1.39	1.67	1.94	2.22	2.22	2.50
Maximal measured NF (dB)	9.0	7.5	8.4	8.2	6.9	13.1	14.9
Maximal NF of the optical bandwidth (dB)	9.0	7.5	8.4	8.2	6.9	9.4	9.0
Minimal NF of the optical bandwidth (dB)	5.1	5.1	4.4	5.8	5.1	4.8	7.7

Table 61. NF performances at flat gain current for 2-step SIBH SOAs.

Design	RSOA		
	A1	A2	B1
Flat gain current density (kA/cm²)	1.39	1.94	1.94
Maximal measured NF (dB)	12.7	10.4	10.1
Maximal NF of the optical bandwidth (dB)	12.5	10.4	9.3
Minimal NF of the optical bandwidth (dB)	7.3	7.2	6.1

Table 62. NF performances at flat gain current for 2-step SIBH RSOAs.

The best SOAs in terms of NF are the ones based on the A2 and A2R designs for the C+L-Band and on the O1 design for the O-Band. However, for the RSOAs, the B1 design shows lower NF values than the others. Put together with the gain measurements, the B1 is an interesting device to reach high gain with lower and flatter NF.

The last parameter to measure with the 2-step SIBH is the saturation output power.

1.5. Saturation output power - P_{sat}

The saturation output power is extracted from the gain measurement as function of the optical output power. As described in Chapter II, its value is read on the graphs at $G = G_{\text{max}} - 3 \text{ dB}$. Consequently, the setup for the gain measurement is the same for the P_{sat} measurement. However, this characterization is operated at a constant injection current (500 mA) and for the different wavelengths. The output power is modified by changing the input power of the SOA. To do this, the variable attenuator placed after the laser source is required. However, the laser source is limited to 0 dB in terms of power. So, the saturation output power has been measured for only 2 SOAs, the ones presenting the higher optical confinements (i.e. the B1 and A1 designs). When the gain or the input signal's power is too low, the reduction of the output power is not visible nor predictable as illustrated in Figure 165.

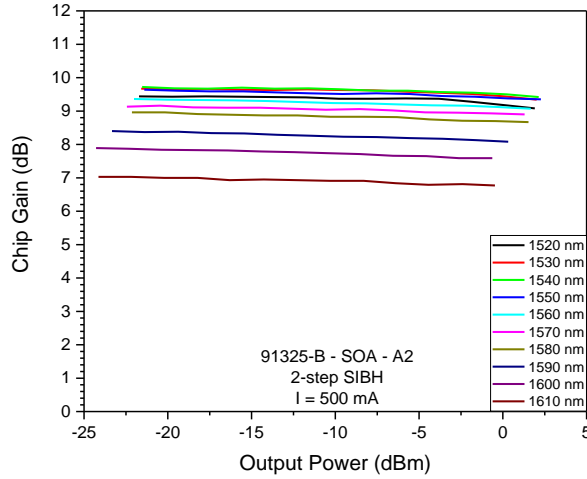


Figure 165. Saturation output power measurement from the A2 design SOA, 500 mA.

This figure represents the A2 SOA's gain as function of its output power at each measured wavelengths measured at 500 mA. The input signal's power of our laser source is too low to saturate the device.

Figure 166 displays the same curves for the A1 and B1 SOAs that could reach their saturation output powers, at 500 mA.

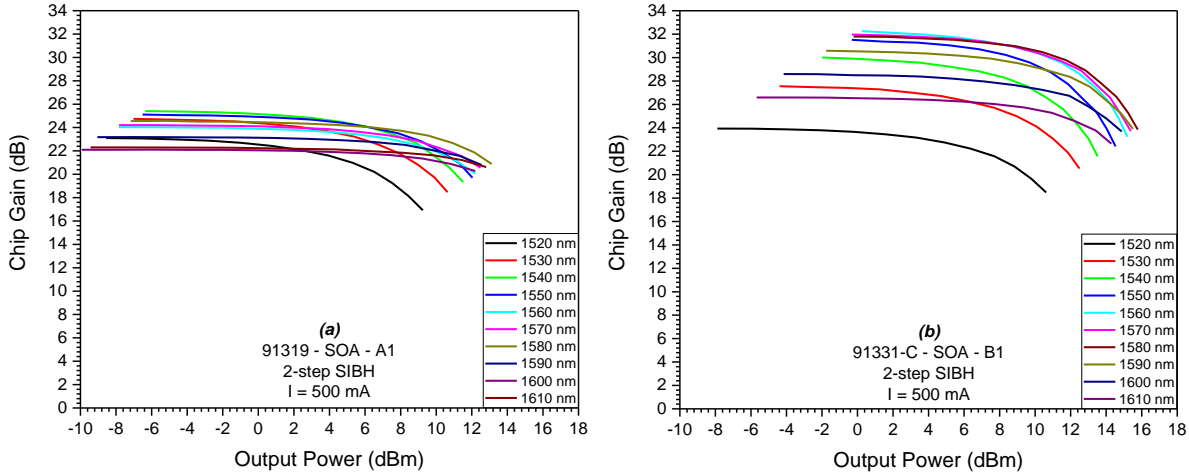


Figure 166. Gain as function of output power for (a) A1 and (b) B1 SOAs.

These curves allow us to obtain the P_{sat} of these device for several wavelengths, and compare them in Figure 167.

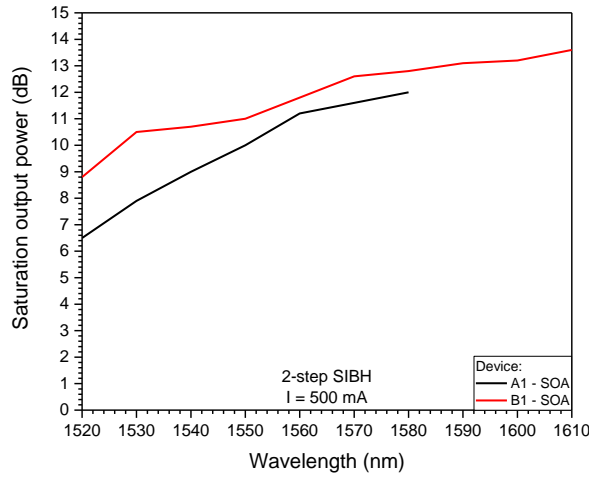


Figure 167. Saturation output power of the A1 and B1 SOAs as function of the wavelength.

As predicted, by theory, P_{sat} is higher at longer wavelengths. This parameter depends on A/Γ , A being the section area of the active material and Γ is the optical confinement. As Γ is more important for the B1 design, we could predict that its P_{sat} performances would be lower than the ones of design A1. However, the modification of the section caused by the thickness reduction from 14 to 11 nm between the two designs enable to reach higher saturation output power with the thinner QW.

The A1 SOA shows P_{sat} values between 6.5 dBm and 12 dBm, while the B1 design's P_{sat} is between 8.8 dBm and 13.6 dBm.

For the O-Band, devices with higher optical confinement are required to be able to measure a saturation output power with our equipment.

2. 1-step SIBH processes

In this section, we focus on the wafers fabricated following the newly developed process, the 1-step SIBH. With this process, we can produce the devices with only one regrowth step instead of two and the implantation step is not required. Moreover, its architecture leads to a better current injection. We will follow the same path as for the 2-step SIBH devices. We present the far field mode profiles, the ASE spectra and finish with the gain, NF and P_{sat} measurements. For the C+L-Band, every designs were produced, except the A2R design and the O-Band design, we were able to complete the fabrication of the O2 design only. For the RSOA, the B1 design could not be characterized due to degraded facet.

2.1. Far field imaging

For the far field measurement, we directly focus on the 2D profiles and analyze the divergence angles. The fabrication process does not modify the active region geometry, but it should allow a decrease of the current leakages and a slight increase the optical output power.

Figure 168 gives the 2D profiles of the far field beam imaging for the 1-step SIBH SOAs, on the left, and of the RSOAs, on the right, for the C+L-Band devices. The presented profiles were measured at 1A for the SOAs and at 500 mA for the RSOA to compare their shapes for the same injected current density.

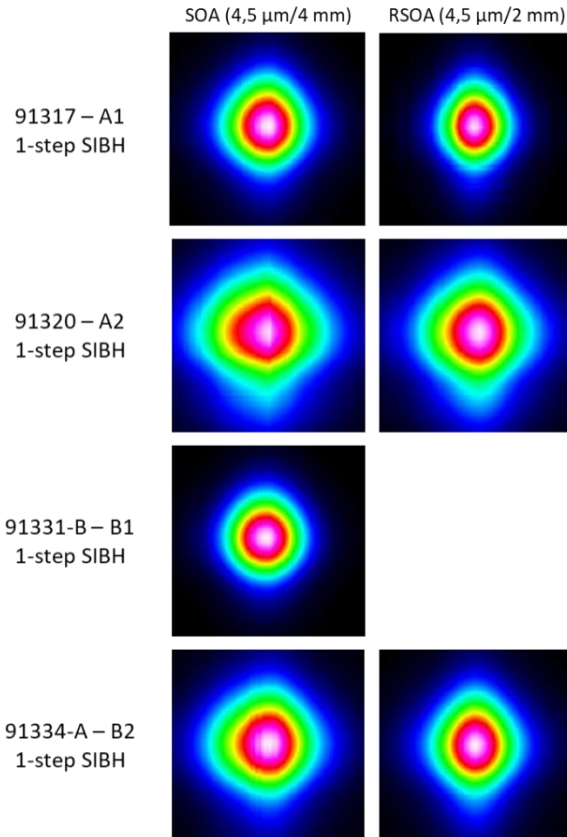


Figure 168. 2D mode profiles measured from the 1-step SOAs on the left and RSOAs on the right.

We observe the same behavior as for the 2-step SIBH devices. The design with lower optical confinement exhibit larger mode profiles. However, the differences between the four processed SOAs and the three processed RSOAs are not as important as for the 2-step SIBH devices.

Figure 169 displays the 2D far field mode profiles of the O-Band SOAs fabricated with the 1-step SIBH process. Only SOAs were characterized as the output power of the RSOAs was too low to provide gain.

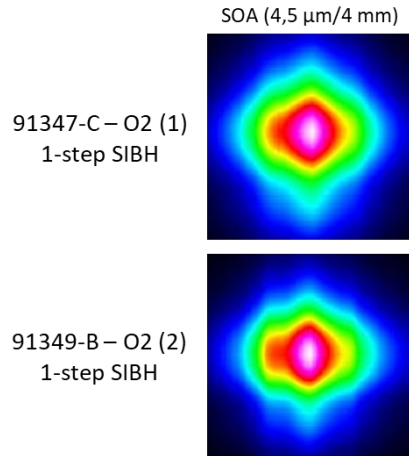


Figure 169. 2D mode profiles measured from the 1-step O-Band SOAs.

Again, the O2 design displays the same mode profile with both fabrication processes. Two devices based on the same design (O2) were processed from two different epitaxy runs to verify the reproducibility of the fabrication process.

Table 63 lists the divergence angles calculated from each device, at FWHM.

Design	SOA		RSOA	
	Horizontal axis	Vertical axis	Horizontal axis	Vertical axis
A1	11.94°	14.00°	10.02°	12.38°
A2	14.33°	16.46°	12.94°	15.70°
B1	12.43°	13.31°	-	-
B2	12.24°	13.53°	11.12°	13.90°
O2 (1)	10.76°	14.32°	-	-
O2 (2)	14.84°	15.35°	-	-

Table 63. Beam divergence angles (2θ) at FWHM for 1-step SIBH devices at 500 mA for every device.

The high values observed for the horizontal axis is due to the mix between spontaneous emission and ASE. The differences between the two O2 SOAs, is due to a more important participation of the spontaneous emission to the mode profile for the O2 (2) device. The angles are mostly similar between horizontal and vertical axis, thus, the coupling with optical fiber should be correct.

2.2. ASE Spectra

2.2.1. C+L-Band

Figure 170 and Figure 171 represent the ASE spectra measured from the C+L-Band SOAs with design Ax and design Bx, respectively.

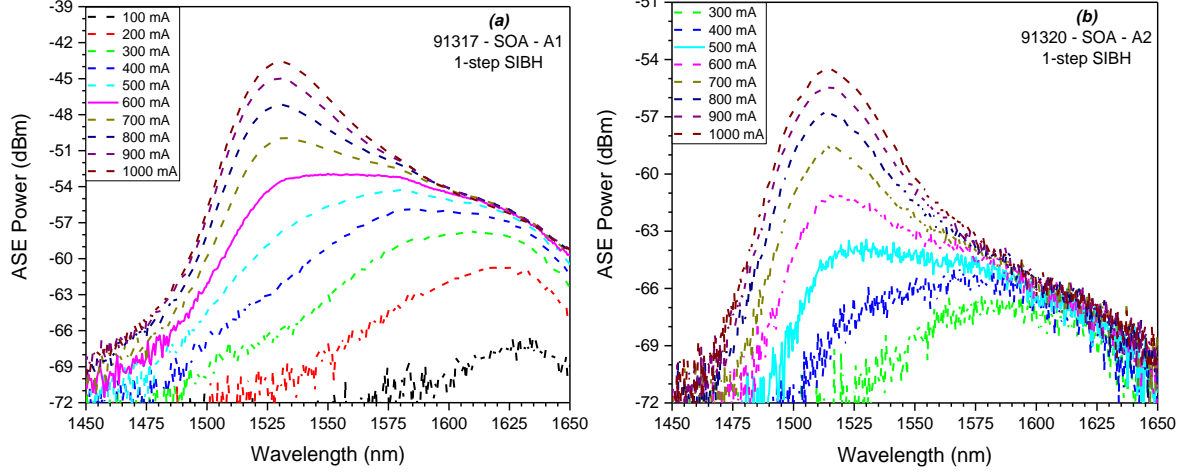


Figure 170. ASE Spectra measured from 1-step SIBH SOAs, based on (a) A1 and (b) A2 designs.

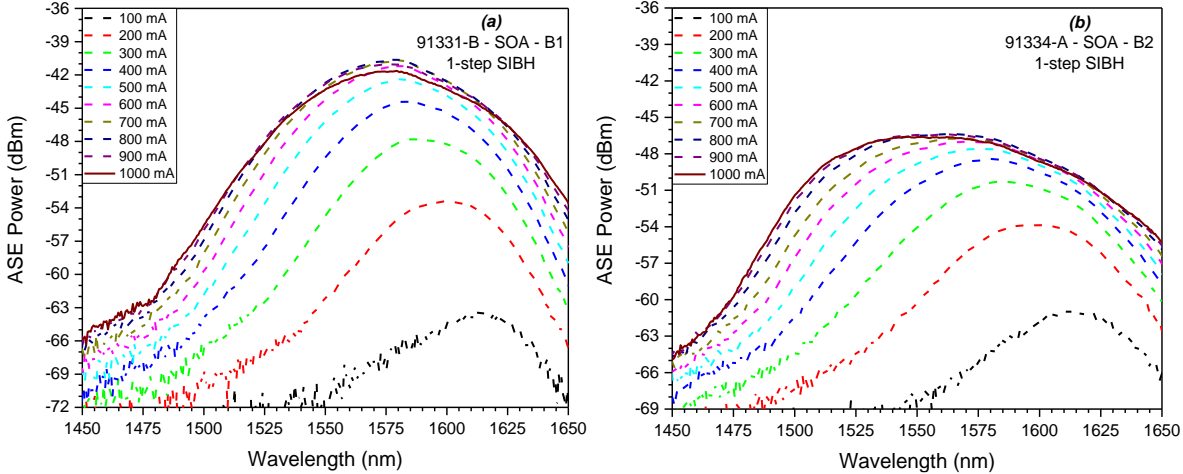


Figure 171. ASE Spectra measured from 1-step SIBH SOAs, based on (a) B1 and (b) B2 designs.

The e_2-hh_2 transition is still more visible with the 14 nm thick QWs than with the 11 nm thick QW based devices. Consequently, the flattest ASE current is still reached at high values with the Bx designs, compared to the Ax designs.

For the A1 design, the flattest ASE spectrum is reached with an injected current of 600 mA (or an injected current density: 1.67 kA/cm²). Its optical ASE bandwidth is 103 nm wide (1519 – 1622 nm). The A2 design shows lower ASE power due to its lower optical confinement, and shows its flattest ASE spectrum at 500 mA (1.39 kA/cm²), with an ASE bandwidth of 89 nm (1507 – 1596 nm). The low power exhibited by this device makes the ASE spectra noisy at its flat ASE spectrum's injected current. So, the bandwidth measurement is only an approximation and will have to be determined with the gain measurements.

The B1 design SOA has a flat ASE spectrum at 1 A (2.78 kA/cm²), showing a bandwidth of 72 nm (1541 – 1613 nm). For the last C+L-Band SOA, with the B2 design, a maximal bandwidth of 103 nm (1509 – 1612 nm) at the same injected current is observable. For both devices, the injected current modification

between 900 mA and 1 A induces a decreasing of the ASE power because of the not optimal thermal management, during the measurement.

The ASE spectra measured for the C+L-Band RSOA are presented in Figure 172 for the A1 and A2 designs, and in Figure 173, for the B2 design.

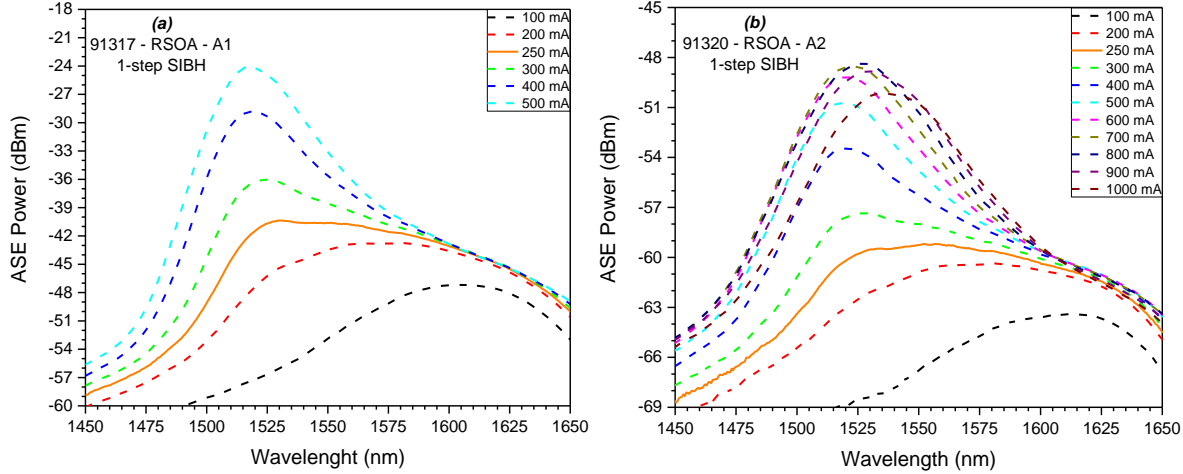


Figure 172. ASE Spectra measured from 1-step SIBH RSOAs, based on (a) A1 and (b) A2 designs.

The A1 RSOA shows a flattest ASE spectrum at 250 mA (1.39 kA/cm^2), with a 90 nm wide bandwidth (1513 – 1603 nm). For the A2 design, the maximal ASE bandwidth of 126 nm (1507 – 1633 nm) is also reached at 250 mA (1.39 kA/cm^2). With this design, we still observe that the thermal management has to be improved to reduce the impact of high injected current densities on the device's performances.

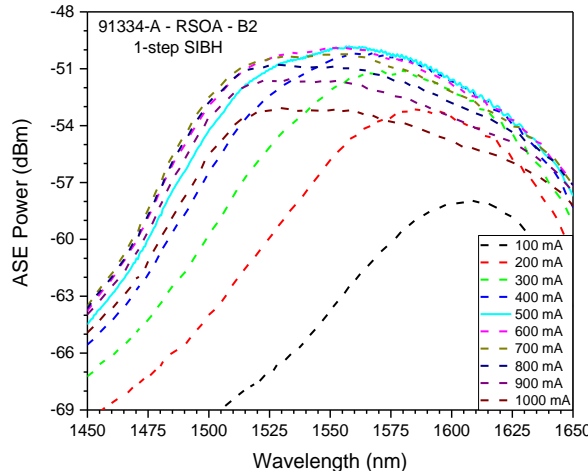


Figure 173. ASE Spectra measured from 1-step SIBH B2 design RSOA.

For the B2 RSOA, the ASE power decreasing caused by the thermal management, make the flattest ASE spectrum measured at 1 A (5.56 kA/cm^2). In this condition, the bandwidth is 128 nm wide (1498 – 1626 nm). Nevertheless, if we only take into account the injected currents that do not suffer the thermal management, the ASE bandwidth is reduced to 108 nm (1508 – 1616 nm), at 500 mA (2.78 kA/cm^2).

2.2.2. O-Band

For the O-Band, the ASE spectra of both devices O2 (1) and O2 (2) are presented in Figure 174. Again, the atmosphere's humidity tends to impact the optical power exhibited by the devices. Without taking it into account, the O2 (1) SOA gives a maximal bandwidth of 105 nm (1274 – 1379 nm), at 1 A (2.78 kA/cm^2). The O2 (2) SOA reaches a similar bandwidth of 99 nm (1246 – 1345 nm) at the same injected current. It is again visible that the bandwidth of the SOAs are very sensitive to the epitaxy and fabrication processes as the second SOA shows a shifted bandwidth to the shortest wavelengths.

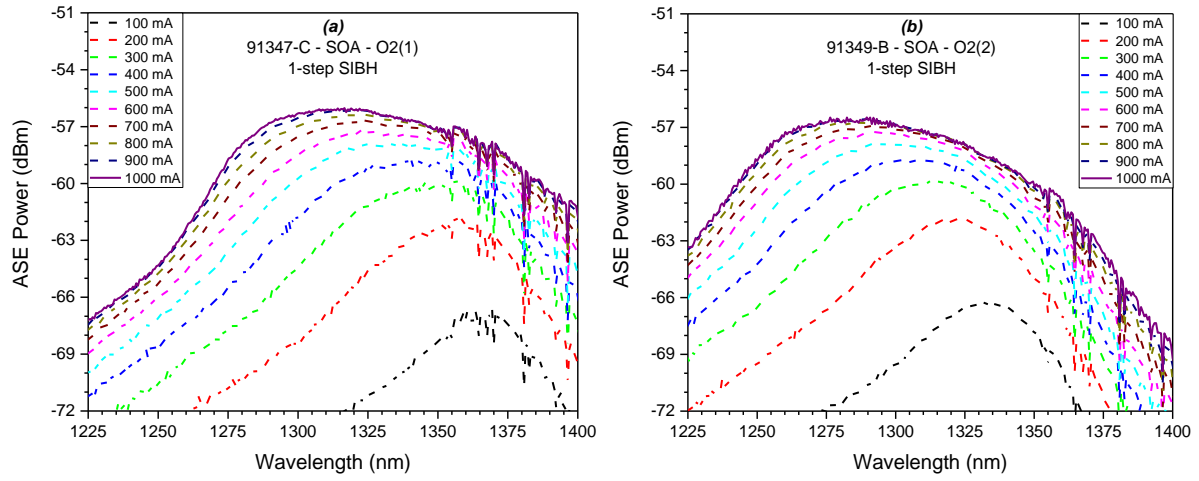


Figure 174. ASE Spectra measured from 1-step SIBH (a) O2(1) and (b) O2(2) SOAs.

2.2.3. Results

The ASE performances of the devices are summarized in Table 64 and in Table 65, for the SOAs and the RSOAs respectively.

SOA						
Design	A1	A2	B1	B2	O2(1)	O2(2)
Flat ASE current (mA)	600	500	1000	1000	1000	1000
Flat ASE current density (kA/cm²)	1.67	1.39	2.78	2.78	2.78	2.78
Simulated Bandwidth (nm)	146		201		131	
PL Bandwidth (nm)	124	129	150	162	106	
ASE Optical Bandwidth (nm)	103	89	72	103	105	99
Lower limit (nm)	1519	1507	1541	1509	1274	1246
Upper limit (nm)	1622	1596	1613	1612	1379	1345

Table 64. ASE performances measured from 1-step SIBH SOAs.

RSOA			
Design	A1	A2	
Flat ASE current (mA)	250	250	500
Flat ASE current density (kA/cm²)	1.39	1.39	2.78
Simulated Bandwidth (nm)	146		201
PL Bandwidth (nm)	124	129	162
ASE Optical Bandwidth (nm)	90	126	108
Lower limit (nm)	1513	1507	1508
Upper limit (nm)	1603	1633	1616

Table 65. ASE performances measured from 1-step SIBH RSOAs.

From the measurements, the A1 SOA and the A2 RSOAs are the most interesting devices to amplify over the C+L-Band.

In the O-Band, none of the devices cover the complete band. The first SOA covers the long wavelengths and the second amplifies the shortest ones.

Finally, contrary to the expectations, the overall current densities required to obtain flat ASE spectra are higher than for the 2-step SIBH process. It shows that the process still needs improvement to reach the same performances in terms of carriers' consumption. However, this behavior still has to be confirmed with the gain measurements.

2.3. Gain Spectra – G

2.3.1. C+L-Band

Figure 175 shows the gain spectra measured for the 1-step SIBH SOA based on the A1 design. The SOA fabricated with the A2 design was damaged between the ASE and the gain measurements.

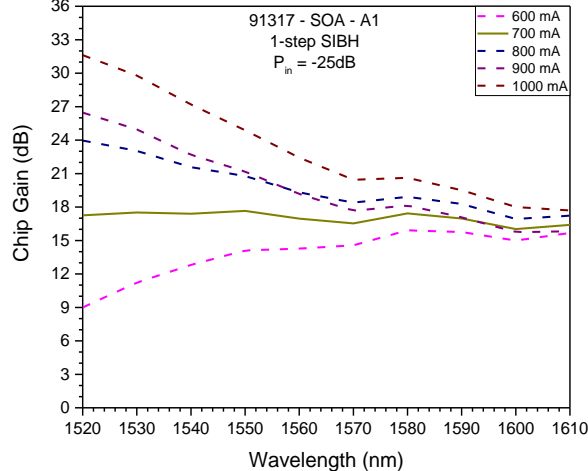


Figure 175. Gain spectra from the 1-step SIBH C+L-Band SOA based on the A1 design.

For this design, fabricated with the 1-step SIBH process, we observe a flat gain at 700 mA (1.94 kA/cm^2). The maximal gain at this injected current density is 17.5 dB and the 90 nm bandwidth covered the complete measured wavelength range.

Figure 176 displays the C+L-Band gain spectra measured from the SOA based on the B1 and B2 designs.

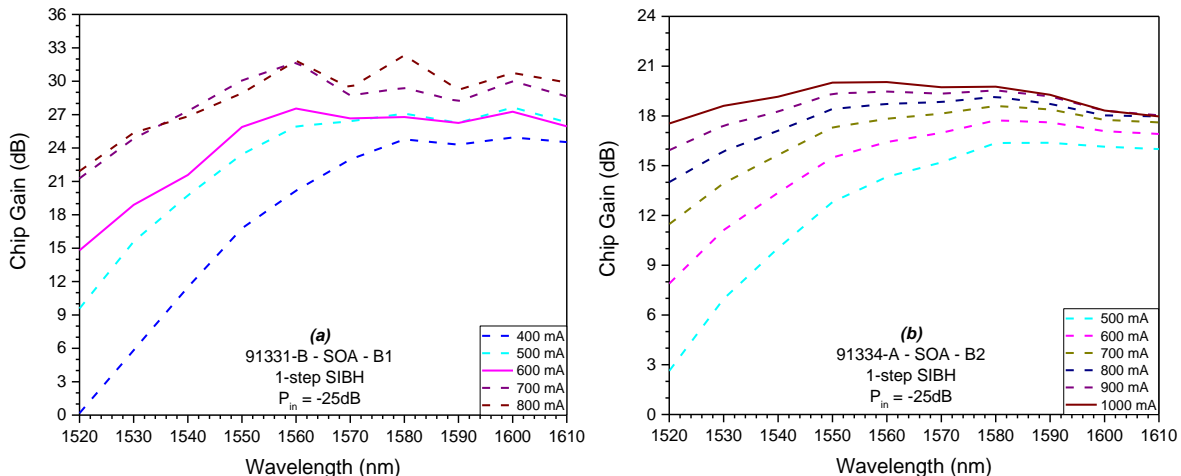


Figure 176. Gain spectra from the 1-step SIBH C+L-Band SOAs based on the (a) B1 and (b) B2 designs.

The B1 design has its largest bandwidth, of 63 nm (1547 – 1610 nm), covering the long wavelengths, while the B2 design shows a flattest bandwidth of 90 nm, limited by the wavelength measurement range. Their flat gain injected currents are 600 mA (1.67 kA/cm^2) and 1 A (2.78 kA/cm^2) for the B1 and B2 designs, respectively. Their maximal gain in these conditions are 27.5 dB, at 1560 nm for the B1 SOA, and 20 dB, at 1550 nm, for the B2 SOA.

The RSOAs' gain spectra are presented in Figure 177 for the ones base on the Ax designs. The Bx designs based RSOA were not measured with the gain, NF, P_{sat} measurement bench.

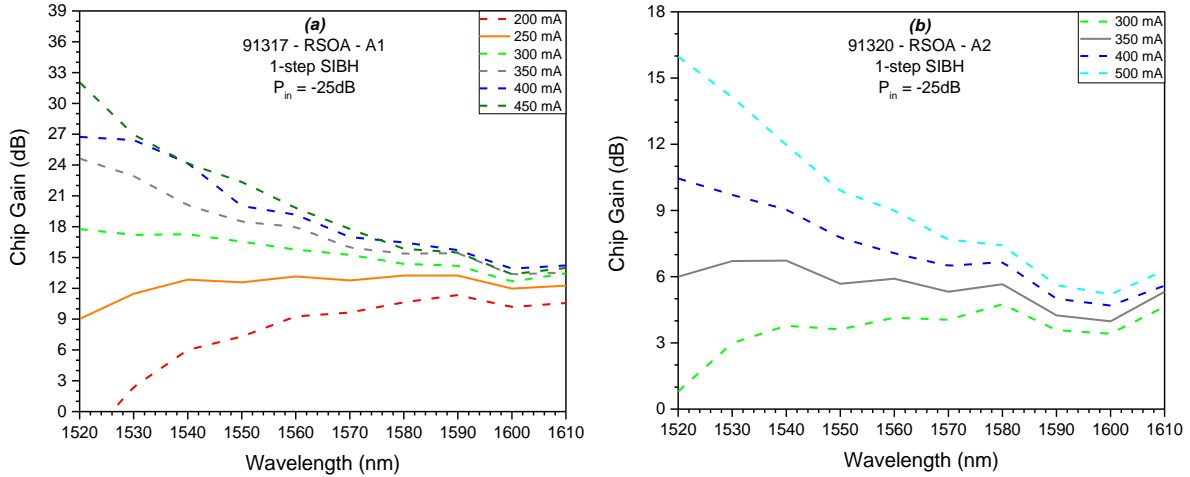


Figure 177. Gain spectra from the 1-step SIBH C+L-Band RSOAs based on the (a) A1 and (b) A2 designs.

The A1 RSOA shows its flattest gain spectrum, with a maximum of 13 dB, at 1590 nm, at 250 mA (1.39 kA/cm^2). The measured bandwidth is 85 nm wide (1525 – 1610 nm). For the A2 design, the flat gain is obtained at an injected current of 350 mA (1.94 kA/cm^2). The gain has a maximum of 7 dB, at 1540 nm and the bandwidth covers the complete measured wavelength range.

2.3.2. O-Band

For the O-Band, we will only focus on one device to reduce the time required for the devices' characterization. Figure 178 shows the gain spectra measured from the O2 (2) SOA.

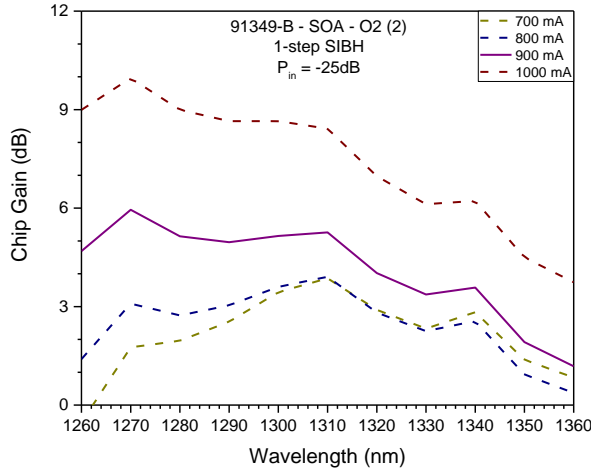


Figure 178. Gain spectra from the 1-step SIBH O2(2) SOA.

Like for the C+L-Band, the low optical confinement of this design results in low gain. With an injected current of 900 mA (2.50 kA/cm^2), the maximal gain is 6.0 dB at 1270 nm and the bandwidth is 84 nm wide (1260 – 1344 nm). The bandwidth is expected to be larger at the short wavelengths, but the gain performance is too low to be used in systems.

2.3.3. Results

The bandwidths, their limits, the maximal gains and flat gain injected current densities, extracted from the previously presented graphs are listed in Table 66 for the SOAs and RSOAs.

Again, the Bx designs have higher carrier consumption than the Ax designs. It is interesting to observe that the B2 design presents a higher maximal gain than the A1 design at their flattest gain spectrum, even if its optical confinement is lower. It results from the higher carrier consumption of the B2 design

coupled with the carrier losses related to non-radiative recombination mechanisms, impacting more the A1 design. Indeed, less gain is exhibited at the longest wavelengths by the A1 SOA.

<i>Design</i>	<i>SOA</i>				<i>RSOA</i>	
	<i>A1</i>	<i>B1</i>	<i>B2</i>	<i>O2(2)</i>	<i>A1</i>	<i>A2</i>
<i>Simulated optical confinement (%)</i>	<i>5.33</i>	<i>5.97</i>	<i>4.34</i>	<i>3.13</i>	<i>5.33</i>	<i>3.38</i>
<i>Flat gain current (mA)</i>	700	600	1000	900	250	350
<i>Flat gain current density (kA/cm²)</i>	1.94	1.67	2.78	2.50	1.39	1.94
<i>Maximal gain (dB)</i>	17.5	27.5	20	6	13	7
<i>Optical bandwidth (nm)</i>	90	63	90	84	85	90
<i>Lower limit (nm)</i>	1520	1547	1520	1260	1525	1520
<i>Upper limit (nm)</i>	1610	1610	1610	1344	1610	1610

Table 66. Gain performances of the 1-step SIBH fabricated devices.

The O2(2) SOA, as well as the A2 RSOA present low gain values that are similar to their NF values as we will see in the next section. Also, we still observe that the B1 design exhibits much more gain than the A1 design for a lower injected current density, at the cost of a narrower bandwidth.

2.4. Noise Figure - NF

2.4.1. C+L-Band

The NF is represented for the 1-step SIBH A1 SOA in Figure 179. As we did for the 2-step SIBH fabricated devices, we will focus on the NF spectra at the current densities corresponding to the flat gain spectra.

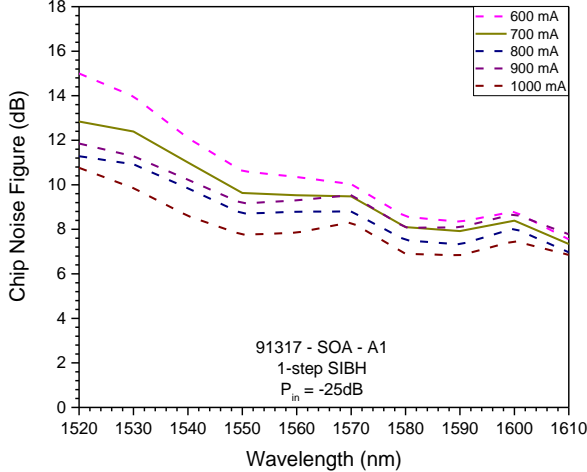


Figure 179. NF from the 1-step SIBH C+L-Band SOA based on the A1 design.

For the A1 SOA, the NF is between 12.8 and 7.3 dB in the measured wavelength range. The maximum is higher than the target of 10 dB we set for the NF.

Figure 180 shows the NF measured from the SOAs based on the Bx designs.

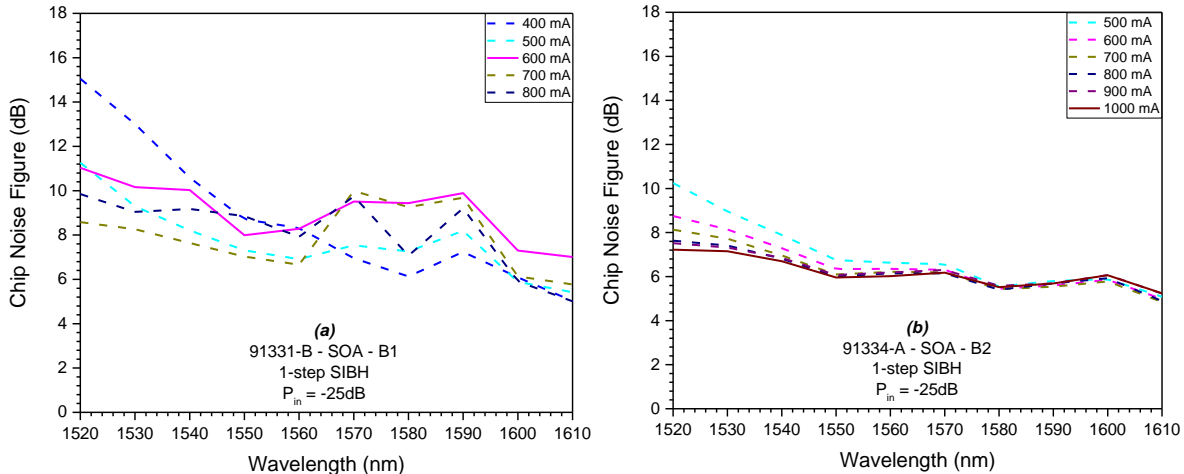


Figure 180. NF from the 1-step SIBH C+L-Band SOAs based on the (a) B1 and (b) B2 designs.

At 1.67 kA/cm² injected current density, the B1 SOA shows a NF varying from 9.9 dB to 7.0 dB in the measured bandwidth. The highest NF value is reached at 1590 nm, which is not consistent with the other measurements showing the highest NF values at the shortest wavelengths. By comparing the gain spectra to the NF spectra, we observe that this NF increase is coherent to a decrease of the gain. This phenomenon can be caused by a variation of the coupling efficiency during the measurement. For the B2 SOA, the NF is between 7.2 dB and 5.2 dB at 1 A (2.78 kA/cm²). These values are the lowest we measured for the C+L-Band devices.

The RSOAs were also measured in terms of NF and their results are visible in Figure 181. They show a NF varying between 11.6 dB and 7.7 dB for the A1 design. This device shows similar gain and NF

values which is detrimental for its use in systems. For the A2 design, the NF is between 11.2 and 7.3 dB at the flattest gain's injected current density, which are values higher than the measured gain.

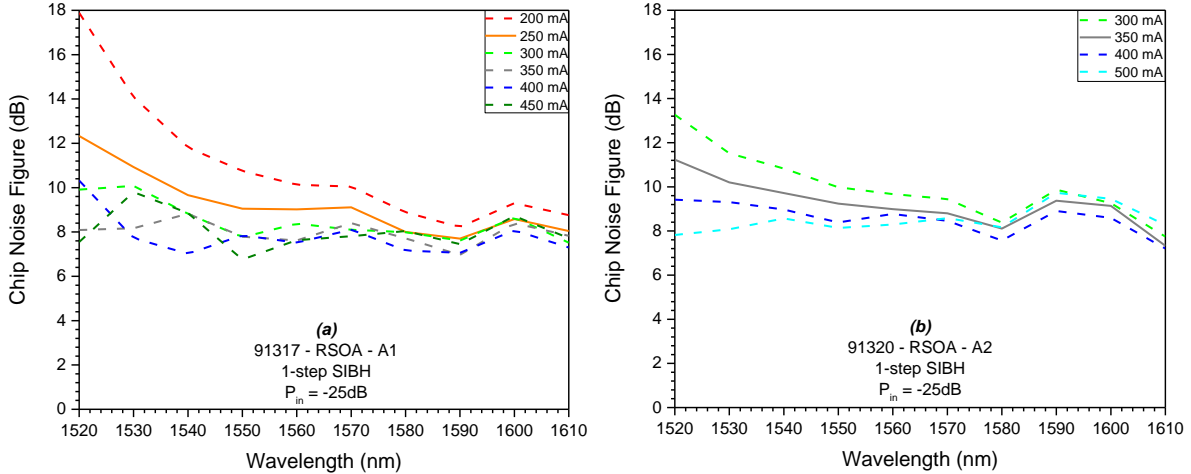


Figure 181. NF from the 1-step SIBH C+L-Band RSOAs based on the (a) A1 and (b) A2 designs.

2.4.2.O-Band

For the O-Band, Figure 182 represent the NF measured for the O2 (2) SOA.

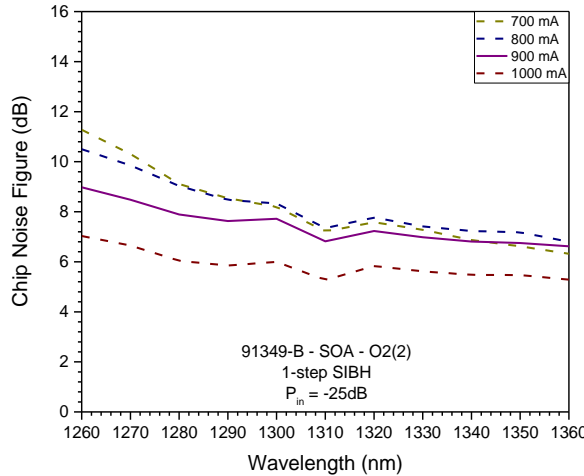


Figure 182. NF from the 1-step SIBH O2(2) SOA.

The NF is between 9.0 dB and 6.8 dB, for the bandwidth measured in the previous section. Consequently, for this device, the NF is higher than the gain at the injected current of 900 mA (2.50 kA/cm^2). To decrease the NF and increase the gain, higher current is required, but the bandwidth is degraded by the gain limitation observed at the longest wavelengths of the measured range.

2.4.3.Results

The NF values are summarized in Table 67. We observe that the Ax design reaches NF values higher than the targeted 10 dB, in both SOA and RSOA configuration. Moreover, we saw that the O2 (2) SOA and A2 RSOA's NF values are higher than the gain values, thus, must be improved to be used.

Design	SOA				RSOA	
	A1	B1	B2	O2(2)	A1	A2
Flat gain current density (kA/cm^2)	1.94	1.67	2.78	2.50	1.39	1.94
Maximal NF (dB)	12.8	11.0	7.2	9.0	12.3	11.2
Maximal NF of the optical bandwidth (dB)	12.8	9.9	7.2	9.0	11.6	11.2
Minimal NF of the optical bandwidth (dB)	7.3	7.0	5.2	6.8	7.7	7.3

Table 67. NF performances of the 1-step SIBH fabricated devices.

2.5. Saturation output power - P_{sat}

As explained in the section dedicated to the 2-step SIBH measurement, a high enough gain is required to measure the P_{sat} of the devices. Because of this, we were only able to observe the gain decrease with the output power increase of the B1 SOA at 500 mA, illustrated in Figure 183.

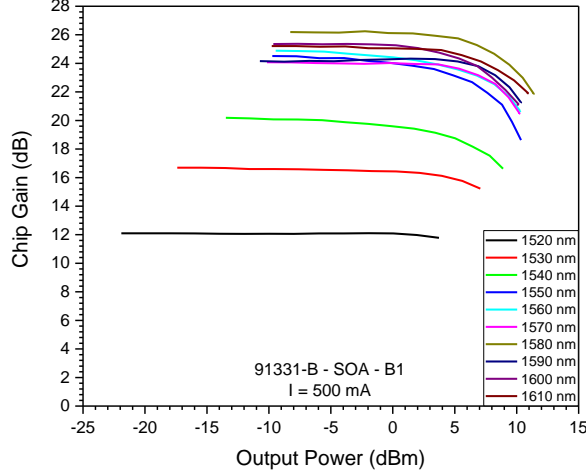


Figure 183. Gain as function of the output power of the 1-step SIBH SOA based on the B1 design.

From this graph, we are able to extract the P_{sat} of the device for the wavelengths between 1540 nm and 1610, as shown in Figure 184.

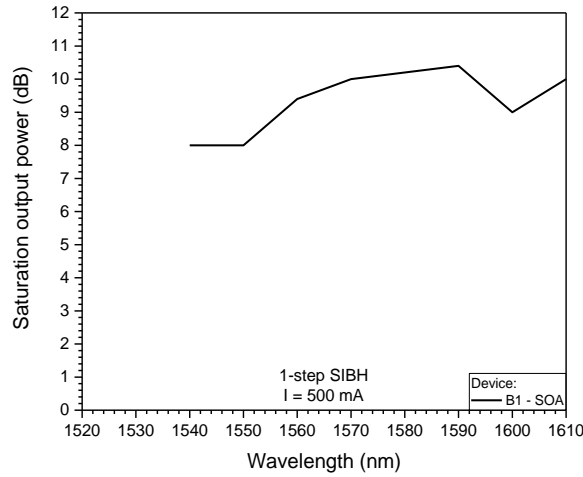


Figure 184. P_{sat} of the B1 SOAs as function of the wavelength.

At the injected current density of 1.39 kA/cm², the P_{sat} of the SOA based on the B1 design is between 8.0 dBm and 10.4 dBm. The P_{sat} values obtained with this device are lower than the ones measured with the device fabricated with the 2-step SIBH. The two processes' performances are compared in the next section.

3. Comparison between the fabrication processes

In the previous section, we focused on the performances of each device, comparing the designs. Now, we will use the observed performances to compare the fabrication processes that are the 2-step SIBH and the 1-step SIBH.

The far field measurements highlight that the 2-step SIBH fabricated devices display slightly narrower divergence angles as illustrated in Figure 185.

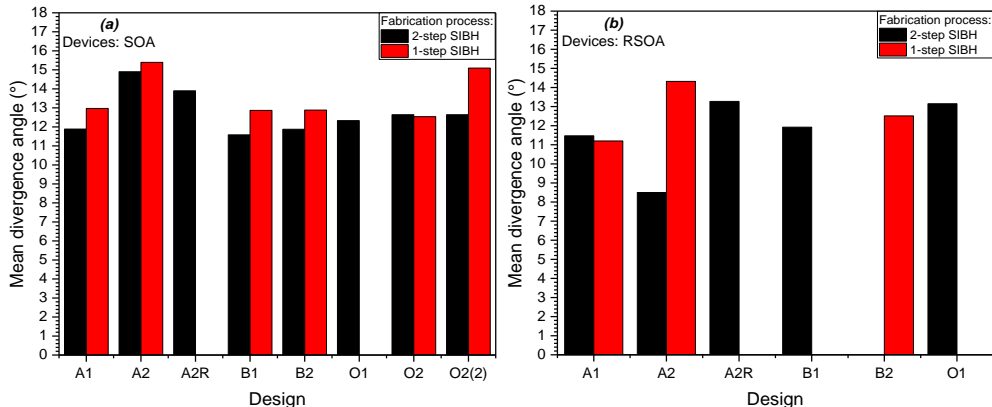


Figure 185. Comparison between the mean divergence angles of the (a) SOAs and (b) RSOAs, manufactured with both fabrication processes.

Consequently, the coupling efficiency between the 2-step SIBH devices and the optical fibers should be better than for the 1-step SIBH devices.

From the ASE spectra results, we observe a higher carrier consumption from the Ax devices when manufactured with the 1-step SIBH process. Depending on the design, the ASE bandwidths are different with both processes, as illustrated in Figure 186 (a) for the SOAs and in Figure 186 (b) for the RSOAs.

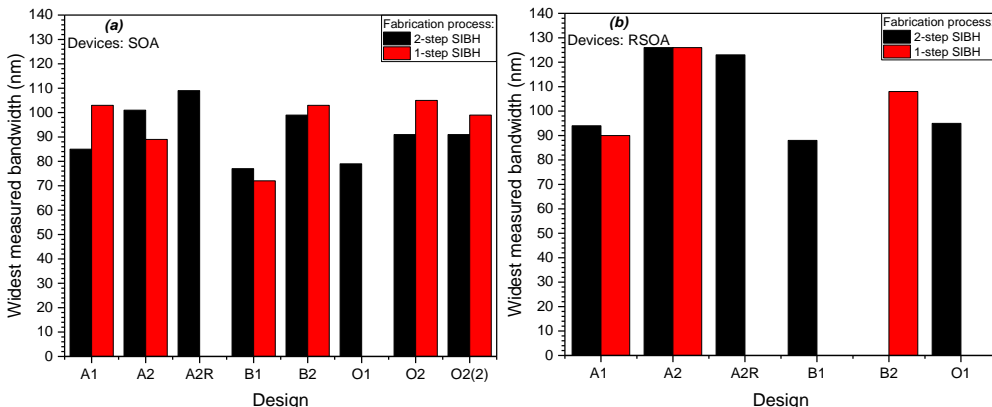


Figure 186. Comparison between the ASE bandwidths of the (a) SOAs and (b) RSOAs, manufactured with both fabrication processes.

We cannot determine a general behavior in function of the fabrication process (1-step or 2-step SIBH), but the bandwidth is impacted by the fabrication steps' conditions (during the epitaxy, as well as during the technological process). Nevertheless, to compare the processes, we should focus on the main parameters of an optical amplifier, the gain, the NF and the P_{sat} .

In terms of bandwidth, the measurements cannot always be compared because of the bench limitations, as illustrated in Figure 187. When they can be compared, the 2-step SIBH process seems to show larger bandwidths.

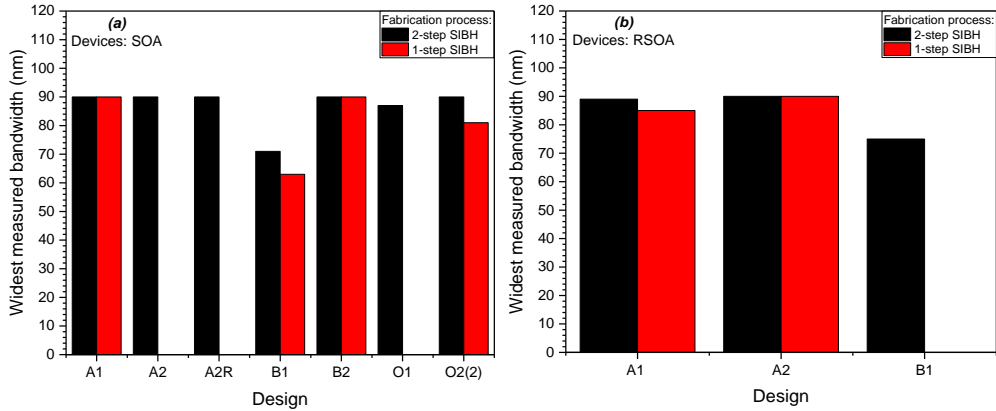


Figure 187. Comparison between the gain bandwidths of the (a) SOAs and (b) RSOAs, manufactured with both fabrication processes.

However, we can compare the maximal gain of the flat gain spectra, as illustrated in Figure 188 (a) and (b) for SOA and RSOAs, respectively.

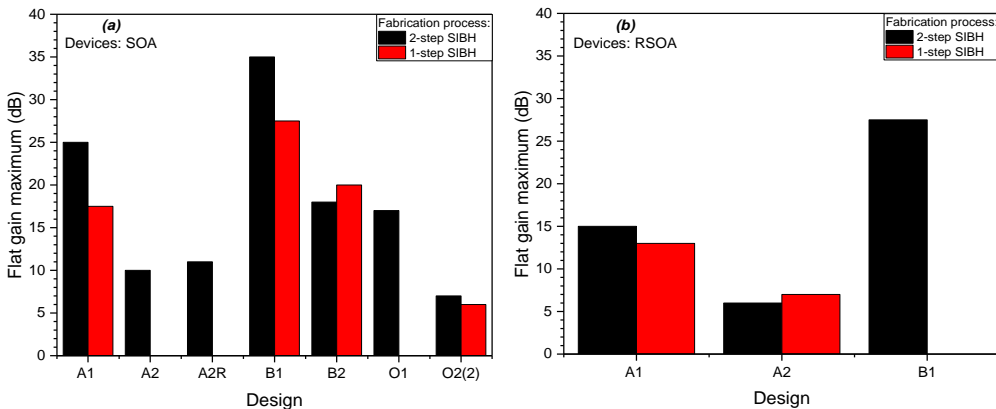


Figure 188. Comparison between the flat gain maxima of the (a) SOAs and (b) RSOAs, manufactured with both fabrication processes.

For the devices exhibiting the highest gain values (A1 and B1), we can conclude that the 2-step SIBH process gives better performances. For the others, we can also analyze the injected current densities required to reach the flat gain. Figure 189 gives us this information for each studied device, comparing 1-step and 2-step SIBH.

With these graphs, we see that the 1-step SIBH devices tend to have the same carrier consumption than the 2-step SIBH ones. This is even more visible with the RSOAs compared in Figure 189 (b).

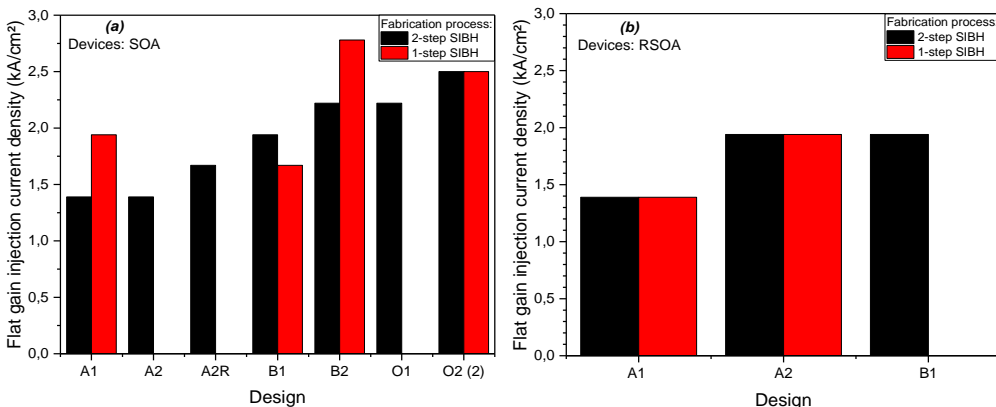


Figure 189. Flat gain injection current densities comparison between the (a) SOAs and (b) RSOAs, manufactured with both fabrication processes.

The NF is compared between the fabrication processes in Figure 190. With these graphs, we observe that for similar devices, the NF often reaches higher values when the fabrication process is the 1-step SIBH.

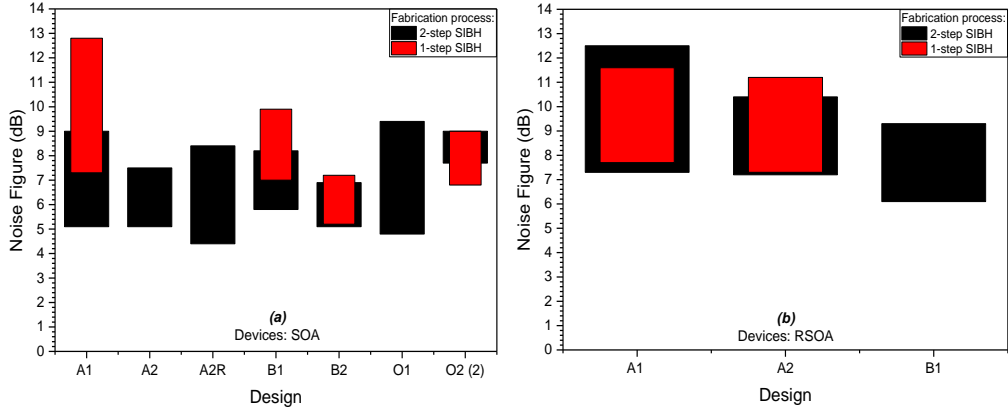


Figure 190. Comparison between the NF at the flat gain spectrum current density of the (a) SOAs and (b) RSOAs, manufactured with both fabrication processes, in the wavelength range corresponding to the optical bandwidth.

The last parameter to analyze is the P_{sat} , which is also better for the 2-step SIBH manufactured devices, as displayed in Figure 191

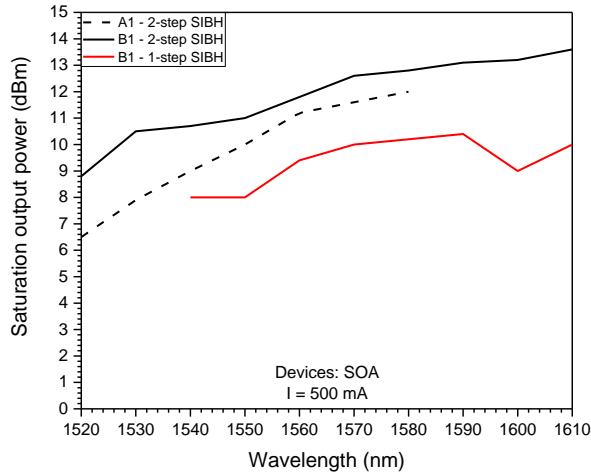


Figure 191. Comparison between the measurable P_{sat} from the SOA manufactured with both fabrication processes.

As a conclusion, the three main performance parameters are generally better with the 2-step SIBH fabrication process, showing that improvements are still required to reach the same performances by reducing the number of fabrication steps to manufacture SOAs and RSOAs. The growth conditions of the 1-step SIBH regrowth are still to be optimized, and the impacts of this regrowth step, that we studied in Chapter III, must be taken into account since the devices' design. Also, in general, the proposed designs are compromises between the gain, NF and P_{sat} performances. The implementation of a variable optical confinement would lead to benefits in terms of performances.

4. Position in the state of the art

In both C+L-Band and O-Band, our devices show correct results, nearly achieving every objective set by the requirements in Chapter I. In this section, we will compare the performances of our devices with the state of the art that can be find in literature but also with commercial devices.

4.1. C+L-Band

In the C+L-Band, we can compare the performances of wideband devices, like in Figure 192, in terms of Gain and NF, that is represented with two blue points for its maximum and minimum values.

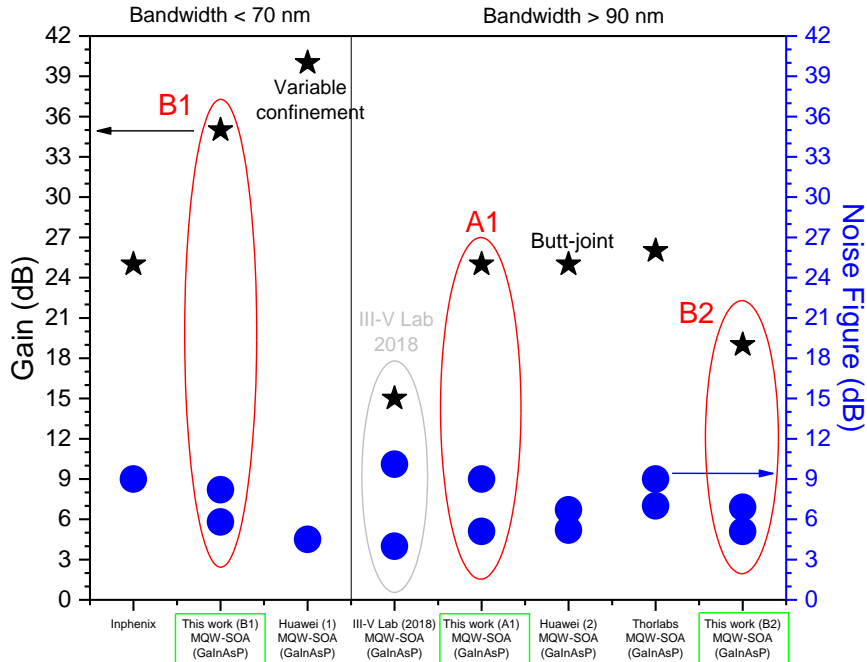


Figure 192. Gain and NF performances comparison in the C+L-Band [7, 8, 9, 10, 11].

In the left part of the graph, we compare devices from InPhenix and Huawei that present state of the art performances in terms of Gain and NF, but with bandwidths under 70 nm, with our B1 SOA. We see that to improve the performances of our device, we have to deal with more complex structures that include variable optical confinement. This technique consists in the growth and the etching of a high refractive index material above the active region to modify the optical confinement along the device.

With the A1 SOA, we highlight the laboratory progress for the fabrication of the SOAs as the performances are better than the ones obtained in the previous projects, with a significantly similar. Also, in Figure 193, we see that the P_{sat} is also better.

For the B2 SOA, we can highlight the NF and the bandwidth that are at the state of the art.

In the C+L-Band, we observe that limits are reached with the use of common MQW-based structures. Consequently, we have to develop new designs to avoid the balance between gain, NF and P_{sat} , by conserving the wideband behavior we succeed to obtain.

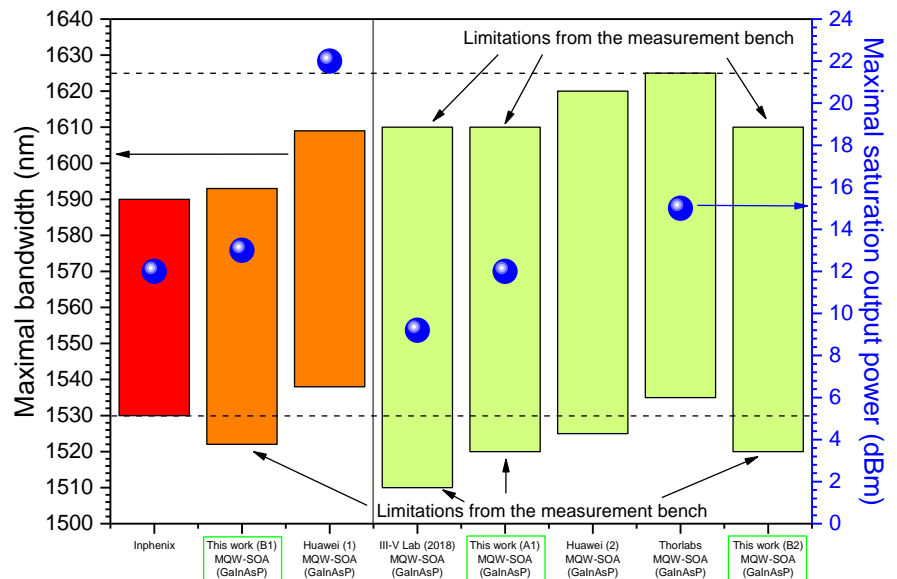


Figure 193. Bandwidth and Saturation output power performances comparison in the C+L-Band.

4.1. O-Band

In the O-Band, there is a lack of wideband devices, as shown by Figure 194. Thus, we must compare the O1 SOA performances with small bandwidth devices from the literature and the commercially available devices.

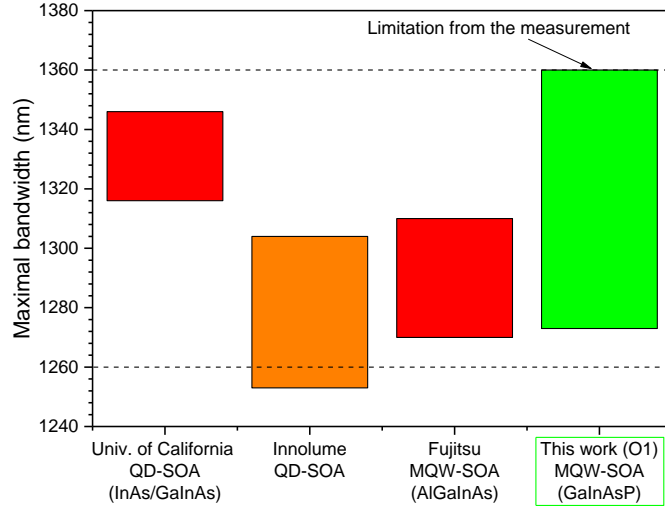


Figure 194. Bandwidth comparison in the O-Band [1, 12].

Figure 195 enables the comparison of these 4 devices in terms of Gain and Noise Figure.

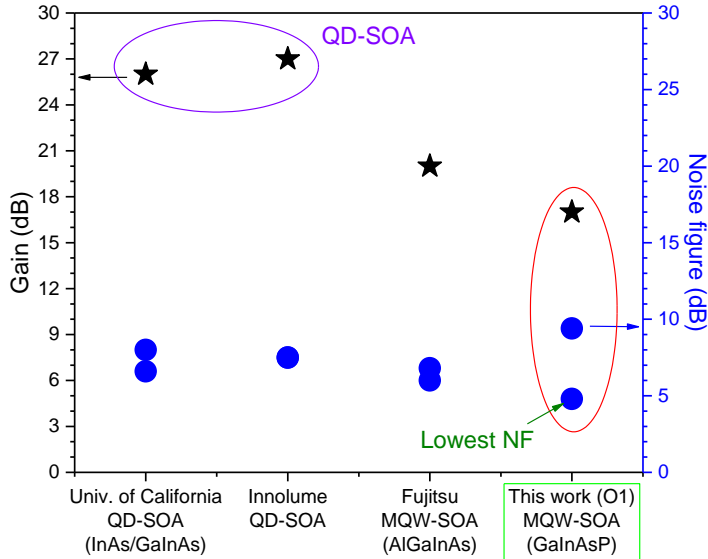


Figure 195. Gain and Noise Figure performances comparison in the O-Band.

In this figure, we can observe that the best gain values are obtained with QD-based active regions. However, our O1 SOA shows interest in terms of NF as it shows the lowest value. Also, the maximal NF measured with our device depends on its wideband behavior, as the NF is increased at the lowest wavelengths of the amplified band.

Consequently, to increase our devices in the O-Band, higher optical confinements have to be studied to reach higher gain values. This would also decrease the P_{sat} that could be measured with our measurement bench.

5. Conclusion

In this chapter, we analyzed the performances of our devices. First, we studied the ones fabricated following the mature 2-step SIBH process. Then, we did the same thing with the newly developed 1-step SIBH processed devices, and compared the different designs. We compared their mode profiles using far field measurement, as well as their ASE spectra in terms of ASE bandwidth and injected current densities to obtain a flat ASE spectrum. We also compared the devices in terms of gain, NF and P_{sat} .

These comparisons were lead in the C+L-Band and the O-Band.

From the C+L-Band devices, we observed that the thinning of the QWs changed the ASE and gain spectra aspect. Because of the lower confinement of e_2 in the MQW, the injected current required to reach the flat gain spectrum is high with thin QWs. Moreover, the $e_2\text{-}hh_2$ quickly exhibits high gain values with the 14 nm thick based designs. This phenomenon leads to the narrowing of the optical bandwidth with the increase of the injected current. With thinner QWs, the $e_2\text{-}hh_2$ transition's wavelength does not show a peak apparition. This enable to keep large bandwidths with high injected currents that are shifted toward smaller wavelengths. Another conclusion is that lower optical confinement leads to wider bandwidths, because of the gain decrease. However, this parameter must be well set to avoid same levels of gain and NF and keeping a large bandwidth. Our B2 design, with a simulated optical confinement of 4.34 % seems to be the best compromise between gain, NF and wide bandwidths, at the cost of high injected current densities. The Bx designs are also opening a way to amplification in the S-Band, which is also interesting for the long distance transmissions.

In terms of RSOAs, the best measured device is the one based on the B1 design, providing much higher gain than NF. However, its bandwidth is still limited to 75 nm (1526 – 1601 nm). Consequently, it would have been interesting to measure a RSOA based on the B2 design, or to manufacture and measure a RSOA structure with an optical confinement value ranging between the ones of the A1 and the B1 designs, 5.33 % and 5.97 %, respectively.

For the O-Band, the 2-step SIBH manufactured SOA based on the O1 design is a first demonstration of a wideband SOA based on a GaInAsP MQW structure, operating in this wavelength range with a gain value of 17 dB, over 87 nm (1273 – 1360 nm) and a minimal NF of 4.8 dB. This device proposes a more compact solution with a wider bandwidth than the existing solutions. However, the gain values still require to be increased with higher optical confinement. The optical confinement of 3.23 % was too low for the O2 design to observe satisfying gain values with SOAs.

Finally, we also compared the fabrication processes used for the SOAs and RSOAs. The 2-step SIBH, that is the classic process used in the laboratory still shows better results than the 1-step SIBH process, that is newly developed.

As perspective, for the C+L-Band, in order to achieve a reduction of the NF, with high gain, high P_{sat} , while keeping a wideband device, works are lead to fabricate variable optical confinement SOAs. The variation of this parameter between the input, the middle part and the output of the device could enable to avoid a compromise between the parameters' performances.

In the O-Band, to enable the fabrication of RSOAs, we should target higher optical confinements than for the O1 design, i.e. 4.79 %. We could also enlarge the QWs to observe the same ASE and gain behavior as in the C+L-Band that could reduce the gain, but also the carrier's consumption and enlarge the bandwidth.

For the 1-step SIBH, improvements such as: (i) better SIBH regrowth conditions, (ii) material modification from the blocking layer or (iii) to take into account the impacts of the SIBH regrowth over the base GSMBE structure since the design phase, are still required to obtain the same performances as the 2-step SIBH and take benefits from its shorter number of steps.

Bibliography

- [1] S. Liu, J. Norman, M. Dumont, D. Jung, A. Torres, A. C. Gossard and J. E. Bowers, "High-performance O-Band quantum-dot semiconductor optical amplifiers directly grown on a CMOS compatible silicon substrate," *ACS photonics*, vol. 6, pp. 2523-2529, 2019.
- [2] H. Wang, E. T. Aw, M. Xia, M. G. Thompson, R. V. Penty, I. H. White and A. R. Kovsh, "Temperature independent optical amplification in uncooled quantum dot optical amplifiers," in *OFC*, San Diego, CA, USA, 2008.
- [3] N. K. Thipparapu, A. A. Umnikov, P. Barua and J. K. Sahu, "Bi-doped fiber amplifier with a flat gain of 25 dB operating in the wavelength band 1320-1360 nm," *Optics letters*, vol. 41, no. 7, pp. 1518-1521, 2016.
- [4] Y. Nishida, M. Yamada, T. Kanamori, K. Kobayashi, J. Temmyo, S. Sudo and Y. Ohishi, "Development of an efficient praseodymium-doped fiber amplifier," *IEEE journal of quantum electronics*, vol. 34, no. 8, pp. 1332-1339, 1998.
- [5] S. Tanaka, A. Uetake, S. Okumura, M. Ekawa, G. Nakagawa and K. Morito, "Uncooled, polarization-insensitive AlGaInAs MQW-SOA module operable up to 75°C with constant current," in *ECOC*, Geneva, SWITZERLAND, 2011.
- [6] B. Kanwal, A. Armghan, S. Ghafoor, A. Atieh, M. Sajid, T. Kausar, J. Mirza and Y. Lu, "Design and analysis of an O+E-Band hybrid optical amplifier for CWDM systems," *Micromachines*, vol. 13(11), no. 1962, pp. 1-13, 2022.
- [7] "InPhenix - Semiconductor Optical Amplifier," [Online]. Available: <https://www.inphenix.com/en/semiconductor-optical-amplifiers/>. [Accessed 9 August 2023].
- [8] S. Yu, A. Gallet, H. Elfaiki, N. El Dahdah and R. Brenot, "Novel semiconductor optical amplifier with large gain and high saturation output power," in *European conference on optical communication (ECOC)*, Bordeaux, FRANCE, 2021.
- [9] A. Verdier, "Modélisation, conception, fabrication, caractérisation et valorisation d'amplificateurs optiques à semiconducteur de très large bande spectrale. (Ph.D Thesis)," Université de Toulouse, Toulouse, FRANCE, 2018.
- [10] S. Yu, A. Gallet, N. El Dahdah, H. Elfaiki, I. Demirtzioglou, L. Godard and R. Brenot, "Flat noise figure semiconductor optical amplifiers," in *European Conference on Optical Communication (ECOC)*, Bordeaux, FRANCE, 2021.
- [11] "L-Band Booster Optical Amplifiers (BOAs), 1590 - 1625nm," [Online]. Available: https://www.thorlabs.com/newgroupage9.cfm?objectgroup_id=3991. [Accessed 9 August 2023].
- [12] "Innolume - Semiconductor Optical Amplifiers," [Online]. Available: <https://www.innolume.com/innoproducts/semiconductor-optical-amplifiers-soa/>. [Accessed 9 August 2023].

Figures

Figure 143. Schematic representation of the far field measurement setup (a) from above and (b) from the front of the detector and slot.....	121
Figure 144. Schematic of the divergence angle calculation.....	122
Figure 145. Gaussian fit showing the determination of x_i for the divergence angle calculation.....	122
Figure 146. Mode profile horizontal and vertical sections, from SOAs on the left and RSOAs on the right.....	123
Figure 147. 2D mode profiles measured from the 2-step SIBH SOAs, at 1 A, on the left and RSOAs, at 500 mA, on the right.....	124
Figure 148. Comparison between P(I) measurement (red line) and far field mode profile for SOA with design A1.....	125
Figure 149. Comparison between P(I) measurement (red line) and far field mode profile for SOA with design A2.....	125
Figure 150. 2D mode profile from 2-step SIBH SOAs and RSOA operating in O-Band.....	126
Figure 151. ASE Spectra measured from 2-step SIBH SOAs based on (a) the A1 design, (b) the A2 design, (c) the A2R design	127
Figure 152. ASE Spectra measured from SOAs with (a) design B1 and (b) design B2.	128
Figure 153. ASE spectra measured from RSOAs with (a) design A1, (b) design A2 and (c) design A2R.	129
Figure 154. ASE spectra measured from RSOA with design B1.....	129
Figure 155. ASE Spectra measured from O-Band SOAs, based on (a) O1 design and (b) O2 design.	130
Figure 156. ASE spectra measured from the O1 design RSOA.....	130
Figure 157. Schematic representation of the optical gain measurement setup, with a SOA CoC.....	132
Figure 158. Schematic representation of the optical gain measurement setup, with a RSOA CoC.	132
Figure 159. C+L-Band SOAs' Gain spectra from devices based on (a) A1, (b) A2, (c) A2R, (d) B1 and (e) B2 designs.....	134
Figure 160. C+L-Band RSOAs' Gain spectra from devices based on (a) A1, (b) A2 and (c) B1 designs.	135
Figure 161. O-Band SOAs' Gain spectra based on (a) O1 and (b) O2 designs.....	136
Figure 162. NF measured from C+L-Band SOAs, based on (a) A1, (b) A2, (c) A2R, (d) B1 and (e) B2 designs.....	139
Figure 163. NF measured from C+L-Band RSOAs, based on (a) A1, (b) A2 and (c) B1 designs.....	140
Figure 164. NF measured from O-Band SOAs, based on (a) O1 and (b) O2 designs.....	140
Figure 165. Saturation output power measurement from the A2 design SOA, 500 mA.....	142
Figure 166. Gain as function of output power for (a) A1 and (b) B1 SOAs.	142
Figure 167. Saturation output power of the A1 and B1 SOAs as function of the wavelength.....	143
Figure 168. 2D mode profiles measured from the 1-step SOAs on the left and RSOAs on the right.	144
Figure 169. 2D mode profiles measured from the 1-step O-Band SOAs.....	145
Figure 170. ASE Spectra measured from 1-step SIBH SOAs, based on (a) A1 and (b) A2 designs..	146
Figure 171. ASE Spectra measured from 1-step SIBH SOAs, based on (a) B1 and (b) B2 designs...	146
Figure 172. ASE Spectra measured from 1-step SIBH RSOAs, based on (a) A1 and (b) A2 designs.	147
Figure 173. ASE Spectra measured from 1-step SIBH B2 design RSOA.	147
Figure 174. ASE Spectra measured from 1-step SIBH (a) O2(1) and (b) O2(2) SOAs.....	148
Figure 175. Gain spectra from the 1-step SIBH C+L-Band SOA based on the A1 design.....	149
Figure 176. Gain spectra from the 1-step SIBH C+L-Band SOAs based on the (a) B1 and (b) B2 designs.	149
Figure 177. Gain spectra from the 1-step SIBH C+L-Band RSOAs based on the (a) A1 and (b) A2 designs.....	150

Figure 178. Gain spectra from the 1-step SIBH O2(2) SOA.....	150
Figure 179. NF from the 1-step SIBH C+L-Band SOA based on the A1 design.....	152
Figure 180. NF from the 1-step SIBH C+L-Band SOAs based on the (a) B1 and (b) B2 designs.	152
Figure 181. NF from the 1-step SIBH C+L-Band RSOAs based on the (a) A1 and (b) A2 designs ..	153
Figure 182. NF from the 1-step SIBH O2(2) SOA	153
Figure 183. Gain as function of the output power of the 1-step SIBH SOA based on the B1 design.	154
Figure 184. P_{sat} of the B1 SOAs as function of the wavelength	154
Figure 185. Comparison between the mean divergence angles of the (a) SOAs and (b) RSOAs, manufactured with both fabrication processes.	155
Figure 186. Comparison between the ASE bandwidths of the (a) SOAs and (b) RSOAs, manufactured with both fabrication processes.	155
Figure 187. Comparison between the gain bandwidths of the (a) SOAs and (b) RSOAs, manufactured with both fabrication processes.	156
Figure 188. Comparison between the flat gain maxima of the (a) SOAs and (b) RSOAs, manufactured with both fabrication processes.	156
Figure 189. Flat gain injection current densities comparison between the (a) SOAs and (b) RSOAs, manufactured with both fabrication processes.	156
Figure 190. Comparison between the NF at the flat gain spectrum current density of the (a) SOAs and (b) RSOAs, manufactured with both fabrication processes, in the wavelength range corresponding to the optical bandwidth.	157
Figure 191. Comparison between the measurable P_{sat} from the SOA manufactured with both fabrication processes.....	157
Figure 192. Gain and NF performances comparison in the C+L-Band [7, 8, 9, 10, 11].	158
Figure 193. Bandwidth and Saturation output power performances comparison in the C+L-Band. ..	159
Figure 194. Bandwidth comparison in the O-Band [1, 12].	160
Figure 195. Gain and Noise Figure performances comparison in the O-Band.	160

Tables

Table 55. Beam divergence angles (2θ) at FWHM for 2-step SIBH devices at 500 mA for every device.	126
Table 56. ASE performances measured from 2-step SIBH SOAs.	131
Table 57. ASE performances measured from 2-step SIBH RSOAs.....	131
Table 58. Gain performances from the 2-step SIBH SOAs.	136
Table 59. Gain performances from the 2-step SIBH RSOAs.	137
Table 60. Gain comparison between the O1 device and the literature in terms of gain and bandwidth.	137
Table 61. NF performances at flat gain current for 2-step SIBH SOAs.....	141
Table 62. NF performances at flat gain current for 2-step SIBH RSOAs.	141
Table 63. Beam divergence angles (2θ) at FWHM for 1-step SIBH devices at 500 mA for every device.	145
Table 64. ASE performances measured from 1-step SIBH SOAs.	148
Table 65. ASE performances measured from 1-step SIBH RSOAs.....	148
Table 66. Gain performances of the 1-step SIBH fabricated devices.....	151
Table 67. NF performances of the 1-step SIBH fabricated devices.	153

Conclusions & Perspectives

The growth and fabrication of devices such as SOAs and RSOAs represents a challenge, because of the high performance targets and the difficulty of achieving a compromise on all these performances. Their development to offer wideband amplification with high gain values, low NF and high P_{sat} still needs to be pursued.

During this work, we focused on the design of different structures enabling us to study the behavior of these devices according to several parameters: (i) the optical confinement, (ii) the QWs' thickness and (iii) the fabrication process used with variants for the top cladding regrowth. It gave us considerable amount of data to deepen our knowledge of these devices. This work has also allowed us to manufacture, for the first time, a O-Band SOA based on a GaInAsP MQW structure.

In the first chapter, we set out the context to the development of SOAs and RSOAs for various applications. Telecommunications are at the forefront, but security, environmental monitoring and healthcare also require this type of device. We also presented the different technologies used for optical amplification, namely xDFAs and Raman amplifiers. For SOAs and RSOAs, we focused this section on the materials used for amplification at the desired wavelengths (C+L-Band and O-Band), as well as on the key parameters of these devices (Gain, Bandwidth, NF, P_{sat} , ...) in order to determine our performance objectives. We also explored broadband amplification solutions, such as the addition of passive elements or the combination of multiple amplifiers. We concluded our first chapter with a review of the state-of-the-art and a presentation of previous projects carried out at the III-V Lab on the development of SOAs and RSOAs and defined the targets of this work.

The main theme of our second chapter is the conception of several SOA designs. We explained the impact of stress on the bandgap energies and polarization sensitivity of the devices. We also presented SOA designs based on "thin" wells and made comparison with ones based on "thick" wells to justify our orientation towards this second category. We also carried out material gain and band structure simulations, which led to the design of 3 different active zones (2 in C+L-Band and 1 in O-Band). We optically simulated all our structures using refractive indices obtained from various models presented in the literature. By comparing these models with laboratory measurements, we were able to propose 6 different SOA designs, 4 in C+L-Band and 2 in O-Band. These designs were used to analyze two characteristics of the structures: the thickness of the quantum wells and the optical confinement in the active zone.

The third chapter was devoted to the fabrication of our structures. Initially, we focused on presenting the two involved epitaxy techniques, namely MOCVD and MBE, more specifically, GSMBE. We presented in detail the reactor used for the growth of the SOAs' base structures, as well as the steps required to obtain layers of high crystalline quality material. The growth of GaInAsP quaternary compound, particularly in the active zones, is not trivial. Material characterizations carried out on our layers have highlighted miscibility gap phenomenon, as well as critical thickness issues. Optimizing the growth conditions was a key step in the success of this work, as they have a major influence on the performance of the final devices. Once the building blocks for the structures were calibrated (Slab, GaInAsP quaternary compounds, MQW, top cladding), we were able to grow and characterize the base structures of our SOAs and RSOAs. Photoluminescence, X-ray diffraction, C-V and photocurrent measurements were performed. We were also able to study technology transfer between two GSMBE reactors, thanks to the acquisition of a new MBE412, during this work. A total of 21 wafers were produced by GSMBE. Two fabrication processes were explored for SOAs and RSOAs at the III-V Lab: the mature 2-step SIBH and the newly developed, 1-step SIBH. The growth of several twin wafers

enabled us to compare devices' performance between these processes. The use of these two processes provided an opportunity to study their impact during the re-growth stages. 15 wafers were finalized (7 using the 1-step SIBH process and 8 using the 2-step SIBH). Finally, we detailed the back-end steps involved in obtaining the unit components from the wafers. Among these steps, a preselection of the most interesting devices was performed to limit the number of sub-base assemblies executed for this work.

The final chapter focused on the characterization of the various devices and the processing of this data. These characterizations included measurements of: (i) far-fields images, to analyze the coupling with the fiber, (ii) ASE spectra, to determine a first ASE bandwidth, (iii) gain, to know the maximum values reached for broadband amplification, but also to analyze the real bandwidths of the components, as well as their consumption, (iv) NF, and finally (v) P_{sat} , for the devices allowing their achievement. For C+L-Band gain measurements, the bandwidth is generally limited by the laser source used in the test bench. The power of this source also severely limits the measurement of our devices' P_{sat} . For the O-Band, the measured bandwidth corresponds to the wavelength range (1260 – 1360 nm), but the source's power keeps limiting the P_{sat} measurements.

The first comparisons were made for structures manufactured with the 2-step SIBH. Among the SOAs measured in C+L band, the reference structure based on 14 nm wells and 5.33% optical confinement, showed the best performances, with a maximum gain of 25 dB and an optical bandwidth of more than 90 nm. The structure based on 11 nm wells and 5.97% optical confinement also provided encouraging results, with a maximum gain of 35 dB. However, the low electronic confinement of the e_2 level is detrimental in terms of bandwidth (71 nm) and power consumption. On the other hand, the bandwidth of this second design is shifted towards shorter wavelengths, making it interesting for the S+C band. The NF of these two designs remains similar, with values ranging from 9.0 to 5.1 dB and from 8.2 to 5.8 dB for these designs, labelled "A1" and "B1", respectively. Moreover, they are the only ones whose P_{sat} could be measured, with better values obtained by the "B1" design, due to its thinner QW. The designs realized with optical confinement values of 4.34 and 3.38%, noted "B2" and "A2", respectively, presented reduced gain values of 19 and 10 dB. However, the ASE spectra showed that they have the widest ASE bandwidths. A variant of the "A2" design, the "A2R" design, was introduced to observe whether the growth technique used for the P-type cladding regrowth influences performance. According to our characterizations, the results obtained did not reveal any major impact. With RSOAs, the same conclusions as for SOAs can be drawn. However, it is important to note that the gain values are significantly lower for these devices, with 15 dB for the "A1" design and 27.5 dB for the "B1" design. Their NFs are also significantly higher than the ones measured for SOAs. Further development of RSOAs is still needed to achieve the performance shown by SOAs. In O-band, the "O1" and "O2" designs were based on 11 nm wells. The results of the "O2" design are not satisfying enough to be implemented in systems, but do pose a limit on optical confinement, that must be taken into account for future developments. The "O1" design presented very promising results for the development of high-performance SOAs operating in the O-Band. It is the first demonstration of a SOA based on GaInAsP QW amplifying in this wavelength range. The maximum gain achieved is 17 dB, over a bandwidth of 87 nm. The NF, in this bandwidth, is high at short wavelengths (9.4 dB), but low at the longest wavelengths (4.8 dB). Unfortunately, P_{sat} could not be observed for these components.

We also characterized the devices manufactured following the 1-step SIBH process, and compared their performances with the ones of the 2-step SIBH devices. With the 1-step SOAs and RSOAs, we observe the same behaviors as with the 2-step SIBH devices. The 14 nm thick based structures show wider bandwidth, but lower gain than the 11 nm thick based structures. Nevertheless, the "B2" design showed a higher maximum gain value for its flat gain (20 dB) than the "A1" design (17.5 dB). This is explained by the higher current density required to achieve the flattest gain with the "B2" design. The RSOAs keep providing less gain than the SOAs with similar bandwidth but higher NF values.

By comparing the 1-step SIBH and 2-step SIBH devices' performance, we observe that the 2-step SIBH devices are better than the 1-step SIBH ones. This second process is still under development to improve the resulting performance, while benefiting from its reduced number of steps.

SOAs and RSOAs are also being developed, with a variable optical confinement, both at III-V Lab and competitive companies. A way to achieve it is to grow a high refractive index material on the top of the ridges and modify this layer's geometry to control the optical confinement along the devices' ridges [1]. It would enable low optical confinement to be achieved at the input and output facets of the devices, reducing the NF and allowing to reach high P_{sat} values. In the middle part of the devices, the optical confinement would be increased to provide high gain values. With our reference design, in the C+L-Band, the gain and the P_{sat} are the performances to increase. To increase the gain values, a solution is to raise the optical confinement. It is more difficult for the P_{sat} which would decrease with this modification. For this parameter, the SOAs made with "thin" QWs provided an interesting option, but the bandwidth has to be enlarged to cover the 95 nm of the C+L-Band. In this view, the active region's materials should be modified, or the QW should be slightly thicker to enhance the high energy transitions' contributions to the gain spectrum. Finally, we can add an optical filter to extend the bandwidth at the cost of a lower maximal gain. The "thin" QW based structures also showed basis for the realization of S+C-Band devices. This is an important point, as the S-Band will be soon a wavelength range of interest for optical communication data traffic. For the O-band, the results lay the foundations for the possible development of wideband SOAs covering this wavelength range entirely, with satisfactory gain and NF values to boost the performance of systems used for short distances transmissions. The gain must be increased with higher optical confinement and the bandwidth has still to be enlarged to cover the lower wavelengths of the O-Band. This second objective is much more difficult to achieve in this wavelength range than in the C+L-Band. However, the 14 nm thick QW structures, designed for the C+L-Band, showed larger optical bandwidths than the 11 nm thick QW based devices. Consequently, we could try to enlarge the QW thickness, even if in the theory, it should reduce the optical bandwidth. Finally, for the 1-step SIBH, even if the devices' performances are lower the ones of the 2-step SIBH, this process is still under development at III-V Lab, with extensive work over the regrowth conditions and their impacts on the base structure.

Bibliography:

- [1] S. Yu, A. Gallet, H. Elfaiki, N. El Dahdah and R. Brenot, "Novel semiconductor optical amplifier with large gain and high saturation output power," in *European conference on optical communication (ECOC)*, Bordeaux, FRANCE, 2021.

Acronyms

A

AON – Active Optical Network

APCVD – Atmospheric Pressure Chemical Vapor Deposition

AR – Anti-Reflection coating

ASE – Amplified Spontaneous Emission

Al – Aluminum

AlGaInAs – Aluminum Gallium Indium Arsenide

AlGaInAsPSb – Aluminum Gallium Indium Arsenide Phosphide Antimonide

Ar - Argon

As – Arsenic

AsH₃ – Arsine

Au – Gold

B

BB – Building Block

BDFA – Bismuth Doped Fiber Amplifier

BEP – Beam Equivalent Pressure

BRS – Buried Ridge Structure

Be – Beryllium

Bi – Bismuth

C

CCS – Closed-coupled Showerhead

CD – Chromatic Dispersion

CoC – Chip on Carrier

CVD – Chemical Vapor Deposition

CHF₃ – Trifluoromethane

D

DBR – Distributed Bragg Reflector

DFB laser – Distributed Feedback laser

DIBS – Dual Ion Beam Sputtering

E

E-beam – Electron beam

ECV – Electrochemical Capacitance-Voltage measurement

EDFA – Erbium Doped Fiber Amplifier

EDTFA – Erbium Doped Tellurite Fiber Amplifier

e-gun – Electron gun

Er – Erbium

E_g – Bandgap Energy

E_p – Bound state Energy

F

FEL – Fast Entry Load-lock

FFT – Fast Fourier Transform

FMF – Few-Mode Fiber

FP – Fabry-Pérot

FWHM – Full Width at Half Maximum

Fe - Iron

G

GSMBE – Gas Source Molecular Beam Epitaxy

Ga – Gallium

GaAs – Gallium Arsenide

GaInAs – Gallium Indium Arsenide

GaInAsP – Gallium Indium Arsenide Phosphide

GaP – Gallium Phosphide

G – Gain

G_{chip} – Chip Gain

G_{ff} – Fiber to Fiber Gain

H

HBT – Heterojunction Bipolar Transistor

HR – High-Reflection coating

HRXRD – High Resolution X Ray Diffraction

HF – Fluoric acid

H_2 – Dihydrogen

H_2SO_4 – Sulfuric Acid

I

IBVA – Intervalence Band Absorption

ICP – Inductively Coupled Plasma

IR - Infrared

ITU – International Telecommunication Union

In – Indium

InAs – Indium Arsenide

InP – Indium Phosphide

K

KOH – Potassium hydroxide

L

LPCVD – Low Pressure Chemical Vapor Deposition

LPE – Liquid Phase Epitaxy

LSHB – Longitudinal Spatial Hole Burning

LN_2 – Liquid nitrogen

M

MBE – Molecular Beam Epitaxy

ML – Mono Layer

MOCVD – MetalOrganic Chemical Vapor Deposition

MQW – Multi-Quantum Wells

N

nid – Non Intentionally Doped

NIR – Near InfraRed

Nd – Neodymium

NF – Noise Figure

N_{shot} – Shot Noise

$N_{\text{sp-sp}}$ – Spontaneous-Spontaneous beat Noise

$N_{\text{s-sp}}$ – Signal-Spontaneous beat Noise

O

OCT – Optical Coherence Tomography

OLT – Optical Line Terminal

ONU – Optical Network Unit

OSA – Optical Spectrum Analyzer

OSNR – Optical Signal to Noise Ratio

O - Oxygen

O₂ – Dioxygen

P

pBN – Pyrolytic Boron Nitride

PDFA – Praseodymium Doped Fiber Amplifier

PECVD – Plasma Enhanced Chemical Vapor Deposition

pHEMT – pseudomorphic High Electron Mobility Transistors

PL – Photoluminescence

PLD – Pulsed Laser Deposition

PON – Passive Optical Network

POS – Passive Optical Splitters

PVD – Physical Vapor Deposition

P(I) – Power-Intensity measurement

P – Phosphorus

P_{black} – Black phosphorus

P_{red} – Red phosphorus

P_{white} – White phosphorus

PH₃ – Phosphine

Pr – Praseodymium

Pt – Platinum

P_{ASE} – Amplified Spontaneous Emission Power

P_{in} – Input Power

P_{out} – Output Power

P_{sat} – Saturation Output Power

Q

QD – Quantum Dot

QMS – Quadrupole Mass Spectrometer

QW – Quantum Well

Q_{1.03} – GaInAsP compound emitting a wavelength of 1.03 µm

Q_{1.17} – GaInAsP compound emitting a wavelength of 1.17 µm

R

REAM SOA – Reflective Electro-Absorption Modulator Semiconductor Optical Amplifier

RHEED – Reflection High Energy Electron Diffraction

RIE – Reactive-Ion Etching

RIN – Relative Intensity Noise

RSOA – Reflective Semiconductor Optical Amplifier

R&D – Research and Development

S

SAG – Selective Area Growth

SCH – Separate Confinement Heterostructure

SCOW – Slab Coupled Optical Waveguide

SDM – Spatial Dimension Multiplexing

SEM – Scanning Electron Microscopy

SIBH – Semi-Insulating Buried Heterostructure

SIMS – Secondary Ion Mass Spectrometry

SL – Super Lattice

SLED (or SLD) – Super Luminescent Electro Diode

SMF – Single Mode Fiber

SOA – Semiconductor Optical Amplifier

SSMBE – Solid Source Molecular Beam Epitaxy

Sb – Antimony

SF₆ – Sulfur hexafluoride

Si – Silicon

SiO₂ – Silicon dioxide

T

TDFA – Thulium Doped Fiber Amplifier

TE – Transverse Electric

TM – Transverse Magnetic

Ti – Titanium

TiO₂ – Titanium dioxide

Tm – Thulium

TMAI – Trimethylaluminum

TMGa – Trimethylgallium

TMIn – Trimethylindium

U

UHV – Ultra High Vacuum

V

V(I) – Voltage-Intensity measurement

W

WDM – Wavelength Dimension Multiplexing

X

xDFA – Rare-earth Doped Fiber Amplifier

XRD – X-Ray Diffraction

Y

Yb – Ytterbium

Z

Zn - Zinc

Symbols

Γ – Optical confinement

Γ_{QW} – Optical confinement in the quantum wells

Γ_p – Optical confinement in the p doped top cladding

λ – Wavelength

2θ – Beam divergence angle

List of publications

Conference proceeding paper

H. Carrere, C. Calò, A. Balocchi, J.S. Rapagopal, X. Marie, A. Wilk, **Q. Hochart**, O. Delorme "Materials for wide-band amplification," *2022 13th International Symposium on Communication Systems, Networks and Digital Signal Processing (CSNDSP)*, Porto, Portugal, 2022, pp. 686-689, *IEEE Proceedings*. DOI: 10.1109/CSNDSP54353.2022.9907902.

Oral presentations at international conferences

ICMBE 2022: "Gas-source MBE of GaInAsP-based Ultra-Wide Band Semiconductor Optical Amplifiers for telecom applications" **Q. Hochart**, O. Delorme, R. S. Joshya, H. Carrere, A. Balocchi, A. Elias, A. Bobin, C. Calò, D. Lanteri, K. Mekhazni, A. Wilk.

International Conference on Molecular Beam Epitaxy, from the 4th to the 9th of September 2022, Sheffield, ENGLAND.

EMRS Spring 2022: "Gain material for wide band amplification in long haul telecommunications" **Q. Hochart**, R. S. Joshya, A. Balocchi, O. Delorme, C. Calò, A. Wilk, H. Carrère

European Materials Research Society, from the 30th of May to the 3rd of June 2022, virtual conference.

CSW 2023: "Wideband semiconductor optical amplification covering both C+L-Band and O-Band" **Q. Hochart**, A. Elias, A. Bobin, C. Fortin, D. Lanteri, K. Mekhazni, O. Delorme, H. Carrère, A. Wilk

Compound Semiconductor Week, from the 29th of May to the 2nd of June 2023, Jeju, SOUTH KOREA.

COST Opera Workshop "Fundamental research – New materials" 2023: "Combining Molecular Beam Epitaxy and Metal-Organic Chemical Vapor Deposition for GaInAsP-based Ultra-Wide Band Semiconductor Optical Amplifiers for device's performance optimization" **Q. Hochart**, O. Delorme, A. Elias, H. Carrère, A. Wilk

European Cooperation in Science and Technology, European Network for Innovative and Advanced Epitaxy, from the 19th to the 21st of April 2023, Madrid, SPAIN.

Poster presentations

GDR Pulse Summer school 2021: "MBE-grown Be-doped InP and related materials behavior after high temperature annealing" **Q. Hochart**, A. Elias, O. Delorme, H. Carrère, A. Wilk

GDR Pulse Summer school 2021: "InGaAsP quantum-well active regions for telecom devices: design, growth and optical characterization" R. S. Joshya, **Q. Hochart**, A. Balocchi, O. Delorme, A. Wilk, H. Carrère

GDR CNRS "Processus Ultimes en épitaxie de Semiconducteurs", from the 2nd to the 8th of July 2021, Porquerolles, FRANCE.

Patent

"Planar Flip Chipped SiBH SOA" A. Garreau, **Q. Hochart**, J.F. Paret (submitted)

Abstract

Data transfer in optical fibers is constantly evolving and requires ever increasing data rates. As the spectral efficiency of transmitters is reaching its limit, it is now necessary to extend the spectral bandwidth used in the fibers. For long distance transmissions, in the C+L band (1530-1625 nm), for which absorption is minimal in optical fibers, Erbium Doped Fiber Amplifiers (EDFA) are currently used. However, their bandwidth is limited to 40 nm. Semiconductor Optical Amplifier (SOA) and Reflective SOA (RSOA) are serious candidates to replace them, with wide optical bandwidth up to 100 nm. During this thesis, we have designed and fabricated ultra-wideband SOAs and RSOAs showing performances equal to or better than the state of the art in C+L band. For short distance transmissions, in O band (1260-1360 nm), corresponding to the minimum chromatic dispersion in the fiber, there are no wideband amplification solutions. We have therefore designed and manufactured wideband SOAs to improve the capabilities of Access networks.

We have started the conception of ultra-wideband SOA structures in C+L and O-Bands by designing the band structures and the confinement of the electronic levels in the active region. This region is made of multiple quantum wells (MQW) based on GaInAsP. Then, we designed a super lattice of GaInAsP/InP layers with high refractive indices under the active region (bottom cladding). This electronic and optical confinement layer allows the regulation of the optical confinement in the active area, by attracting the mode towards the bottom of the structure, which limits the optical losses. We have designed 4 structures in C+L band and 2 in O band.

We grew the base SOA structures by Molecular Beam Epitaxy (MBE). These structures have thick quantum wells (14 and 11 nm), with compressive strain of about 1%. This strain had to be compensated in the barriers of the O-band structures to avoid material relaxation. 2 fabrication processes were then implemented: (i) the 2-step SIBH (for Semi-Insulating Buried Heterostructure), a classical process used for the fabrication of SOA and (ii) the 1-step SIBH, newly developed in the laboratory, allowing a reduction of the number of fabrication steps as well as a better current injection. For these 2 processes, ridges are etched into the base structures to perform the necessary epitaxy regrowth steps. The first step, common to both processes, is the regrowth of InP:Fe on both sides of the ridges to electrically insulate them. This step is performed by MetalOrganic Chemical Vapor Phase Deposition (MOCVD). For the 2-step SIBH, a second regrowth step is necessary to grow the electronic confinement layers, as well as a proton implantation step to electrically insulate the ridges from one another. The wafers are then thinned, metallized and cleaved to allow the mounting of the chips on carriers and their characterization.

The different SOAs and RSOAs obtained allowed the comparison of the 2 fabrication processes in terms of device performances. They all show an ultra-wideband behavior (>90 nm), high gain values (35 dB) and low noise figure (NF) (5 dB) in C+L band. In O band, the SOAs reach gains of 18.5 dB, with a low NF (5 dB) on wide bandwidths up to 75 nm, making the state of the art of wide band amplification in O-band.

Résumé

Les transferts de données par fibre optique sont en constante évolution et requièrent des débits toujours plus importants. L'efficacité spectrale des transmetteurs atteignant leur limite, il faut à présent s'orienter vers l'extension de la largeur spectrale utilisée dans les fibres. Pour les transmissions longues distances, dans la bande C+L (1530-1625 nm), pour laquelle l'absorption est minimale dans les fibres optiques, des amplificateurs à fibres dopées Erbium (Erbium Doped Fiber Amplifier – EDFA) sont actuellement utilisés. Cependant, leur bande passante est limitée à 40 nm. Les amplificateurs optiques à semiconducteur (Semiconductor Optical Amplifier - SOA) et « Reflective » SOA (RSOA) sont de sérieux candidats pour les remplacer, avec des larges bandes optiques pouvant atteindre 100 nm. Durant cette thèse, nous avons conçu et réalisé des SOA et RSOA très large bande montrant des performances supérieures ou égales à l'état de l'art en bande C+L. Pour les transmissions courtes distances, en bande O (1260-1360 nm), correspondant au minimum de dispersion chromatique dans la fibre, il n'existe pas de solutions d'amplification large bande. Nous avons donc conçu et fabriqué des SOA large bande, afin d'améliorer les capacités des réseaux d'accès.

Nous avons débuté la conception, en bandes C+L et O, de structures SOA très large bande par le design des structures de bande et du confinement des niveaux électroniques dans la zone active. Cette zone est faite de multi-puits quantiques (Multiple Quantum Wells – MQW) à base de GaInAsP. Nous avons ensuite conçu un super réseau de couches GaInAsP/InP à forts indices de réfraction sous la zone active (« Cladding » inférieur). Cette couche de confinement électronique et optique permet la régulation du confinement optique dans la zone active, en attirant le mode vers le bas de la structure, ce qui limite les pertes optiques. Nous avons ainsi conçu 4 structures en bande C+L et 2 en bande O.

Nous avons fabriqué les structures de base des SOA par épitaxie par jets moléculaires (Molecular Beam Epitaxy – MBE). Ces structures possèdent des puits épais (14 et 11 nm), avec des contraintes en compression de l'ordre de 1%. Cette contrainte a dû être compensée dans les barrières des structures en bande O pour éviter la relaxation du matériau. 2 processus de fabrication ont ensuite été mis en œuvre : (i) le SIBH 2 étapes (pour Semi-Insulating Buried Heterostructure), processus classique utilisé pour la fabrication des SOA et (ii) le SIBH 1 étape, nouvellement développé au laboratoire, permettant une réduction du nombre d'étapes de fabrication ainsi qu'une meilleure injection de courant. Pour ces 2 processus, les rubans sont gravés dans les structures de base pour réaliser les étapes de reprise d'épitaxie nécessaires. La première reprise, commune aux deux processus, est la croissance d'InP:Fe de part et d'autre des rubans pour les isoler électriquement. Cette étape est réalisée par dépôt en phase chimique aux métal-organiques (MetalOrganic Chemical Vapor Phase Deposition – MOCVD). Pour le SIBH 2 étapes, une seconde reprise est nécessaire pour la croissance des couches de confinement électronique ainsi qu'une étape d'implantation de protons pour isoler électriquement les rubans entre eux. Les plaques sont ensuite amincies, métallisées et clivées pour permettre le montage sur embase des composants et leurs caractérisations.

Les différents SOA et RSOA obtenus ont permis la comparaison des 2 processus de fabrication en terme de performances de composants. Ils présentent tous un comportement très larges bande (>90 nm), des valeurs de gain élevées (35 dB) et de faibles facteurs de bruit (Noise Figure – NF) (5 dB) en bande C+L. En bande O, les SOA atteignent des gains de 18,5 dB, avec un faible NF (5 dB) sur de larges bandes passantes allant jusqu'à 75 nm, faisant l'état de l'art de l'amplification large bande en bande O.